Advanced Ti – based AB and AB2 hydride forming materials

Wafeeq Davids

A thesis submitted in fulfillment of the requirements for the degree of Doctor Philosophiae in the Department of Chemistry, University of the Western Cape

Supervisor: Prof. V.M. Linkov

Co-supervisor: Dr. M.V. Lototsky

Scientific consultant: Prof. V.A. Yartys (Norway)

November 2011

Student Number: 2235735

DECLARATION BY CANDIDATE

I declare that *Advanced Ti – based AB and AB2 hydride forming materials* is my own work, that it has not been submitted before for any degree or examination in any other university, that all the sources I have quoted have been indicated and acknowledged as complete references.

Wafeeq Davids   **November 2011**

Signed: ……………..

ii

ACKNOWLEDGMENTS

I want to express my deepest gratitude to my family, whose support has been invaluable to me. To my parents Abedah and Magedien Davids, I am grateful for your love, understanding and patience with me always.

Finally, I would like to thank my wife **Fathiyah Davids**, for always being there for me. Thank you for your constant and endless love, support, understanding, patience and encouragement.

ABSTRACT

Ti – based AB and AB_2 hydride forming materials have shown to be very promising hydrogen storage alloys due to their reasonable reversible hydrogen storage capacity at near ambient conditions, abundance and low cost. However, these materials are not used extensively due to their poor activation performances and poisoning tolerance, resulting in significant impeding of hydrogen sorption. The overall goal of this project was to develop the knowledge base for solid-state hydrogen storage technology suitable for stationary and special vehicular applications focussing mainly on Ti – based metal hydrides. In order to accomplish this goal, the project had a dual focus which included the synthesis methodology of Ti – based AB and AB_2 materials and the development of new surface engineering solutions, based on electroless plating and chemical vapour deposition on the surface modification of Ti – based metal hydride forming materials using Pd-based catalytic layers.

TiFe alloy was synthesised by sintering of the Ti and Fe powders and by arc-melting. Sintered samples revealed three phases: TiFe (major), Ti_4Fe_2O, and β-Ti. Hydrogen absorption showed that the sintered material was almost fully activated after the first vacuum heating (400 ^{0}C) when compared to the arc-melted sample requiring several activation cycles. The increase in the hydrogen absorption kinetics of the sintered sample was associated with the influence of the formed hydrogen transfer catalyst, viz. oxygen containing $Ti_4Fe_2O_{1-x}$ and β-Ti, which was confirmed by the XRD data from the samples before and after hydrogenation. The introduction of oxygen impurity into TiFe alloy observed in the sintered sample significantly influenced on its PCT performances, due to formation of stable hydrides of the impurity phases, as well as destabilisation of both β-TiFeH and, especially, γ-$TiFeH_2$.

This finally resulted in the decrease of the reversible hydrogen storage capacity of the oxygen-contaminated sample.

TiFe alloy was also prepared via induction melting using graphite and alumo-silica crucibles. It was shown that the samples prepared via the graphite crucible produced TiFe alloy as the major phase, whereas the alumo-silica crucible produced $Ti_4Fe_2O_{1-x}$ and $TiFe_2$ as the major phases, and TiFe alloy as the minor one.

A new method for the production of TiFe – based materials by two-stage reduction of ilmenite ($FeTiO_3$) using H_2 and CaH_2 as reducing agents was developed. The reversible hydrogen absorption performance of the TiFe – based material prepared via reduction of ilmenite was 0.5 wt. % H, although hydrogen absorption capacity of TiFe reported in the literature should be about 1.8 wt. %. The main reason for this low hydrogen capacity is due to large amount of oxygen present in the as prepared TiFe alloy. Thus to improve the hydrogen absorption of the raw TiFe alloy, it was melted with Zr, Cr, Mn, Ni and Cu to yield an AB_2 alloy. For the as prepared AB_2 alloy, the reversible hydrogen sorption capacity was about 1.3 wt. % H at P=40 bar and >1.8 wt.% at P=150 bar, which is acceptable for stationary applications. Finally, the material was found to be superior as compared to known AB_2-type alloys, as regards to its poisoning tolerance: 10-minutes long exposure of the dehydrogenated material to air results in a slight decrease of the hydrogen absorption capacity, but almost does not reduce the rate of the hydrogenation.

Hydrogen storage performance of the TiFe-based materials suffers from difficulties with hydrogenation and sensitivity towards impurities in hydrogen gas, reducing hydrogen uptake rates and decreasing the cycle stability. An efficient solution to this problem is in modification of the material surface by the deposition of metals (including Palladium)

capable of catalysing the dissociative chemisorption of hydrogen molecules. In this work, the surface modification of TiFe alloy was performed using autocatalytic deposition using $PdCl_2$ as the Pd precursor and metal-organic chemical vapour deposition technique (MO CVD), by thermal decomposition of palladium (II) acetylacetonate ($Pd[acac]_2$) mixed with the powder of the parent alloy. After surface modification of TiFe – based metal hydride materials with Pd, the alloy activation performance improved resulting in the alloy absorbing hydrogen without any activation process. The material also showed to absorb hydrogen after exposure to air, which otherwise proved detrimental.

UNIVERSITY *of the*

WESTERN CAPE

LIST OF FIGURES

LIST OF TABLES

LIST OF ABBREVIATIONS

AAS	Atomic absorption spectroscopy
ABS/DES	Absorption/desorption
CSIR	Centre for Scientific and Industrial Research
DOE	Department of Energy
EDS	Energy dispersive spectroscopy
FC	Fuel cell
HCL	Hollow cathode lamp
IMC	Intermetallic compounds
JMA	Johnson-Mehl-Avrami
LH$_2$	Liquid hydrogen
LT-PEMFC	Low temperature proton exchange membrane fuel cell
MH	Metal hydride
MOFs	Metal organic frameworks
PCI	Pressure composition isotherm
PCT	Pressure – composition – temperature
PGM	Platinum group metals
PMT	Photo multiplier tube
RE	Rare earth
RT	Room temperature
SEM	Scanning electron microscopy
XRD	X-ray diffractometry

TABLE OF CONTENTS

Chapter 1:   Introduction

1.1   Problem Identification and Motivation of Research

The current interest in hydrogen is primarily due to environmental concerns owing to harmful pollutants from current hydrocarbon – based fuels. In fact, the widespread use of fossil fuels within the current energy infrastructure is considered as the largest source of anthropogenic emission of carbon dioxide, which is largely blamed for global warming and climate change. In addition, the declining crude oil supplies and political instability in the regions with large oil reserves, and strict emission regulations are creating a need for alternative fuels. Hydrogen is considered to be an ideal fuel, which can potentially eliminate the problems found with modern hydrocarbon fuels [1–3]. Compared to hydrocarbons, hydrogen has an energy density that is three times greater than the average hydrocarbon fuel [1-4]. Relative to hydrocarbon based fuels, only 4kg of hydrogen are needed for a 400 km journey in a modern car, while 24 kg of a hydrocarbon-based fuel is needed [1,2,4]. It is believed that hydrogen will within a few years become the fuel that powers most vehicles and portable devices. Hydrogen can be produced by various renewable sources of energy – hydroelectric, wind, solar, geothermal, with water being the only raw material needed, thus in terms of obtaining and distribution of hydrogen as a fuel source, a country's reliance on foreign energy resources can be drastically reduced. Therefore, hydrogen presents immense positive socio–economic incentives. However, while hydrogen has many advantages, one of the major shortcomings of widespread use of hydrogen as an energy source is its effective storage.

Hydrogen storage is a "critical path" technology that is a bottleneck for the commercialisation of hydrogen energy. Research on gaseous and liquid methods to inexpensively store hydrogen in a safe, compact and lightweight package has been on-going for several decades. The U.S.A Department of Energy (DOE) Hydrogen, Fuel Cells & Infrastructure Technologies programme, has been instrumental in developing state-of-the-art compressed hydrogen tanks. However, the future focus will be on solid-state materials that will enable the storage of hydrogen at low pressure. Despite tremendous advances in recent years, no approach currently meets the storage density and/or charge-discharge requirements [5,6].

Most countries import more than 80% of their petroleum, and this value is projected to rise by 2025. The transportation sector is the major consumer of petroleum imports. Use of hydrogen as a fuel offers the opportunity to shift the energy requirements for transportation from imported oil to diverse, domestically available resources. Hydrogen-powered fuel cell vehicles are a tremendously attractive alternative to gasoline and diesel powered automobiles as they emit only water with essentially no serious pollutants. The hydrogen fuel itself may be generated by several different means, including thermo-chemical processing of primary energy sources such as coal, oil, biomass, or generated by electrolysis using electricity which may be derived from renewable sources such as wind power, and/or photo-voltaics. Producing hydrogen at central locations will enable pollutants and greenhouse gases to be contained and more easily dispensed. The high efficiency of fuel cells will make hydrogen a cost effective, energy efficient, and environmentally friendly alternative to current fuels when considering the full lifecycle. Thus, the concept of a hydrogen-based energy and transportation system offers energy resource flexibility and the potential for energy

independence, as well as the elimination of net carbon dioxide, sulphur dioxide, and nitrogen oxides emissions.

1.2 Hydrogen as a future energy carrier: perspectives and challenges

Hydrogen is the lightest element; it is colourless, odourless, tasteless and nontoxic. It is the most abundant element in the universe, making up 75% of normal matter by mass and over 90% by number of atoms [7]. Hydrogen is envisaged to be of great importance for future energy application, in particular, as an alternative fuel for both fuel cells and combustion engines. If hydrogen is burned with oxygen to produce energy in a fuel cell or combustion engine, the only product produced is pure water vapour, H_2O (gas). A hydrogen economy based on renewable sources is entirely pollution free, due to the fact that it has zero CO_2 emissions to the atmosphere.
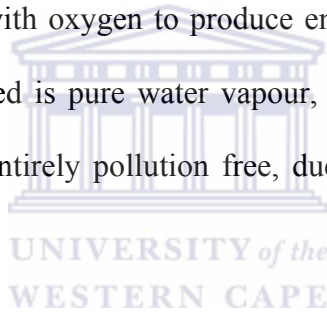
Today, more than 85% of the world's energy demand is based on fossil fuels. These include coal, natural gas, petroleum and its derivatives. Figure 1.1 below shows the decomposition of the world's energy consumption by fuel type. The world's energy demand is predicted to increase by 70% from the year 2000 to 2030. It is expected that fossil fuels will supply a significant portion of the demand in the coming years. However, the amount of fossil fuels is limited and cannot be the ultimate solution to the energy problems in the future. The environmental consequences of burning fossil fuels at a large scale are also not hard to imagine. It is predicted that when all fossil reserves are consumed, the CO_2 released will raise the atmospheric temperature by $6\,^0C$ [8]. Such a rise in temperature can harmfully affect the natural life on earth.
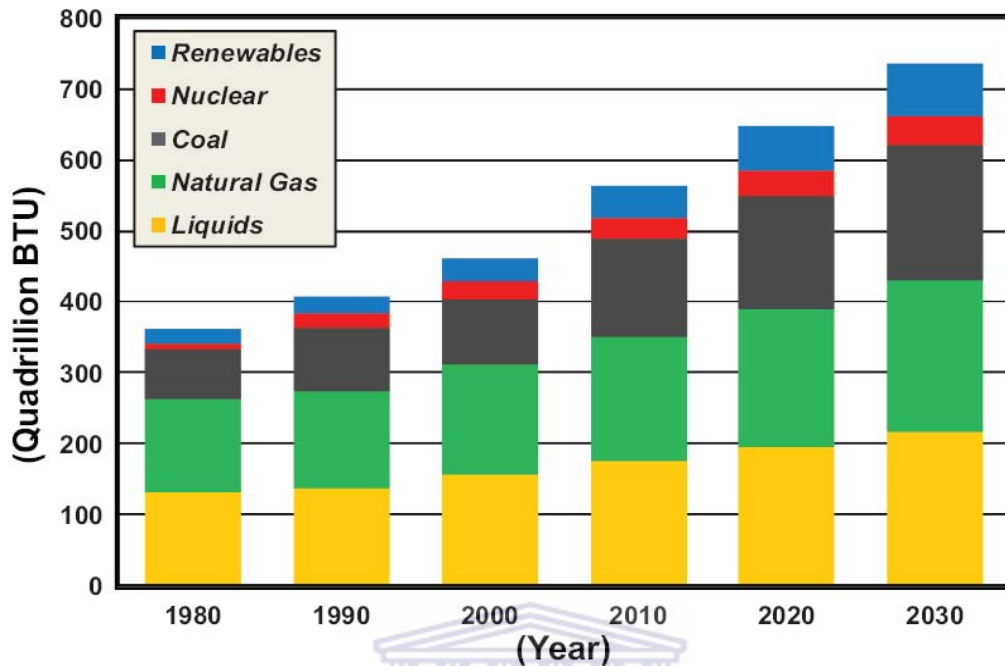
Figure 1.1: *World energy consumption by fuel type. Renewable energies are the fastest growing source of world energy with a projected annual rate of 3.0 %, whereas the liquids are the world's slowest growing source of energy with an annual rate of 0.9 %. [9].*

According to figure 1.1 above, the fastest growing source of the world energy are renewables. Unfortunately, the share of the renewable energy source is still small and definitely not enough to satisfy the world energy demand entirely. The problems associated with renewable energy systems can be classified into three main categories:

i. The efficient conversion of energy into electricity

ii. The storage of energy in the form of hydrogen

iii. The conversion of hydrogen into work

In this study, we focused on the storage aspect of hydrogen.

1.3 Hydrogen storage and related applications

The success of using hydrogen as an alternative fuel for driving vehicles and stationary applications depends on its proper distribution and storage. Hydrogen fuel exhibits the highest energy content compared to its weight and very low energy content to its volume. Complete commercialisation of hydrogen as an energy carrier requires the need for storage systems that can contain sufficient hydrogen that matches up with conventional fossil fuel storage methods. Hydrogen storage systems should account for inherent safety as well as high volumetric and gravimetric efficiency. The storage of hydrogen can be narrowed down to two general types, namely; physical methods and physical–chemical methods.

Physical methods use physical processes to compact hydrogen gas. Hydrogen being stored by physical methods contains hydrogen molecules which do not interact with a storage medium, e.g. storage as compressed gas (in high-pressure cylinders), hydrogen storage as liquid hydrogen (LH2). Physical–chemical methods provide hydrogen storage using physical–chemical processes of its interaction with some materials. The methods are characterised by an essential interaction of molecular or atomic hydrogen with the storage environment e.g. hydrogen storage in metal hydrides.

1.4 Compressed gas

Large volumes of gaseous hydrogen are not much more difficult to store at atmospheric and increased pressure than natural gas. For this purpose, gas holders, natural and artificial underground tanks and other systems are applied. Gaseous hydrogen is usually stored and transported under pressures of up to 35 Mpa in cylinders from several litres to several cubic meters in capacity [10,11].

Hydrogen storage in high pressure cylinders is the most convenient and industrially approved method. Usually, steel gas cylinders of low (up to 12 litres) or medium (20 to 50 litres) capacity are in use for storage and transportation of moderate quantities of compressed hydrogen at temperatures from -50 ^{0}C to 60 ^{0}C.

The main way to improve the characteristics of hydrogen storage in cylinders is to reduce cylinder weight by the usage of lighter metals or composite materials and to increase the working pressure. The main advantages of compressed gas storage are reliability, indefinite storage time, easy usage and affordability. Its main disadvantage is the low storage density which depends on the storage pressure. High–pressure storage results in higher capital and operating costs. Storage of hydrogen in pressurised cylinders is not likely to be applied in the future due to potential explosion risk for the high – pressure hydrogen storage in gas cylinders especially for vehicular application, due to low density and high cost of high pressure storage.
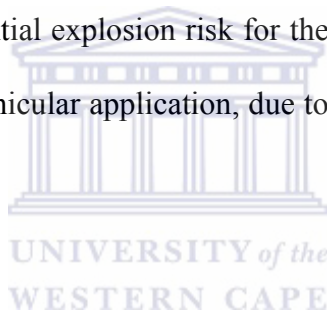
1.4.1 Cryogenic Liquid

The storage of the liquefied hydrogen requires high-efficiency cryogenic containers. As hydrogen has a critical temperature of -241 ºC, large amounts of energy (~15 kWh/kg) are required to liquefy hydrogen and limit boil-off. At the temperature of liquid hydrogen, many materials in contact with it become brittle and contract from their dimensions at ambient temperature. Also, the exposure of liquid hydrogen in the atmosphere of air will condense the oxygen in the air into the liquid hydrogen, presenting a high risk of explosion. For the above reasons, liquid hydrogen containment tanks are designed differently to usual gasoline storing tanks.

In a hydrogen molecule, each of the two hydrogen atoms holds one proton. Each proton carries a charge and spin, and when the two protons take a spin in the same direction, this is referred to as ortho-hydrogen molecules or in the opposite direction, which is referred to as para-hydrogen molecules. The direction of the spin may differ but their charge on the proton is the same as shown in figure 1.2 below. Thus depending on the spin of the proton, the hydrogen molecules exist as either ortho-hydrogen or para-hydrogen molecules.

Orthohydrogen molecule – Nuclear spins parallel (same direction)

Parahydrogen molecule- Nuclear spins anti-parallel (opposite direction)

Figure 1.2: Hydrogen molecular form - orthohydrogen / parahydrogen

Liquefaction of hydrogen is an energy consuming process and requires compression and expansion of hydrogen in multiple phases. When H_2 is liquefied, its ortho-para composition corresponds to RT, and spontaneous ortho-para conversion to approach equilibrium at low temperature takes place. The spontaneous o-p conversion is exothermic (~1 kJ/mole H_2), hence even without heat exchange with environment there will be heat evolution in the liquefied H_2 resulting in its boil-off. To avoid this, catalytic ortho–para conversion must be done in the liquefied H_2 that additionally complicates the process. Liquid

hydrogen is stored in cryogenic storage systems and is highly–insulated to prevent heat leakage. This method shows a higher storage capacity and better safety consideration than gas storage cylinders due to much lower operational pressures required.

However, its viability for commercial use is limited due to very high power inputs required for sustaining the process. Hydrogen stored in a liquid form is substantially more compressed than in gaseous form. Therefore, it appears as an appealing means of energy storage, but there are various contributory negative factors. Primarily, liquefaction requires a large expenditure of energy (30–50% of H_2 heating value) and secondly, through the use of insulation, liquid hydrogen must be kept at a low temperature (<20K). There are risks associated with this constant low temperature. For instance, due to high expansion ratio of liquid hydrogen, extremely high pressures could accumulate and result in damage or an explosion.

1.4.2 Physical – chemical and chemical hydrogen storage methods

The utilisation of hydrogen as an energy carrier in the future will rely on the development of hydrogen sorption media with attractive characteristics such as rapid hydrogen uptake and release kinetics, poisoning resistance and cycle stability. Materials which interact with atomic or molecular hydrogen by physical-chemical processes could be identified as attractive sorption media for hydrogen. The literature on hydrogen storage materials has shown that the best competitive position in the future for hydrogen storage would be to combine physical and chemical methods. The combination would produce small, medium and large scale hydrogen storage units. Conditionally, all the materials which are able to store bounded hydrogen can be divided starting from the bond energy of the hydrogen atom or molecule either with the matrix (host material) or with the other atoms in a molecule.

1.4.2.1 Adsorption

- **Zeolites:** Zeolites can potentially be employed as hydrogen sorption media as the diameter of their channels can be controlled by exploiting ion–exchange properties to modify the valence state and the size of the exchangeable cations. However, the uptake of hydrogen by adsorption is below 0.5 wt. % at ambient conditions and below 2 wt. % at 77 K and elevated pressures [12]. The sorption of hydrogen in zeolites, occurs due to movement of hydrogen molecules into the framework of the zeolite; when cooled to below room temperature the hydrogen becomes trapped within the zeolite. Subsequent heating of the zeolite leads to the discharge of hydrogen. However, the maximum sorption capacity (less than $1.0 - 1.8$ wt. % H_2) is too low to compete with other sorption systems [13].

- **Metal Organic frame works:** Metal organic frameworks (MOFs) appear to be highly promising storage materials for hydrogen as these materials combine both high surface areas and large micropore volumes. MOFs (e.g. $Zn_4O[O_2C-C_6H_4-CO_2]_3$) have similar microporous structure to zeolites and show promise as potential hydrogen sorption materials due to their tuneable pore size and functionality. These materials have large specific surface areas (i.e. $2500-3000$ m^2/g) and can absorb up to 7.5 wt. % H_2 at -196 ^0C and $P_{H2} = 20$ bar [13].

- **Carbon:** There has been special research attention to hydrogen storage in carbon materials. It has been reported that low–density charcoal can absorb up to $7 - 8$wt% of hydrogen at ~4MPa and $65 - 78$K [6]. In the later 1990s, the information on high capacity carbon nanotubes and nanofibers appeared [14,15]. However, these works proved to be insufficiently reliable and failed to be confirmed by later experimental

and theoretical studies. Carbon nanomaterials include graphitic nanofibres, nanotubes, carbon black and carbon molecular sieves. These materials interact with hydrogen through physisorption and dissociative chemisorption of hydrogen molecules. Under ambient conditions (T = 20^0C, P_{H2} = 1.0 bar) these materials are known to exhibit insignificant hydrogen absorption capacities ($\leq$ 1.0 wt. % H_2). Other disadvantages of carbon nanomaterials include the need for high pressure hydrogen feeds, and the requirement of exceptionally large surface areas and fragility of materials [16,17,18].

1.4.2.2 Bulk Absorption: Metal hydrides

One of the promising methods for hydrogen storage is the use of metal hydrides. Metal hydrides are compounds that are able to reversibly absorb hydrogen. Metal hydrides are usually formed through direct reaction of certain metals or metal alloys with hydrogen; they are capable of absorbing the hydrogen and restoring it when required. The use of metal hydrides, in which hydrogen is accommodated by the host metal structure, holds considerable promise for meeting the hydrogen economy targets, but no completely satisfactory material has yet been identified. An optimum metal hydride storage material must have the following characteristics [19,20]:

- High volumetric / gravimetric hydrogen storage capacity

- Fast absorption / desorption kinetics

- Near room temperature and ambient pressure operation

- Light-weight materials

- Long cycle lifetime for hydrogen sorption

- Low cost of material

The metal hydride (MH) method of hydrogen storage which is our primary focus in this research activity is based on the process of the reversible hydrogen adsorption into hydride forming metals or intermetallic compounds with the formation of hydrides. In this process, hydrogen is placed inside the interstitials of the crystal structure of the matrix of the metal, as individual H atoms not associated in molecules. The reaction is reversible, which means a small change of temperature or pressure will change the process from charging with hydrogen to the opposite (hydrogen discharge) and vice versa. The advantage of the system is that hydrogen is being stored at low pressure and being stored with less volume than compressed gaseous or liquid hydrogen. The hydrogen is absorbed at a lower temperature and when the hydrogen gas is needed the gas is recaptured by lowering the pressure below, or raising the temperature of the metal hydride above the corresponding equilibrium value.

1.4.2.3 Chemical Interaction

The chemical method for hydrogen storage is characterised by strong interaction between H atoms and the storage material. The group one, two and three light elements (e.g. Li, Mg, B, Al) form a large variety of metal–hydrogen complexes. Due to their light weight and high atomic ratio of hydrogen to other elements, they are very interesting materials for hydrogen storage. The main difference between complex hydrides and metallic hydrides is the transition to an ionic or covalent compound of the metal upon hydrogen absorption.

- **Complex hydrides:** Compounds such as $LiBH_4$ (lithium borohydride) and $NaAlH_4$ (sodium alanate) are among the most widely studied chemical hydrides [21-23]. $LiBH_4$ can carry a capacity of 18wt. % H_2. However, this capacity cannot be reached

practically due to high temperatures required to release H_2 [24]. Zuttel *et al.* have also shown that the decomposition temperature of $LiBH_4$ could be brought down from 600 to 400 $^{\circ}C$ by the addition of SiO_2. It is believed that the SiO_2 increases the surface area of the molten borohydride and therefore enhances the dehydrogenation kinetics [25]. However, these materials as hydrogen sorption media are not favourable due to the extremely high toxicity of diborane which is produced during side reactions in the hydrolysis and thermolysis of borohydrides. In addition, $NaAlH_4$ has a theoretically reversible H_2 storage capacity of 5.6 wt. % release H_2 through a series of decomposition reactions as shown in the following equations.

$$NaAlH_4 \rightleftharpoons 1/3\ Na_3AlH_6 + 2/3\ Al + H_2 \qquad \textbf{1.1}$$

$$Na_3AlH_6 \rightleftharpoons 3NaH + Al + 3/2\ H_2 \qquad \textbf{1.2}$$
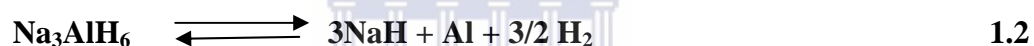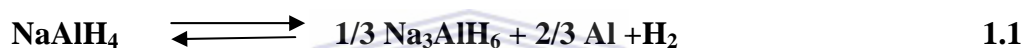
Stoichiometrically, the first step consists of 3.7 wt. % H_2 release and the second step 1.9 wt. % for a theoretical net reaction of 5.6 wt. % reversible gravimetric H_2 storage capacity [26,27]. The hydrogen absorption /desorption kinetics are relatively slow and the reversibility is only achieved under severe conditions which limits their industrial application for hydrogen storage materials.

- **Fullerenes:** The interaction of hydrogen with fullerenes is an attractive hydrogen storage technology. The reaction that takes place is ($C_{60} + 24H_2 \longrightarrow C_{60}H_{48}$). In such a process, the C_{60} fullerene can be hydrogenated up to 6.3 wt. % H_2. However, the high temperatures (400 – 450 ^{0}C) required to bring about dehydrogenation of these materials is unattractive [16,17,28]. Also, hydrogenation of fullerenes is only initiated at high hydrogen pressures (P_{H2} = 50 – 85 MPa). The uses of intermetallic

compounds are proved to be efficient catalysts in reducing the required pressure. However, the dehydrogenation temperature (more than 400^0C) is still too high for practical purposes.

- **Ammonia and methanol:** The use of ammonia and methanol is attractive for hydrogen storage and transportation due to high hydrogen volume densities (109 g/L for liquefied ammonia at T = 15^0C; and 99 g/L for CH_3OH at T = 20^0C) [16]. These compounds can be decomposed with the release of hydrogen [29]. Hydrogen is obtained by the following catalysed reactions for ammonia and methanol:

$$2NH_3 \longrightarrow N_2 + 3H_2 \qquad\qquad \textbf{1.3}$$
$$CH_3OH + H_2O \longrightarrow CO_2 + 3H_2 \qquad\qquad \textbf{1.4}$$
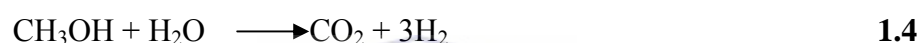
The dissociation of ammonia is carried out at high temperatures $(800 - 900^0$C) using iron as a catalyst. The process of hydrogen generation from CH_3OH requires moderate temperature $(300 - 400^0$C) in the presence of zinc–chromium catalyst. A major limitation in the use of ammonia and methanol as hydrogen storage media is their irreversibility in hydrogen storage. Hydrogen generation from methanol requires the use of hydrogen reformers which have slow yield rates and are costly. Large scale methanol steam reforming also leads to the generation of large quantities of CO and CO_2, which may add to the environmental burden [30]. Ammonia is not a greenhouse gas; it quickly forms hydrogen bonds to water vapour and returns to the ground in alkaline rain, is toxic and release heat on contact with water [30].

1.5 Hydrogen storage on the basis of metal hydrides and related applications

- **Hydrogen storage for mobile applications:** The requirements for hydrogen storage systems are highly dependent on the characteristics of the corresponding applications. For mobile applications, the low total weight is important, but it is not so critical for stationary systems, e.g. filling stations. Similarly, the low volume occupied by the storage system is essential for small transport, but it is less important for stationary applications.

  The typical target values for mobile hydrogen storage applications are listed in

Table 1.1 below. It should be noted that to fit the performances of each of the above-mentioned hydrogen storage methods into these (or similar) requirements, is a very complicated engineering problem, mainly because of interference from each different parameter. As an example, for solid-state hydrogen storage systems, the increase of refuelling rate results in the deterioration of the storage capacity.

Table 1.1: Main hydrogen storage target values according to the US Department of Energy (DOE) Hydrogen Program [31].

Target parameter	Milestones		
	2005	2010	2015
Weight capacity of H storage system, wt.% H	4.5	6.0	9.0
Volume capacity of H storage system, g_H / litre	36	45	81
Storage system cost, USD / kg H	200	133	67
Refuelling rate, kg H / min	0.5	1.5	2.0
Cycle life (1/4 tank to full), cycles	500	1000	1500
Minimum / maximum temperature of H delivery from storage system, ^{o}C	−20 / 100	−30 / 100	−40 / 100
Peak energy efficiency, %	60		
Safety	Meets or exceeds applicable standards		

- **Hydrogen storage for utility vehicles:** It is feasible to use metal hydride storage units in some special mobile applications, where weight storage capacity is not so critical, but safety and compactness are necessary. One example is a zero emission technological transport, like a tractor or forklift. The latter approach is of special interest in this research because MH hydrogen storage can be mounted as a counter balance.

- **Metal hydrides in the recovery of hydrogen from process gases:** Apart from safe and compact hydrogen storage, this technology enables realisation of a number of other options originating from the unique features of reversible hydrogen interaction with hydride-forming materials [32]. The selectivity of this process allows the development of systems for hydrogen extraction from gas mixtures and its

purification which are simple in layout and operation [33]. However, the main problem hampering application of MH for hydrogen extraction and purification is in the deterioration of the performances of the MH materials caused by gas impurities. The most important impurities are oxygen and water vapours which are typical for electrolytically-produced hydrogen. For hydrogen produced from hydrocarbons, the material should also be stable towards CO, CO_2 and traces of sulphur compounds. For RE-based AB_5 hydrogen storage alloys, these impurities at moderate concentrations are not essential problems (except for CO), but Ti-based AB and AB_2 intermetallide are very sensitive to such impurities [34].

- **Thermally-driven hydrogen compression**: The principle of the operation of heat-driven metal hydride hydrogen thermal-sorption compressors (MH TSC) allows one to transform low-potential heat into mechanical work, to realise different applications including development of temperature sensors and actuators [35], water pumping systems [36], etc. Similar solutions where the closed loop of hydrogen between at least two MH beds (containing metal hydrides characterised by different thermal stabilities) is managed, make it possible to develop efficient heat management systems (heat pumps) which can be used for cooling and / or heating, or can be incorporated into the heat transformers [35]. This is an important field for the industrial use of MH which has developed during the last 15 years

- **Summary**: **Benefits of MH hydrogen storage and related technologies**

Solid state hydrogen storage in metal hydrides (MH) is a promising technology in certain niche applications where system weight is not crucial, but where compactness, safety and technological flexibility are critical issues. An important factor in the implementation of MH hydrogen storage technology is the utilisation of suitable

hydrogen storage materials characterised by fast and reversible hydrogen uptake and release under mild conditions, in combination with low cost and availability, including feasibility of their manufacture based on local resources.

In addition, the thermodynamic features of the "hydrogen – MH" reversible interaction allow one to absorb hydrogen at low pressure and low temperature and to release it at high pressure and high temperature. This makes it possible to develop the heat-driven thermal sorption hydrogen compressors which have no moving parts [37]. Moreover, all these and some other options can be combined within one unified MH apparatus (e.g., for hydrogen extraction–purification–storage–compression); this approach realises the technological flexibility of MH applications and represents their potential benefit against alternative technologies of hydrogen processing [38].

1.6   Hydrogen and fuel cell activities in South Africa

In recent years, most governments are considering the use of hydrogen as energy carrier, combined with fuel cell technologies to produce electricity. The reasons for this are that environmental protection is becoming increasingly dominant and the volatility of oil prices. This is a global move towards developing sustainable energy systems that can significantly contribute towards the reduction of the carbon footprint and ensuring the supply of oil in geopolitics areas. The South African hydrogen and fuel cell activities is mainly based on the role of platinum–group metals (PGMs) based on electro-catalysts as important components of most types of fuel cells. Platinum is a rare mineral, with reserves in only five counties as shown in Figure 1.3 below. Platinum group metals (PGMs) are the key catalytic materials used in most fuel cells and with more than 75% of the world's known platinum (Pt) reserves

found within South African borders, there is a great potential for socio–economic benefits to be obtained from these natural resources.
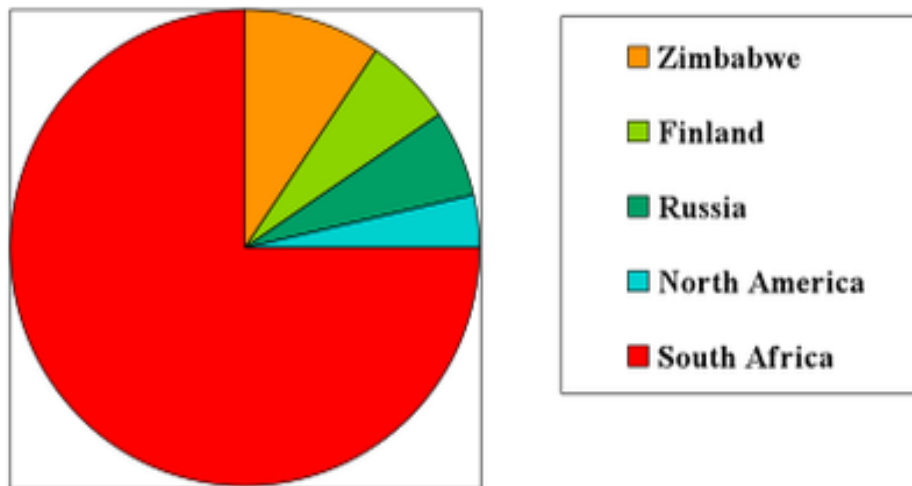
Figure 1.3: *World Platinum reserves (Cawthorn, 1999)*

The objectives of the hydrogen and fuel cell activities are informed by the need for the South African economy to migrate from a resource-based economy towards knowledge-based one. The primary goals of the Hydrogen and fuel cell activities are to:

- Create wealth for South Africa through high value-added manufacturing and development of PGM catalysts with aim of supplying 25% of the global catalyst demand for the global hydrogen and fuel cell market by 2020.

- Build on existing knowledge and capabilities in high temperature gas cooled nuclear reactors and coal gasification Fischer-Tropsch technology, to develop local cost competitive hydrogen generation solution, and

- Promote equity and inclusion in the economic benefits of South African resources.

1.6.1 HySA Program

The Department of Science and Technology (DST) established three centres of competence as an initial effort towards the implementation of South African Hydrogen and Fuel Cell Technologies Research, Development, and Innovation strategy (HySA). These are HySA Systems (hosted by the University of the Western Cape), HySA Catalysis (Co-hosted by the University of Cape Town and Mintek) and HySA Infrastructure (Co-hosted by North West University and the Centre for Scientific and Industrial Research (CSIR)).
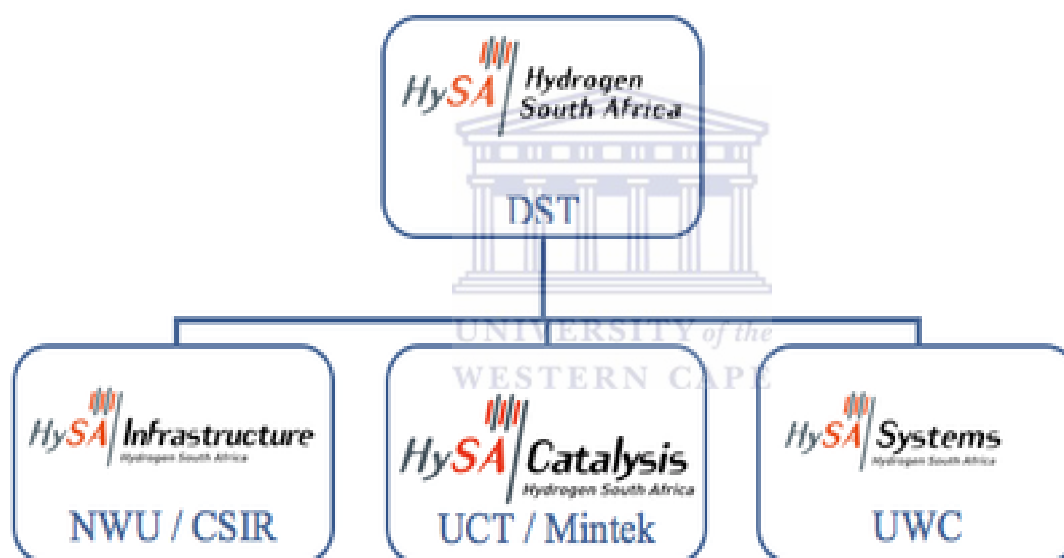
Figure 1.4: Illustration HySA program in South Africa

Each centre has a unique responsibility, but all with the common vision of fostering proactive innovation and developing the human resources required to undertake competitive research and development activities in the field of hydrogen and fuel cell technologies.

HySA Systems, a Systems Integration and Technology Validation Competence Centre on HFCT was established in 2007 at the South African Institute for Advanced Materials

Chemistry (SAIAMC) at the University of the Western Cape (UWC). The main objective with HySA Systems is to perform technology validation and system integration in two key HySA-programmes: (1) Combined Heat and Power (CHP) and (2) Hydrogen Fuelled Vehicles. HySA Systems is also responsible for the development, prototyping, and testing of the following key technologies: Membrane electrode assemblies (MEAs) for high temperature (120-180°C) proton exchange membrane (PEM) fuel cells, metal hydrides for hydrogen storage and compression, and Li-ion batteries.

1.6.2 Metal hydride materials and technologies: South African perspectives

South Africa has several comparative advantages which result in some differences in the national priorities on hydrogen storage, as compared to those for other countries, like the US and EU States, where hydrogen storage for mobile applications is a top priority area. Having well-developed synthetic motor fuels production from coal, South Africa is potentially less dependent on oil imports for petrol production, and could derive more benefits from further developments in this direction.

South Africa has a dominating position in the production of Platinum Group Metals being the world's biggest producer of platinum and the second of palladium. Also, the country has well-developed production of several mineral concentrates containing the metals which are important components of hydrogen storage alloys, such as titanium and zirconium (world's no.2); vanadium (world's no.3); nickel and cobalt; manganese (world's no.1). Other important component metals (rare-earth metals), although not being produced on a large scale, are available in the country, as well as the corresponding mining and processing industry.

These comparative advantages in South Africa make the activities focused on solid state hydrogen storage solutions and related technologies utilising hydrogen storage materials especially promising. In particular, by the application of metal hydrides modified by platinum group metals, it is possible to develop the complex technologies of hydrogen extraction, purification, storage and compression. These platinum group metals are also applicable to hydrogen production technologies and energy conversion/heat management applications. Such approaches can result in the development of novel (even breakthrough) hydrogen technologies that will promote South African research and development and related industries to occupy a unique niche in worldwide hydrogen activities.

1.7   Problem Statement

The main hindrances against widespread use of hydrogen as an energy carrier are effective storage methods. It is necessary to store hydrogen in a manner, which maintains its high-purity, allows for fast rates of absorption and desorption, allows for efficient transport and does not require large amounts of energy in its operation. For these reasons hydrogen storage is a critical technology necessary for the successful implementation of the hydrogen economy as a whole. Solid state storage in which hydrogen is absorbed in a solid material holds considerable promise for meeting the hydrogen economy targets.

In particular, metal hydrides can meet these targets; they have a variety of application due to their ability to absorb H_2 reversible at low temperature and pressures. However, these properties can be lost when these materials are suddenly exposed to air due to the formation of oxide film which prevents dissociation and diffusion of H_2 into the interstitial site of the alloy leading to a reduced reversible H_2 capacity. Activation of the alloy to remove the oxide

layer prior to hydrogenation requires several activation cycles which include heating under vacuum followed by absorption of hydrogen at higher pressures.

1.8   Research area and hypothesis

The main objective of this research project is to study titanium–based intermetallic compounds belonging to AB (TiFe) and AB_2 (A=Ti, Zr, B=Fe, Mn, Cr). The project's sub goals include:

- To study different preparation methods of Ti-based AB- and AB_2-type hydrogen storage alloys;

- To compare performances of TiFe-based materials prepared by different methods;

- To develop new preparation routes for Ti-based AB- and AB_2-type alloys; and

- To improve activation performances and hydrogen sorption kinetics of Ti – based metal hydride forming alloys.

Ti–based intermetallic compounds are rather prospective for stationary and special mobile applications due to their availability, potentially low cost, reasonable hydrogen storage capacity (2 wt. %) and tuneable thermodynamic properties [39,40].

At the same time, the usage of Ti–based metal hydride materials is hampered by a number of difficulties, including poor activation performances and low cycling stability in the presence of gas impurities. As distinct from rare earth (RE)–containing AB_5 alloys, metal hydride materials on the basis of Ti alloys do require more intense activation conditions and are characterised by much lower resistance towards "poisoning" with gas impurities, first of all, oxygen and water vapours [34]. At the same time, these materials show wider

possibilities in their modification by nanotechnological routes, including modification with oxygen and surface deposition of metal films. In so doing, the improvement of activation and H sorption properties in the modified Ti alloys will be more pronounced and these core materials are very convenient model systems to study the effects of the different ways of their modification.

1.9   Thesis outline

Chapter 2: Literature review

This literature review introduces the behaviour of intermetallic compounds upon hydrogenation and also focuses on selection of H_2 absorbing material within the class of IMCs such as AB_5, AB_2, AB, A_2B, Mg-based composites and BCC alloys on the basis of V or T-Cr systems on the basis of their structural and H_2 sorption properties. The preparations of intermetallic metal hydrides via different synthesis methods such as melting, sintering and mechanical alloying are discussed. The effect of substitution of oxygen in the bulk structure of TiFe is also discussed. Surface modification with platinum group metals (PGMs) in particular Pd is elaborated on by looking at the influence of hydrogen sorption kinetics on metal hydrides.

Chapter 3: Methodology

Chapter three fundamentally serves as a continuation of the literature review, but with more emphasis placed on the characterisation techniques employed in the study. It also gives and outline of the different materials that were used in the study.

Chapter 4: Results and discussions

This chapter begins by focusing on the comparison of TiFe based materials synthesised by different preparation methods. The alloys are compared through chemical composition, phase-structural features, morphology and their hydrogen absorption kinetics as well as PCT properties. Synthesis of TiFe and, further, AB_2 intermetallide, via reduction of ilmenite ($FeTiO_3$) is also discussed. This is then followed by the study of influence of Pd deposition via electroless and chemical vapour deposition on TiFe-based metal hydride. The study then shows the activation and hydrogen absorption kinetics of the TiFe alloy modified by Pd. The analysis of hydrogen sorption performances of multicomponent AB_2- type hydride forming materials on the basis of Ti is also studied by looking at their composition and hydrogen absorption performances.

Chapter 5: Conclusion and Recommendations

The study is concluded with a concise discussion of the objectives achieved pertaining to the study of kinetic properties of Ti-based metal hydrides. Recommendations are made, anomalies noted, and the greater relevance and implications of the study are discussed.

Chapter 2:   Literature Review

2.1   Main principles of hydrogen interaction with metallic hydride forming materials

Most of the metals in the periodic table, their alloys or intermetallic compounds react with hydrogen to form metal hydrides. In this sense, the host metallic system acts like a hydrogen sponge. The bonding between hydrogen and the metal can range from ionic, covalent, as well as multi–centred bonds, and metallic bonding. Metal hydride method of hydrogen storage is based on the process of reversible hydrogen adsorption in hydride forming metals and intermetallic compounds with the formation of metal hydrides (MH) with metallic M–H bonding. In this process hydrogen is placed in interstitials of crystal structure of the matrix of the metal, as an individual, not associated in molecules, H atoms [19,20]. The process can be described as gas-solid reaction represented by the equation below.

$$M_{(s)} + X/2 \; H_{2\,(g)} \leftrightarrow MH_{x\,(s)} + heat \qquad \textbf{2.1}$$

Where M denotes hydride forming metal or intermetallic compound; s, g denote the solid and gas phase, respectively.

The reaction is reversible, which means that a small change of temperature or pressure will change the process from charging with hydrogen to the opposite (hydrogen discharge) and vice versa. The advantage of the system is that hydrogen can be stored as a metal at low pressure and with much higher volumetric density than compressed gaseous or liquid hydrogen [6, 41].

A schematic of hydrogen absorption is shown below in figure 2.1. The H_2 molecular approaches the metal surface, which lead to the H_2 molecule physisorbed on the surface and then dissociatively chemisorbed as individual H atoms. The H–atoms can quickly diffuse away from the surface into interstitial sites in the metal crystal lattice. Once in the crystal lattice, H–atoms can take the form of a random solid solution or an ordered hydride structure with distinct bonding to metal atoms and high volumetric packing density [42].
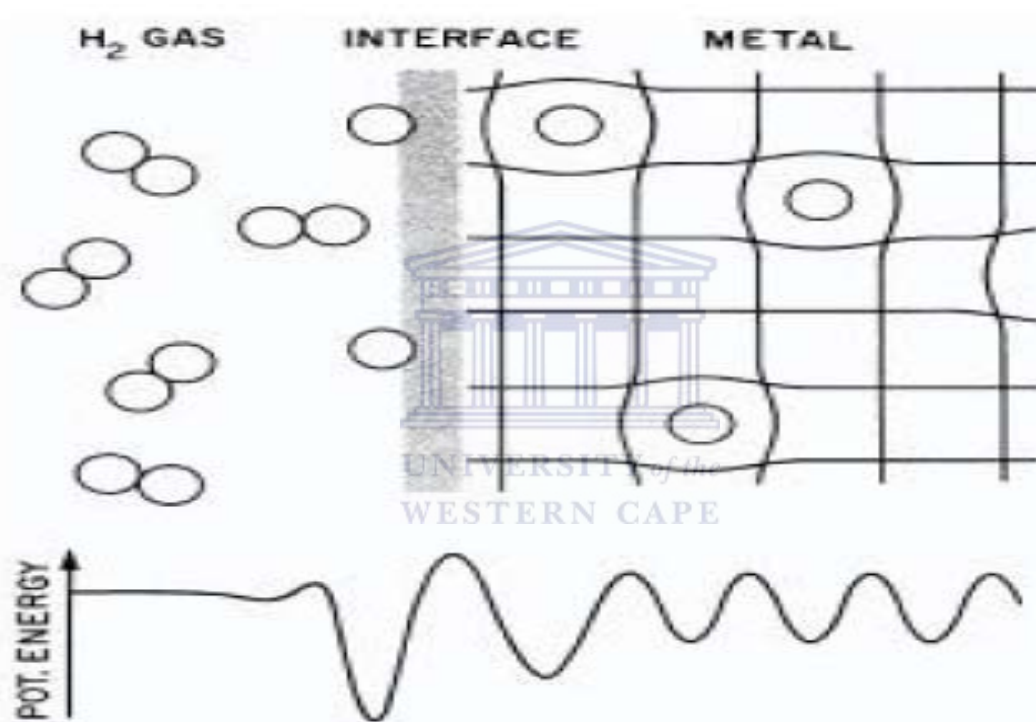
Figure 2.1: *Schematic of Hydrogen absorption in metal [42].*

2.1.1 Mechanisms and Kinetics

Absorption and desorption of H_2 occurs in individual reaction steps including bulk processes and can be divided into several independent steps [43-47] as shown in figure 2.2 that follows and the absorption steps are listed below.

- Dissociation/adsorption: The first step is the dissociative adsorption of H_2 on the metal/ hydride surface (Path 1 in Figure 2.2).

- Surface penetration: From the surface, the H-atoms can penetrate into the sub-surface (Path 3).

- Bulk diffusion: From the sub-surface, the H-atoms can diffuse into the bulk or from the bulk and further in (Path 4).

- Hydride formation: H-atoms in the bulk (corresponding to a solid solution) can create hydride nuclei which can grow to larger hydride grains by trapping of additional hydrogen atoms (Path 6). H_2 diffusion can also take place through the hydride (Path 5).
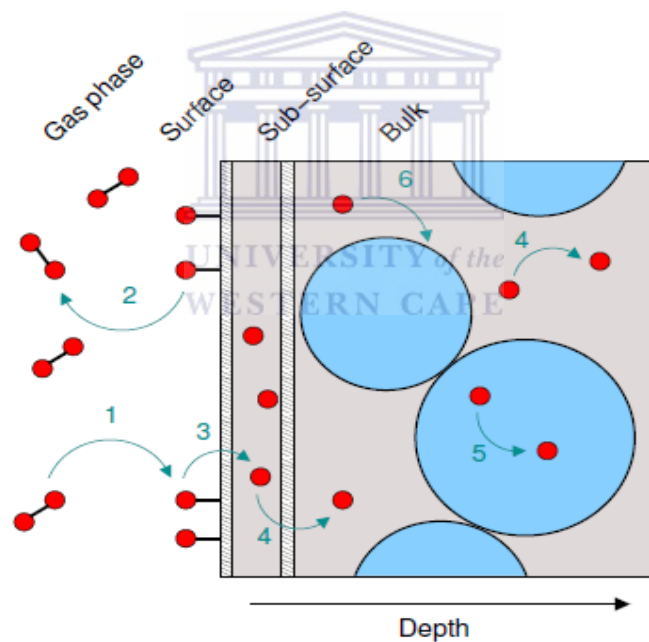
Figure 2.2: *Schematic illustration of the different mechanisms involved in MH formation and decomposition. H-atoms are shown in red, the metal host lattice is shown in grey, and the MH is shown in blue [47].*

For dehydrogenation, the process is the reverse, i.e., the hydride phase decomposes and hydrogen atoms diffuse to the sub-surface and subsequently to the surface, where the H-atoms recombine and desorbs as H_2 (Path 2).

Hydrogen needs to be supplied to a consumer at a sufficiently high rate. A relatively high hydrogen desorption rate is thus required (rapid rate for absorption is also required for rapid charging). Hydrogen desorption actually involves multi steps as shown above. The slowest step determines the overall kinetics of sorption. It is usually difficult but important to specify which step is rate-controlling in hydrogen sorption. Particle refinement/activation and catalysis to reduce energy barriers for hydrogen diffusion or molecule formation/dissociation are common approaches to enhance the overall kinetics [48].

A reaction mechanism and kinetics can be proposed on the basis of the above reversible reactions. Hydrogenation/dehydrogenation curves obtained by plotting macroscopic H_2 uptake/release as a function of time can roughly be divided into two major classes; one with a monotonically decreasing uptake rate and one with a sigmoidal shape [49]. The rate limiting steps can be identified by fitting the experimental data with a kinetic mode or rate equation [49]. Nucleation and growth kinetics is usually explained by a Johnson-Mehl-Avrami (JMA) rate equation [50,51] in the following form.

$$\alpha = 1 - \exp\left(-(kt)^n\right) \qquad\qquad 2.2$$

Where α is a fraction reacted at time, t; and k are the rate constant. The exponent, n, referred as the Avrami exponent is an integer or half-integer, the value of which is governed by the

geometries associated with the rate-controlling process. JMA equation can be used to explain situations where diffusion may be rate limiting, when *n* is allowed to have values of 1 or less. Furthermore, sigmoidal uptake curve can be a result of a hydride with a protective surface oxide layer [52-54].

2.1.2 Structural Changes upon Hydrogenation / dehydrogenation

Metal and hydrogen usually form two different solid phases during hydrogenation and dehydrogenation, α – phase solid solution and β – phase hydride. In α – phase there is only some hydrogen absorbed (H/M<<1), and in the β – phase the hydride is fully formed (H/M~1). For example, Mg_2Ni forms α – $Mg_2NiH_{0.3}$ and Mg_2NiH_4 hydride [55]. When initially charged the hydride-forming metal (alloy) gets to the α – phase and after that when charged and discharged the material usually undergoes the phase transformation such as:

$$Mg_2NiH_{0.3} + 3.7\ H \longleftrightarrow Mg_2NiH_4 \qquad\qquad \textbf{2.3}$$

A schematic of phase transition is presented in figure 2.3 presented below. When charging, hydrogen diffuses from the surface of the particle through the β – phase to the phase – transition interface, and during discharge it diffuses through the α – phase to the surface of the particle where it recombined into the form of molecular hydrogen.
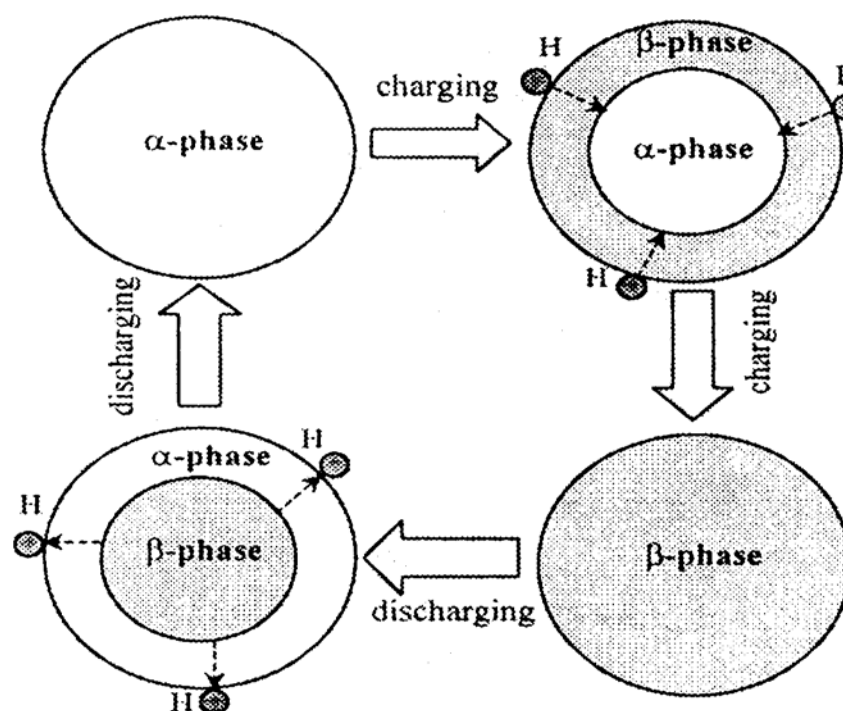
Figure 2.3: *Schematic of phase transition in metal hydrides [55].*

2.1.3 Thermodynamic characteristics of hydrogen sorption process in metal hydrides

This section presents a general description of the thermodynamic features of metal–hydrogen systems. It is imperative to briefly address this area since different thermodynamic implications apply to different applications. This section is meant to offer us the answers to questions regarding selection of metal hydrides on the basis of their pressure– composition–temperature (PCT) properties, for specific application. The thermodynamics of hydrogen sorption process of metal hydrides is of paramount interest to us since we desire metal hydride systems with near ambient operating conditions.

Most experimental measurements are routinely investigated by volumetric analysis, the Sievert's type apparatus and to a less extent by calorimetry or thermogravimetry. Initial studies of the solubility of hydrogen in iron and other metals can be attributed to Sieverts et

al. [56] who found experimentally that amounts of hydrogen dissolved in metal can be directly proportional to the square root of the hydrogen pressure, $P^{1/2}_{H2}$ (atm $^{1/2}$) and the equilibrium can be written as

$$\tfrac{1}{2} H_{2\,(g)} + M = MH_{\,(abs)} \qquad\qquad \textbf{2.4}$$

Thus the solubility of hydrogen, C in metal is

$$C = KP^{1/2}_{H2} \qquad\qquad \textbf{2.5}$$

The most common characterisation method of a metal hydride is the PCT curve in a form of P – C isotherms. An idealised P – C isotherm with α – and β – phases is shown in figure 2.4. The concentration, i.e. the hydrogen capacity is usually defined as hydrogen atoms per metal molecules H/M. In order to characterise the metal hydride it is convenient to use the maximum hydrogen capacity (H/M) $_{max}$. The reversible hydrogen capacity Δ(H/M) defined as the plateau width (see figure 2.4), is also a helpful tool when considering the engineering performances of the metal hydride. The concentration can also be expressed as mass per cent from the total mass, especially for the energy density comparison.
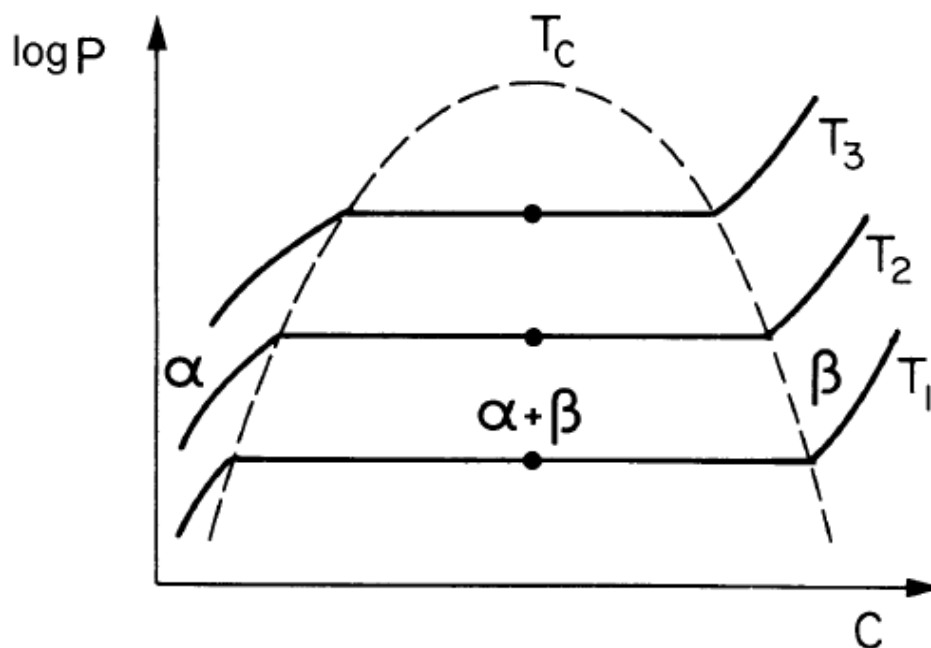
Figure 2.4: Idealised P – C isotherm of a metal hydride [57].

In a real metal hydride, the P – C isotherms show some hysteresis between adsorption and desorption. Also the plateau can exhibit some slope. These properties are shown and defined in figure 2.5 (a) given below. The thermodynamic reaction equilibrium is defined with the equilibrium constant K [58].

$$RT \ln K = \Delta H - T\Delta S ,$$

2.6

Where ΔH is the reaction enthalpy and ΔS is the reaction entropy. For a solid – gas reaction the equilibrium constant reduces to the pressure of the gas. Thus the Van't Hoff equation is obtained [58].

$$\ln P = \frac{\Delta H}{RT} - \frac{\Delta S}{R} .$$

2.7

Plotting the equilibrium (P,T) – values on a lnP versus 1/T scale gives the so – called Van't Hoff plot. The reaction enthalpy can be derived from the slope of the plot with help of the above equation and the plot tells the suitability of P – T behaviour of a hydride for practical application. The theoretical Van't Hoff plot usually describes very well the real properties of the metal hydride [19]. A schematic of a typical Van't Hoff plot is given below in figure 2.5 (b).
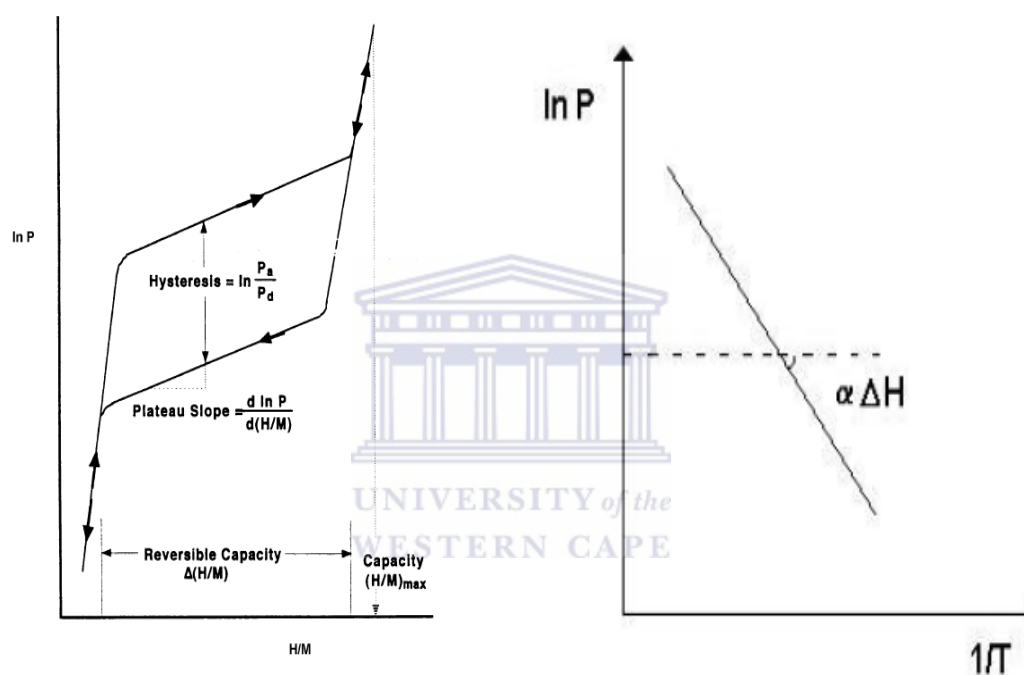
Figure 2.5: *Schematic of real P – C isotherm (a, left) and schematic of Van't Hoff plot (b, right)*

The reaction enthalpy of hydride formation is an important quantity. It is usually negative so the reaction is exothermic and thus the hydride formation releases energy. Therefore, the dehydrogenation needs supply of energy in the form of heat, to be able to take place. Since most of the applications are used at ambient temperature, or at least in the range of $0 – 100\,^{0}C$, the reaction enthalpy should be quite small so that the hydride could take the

low-grade heat from the surroundings, or, e.g., from the fuel cell cooling system, when releasing hydrogen. According to equation 2.7, the reaction enthalpy also directly affects the stability of a hydride since the gas pressure is exponentially proportional to it.

2.1.4 *Metallic hydride forming materials of practical importance*

The feasibility of MH hydrogen storage systems is in the multi functionality of the system (possibility of hydrogen purification due to high selectivity of hydrogen adsorption / desorption processes, easy pressure control at the output of the MH storage unit, the increased chemical activity of supplied hydrogen, etc). These factors make the systems the most preferable, for example, in laboratory applications and hopefully soon, a wide range of other applications.

It is important also to note that the amount of hydrogen that a material can release, rather than only the amount the material can hold, is a key parameter used to determine net, or reversible gravimetric and volumetric capacities.

Hydrogen reacts with many individual metals to form binary hydrides, MH_x. The formation of the binary hydrides is accompanied by essential changes in the mutual location of the M atoms taking place. The latter either remains invariant, or in major cases rearranges itself [3, 19]. A strong M-H bond must be formed for the efficiency of this system. Apart from binary hydrides, there is also another class of hydrides called intermetallic hydrides denoted by the formula $A_xB_yH_z$. They are generally characterised by excellent kinetics of reversible hydrogen sorption – desorption taking place at moderate temperatures.

Widely researched binary and intermetallic hydrides are presented in figure 2.7 below with regards to their weight and volume capacities. A comparison is also drawn with compressed hydrogen and liquid hydrogen.

It can be deduced from the figure that metal hydride hydrogen storage method can compete with conventional ones in terms of compactness, but is inferior in hydrogen weight capacity. The latter is somewhat better for hydrides of the light elements, but the usage as a hydrogen storage medium is problematic in most cases, due to the irreversibility of such hydrides e.g. BeH_2, $LiBH_4$.
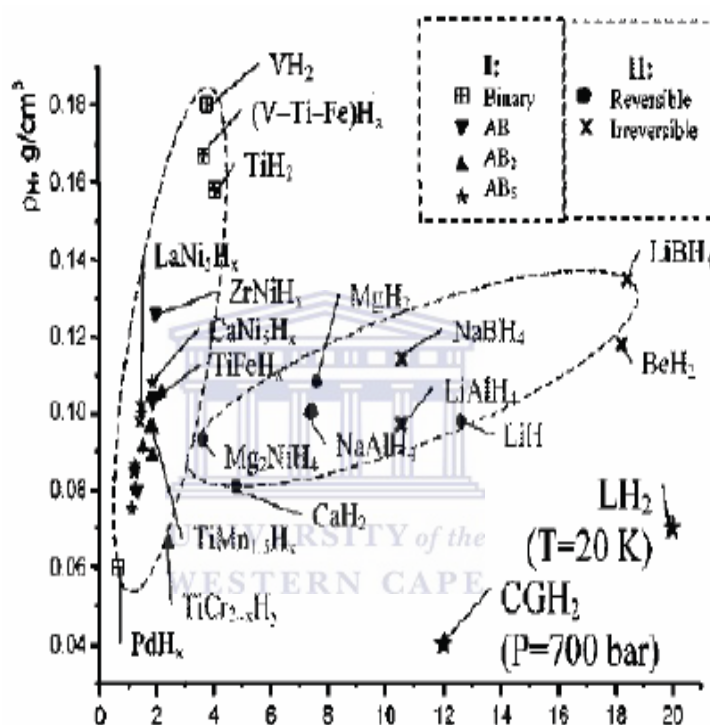
Figure 2.6: *Relation between weight and volume hydrogen capacities for binary and intermetallic hydrides on the basis of transition metals (I), and binary and complex hydrides of the light elements (II) [20].*

2.2 Hydrogen storage materials on the basis of intermetallic alloys

From the family of hydride-forming alloys and complexes presented below; intermetallic compounds appear to be of utmost interest in recent international research reports. Intermetallic compounds (IMC) are strictly ordered alloys of two or more metallic elements, which usually have a crystal structure that is different from either of the parent elements (A and B). There are many hundreds of known intermetallic compounds of several classes and they form the basis of a major branch of metallurgy.
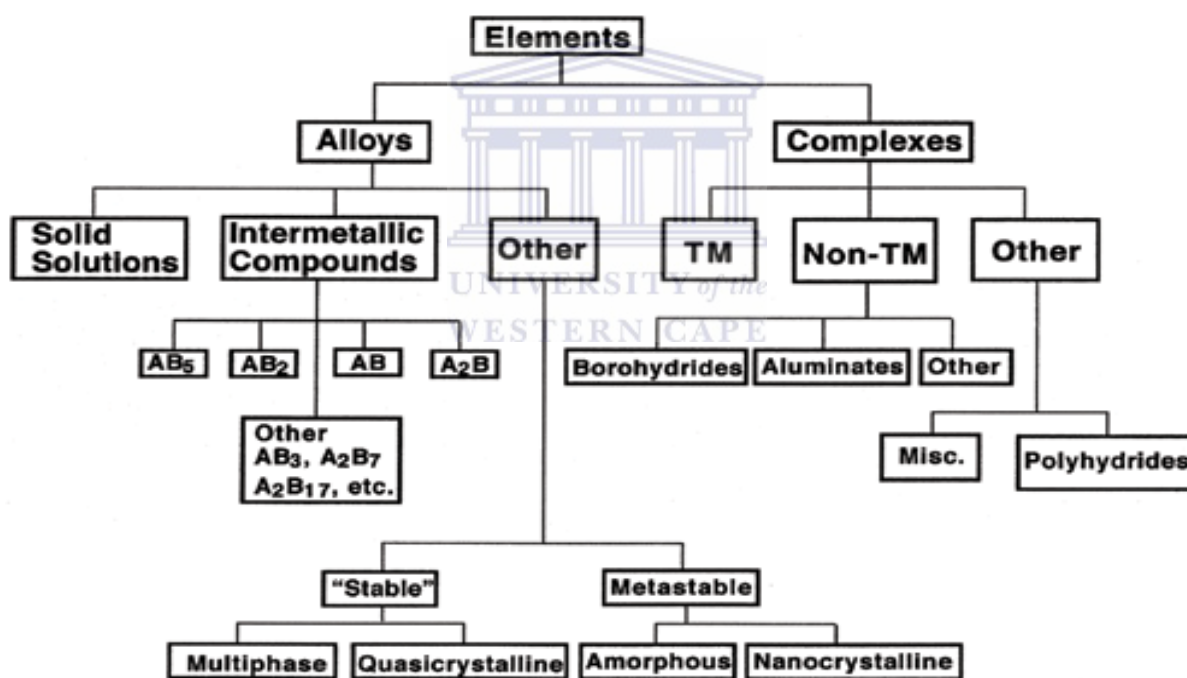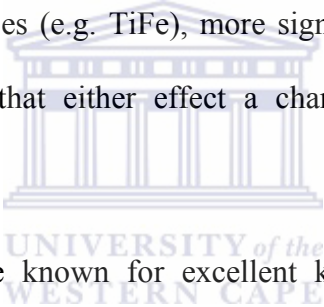
Figure 2.7: Family tree of hydriding alloys and complexes, TM = transition metal [19].

The group of hydrides referred to as intermetallic compounds (IMC) is denoted by the general formula A_xB_y. In this hydride structure, two or more metals are involved. The key to all IMC hydride technology is the combination of a strong hydride forming element A with a

57

weak hydride forming element B to form an intermetallic compound A_xB_y that can react reversibly with hydrogen to form an intermediate strength hydride $A_xB_yH_z$. Hydride forming intermetallides are generally grouped based on their ratio of hydride forming A to the non-hydride forming B components. The most widely acclaimed families of intermetallics hydrides are AB_5 e.g. $LaNi_5$; AB_2 e.g. $TiMn_2$; AB e.g. TiFe and A_2B e.g. Mg_2Ni. Rare earth metals and calcium are usually the A component in the AB_5. For the AB_2 and AB, A is commonly a member of the titanium sub group. For the A_2B, the A component is commonly magnesium. In all cases, the B component is usually a transition metal (Fe, Co, Ni, V, Mn, Cr etc). Formation of intermetallic hydrides usually involves expansion of the crystal lattice. The symmetry of the metal matrix is expected to be unchanged in the course of the hydride formation. However, in some cases (e.g. TiFe), more significant changes may occur in the arrangement of metallic atoms that either effect a change in symmetry or even cause degradation [20,59].

Intermetallic hydrides are known for excellent kinetics of hydrogen absorption–desorption, according to the above described mechanisms. The added advantage to this is the fact that these reactions occur at near-ambient temperatures. Intermetallic hydrides show the strongest potential as hydrogen storage materials operating at near-ambient conditions compared to other kinds of hydrides, and this has encouraged extensive research for their use. The two basic properties, which make intermetallic hydrides attractive, are their high and reversible hydrogen storage capacity per mole of compound, and the high energy stored per unit volume. The mass of hydrogen that can be stored per unit volume of hydride is larger than can be stored in liquid form while the energy stored may be more than 10 MJl^{-1} of hydride [20]. These figures and the fact that hydrogen plays an important role as a non-polluting fuel in internal combustion engines, as well as non-polluting working fluid in

chemical heat pumps lend strong arguments for supporting research in clean energy systems based on intermetallic hydrides.

The main flaw of intermetallic hydrides, with exception of magnesium-based ones is their low hydrogen weight percentage which, for the most common commercial intermetallic hydrides, still remains below 2 wt. %. [41,60]. The weight limitation is less important for stationary hydrogen storage but is a handicap for transportation. Finally, the ability to maintain the absorption properties over a long term is of paramount importance although the constraints differ strongly according to the use. Obviously, the first step in hydride technology is to find the 'best' intermetallic compounds amongst the hundreds proposed, to operate over the requested pressure and temperature range.

- **AB$_5$ intermetallic compounds:** The AB$_5$ hydriding intermetallics generally have a hexagonal crystal structure. The near ambient PCT properties of these hydrides were first discovered accidentally in 1969 at Philips Eindhoven while the magnet alloy SmCo$_5$ was being studied [19]. The most important example of AB$_5$ class of alloy is LaNi$_5$. This family has an extraordinary versatility because many different elemental species can be substituted into the A and B lattice sites. The usual examples of substitutes for A are Mm (a natural mix of rare earth metals such as Ce, La, Nd, Pr, Sm, etc), Ca, Y, Zr and for B − Al, Mn, Si, Zn, Cr, Fe, Cu and Co. A partial replacement of A and B components significantly changes the alloy properties. For example, replacing some of the Ni in LaNi$_5$ alloy with Co, Mn and Al is known to significantly increase the stabilities of the intermetallic hydrides as shown in Figure 2.9 A-C. However, partial substitution on the B-site with Ce results to reduction of thermal stability of the alloy with increasing content of Ce as illustrated in Figure 2.9

D below. This is attributed to the low metal hydrogen binding energy of Ce and thus makes it easier in expelling hydrogen from the material.
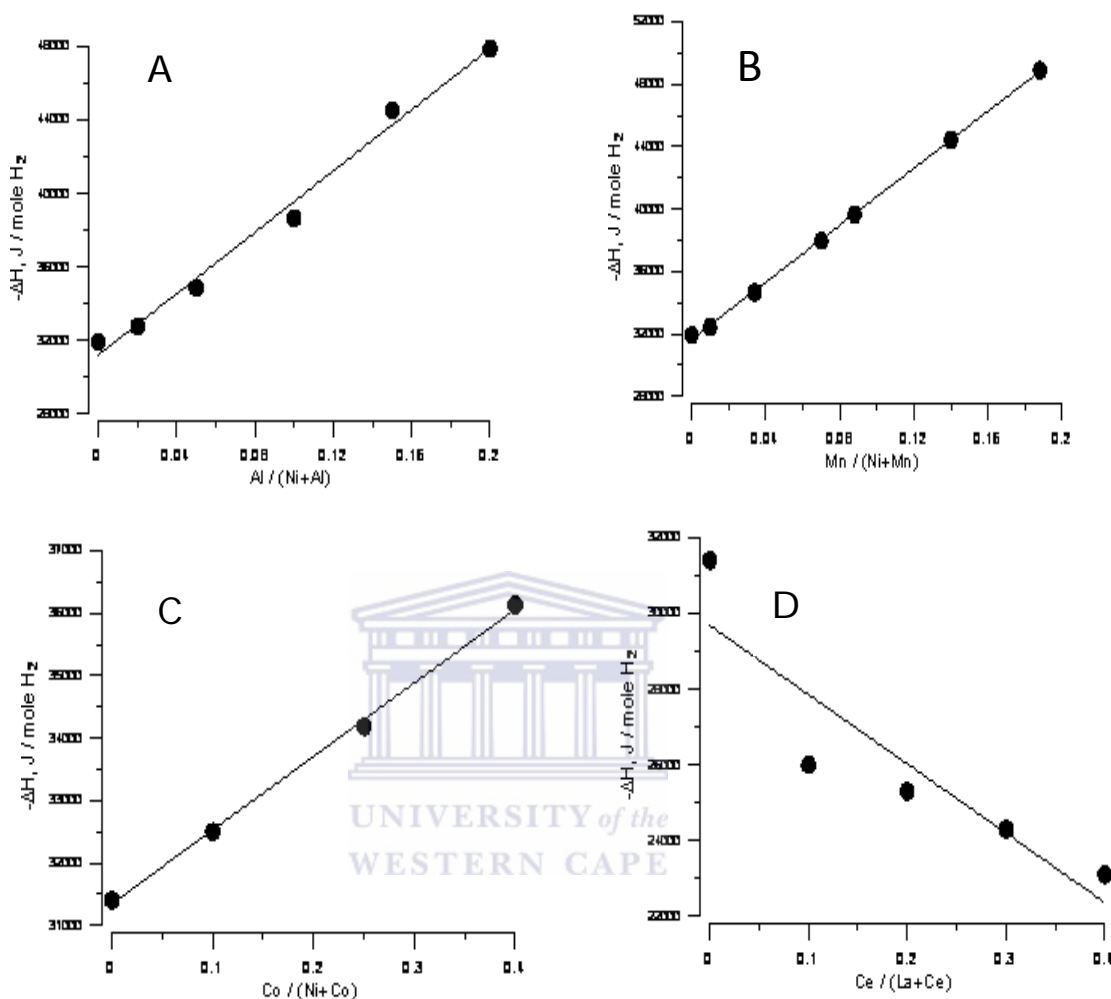
Figure 2.8: *Hydride formation enthalpies for the ternary intermetallides (A) La(Ni,Al)₅ , (B) La(Ni,Mn)₅ , (C) La(Ni,Co)₅ and (D); (La,Ce)Ni₅. The plots were built using reference data [61].*

However, the reversible hydrogen capacity of these hydrides is unfortunately low not exceeding 1.3 wt. %. [19]. Alloy raw material costs are relatively high compared to other alloys of hydriding intermetallics. The AB₅ alloys are easy to activate and

seldom require any heat. They decrepitate to fine powder, which is mildly pyrophoric when exposed to air after the first hydrogen charge / discharge cycle. This is a very relevant factor for safety consideration. Both easy activation and pyrophricity means AB_5 alloys do not form protective oxide layers if there are trace elements of impurities such as H_2O and O_2 along with H_2 in the system. The impurities do not poison AB_5 but only act as reactants which slowly reduce capacity. AB_5 alloy metallurgy is well understood and virtually single phase alloy can be melted into large commercial quantities by vacuum induction melting [19].

- **AB_2 intermetallic compounds:** Like the AB_5 alloys, the AB_2 alloys represent a large and versatile group with favourable PCT properties near ambient temperature. The A-elements are usually group IV metals e.g. Ti, Zr. The B-element are usually transition metals with an atomic number from 23-26 e.g. Fe, Mn, V etc. A wide variety of substitution possibilities are possible for both A and B components, and this means PCT properties can be fine tuned to a large extent. AB_2 alloys are based on two related Laves phase crystal structures, the hexagonal prototype and the cubic prototype. The hydrogen capacity of AB_2 alloys are comparative to AB_5 alloys on a reversible (plateau pressure) basis but are generally higher on a reversible capacity basis.

When lower temperature and higher pressure are available, AB_2 alloys tend to show higher capacities than AB_5 alloys. AB_2 alloys offer better alternative than AB_5 in terms of cost, especially if the A-content is Ti. AB_2 alloys are generally more difficult to activate than AB_5 especially for those alloys high in Zr or Mn. Once activated, hydrogenation / dehydrogenation kinetics is very high. It is also observed that AB_2

alloys are very sensitive to impurities like CO and H_2O in the H_2. Like the AB_5 alloy AB_2 decrepitates into fine powders. AB_2 alloys high in Zr and Mn are pyrophoric in the activated state whereas those high in Ti and Cr tend not to be. The production of AB_2 alloys requires high metallurgical care.

- **AB intermetallic compounds:** The first demonstration of reversibility in intermetallic hydrides was done using AB alloy ZrNi in 1958 by Libowitz. Unfortunately ZrNi as a 1 atm desorption temperature of about 300 ^{0}C and did not present a viable option in terms of practical application. The first practical AB alloy demonstrated was with TiFe in 1970 by Reilly and Wiswall at Brookhaven National laboratory, USA [19]. TiFe alloys and its substitutional modification remain the most viable AB alloys today. TiFe structure is based on an ordered body centered cubic structure. They tend to have two plateaus (forming two hydrides) both with reasonable pressures at ambient temperatures. The alloy TiFe will react directly with hydrogen to form a mono-hydride and a dihydride. The reactions which take place stepwise maybe written (starting with hydrogen saturated metal) as follows:

$$FeTiH_{0.1} + 0.515\,H_2 \longrightarrow FeTiH_{1.04} \qquad\qquad \textbf{2.8}$$

$$FeTiH_{1.04} + 0.405\,H_2 \longrightarrow FeTiH_{1.85} \qquad\qquad \textbf{2.9}$$
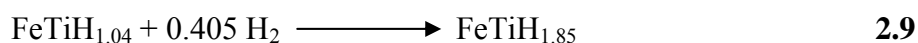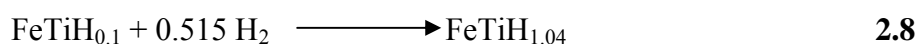
The products of the reactions are grey metal–like solid with essentially the same appearance as the initial alloy.

TiFe shows good volumetric and gravimetric hydrogen capacities competitive with the best AB_5 and AB_2 alloys. TiFe also offers the lowest price, lower on a per unit H_2 storage capacity than any other intermetallic alloy extensively researched on.

Activation is difficult for the TiFe based alloys. TiFe needs to be heated to destroy the natural oxide surface layer. As expected, the susceptibility of TiFe alloy to impurities in the H_2 to form oxide layers is very high. On the other hand, this alloy exhibits little or no tendency for pyrophoricity because of the formation of surface Ti-oxides. The melting of TiFe based AB alloys requires special care. The metallurgy is made a bit complex because of the tendency of the alloy to pick up oxygen, which overtime lowers the reversible capacity. In summary, PCT properties of TiFe are acceptable. Another incentive is the low raw material cost and high abundance of raw material from which the staring material can be produced. However, the issues to be addressed if it is to be viable for commercial use are its susceptibility to gaseous impurities and the problems associated with activation.

- **A_2B intermetallic compounds:** The A_2B family of compounds represents an area of historical activity. Various crystal structures are possible. In one subfamily, A is typically of Group IV elements Ti, Zr and B is a transition metal typically Ni. Another family is based on Mg_2Ni, discovered in the late 1960s by Reilly and Wiswall (USA) [19]. Unfortunately, the A_2B based hydrides are too stable and offer close to zero reversible hydrogen capacity in the 0-100 ^{0}C, 1-10atm range, at least with the present state of the art. There has been extensive work on Mg_2Ni for nearly three decades, both from fundamental and application point of view. Hydrogen capacity and cost properties of Mg_2Ni are attractive, but desorption temperatures have not been particularly successful. There have been several successful efforts to increase adsorption and desorption kinetics by surface treatment or nanocrystalline and amorphous versions of Mg_2Ni related alloys but the basic hydride thermodynamics have not been improved much.

Based on the above characteristics offered by the different intermetallic compounds, the table below presents a qualitative overview of their attributes.

Table 2.1: *Qualitative overview of hydride types as to attributes [19]:*

Attribute	AB_5	AB_2	A_2B	AB
(i) Versatility	+	+	- / 0	+
(ii) H- capacity	0	+ / 0	+	+ / 0
(iii) PCT	+	+	-	+
(iv) Activation	+	0	0	- / 0
(v) Impurity effect	+	0	0	-
(vi) Cyclic stability	+ / 0 / -	0 / ? / -	0 / ?	- / 0
(vii) Ease of manufacture	+	0	0	+
(viii) Pyrophoricity	0	-	+	+
(ix) Cost	0	+	+	+

Key to table: - good +, neutral 0, poor -, uncertain?

2.3 Intermetallic hydride forming materials on the basis of TiFe

TiFe–based intermetallic compounds are well–studied hydrogen storage materials known for more than 30 years [62]. TiFe is one of the most promising hydrogen storage alloys, due to its reasonable reversible hydrogen storage capacity at near ambient conditions, abundance and low cost. One of the main shortcomings of TiFe intermetallic compounds is that they have poor activation performances and poisoning tolerance resulting in significant impeding of hydrogen sorption even by trace amounts of gas species, including oxygen and water vapour. As a result, the synthesis methods for the preparation of TiFe–based metal hydride material are very important. TiFe–based metal hydride material can be prepared by various methods such as arc–melting, induction–melting, sintering, mechanical alloying and direct reduction from metal oxide materials. Despite the fact that the listed methods were shown to be rather efficient, special precautions must be taken during the synthesis process because of the ability of the TiFe–based material to easily pick up oxygen and the possibility of the formation of $TiFe_2$ which does not absorb hydrogen under acceptable pressure–temperature conditions.

This section presents details about the features of TiFe- based hydrogen storage materials including their hydrogen sorption performances that have been published in existing literature.

2.3.1 Phase diagram Ti–Fe

The Ti–Fe phase diagram is presented in figure 2.9. The TiFe intermetallic compound (CsCl structure type) is formed by peritectic reaction below 1317 ^{o}C and has the widest homogeneity region at T = 1085 ^{o}C from 49.7 to 52.4 at. % Ti (stoichiometric range from $TiFe_{1.01}$ to $Ti_{1.1}Fe$). Another compound formed in the system is hexagonal ($MgZn_2$ type)

TiFe$_2$ Laves phase formed by solidification of the melt at T < 1427 ^{o}C and having rather wide homogeneity region, from 27.9 to 35.2 at.% Ti at T = 1300 ^{o}C. The system is also characterised by wide concentration ranges of Fe and Ti-based solid solutions at high temperatures, including solution of Ti in α-Fe (up to 9.9 at% Ti at T = 1289 ^{o}C) and solution of Fe in high-temperature β-modification of Ti (up to 22 at.% Fe at T = 1085 ^{o}C).
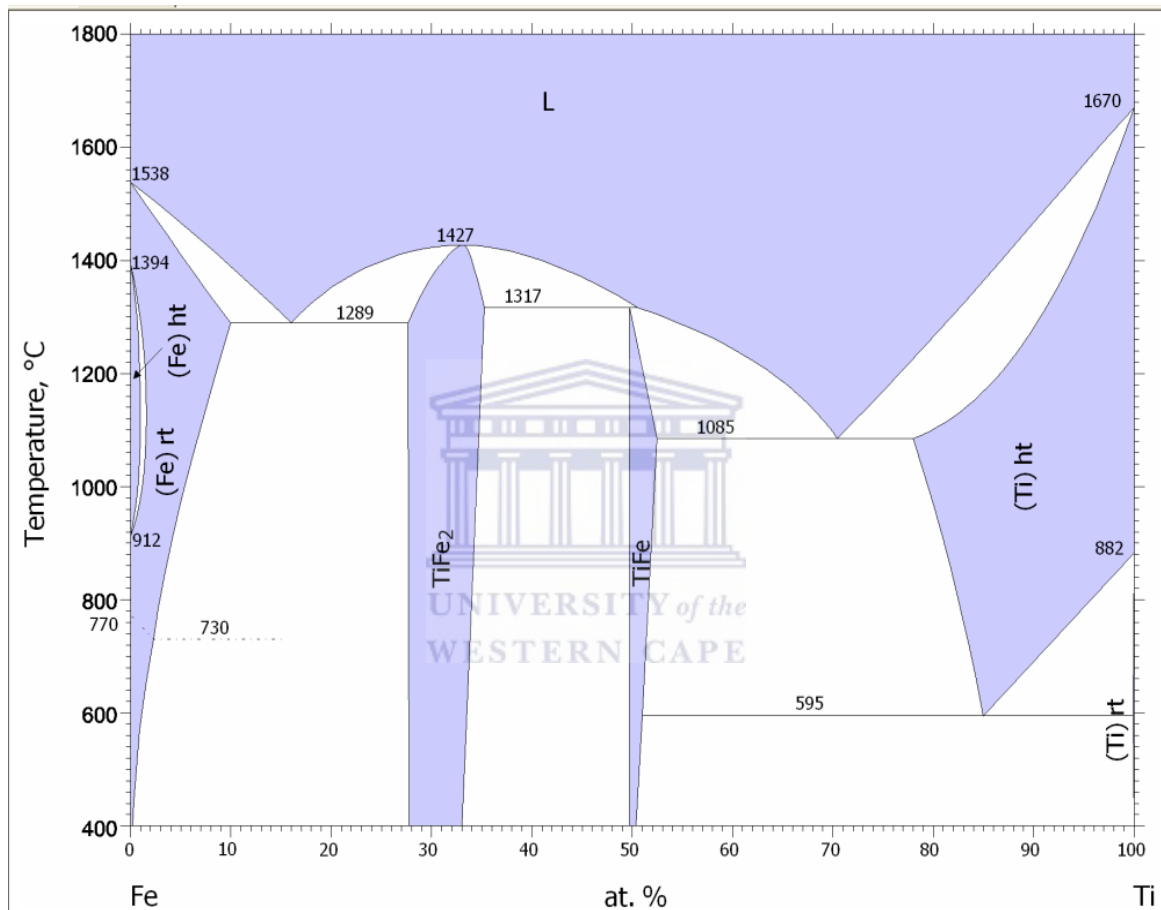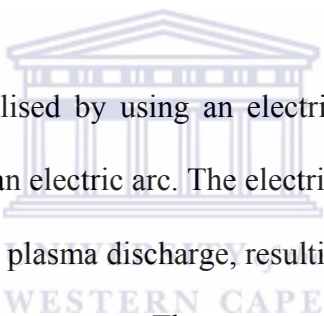
Figure 2.9: *Ti–Fe phase diagram [63].*

2.3.2 Preparation routes

Hydrogen storage alloys, particularly TiFe, may be prepared by various techniques. These include mechanical alloying, arc–melting, induction melting, sintering, etc. The preparation method plays an important role in the hydrogen absorption and desorption performances of the synthesised materials.

2.3.2.1 Melting of the constituents

The two commonly used techniques used in the preparation of intermetallic hydrogen storage materials include arc-melting and induction melting of constituents in an inert atmosphere.

Arc-melting: Arc–melting is realised by using an electric arc–furnace where the charged materials are heated by means of an electric arc. The electric arc is an electrical breakdown of a gas which produces an on-going plasma discharge, resulting from a current flowing through a nonconductive media such as air or argon. The arc occurs in the gas–filled space between two conductive electrodes and it results in a very high temperature, which is capable of melting various materials. Before arc–melting the raw metallic materials have to be placed in a crucible. The crucible is typically made of copper and is surrounded by a water jacket used to cool the melt and control the solidification rate. It is highly essential to control the current, cooling water and electrode gap for effective control of the process and the production of defect free materials.

The arc–melting technique provides several advantages, which include: (1) great versatility in terms of the types of materials which can be processed, (2) limited reactivity of the melt with cold crucible material and thus high purity of the final ingot and (3) relatively low initial

equipment costs for small scale arc–melting systems. While arc–melting could be used for the production of hydrogen storage alloys, it also has its disadvantages. Its main disadvantage is the inherent hazard present in the high current arc which is formed between the cathode and the water cooled copper lined anode. The high current arc has been documented to have melted through the water cooled copper lining, thereby contacting the water and resulting in a violent reaction as well as damage to expensive crucible assembly. Other disadvantage associated with arc–melting is high inhomogeneity, of the ingot. The process efficiency of arc–melting is low, resulting in very high costs. A great deal of power extended to melt the raw materials is directed towards the water cooling medium rather than heating the raw materials.

Induction melting: Induction melting in vacuum or protective gas atmosphere is well known to be an effective method for melting various metals such as titanium, tantalum, niobium and molybdenum [64,65,66]. It is a process of melting of an electrically conducting object (usually a metal) by electromagnetic induction, where eddy currents (currents induced in conductors to oppose the change in flux that generated them) are generated within the metal, and resistance leads to Joule heating of the metal. The process is maintained by an induction coil, through which a high – frequency alternating current (AC) is passed.

The main advantage of induction melting is the high degree of homogeneity of the alloys that are prepared. A feature of induction melting is stirring, which occurs due to strong magnetic fields within the induction coil. These strong fields induce movement of the molten materials through the crucible thus assuring a high degree of homogeneity of the alloy. Another advantage is the fact that reproducibility from sample to sample is very high. Also, due to stirring caused by the induction melting process, the role of the operator in assuring

homogeneity and process efficiency is relatively low, thus minimising errors in sample preparation by operators. Since operator interaction is minimised, the likelihood of producing unacceptable materials is also minimised thus increasing process efficiency. The main disadvantage of induction melting is in contamination of the ingot by crucible material interacting with the melt at high temperatures. In most cases, graphite crucibles are used to melt material, but in some cases it has been reported that contamination by carbon takes place [66]. Generally, oxide (SiO_2, Al_2O_3, etc.) crucibles are applied instead of the graphite ones to avoid the carbon contamination, but their usage can result in oxygen contamination of the product due to interaction between the melt with the oxides. It has been reported [67] that silicon nitride or boron nitride coating of the inner wall of the crucible reduces the contamination. However, this is not a fundamental solution because the coating material peels easily.

2.3.2.2 Mechanical alloying

Mechanical alloying (MA) is a technique used in the synthesis and modification of various intermetallic alloys, including hydrogen storage ones. MA is a process used mainly to form amorphous or nano-structured materials. During MA metallic particles are fractured into smaller fragments that are cold welded together. By repeated fracture and welding, new surfaces are generated, which lead to the formation of new intermetallic compounds by inter-diffusion through interfaces [68].

TiFe alloys synthesised by MA have been extensively studied [69,70] and showed that the material can absorb relatively high amounts of hydrogen. Although MA is an attractive method that can be used to synthesise novel intermetallic materials, there are problems associated with the method. Problems related with MA are that the alloying process

is relatively time consuming and high energy is needed to synthesise the alloys. Increase in temperature and sticking of powders to vessels or balls during MA and contamination of the product by the material of balls or vial influences on the structure and properties of the synthesised alloy [71]. Studies have shown that post–annealing after MA can assist in limiting some problems related to MA during synthesising of alloys [71]. However, it is still time consuming and an energy consuming process.

2.3.2.3 Direct synthesis of TiFe from ilmenite

TiFe-based hydride forming alloys are less expensive when compared to AB_5 alloys. However, due to abrupt increase of prices for titanium metal during last decade [72], the price for these materials prepared by conventional method of melting the metallic components becomes unacceptably high. At the same time, the available titanium-containing raw materials are much cheaper. According to data reported by Van Vuuren [73], the corresponding average prices sharply increase from 0.09 USD/kg for ilmenite and 0.4–2.1 USD/kg for titanium dioxide of different grades to 10, 20 and 40 USD/kg for titanium sponge, ingot and mill products, respectively. Such big differences are caused by the complexity and high costs of production of metallic titanium where a significant part of the process is related to the separation and refining of the pure metal.

Iron and Titanium are the fourth and ninth most abundant elements in the earth's crust. Particularly, the two co-exist in the form of ilmenite ($FeTiO_3$), which is a common natural mineral with a known world total resource of ~2 $\times 10^{12}$ kg [74]. Of a number of titanium-containing raw materials, the ilmenite, ($FeTiO_3$), is characterised by the lowest cost and wide availability. So, it is a very attractive feedstock for the manufacturing of titanium-containing metal hydrides.

The utilisation of ilmenite includes its reduction to yield a mixture of metallic iron and titanium oxide which are further separated by various routes. As an example, Yoshikoshi and Nakahara disclosed a method of production of synthetic rutile from ilmenite [75], by its reduction with hydrogen contained in coke-oven gas processed using hydrocracking catalyst; then reduced iron is leached out by an acid to obtain a material having a high content of titanium, and the material is dried and baked to produce synthetic rutile. Another approach illustrated in the solution patented by Joseph and Whellock [76] involves the chlorination of the ilmenite ore followed by the distillation or other procedure to form pure titanium tetrachloride (TiCI$_4$), and, finally, reducing TiCl$_4$ to yield titanium metal. Both approaches utilise multistage processes of separation of iron and titanium where each stage is characterised by high power and labour consumption, necessity of aggressive and toxic chemicals, availability of specialised chemical-metallurgical equipment, and technological complexity. This largely explains the above-mentioned sharp increase in the cost of products in the titanium value chain.
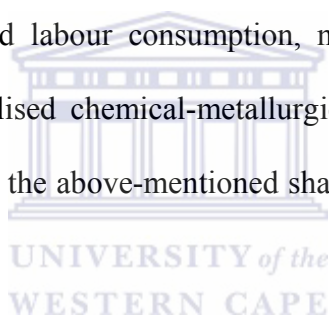
The synthesis of TiFe alloy via the reduction of ilmenite (FeTiO$_3$) has been attempted in various laboratories. Wu *et.al* reported about synthesis of TiFe by metal-thermic reduction of ilmenite with magnesium [77]. The process was carried out in a combustion mode (Self-propagating High-temperature Synthesis, SHS), after 6 hours-long grinding the mixture FeTiO$_3$ + 4 Mg followed by its compacting to 60% of the theoretical density. Apart from the target TiFe and MgO by-product, the final products also contained noticeable amounts of TiFe$_2$, Fe, Mg$_2$TiO$_4$ and TiO. This shows that the reduction process was incomplete, despite 33% excess of magnesium over the stoichiometric amount (FeTiO$_3$ + 3 Mg) applied in this study.

A promising technique for the preparation of TiFe alloy from ilmenite ($FeTiO_3$) is the electrochemical reduction route. A novel electrochemical method of ilmenite reduction to TiFe-based alloys was suggested by Ma *et.al* and further improved by Ye *et.al* [78,79]. The method is based on direct electrochemical reduction of $FeTiO_3$ in molten $CaCl_2$ at a high temperature (T~1000 ^{o}C). For getting final product of a reasonable quality, the process requires quite long time, 3 hours and more. Despite its apparent simplicity, the electrochemical method of preparation of TiFe-based hydride forming alloy from ilmenite requires careful and labour-consuming procedure of the preparation of starting materials, and has very high power consumption. The necessity of special electrochemical equipment able to withstand cyclic operation under hard conditions, including long-time work at high temperature in chemically aggressive environment, is another challenging issue militating against the wide-scale implementation of the method.

2.3.2.4 Problems in the preparation of TiFe and its derivatives

During the preparation of TiFe based materials, special precautions must be taken due to the ability of TiFe-based materials to easily pick – up oxygen and the possibility of the formation of $TiFe_2$, which does not absorb hydrogen under acceptable pressure–composite–temperature conditions. To avoid these complications, Ti is taken in 10 – 30 % excess as compared to the stoichiometric TiFe ratio, and/or deoxidisers like rare earth metals are introduced. These modifications improve hydrogen performances, in particular, two hydrogen absorption – desorption plateaux for $Ti_{1-x}Fe$ are merged thus providing high hydrogen storage capacities at reasonable hydrogen pressures [19,62,80] as well as having an easier activation of the $Ti_{1+x}Fe/Re$ alloys [81,82].

An additional problem is in intrinsic feature of TiFe itself, whose hydrogen sorption performances are very sensitive to minor variations of the alloy's composition and preparation route, as well as to the poisoning with gas impurities in gaseous hydrogen [83].

2.3.3 The structure of TiFe and its hydrides

TiFe-based AB alloys are based on an ordered body-centred cubic structure (prototype CsCl, strukturbericht B2, Pearson cP2, space group *Pm-3m*). In the CsCl-type structure, hydrogen atom occupies a central site of the octahedron which is constructed with four Ti and two Fe atoms (hereafter referred to as the Ti_4Fe_2H octahedron). The H_2 absorption capacity in TiFe is known to be smaller (H/M=1.0) than the value (H/M=1.5) which would be expected from their crystal geometry [84, 85]. This is due to the existence of another octahedron which is constructed with two Ti and four Fe atoms (Ti_2Fe_4H octahedron) as shown below in figure 2.10.
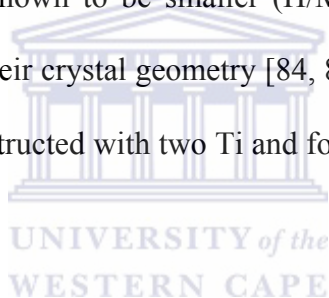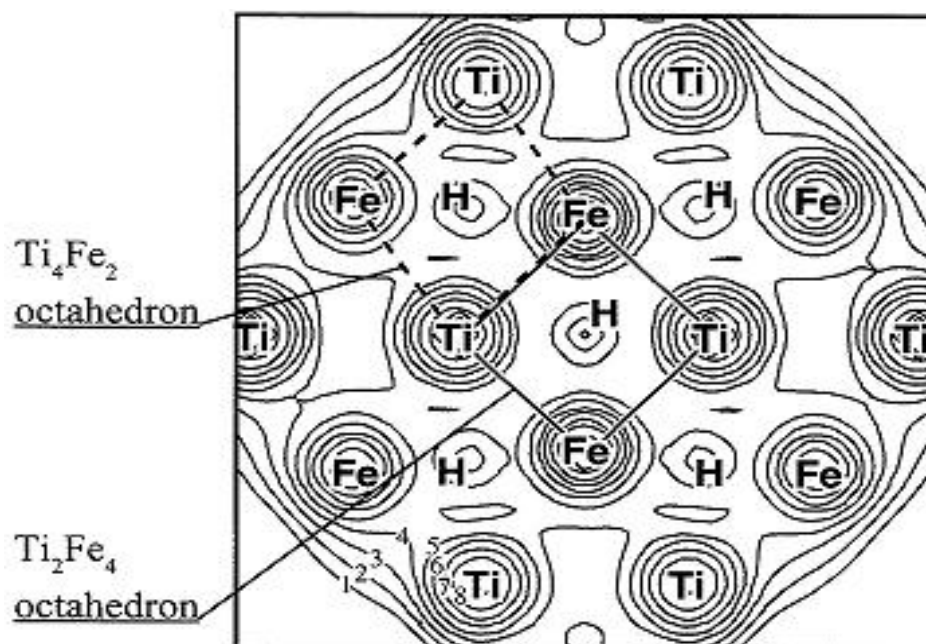
Figure 2.10: *Contour maps of electronic densities on the atomic plane of $Ti_{20}Fe_{20}H_{43}$ cluster [85].*
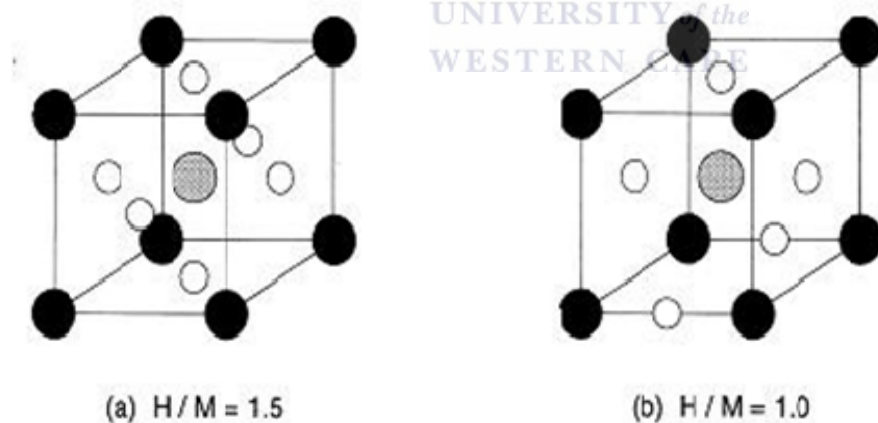
Figure 2.11: *Schematic illustration of the hydride of the compounds with CsCl-type structure; (a) simple hydride, (b) TiFe hydride [85]*

Once the Ti_2Fe_4 sites are occupied by H atoms as shown in figure 2.11 (b), the nearest Ti_4Fe_2 octahedral sites cannot be occupied anymore by H atoms .Therefore, the H-capacity expected for Ti compound with CsCl structure as illustrated in figure 2.11 (a) is reduced from 1.5 to 1.0 due to lesser number of Ti atoms which serve as H_2 absorbing atoms in comparison to Ti_4Fe_2 octahedral sites.

Figure 2.12 indicates schematically the structure of $\beta - Ti_{0.5}Fe_{0.5}H_{0.5}$. The average atomic volume increases with increasing hydrogen concentration x if $Ti_{0.5}Fe_{0.5}H_x$ according to the empirical relation $\Delta v/vo = 0.15x$, which is similar to the behaviour of well–studied systems Pd-H, Nb-H, Ta-H and V-H. The value of expansion of the host lattice during dissolution of hydrogen is an extremely important parameter which controls the disintegration of large grains of materials into fine particles and thus controls the kinetics of hydriding and dehydriding [86].
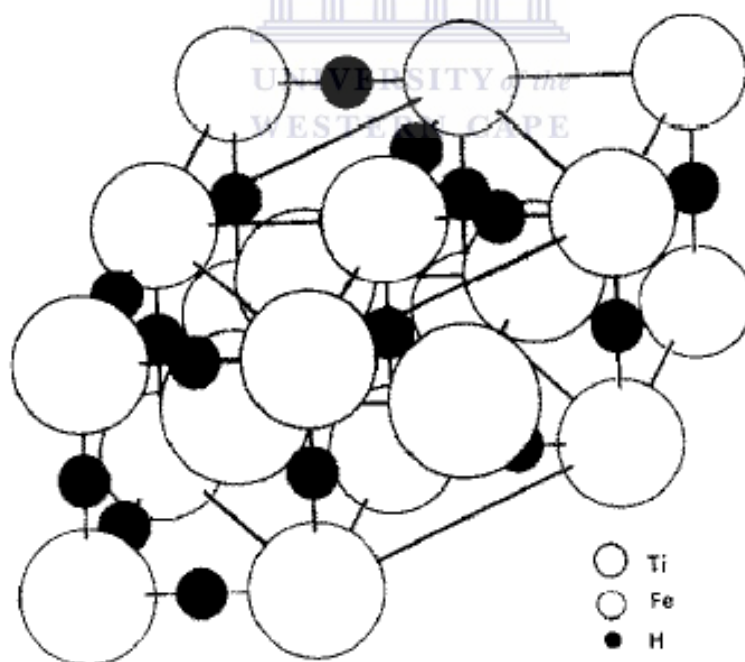
Figure 2.12: Three unit cells of the CsCl structure of FeTi with hydrogen on octahedral sites between nearest-neighbour iron atoms arranged in an ordered way as in β-FeTiH[86].

75

2.3.4 Hydrogen absorption – desorption performance of TiFe and its derivatives

The interaction of intermetallic compound TiFe with hydrogen yields two phases, viz. β – monohydride and γ – dihydride. The Pressure Composition Isotherms (PCT) of TiFe are shown below in figure 2.13 [62]. The shape of the isotherms in figure 2.13 can be interpreted as follows: on the left, where the isotherms rise steeply as the hydrogen content of the solid increase, is the region of solid solution of hydrogen in the TiFe metal lattice. This solid solubility region is known as α - phase in the TiFe-H system. As the hydrogen content of the solid increases the equilibrium pressure remains constant and forms a plateau. The composition at which the plateau begins, marks the maximum solubility of hydrogen in α – phase. At room temperature, the composition corresponds to $FeTiH_{0.10}$ {(H/M) = 0.05}. The new phase is the monohydride or β – phase of the TiFe-H system. Both the α and β phase co– exist until the solid composition corresponds to $FeTiH_{1.04}$ where the isotherm begins a step ascent. At this point α – phase disappears. As the hydrogen content of the β – phase increases a new phase appears, the γ – dihydride phase.
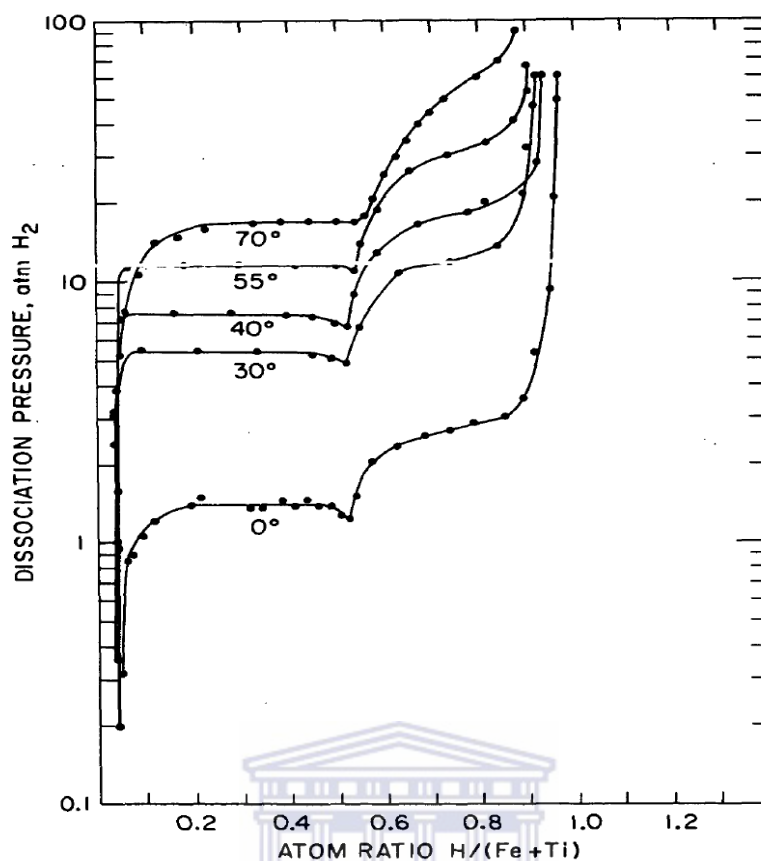
Figure 2.13: PCT Diagram of FeTi-H system [62].

The reaction taking place in the TiFe-H system may be written as follows. In the lower plateau region

$$FeTiH_{0.10} + 0.515\ H_2 \longrightarrow FeTiH_{1.04} \qquad\qquad \textbf{2.10}$$

which is followed by

$$FeTiH_{1.04} + 0.455\ H_2 \longrightarrow FeTiH_{1.95} \qquad\qquad \textbf{2.11}$$
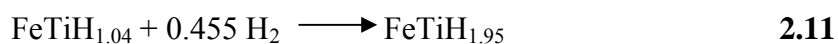
Hydrogen sorption performances of TiFe can be illustrated by phase diagram (Figure 2.14) taken from review [87]. The diagram shows the existence of β-hydride at H/(Ti+Fe) ~

0.55 and γ-hydride at H / (Ti + Fe) ~ 0.95; at higher hydrogen concentrations ε-phase

appears. There were also indications about formation of δ-hydride at H / (Ti + Fe) ~ 0.6. The

β-hydride is stable up to T~ 500 K, and γ-one up to T ~ 350 K.
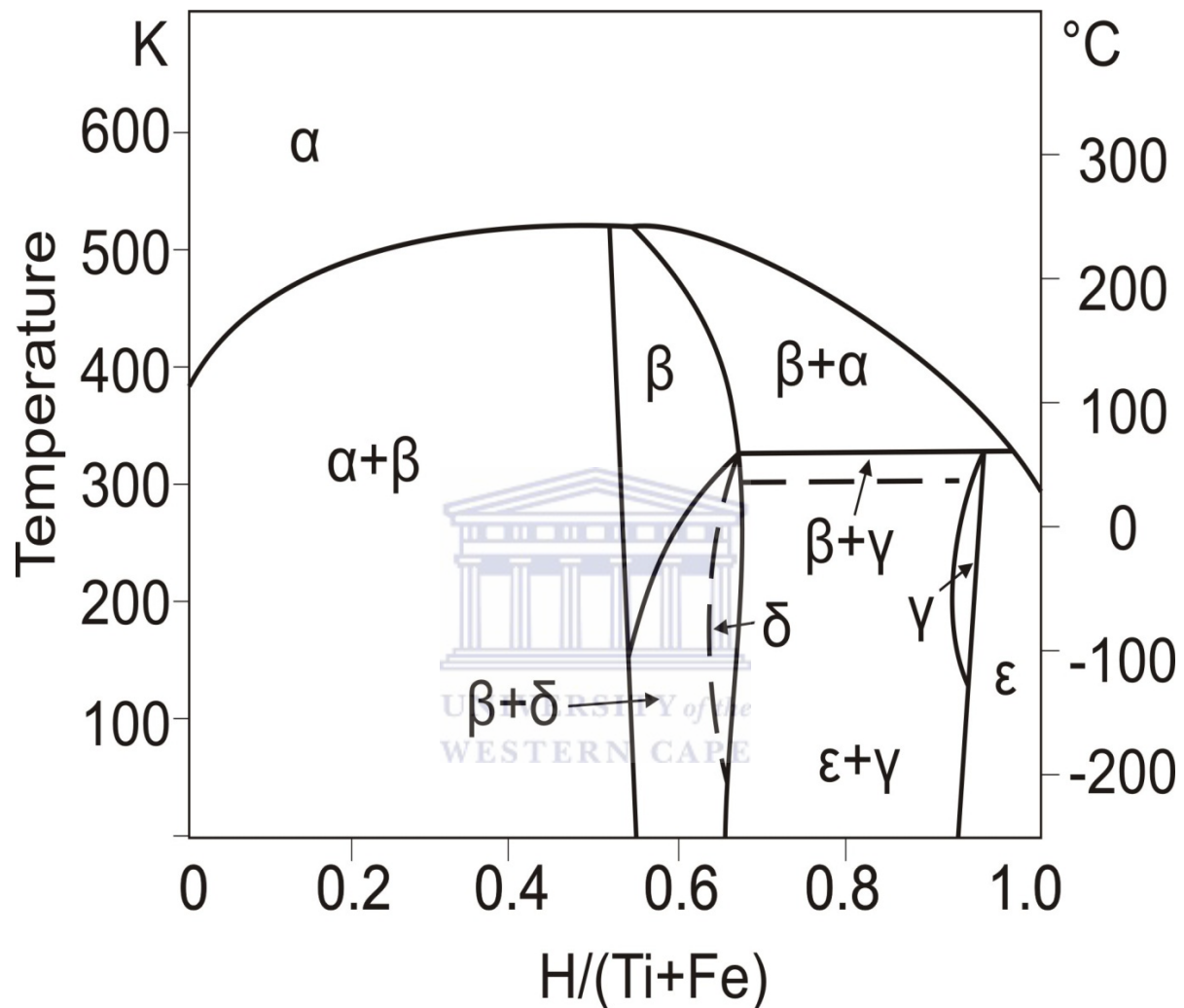
Figure 2.14: *Phase diagram of H – TiFe pseudo-binary system [88].*

Figure 2.15 below illustrates the pressure–composition isotherms of TiFe-based alloys

with various ratios of Ti and Fe. From figure 2.15, isotherm B the TiFe alloy has a ratio of

49.3% Ti and 50.7% Fe, the isotherm has been significantly distorted, the equilibrium

dissociation pressure decreased and the boundary between the lower and higher hydride is almost indistinguishable. When the Ti content was increased to 63.2 %, the pressure–composition isotherm C is greatly distorted. The increased amount of residual hydrogen in the solid phase is undoubtedly due to the presence of stable titanium hydride. When increasing the Fe content to 60.5 wt. % it was noticed from the isotherm A, that a reduction in the amount of hydrogen absorbed takes place. The reduction in the amount of hydrogen absorbed is due to the mere physical presence of $TiFe_2$.
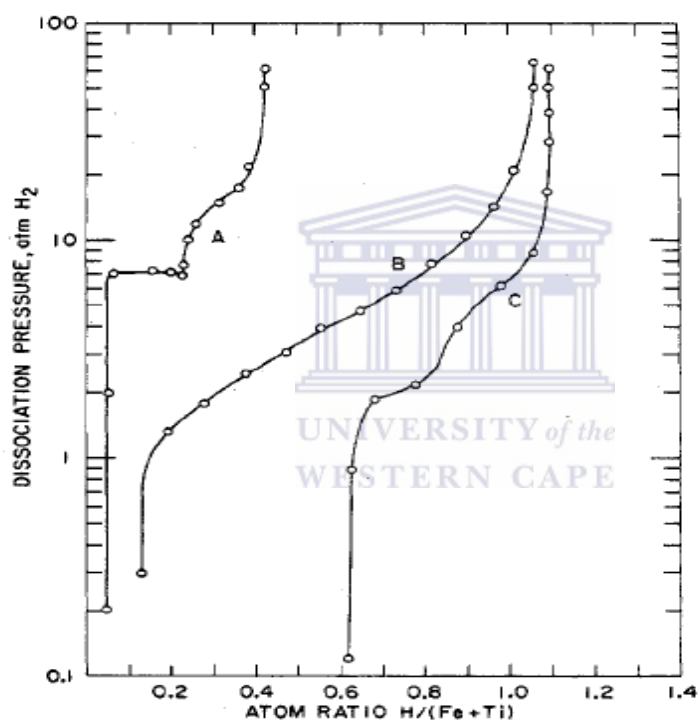
Figure 2.15: *Pressure-composition isotherms for alloys of various Fe/Ti ratios at 40 ^{0}C: (A) 60.5 wt. % Fe, 39.5 wt. %Ti; (B) 50.5 wt. % Fe, 49.2 wt. % Ti; (C) 36.7 wt. % Fe, 63.2 wt. %Ti [62].*

2.3.5 Limitation of hydrogen sorption using TiFe alloy

- **Surface poisoning:** Surface poisoning seems to be the biggest shortcoming in the uptake of hydrogen from gaseous mixtures containing aggressive components using Ti–based hydride forming alloys [89]. Ti–based alloy materials exhibit low rates of hydrogen absorption, and this shortcoming is caused by the formation of oxide layers on the surface of the titanium after exposure of the alloy to air [19,20]. As a result, the surface catalytic sites are deactivated and hydrogen absorption can no longer be initiated at reasonable rates. Increasing exposure to air leads to an incubation period in which hydrogen absorption rates are insignificant. Long exposure to air increases the difficulty involved in thermal activating the alloy under hydrogen pressure [19,89].

- **Activation and incubation periods:** One of the main problems associated with TiFe alloys is that they do not readily absorb hydrogen under ambient conditions and have to be thermally activated prior to hydrogenation [70]. The activation of metal hydride alloys plays a key role in the sorption process, since it defines the rate of the reaction of hydrogen with the metals and the incorporation of hydrogen into the bulk structure of the metal. During activation, different processes occur, such as reduction or protonation of surface oxides. The dissolution of surface oxides in the bulk alloy culminates in segregation of surface metallic clusters which are able to catalyse hydrogen dissociation. Recent surface studies confirmed that electron transfer between the surface and H_2 molecules is crucial for the occurrence of H_2 dissociation. Therefore, the ready dissociation of H_2 molecules on the metal surface is crucial for the initial activation of metals [90]. During the synthesis of metal hydride materials it is very difficult to avoid surface contamination. The only solution is to maintain

80

ultra-high vacuum conditions, but this is very expensive. In order to restore good hydrogen sorption properties some kind of activation procedure has to be applied. However, this requires repeated heating in hydrogen to pulverise the alloy and generate fresh surface for the reaction. During hydrogen absorption by metal hydride-forming materials, a period of incubation may be observed [91]. The incubation period is due to the presence of an oxide layer that has to be disintegrated through repeated activation cycles.

- **The effect of impurities on hydrogen absorption in TiFe alloys:** The kinetics of hydrogen absorption depends strongly on the surface structure of the metal hydride, whereas sorption capacity is determined by the bulk properties of the metal hydride-forming alloy. Impurity effects on metal hydrides are a result of the interaction of gaseous impurities, present in the hydrogen gas, with the material. Since the absorption and desorption of hydrogen is highly dependent on surface structure, surface poisoning can have a very dramatic effect on hydrogen sorption properties. Poisoning of metal hydride-forming alloy materials is observed by a rapid loss in the H_2 sorption capacity and a large decrease in the overall kinetic properties of the material. If the adsorption of an impurity at the metal surface by either a physical or a chemical mechanism dominates the adsorption of hydrogen, the impurity will displace the hydrogen atoms from the surface [92]. The vulnerability of TiFe alloy to surface contamination by aggressive gases, especially CO, H_2S, H_2O and O_2 is a major problem. These poisoning species form surface films (i.e. oxides, sulphides, carboxides, etc.) which prevent the process of molecular hydrogen dissociation ($H_2 - 2H$). F.R.Block *et.al* have observed rapid losses in hydrogen sorption capacity and kinetics when cycling TiFe alloy in H_2S containing H_2 gas streams with 0.2 vol %

H_2S in H_2 [92]. The presence of as little as 1.0 vol % O_2 in H_2 results in the reduction in the hydrogen sorption properties of TiFe alloy [93]. Exposure of TiFe with H_2O (as water vapour) is also associated with the occurrence of surface oxides [94]. Surface oxidation renders Ti sites inactive towards catalysis H_2 surface dissociation processes due to the formation of stable titanium oxide films (TiO_2), which acts as a hydrogen diffusion barrier due to poor diffusivity and solubility of hydrogen through the layer. TiO_2 layers are also formed upon exposure of TiFe to water vapours and CO. The stable TiO_2 layer formed inhibits any further surface reaction as TiO_2 is a non-catalytic towards the dissociation of H_2. The negative influence of surface poisoning species on the hydrogenation of TiFe can be observed in figure 2.16.

Cycle Number
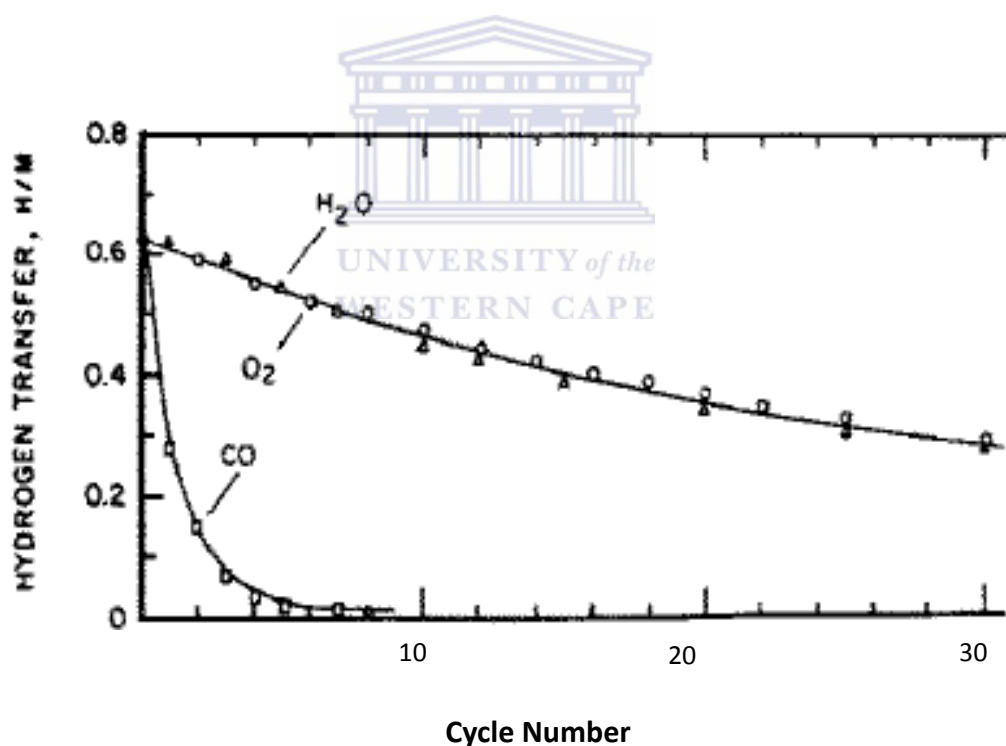
Figure 2.16: The effect of cycling at room temperature with H_2 containing 300 ppm O_2, H_2O, and CO. The curves show the quantitative loss of transfer capacity in terms of the atomic hydrogen to metal ratio (H/M) [95].

- **The Influence of the introduction of Oxygen in Ti-Fe Alloys:** At high temperatures TiFe has extremely high affinity towards oxygen, including chemically bound one. The introduction of oxygen in Ti-Fe system assists in the hydrogen absorption kinetics. Oxygen doped TiFe usually forms the phase $Ti_4Fe_2O_{1-x}$ [96,97]. The $Ti_4Fe_2O_{1-x}$ oxide phase is usually distributed in the TiFe phase and causes it to become brittle. Therefore, it becomes easy to expose fracture surfaces of the TiFe phase uncontaminated by air and allows the hydrogenation to advance at the surface. The $Ti_4Fe_2O_{1-x}$ oxide phase acts as a catalyst and promotes the reaction between hydrogen and the TiFe phase on the surface.

On the other hand, the introduction of oxygen in TiFe culminates in the following side reaction:

$$6 \ TiFe + [O] \rightarrow Ti_4Fe_2O + 2 \ TiFe_2. \qquad\qquad \textbf{2.12}$$

The first product of the side reaction (2.12) is the mixed oxide Ti_4Fe_2O that can absorb hydrogen, but the formed hydride is too stable and requires high temperatures / low pressures to release hydrogen back. The second product, $TiFe_2$, does not absorb hydrogen at reasonable pressure / temperature conditions. According to our calculations [98], if all the target alloy undergoes the side reaction (2.12), that corresponds to only ~2.5 wt.% of oxygen contents therein, its reversible hydrogen storage capacity will be completely lost.

2.4 AB$_2$ – type intermetallides on the bases of Ti

AB$_2$ alloys with Laves phase structures have attracted a great deal of attention as hydrogen storage materials because of their substantial hydrogen storage capacity. Ti-Mn Laves phase alloys are promising hydrogen storage materials with easy activation, good hydriding / dehydriding kinetics, high hydrogen storage capacity and relatively low cost. However, the major problem of TiMn$_2$ alloy is its high equilibrium plateau pressure. The Zr-based AB$_2$ systems usually show larger hydrogen storage capacity, rapid kinetics and relatively longer electrochemical charge-discharge cycle life. Among the Zr-based AB$_2$ alloys, ZrMn$_2$, ZrCr$_2$, and ZrV$_2$ contain much absorb hydrogen while ZrFe$_2$ and ZrCo$_2$ have hydrogen absorption that are quit low. Most of the studies aimed at improving hydrogen storage properties of AB$_2$ type alloys, are confined to material tailoring through substitution an A or B sites [99]. However, it has been recognised that the material tailoring involving substitution at both A and B sites is a better option for improving several hydrogenation features particularly storage capacity and desorption kinetics [100,101].

A typical representative of Ti-based AB$_2$-type intermetallic compounds of practical importance is hexagonal (MgZn$_2$ type or C14) Laves phase, TiMn$_2$. It solidifies from Ti–Mn melt at T ≤ 1325 ^{o}C (see phase diagram in figure 2.17) and has quite wide homoheneity region, from 30.5 to 41.0 at % Ti at T = 1200 ^{o}C that corresponds to Mn / Ti (B/A) stoichiometric ratio from 1.44 to 2.28. Substitution both from A (Ti for Zr) and B-side (Mn for Fe, Cr, Ni, V, etc.) is possible in quite wide ranges for TiMn$_{2\pm x}$, that, together with the possibility of B/A stoichiometry variation, makes this kind of hydride-forming intermetallides exceptionally versatile towards control of their hydrogen sorption performances by the variation of the component composition.
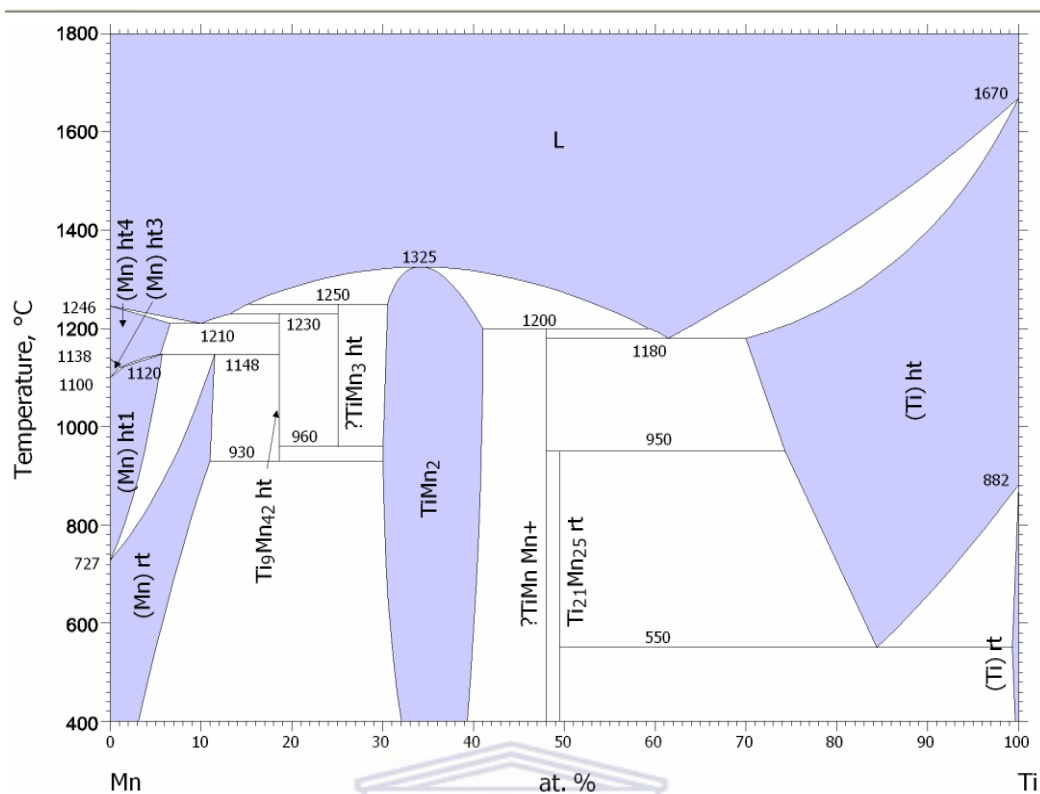
Figure 2.17: *Ti–Mn phase diagram [88].*

2.4.1 The Composition and Structural Features of AB₂ type intermetallides on the basis of Ti

J. L. Bohet *et.al* studied the hydrogen sorption properties of $Ti_{0.95}Zr_{0.05}Mn_{1.95}$ based alloys by substituting the B component with Ni, Co, Cr, V and Al. He concluded that Cr, V and Al substitution could be the most suitable to obtain the optimum hydriding properties due to the fact that they lower the plateau pressure of the $TiMn_2$ system as a result of increasing the lattice parameters which increases the size of interstitial sites [102].

Guanping Li *et.al* studied the crystal structure of $Ti_xZr_{1-x}Mn_2$ system; their results revealed that $Ti_xZr_{1-x}Mn_2$ alloys with x = 0, 0.1, 0.2 and 0.3 crystallized in the C14 Laves phase structure and showed that Ti atoms preferentially occupied Zr sites. The alloys did not

change their crystal structure type on hydriding but significantly expanded. They also observed that as the Ti content increased, the equilibrium pressure of the studied also increased [103].

2.4.2 The effect of stoichiometry and component substitution of AB_2 type alloys on the basis of their hydrogen absorption – desorption performances.

Of all the Zr-based AB_2 alloys spares studies have been done on $ZrFe_2$ probably due to its poor hydrogenation absorbing capacity. It has been shown that the ideal material for $ZrFe_2$ systems is to substitute Cr at the Fe site which corresponds to $ZrFe_{1.4}Cr_{0.6}$. [104]. S. Roy *et.al* used $ZrFe_{1.4}Cr_{0.6}$ as a reference material in their work; they substituted the Zr site with Ti and Mn. The reason for substituting Zr is that Zr is known to form very stable interstitial hydrides which do not readily desorb hydrogen. Ti substitution at the Zr site is expected to obtain a hydride which would desorb easily. Mn substitution at the Zr site is expected to obtain larger unit cell volume, which could lead to increase in interstitial size thereby increasing the occupation of higher number of interstitial sites by hydrogen and hence enhancement of the storage capacity. Roy *et.al* showed that the kinetics of substituted $ZrFe_{1.4}Cr_{0.6}$ with x = 0.05 $(Zr_{0.9}Mn_{0.05}Ti_{0.05}Fe_{1.4}Cr_{0.6})$ was 3.5 times faster than the parent alloy. The hydrogen storage capacity also increased [105].

JI. Yali *et.al* studied the effect of Ti content on the hydrogen storage properties of $Zr_{1-x}T_xMn_2Ce_{0.015}$ (x = 0, 0.2, 0.3, 0.5). Figure 2.18 below shows the p-c isotherm curves of the $Zr_{1-x}T_xMn_2Ce_{0.015}$ alloys measured at 393K. JI. Yali *et.al* observed that as the Ti content increases, the plateau pressure and the amount of hydrogen desorbed above the pressure of 0.1 MPa increases but the maximum hydrogenation capacity of the alloys decreases. The changes of the hydrogen storage capacity can be explained by the fact that the unit cell

86

volume of the alloy decreases with increasing Ti content, which leads to the decrease of interstitial size of the per unit cell. Therefore, as the Ti content increases the unit cell volume becomes smaller, which results in a decrease in the amount of hydrogen storage in the alloy. JI. Yali *et.al* illustrated that as the Ti content increase, the lattice parameters, unit cell volume and maximum hydrogenation capacity decreases and the plateau becomes steep, but the reversible hydrogen desorption capacity increases [106].
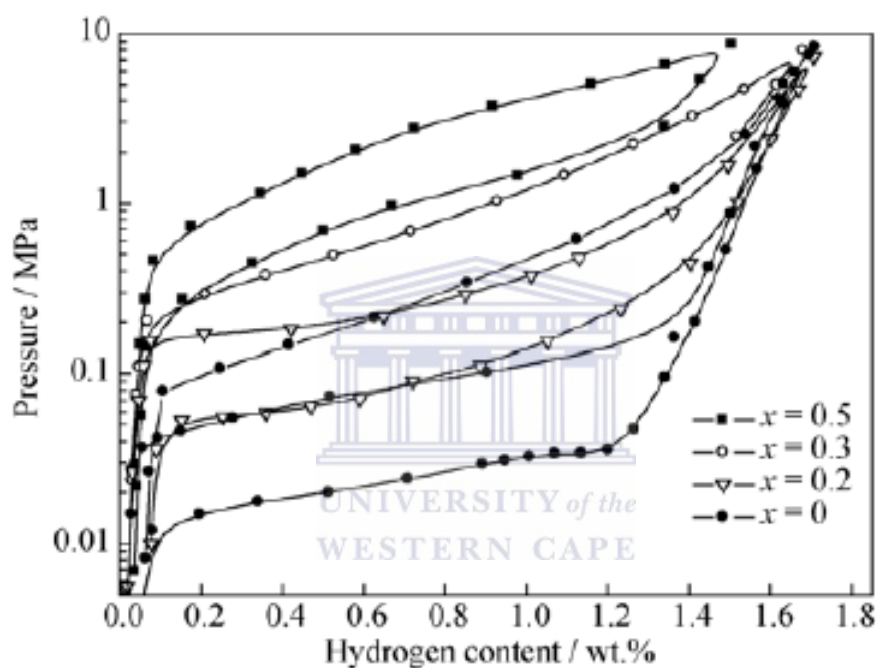
Figure 2.18: *Absorption/desorption p-c isotherm curves of $Zr_{1-x}Ti_xMn_2Ce_{0.015}$ alloys measured at 393 K (x = 0, 0.2, 0.3, and 0.5) [106].*

2.5 Platinum Group Metals (PGM's) for the promotion of hydrogen sorption in metal hydrides.

Platinum group metals (PGM's) are used in surface modification of metal hydride alloys [107,108]. The PGMs are known to be good catalysts for various chemical and electrochemical reactions. PGMs have the ability to dissociate hydrogen molecules into hydrogen atoms, which can be transported into the crystal structure of the metal. Pd exhibits a higher permeability towards hydrogen at lower temperature compared to other PGMs [109]. For this reason, the application of Pd as a catalyst on metal hydride-forming alloys has been extensively researched [110-113]. Surface coatings of Pd have the potential to add poisoning resistance to metal hydride-forming materials in oxidising environments over extended period of time, as they themselves are not easily oxidised [114]. Pd catalysis has shown to potentially increase hydrogen sorption rates and offer protection towards the surface of metal hydride-forming alloys, and for this reason was investigated as a potential surface modification technology.

2.5.1 Hydrogen sorption in Palladium

Hydrogen is highly soluble in Pd metal and diffuses through the lattice by a solution diffusion mechanism, which is unique to Pd-H systems [110]. The hydrogenation behaviour of Pd is shown in its characteristic pressure–composite isotherm (PCT) in figure 2.19.
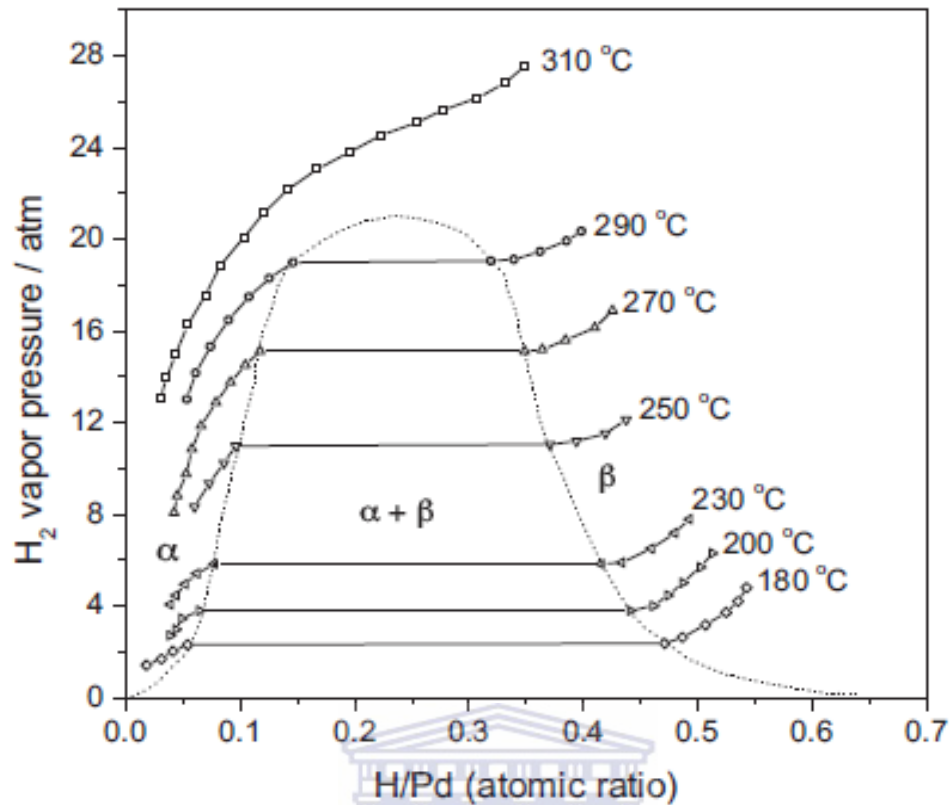
Figure 2.19: *PCT diagram of Palladium – hydrogen system [115].*

The α – phase is formed at low pressures. In this region, the hydrogen occupies interstitial sites within the Pd crystal lattice. The β – phase is only observed once higher concentrations of hydrogen are absorbed into the Pd. The absorbed hydrogen occupies tetrahedral and octahedral sites in the face–centred cubic crystal structure of the Pd [116].

The mechanism of hydrogen diffusion through Pd is well-known; it generally follows a solution–diffusion mechanism illustrated below in figure 2.20.

High Concentration

Low concentration
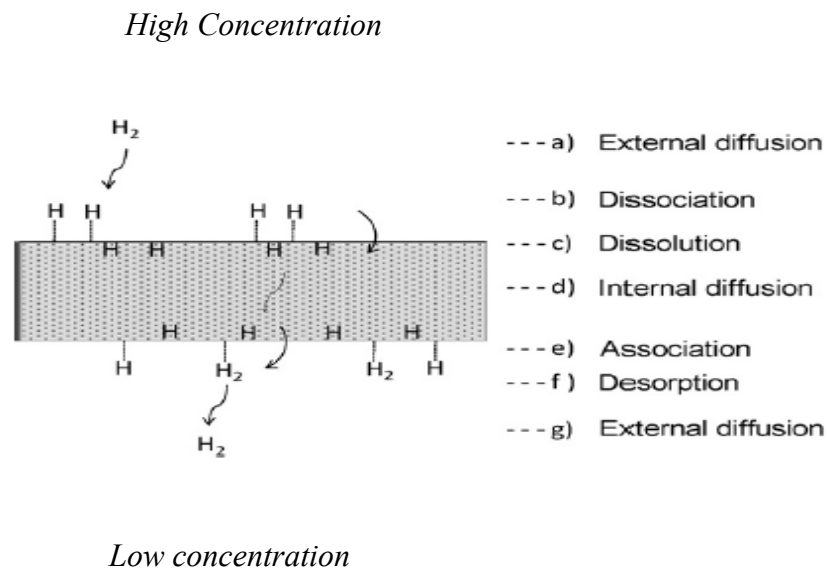
Figure 2.20: Solution – diffusion transport mechanism of H2 through Pd [115].

The solution – diffusion phenomenon exhibited by Pd is constituted by stepwise processes, given as follows:

a) Diffusion of molecular hydrogen to the surface of the palladium

b) Dissociative adsorption on the Pd surface

c) Dissolution of atomic hydrogen into the bulk metal

d) Diffusion of atomic hydrogen through the bulk metal

e) Association of hydrogen atom on the Pd surface

f) Desorption of molecular hydrogen from the surface

g) Diffusion of molecular hydrogen away from the surface

The basic driving force behind this type of diffusion through Pd is a concentration gradient.

2.5.2 Enhancing hydrogen sorption kinetics and poisoning resistance by surface deposition of palladium on metallic hydride – forming materials

The development of composite materials by combining properties of Pd and metal hydride alloys may potentially have excellent characteristics due to a synergistic effect between the unique properties of two components. These composite materials may potentially produce a remarkable change in hydrogenation and kinetic properties compared to that of the parent alloy.

The presence of Pd enables hydrogen to pass rapidly through the surface of the alloy to the bulk, while maintaining the hydrogenation activity even after extensive exposure to an oxidising environment [117,118]. Palladium deposition provides metal hydride–forming alloys the ability to absorb hydrogen at low temperature without a special activation steps, enhanced absorption properties and enhanced activation rates [119]. Furthermore, Pd is not oxidised by H_2O, CO, CO_2, and O_2 which may thereby increase the poisoning resistance of support materials towards these specific poisoning species [111]. Zaluski *et.al* reported that the presence of Pd as a catalyst in nanocrystalline Mg_2Ni, $LaNi_5$ and TiFe systems enhance the absorption rates even at low temperature and maintain less sensitivity to air exposures [120]. Even small addition of Pd (0.25 wt%) can greatly improve the activation behaviour of metal hydride–forming materials [121].

2.5.3 Method and Mechanisms of surface modification of metallic hydride – forming materials with PGMs

Surface modification of metal hydride materials with PGMs can be achieved by different methods and techniques. Different deposition methods give layers with different microstructures, particle size and morphology. The catalytic surface layers can be deposited by physical or chemical methods. These methods are mechano–chemical deposition, physical vapour deposition, chemical vapour deposition, electrolytic plating and electroless plating. The deposition methods will further be discussed below.

2.5.3.1 Mechano –chemical deposition

Mechano–chemical deposition of PGM catalysts on the surface of metal hydride – forming alloys is done by ball milling. Although ball milling does not deposit metal layers on the surface of the hydride materials, it is still considered as a deposition technique since it promotes changes in the hydrogenation properties by the introduction of dopants. Ball milling of small amounts of Pd with metal hydride–forming alloys was shown to greatly improve their hydrogen sorption kinetics [121].
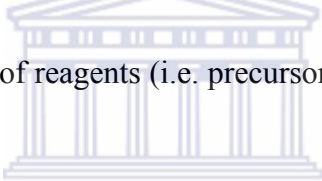
2.5.3.2 Physical vapour deposition (PVD)

Physical vapour deposition (PVD) is a vapourisation coating technique involving transfer of material at an atomic level by bombardment of solid precursor with the aid of a high energy such as a beam of electrons or ions in a vacuum [115]. The process is similar to the chemical vapour deposition (CVD) method except that the chemical decomposition reactions are generally not involved in the surface reactions. This is due to the fact that the precursors are usually pure metal, whereas in CVD, the precursors are chemical compounds in a vapourised state. Magnetron sputtering is an example of PVD method.

Mc. Cool *et.al* reported that Pd-based layers deposited using sputtering revealed lower hydrogen permeance than that prepared by CVD and electroless plating [122]. PVD technique is not a practically preferred for application in surface modification of metal hydride–forming alloys because the equipment used is usually expensive and the geometry of the substrate is also limited to a flat substrate, which severely restricts practical applications [123].

2.5.3.3 Chemical Vapour Deposition (CVD)

Chemical vapour deposition (CVD) is a method for obtaining thin films on a substrate by thermal decomposition of one or several precursors on the surface of the substrate. The overall CVD reaction follows several key steps [124].

1. Evaporation and transport of reagents (i.e. precursors) in the bulk gas flow region into the reactor.

2. Gas phase reaction of precursors in the reaction zone to produce reactive intermediates and gaseous by–products.

3. Mass transport of reactants to the substrate surface.

4. Adsorption of the reactants on the substrate surface.

5. Surface diffusion to growth sites, nucleation and surface chemical reactions leading to film formation.

6. Desorption and mass transport or remaining fragments of the decomposition away from the reaction zone.

CVD method is an attractive technique for obtaining Pd layers of controlled thickness [125]. It was first reported as a method for the formation of Pd composite membranes using $PdCl_2$ as the metal source by Ye et.al. [126]. To obtain thin and highly selective layers via

CVD method, it requires Pd precursors of high volatility and good thermal stability, which are necessary for short processing times and high yields [127]. Highly volatile organometallic Pd precursors such as $Pd(C_3H_5)_2$, $Pd(C_3H_5)(C_5H_5)$ and $Pd(C_5H_5)_2$ are available and are used for fabrication of Pd films by metal organic CVD (MOCVD). Two of the main drawbacks of the use of the CVD method in the preparation of Pd films are the high cost of the Pd precursors and the contamination by residual carbon from organometallic Pd precursors [128].

2.5.3.4 Electrolytic Plating

Electrolytic plating is a liquid–phase electrochemical method in which metal ions are transported by the action of an electric potential and deposited on a substrate, which also acts as an electrode. The substrate is a cathode and the positive metallic ions are reduced to metal and deposited on the substrate [129]. The use of electrolytic plating for powdered materials is limited due to the fact that the materials need to be compressed into electrodes, resulting in limited surface contact with the metal precursor solution, leading to only the external surfaces to be modified.

2.5.3.5 Electroless Plating

Electroless plating is an autocatalytic oxidation–reduction reaction in which ions are reduced and deposited as metal atoms [115]. It is similar to electroplating, but no external current is applied. Most PGMs can be plated onto surfaces using this technique. Electroless plating involves the reduction of a metallic salt complex on the surface of a support material and thus an activation step is needed to initiate the reaction because the platted metal on the surface acts as a catalyst for further reduction. The advantage of electroless plating method includes ease of coating on materials of any shape, low cost and the use of very simple

equipment. The main drawback of electroless plating is the time consuming nature of the method due to the requirement of a number of pre–treatment steps such as activation and sensitisation before final plating of metal can be carried out.

2.6 Conclusion of the Literature Review

This summary is based on the literature survey carried out in this chapter. It has to be noted that there are no ideal alloys that can store hydrogen. Ti–based AB and AB_2 intermetallic compounds offer the best options for near room–temperature absorption. The attractiveness of Ti–based AB and AB_2 compounds is due to the low raw material cost, good hydrogen storage capacity (1.7 – 2.0 wt.%), and reasonable sorption kinetics.

However, one of the main drawbacks of the use of Ti–based AB and AB_2 alloys is surface poisoning by impurities in hydrogen gas streams e.g. CO, H_2S, H_2O and O_2. The presence of these impurities leads to the formation of oxide layers on the surface of the alloys, which in turn lowers the rate of hydrogen absorption.

To improve the hydrogen sorption properties of Ti–based metal hydride–forming materials we have recommended approaches aimed at changing the bulk properties of the parent materials and modifying the surface characteristics of the parent materials.

The purpose of this research study is to prepare Ti–based alloys via different methods and compare their performances and then develop new preparation routes for Ti–based alloys as well as to improve the hydrogen sorption kinetics of Ti–based metal hydride–forming alloys. To change the bulk properties of Ti–based metal hydride materials we have chosen to introduce oxygen within the bulk material. This will assist in the hydrogen absorption kinetic due to the fact that Ti_4Fe_2O can absorb hydrogen which causes the parent alloy to become

brittle, which allows for easier diffusion of hydrogen in the parent alloy. To address the problem of surface poisoning, modification of the surface with Pd was investigated. Deposition of a Pd metal layer over Ti–based metallic hydrides was identified as an attractive method, due to the enhancement of hydrogenation performance, increased surface poisoning resistance and improvement of H_2 dissociation rate. Pd encapsulation was investigated as a suitable modification technology due to its high affinity towards the absorption of hydrogen and offers protection towards the surface of the metal hydride–forming alloy.

Chemical vapour deposition (CVD) and electroless plating were identified as the methods for surface–modification of Ti–based metal hydride–forming materials as it allows for the ability to control the surface chemistry of the modified system.

Chapter 3:   Methodology

In this chapter, the methodology and materials that were used to synthesise the Ti-based AB and AB$_2$ hydride forming–materials will be presented, as well as the preparation approach for surface–modification of Ti-based AB metal hydride. The functioning of various characterisation techniques employed for analysis of these materials is explained.

3.1   Materials

All materials used and suppliers are listed below:

Table 3.1: *List of materials and suppliers*

Materials	Supplier
Iron (99.98%)	Alfa Aesar
Titanium (99.98%)	Alfa Aesar
Natural Ilmenite	Saldanha Steel
Palladium Chloride (99%)	SA Precious Metals
Palladium (II) acetlyacetonate (34% Pd)	Fluka
Ammonium hydroxide (28%)	Sigma Aldrich
HCl (32%)	Kimix
Ammonium Chloride	Kimix
Sodium hypophosphite	Sigma Aldrich
Tin Chloride (98%)	Alfa Aesar
Sodium Ethyl diamine tetra acetate	Sigma Aldrich
Pd Standard Solution (1000 ppm)	B & M Scientific
Ar (99%)	Afrox (South Africa)
Ar/H2 mixture (75/25%)	Afrox (South Africa)
Ethylene (98%)	Afrox (South Africa)

3.2 Method of synthesis of metallic Ti-based hydride forming – materials

3.2.1 Arc–Melting

TiFe intermetallic alloy was prepared by arc–melting at the Institute for Energy Technology (IFE), Norway. High–purity metals (> 99.99%) taken in equiatomic amounts total mass ~ 10g were melted on a water cooled crucible in protective argon atmosphere.

The alloys TiFe + x wt. % O (x=0.1, 0.2, 0.5, 1) were prepared in the same manner; the necessary amount of oxygen was introduced in the form of TiO_2 (99.9%) and the amounts of Ti and Fe were corrected to provide the overall ratio Ti:Fe=1:1 in the final alloy.

All the prepared ingots were smelted three times to provide homogeneity.
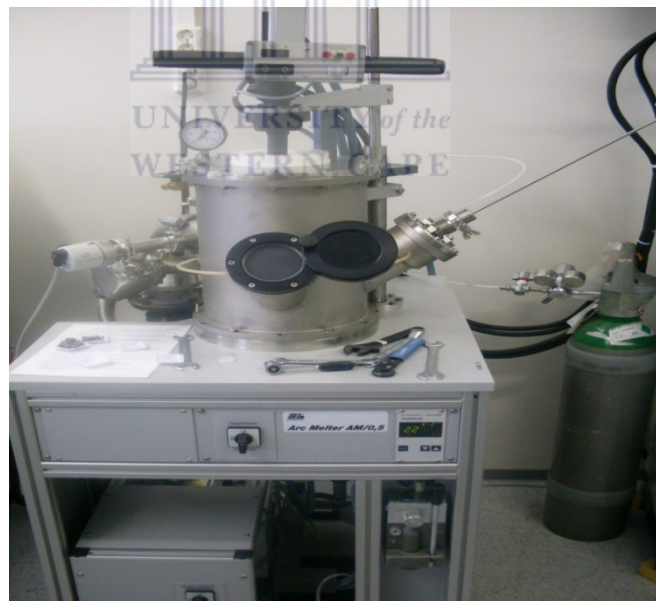
Figure 3.1: *Picture of arc-melter used at (IFE) Norway*

3.2.2 Induction–Melting

TiFe intermetallic alloy was prepared by induction melting at the South African Institute of Advance Material Chemistry (SAIAMC). High–purity metal powders (> 99.99%) were taken in equiatomic amounts with a total mass of ~ 40g. The material was placed in a graphite or alumo-silica crucible. The crucible was placed inside the induction furnace. The furnace was flushed with Ar three times to remove all oxygen from the furnace. The furnace chamber was then evacuated to 0.1 mbar and filled with argon at the pressure about 1.2 bar. The inductor was then switched on and set to 1500 ^{0}C once it obtained its temperature it was kept there for 2 minutes.

Figure 3.2: *Picture of induction furnace at SAIAMC*

3.2.3 Sintering

TiFe intermetallic alloy was prepared by sintering method. Ti (purity > 99.99%) and Fe powders (purity > 99.99%) with a particle size of 44 microns were mixed in 1.1: 0.9

atomic ratio, with a total mass of ~ 10g by grinding. The mixture of Ti and Fe powders was placed into a quartz sample holder. The sample holder was positioned in a quartz tube, which was placed in a tubular furnace (figure 3.3). The tubular furnace was flushed with Ar for 1 hour to displace oxygen. The furnace was then set to 1000 ^{0}C and the sample was kept at that temperature for 1 hour. Samples were cooled down to ambient temperature under Ar flow.
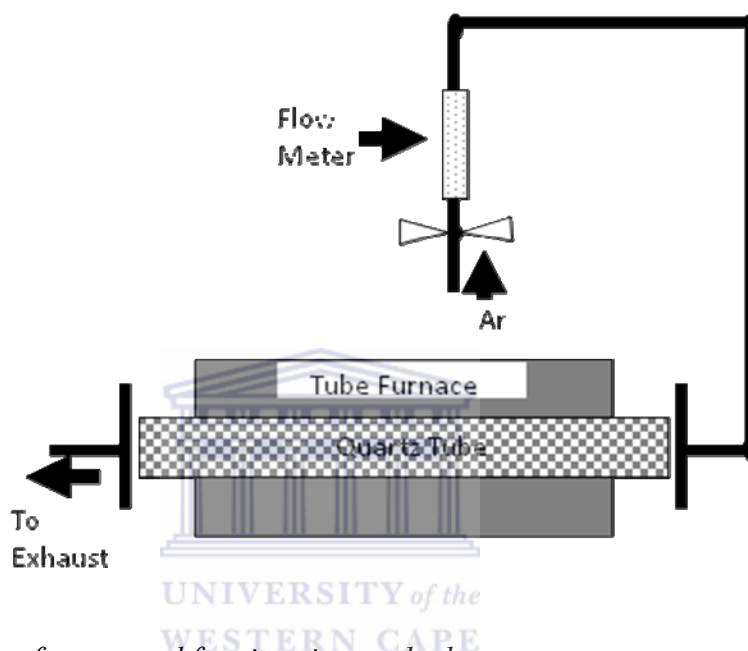
Figure 3.3: *Schematic of setup used for sintering method*

The excess of Ti (~22% as to the stoichiometric amount in the sintered material) was chosen to (i) avoid a formation of inactive in hydrogenation $TiFe_2$ and (ii) increase the Ti/Fe ratio to allow formation of $Ti_4Fe_2O_x$. From experiments (see Section 4, Figure 4.1 (B), Table 4.1) we have found that chosen content of Ti and sintering conditions yielded a mixture of two hydride-forming constituents, TiFe and $Ti_4Fe_2O_{1-x}$ formed in ratio of approximately 3:1.

3.2.4 Synthesis of TiFe from ilmenite

Natural ilmenite ore was obtained from Saldanha Steel, Western Cape, South Africa; the composition of the ilmenite was as follows: 50.78 wt% FeO, 44.48 wt% TiO_2 and 4.74 wt. % impurities, including B, Mn, Al, Mg, Na, Ni, Ca and V.

The synthesis of TiFe from the ilmenite was carried out in two ways. The first one included direct metal-thermic reduction, and the second, involved a two-step process developed within this study [98]. The reduction procedures were carried out using a setup similar to the one described in the previous subsection (Figure 3.3).

The metal thermic reduction was carried out using calcium or magnesium hydride as a reducing agent. The raw ilmenite was mixed with, CaH_2 or MgH_2, taken in 20% excess as to stoichiometric amount corresponding to the equation:
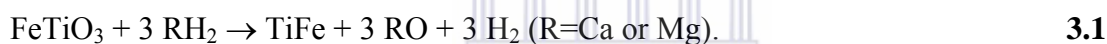
$$FeTiO_3 + 3\ RH_2 \rightarrow TiFe + 3\ RO + 3\ H_2\ (R=Ca\ or\ Mg).$$ **3.1**

The mixture (amount corresponds to 10 g of ilmenite) was ball milled in argon for 2 hours followed by heating in argon flow at 1000 $^{\circ}$C for 1 hour.

The reduction of natural ilmenite ($FeTiO_3$) to form TiFe alloys was also done by a two-step process. The first step was the gas-phase reduction to yield a mixture of metallic iron and titanium oxides, Fe + TiO_2. The second step was a metal-thermic reduction of the Fe + TiO_2 mixture with a reducing agent.

Step 1: Gas–phase reduction

10 g of the natural ilmenite was placed in a quartz sample holder and then the sample holder was placed into a quartz tube inside a tubular furnace. The furnace was first flushed with Ar for 1 hour to remove O_2 from the system. Once all the O_2 was removed, the gas flow

was changed from Ar to H_2 (25%) + N_2 (balance) mixture, at a flow rate of 2 L/min, and the furnace was switched on at the setpoint T~950 ^{o}C. During heating, at T~750 ^{o}C a mist of water vapour coming out the exhaust line appeared illustrating that the reaction had started. Once the furnace temperature reached 950 ^{o}C, it was kept for 2 hours under H_2 + N_2 mixture flow. The furnace was then cooled down to room temperature under Ar flow.

$$FeTiO_3 + H_2 \rightarrow Fe + TiO_2 + H_2 \qquad \textbf{3.2}$$

Step 2: Metal–thermic reduction

The product of the gas-phase reduction of ilmenite was further subjected to metal-thermic reduction treatment using CaH_2 as a reducing agent. CaH_2 was taken in 20% excess as to stoichiometric amount corresponding to the equation:

$$Fe + TiO_2 + 2\ CaH_2 \rightarrow TiFe + 2\ CaO + 2\ H_2 \qquad \textbf{3.3}$$
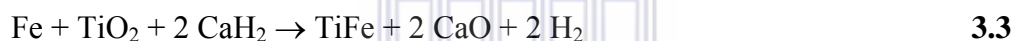
$CaCl_2$ was also added to the mixture (one mole $CaCl_2$ per two moles CaO) to dissolve the CaO formed during the metal-thermic process. After grinding in a mortar in argon atmosphere, the mixture was loaded in the furnace, and metal-thermic process was carried out. The sample was pre-heated to 300 ^{o}C in the Ar flow (2 L/min), followed by heating to 1000 ^{o}C and keeping this temperature for 2 hours followed by cooling down to room temperature in Ar flow.

3.3 Surface modification by deposition of Palladium onto metallic substrate

To improve the hydrogen sorption kinetics of TiFe alloy palladium was chosen as the desired catalyst due to its high affinity for hydrogen. Palladium was deposited on the surface of the TiFe alloy via two methods; these were electroless plating and chemical vapour deposition.

3.3.1 Electroless plating

Prior to deposition of palladium on the surface of TiFe alloy the surface required activation using "*one–step*" sensitisation / activation. 5.0 g TiFe alloy was sensitised / activated in 50 ml of a Pd-Sn colloidal solution for 20 minutes at room temperature. The Pd-Sn colloidal solution was prepared as follows:

Solution A: 0.3 g $PdCl_2$ was dissolved in 2.15 g HCl solution and 5.0 mL deionised water at 70 °C with stirring (300 rpm)

Solution B: 25 g $SnCl_2.2H_2O$ was dissolved in 145 g HCl solution (preheated to 50 °C). The mixture was cooled to room temperature after which 30 mL deionised H_2O was added.

Solution B was added to *solution A* and the mixture was heated to 90-100°C for 15-20 minutes.

Solution C: 8.75 g KCl was dissolved in 250 mL deionised H_2O. 80 mL HCl was then added to the KCl solution.

Solution C was then added to *Solution* (*A+B*) and made up to 500 mL with deionised water.

The activated powder was then immersed in a 10 wt% solution of Na_2EDTA for 10 min as to strip away the tin component, rinsed with deionised water and then allowed to dry at 80 ^oC overnight.

The deposition of Pd layer was carried out by immersion of the activated TiFe powders in 50 ml of the freshly-prepared electroless plating bath. The bath was prepared by first dissolving 2 g of $PdCl_2$ in 4.0 mL HCl (32 %) and 20 mL of deionised water, and then heated at 50 ^oC for 30 min with constant stirring at 300 rpm. After complete dissolvation of $PdCl_2$, 160 mL of NH_4OH (28 %) and 27 g of NH_4Cl were added respectively. The plating bath was then allowed to stir over night without heating. The mixture was then transferred to 1L volumetric flask and made up to the mark with deionised water. The electroless plating bath, containing the activated TiFe alloy, was subjected to constant agitation (300 rpm) for 30 minutes at 50°C. In addition, 50 mL of sodium hypophosphite (reducing agent) was rapidly added to initiate the reaction. The reducing agent was added separately to avoid decomposition during storage of the bath. Finally, the plated powders were washed with deionised water, filtered, and allowed to dry at 80°C.

3.3.2 Chemical vapour deposition

Chemical vapour deposition involves the dissociation and chemical reaction of gaseous reactants in an activated (heat, light or plasma) environment, followed by the formation of a stable solid product. The deposition involves homogeneous gas phase reactions, which occur in the gas phase, and heterogeneous chemical reactions which occur in the vicinity of a heated surface leading to the formation of powders or films.

Surface modification of the powdered TiFe alloy was achieved by MO CVD using palladium (II) acetlyacetonate Pd[acac]$_2$ (FLUKA, 34% Pd) as a precursor. The TiFe powder

was mixed with different amounts of Pd[acac]$_2$ corresponding to Pd loadings of 0.5, 1.0 and 5.0 wt%. The mixture (m~1g) was grinded in a mortar and placed inside a reactor where the CVD process was carried out at T = 400 ^{0}C for a period of 3 hours. The following modes of surface modification were applied:

- *Ex-situ* Pd deposition: The sample was placed in a quartz sample holder which was positioned in a quartz tube inside a tubular furnace. The tube was flushed at room temperature with carrier gas Ar, for 1 h to displace air. This was followed by heating to 400 ^{o}C, maintaining the high temperature for 3.0 h, and cooling down to room temperature under Ar flow (0.5 to 2 L/min). The composition of the output carrier gas was analysed using a QMS200 mass spectrometer (Stanford Research Systems, USA) equipped with O100SSC capillary for sampling the atmospheric pressure gas directly from the output pipeline. The analysis was carried out by continuous scanning in the range of mass numbers m/z=1–200 or 1–65 a.m.u., with the resolution of 10 points per a.m.u., using ionisation by electron impact (70 eV). Reference mass spectra were taken at the same conditions for individual gases (Ar, CO_2, N_2, CO, O_2, CH_4, H_2; Afrox Ltd., purity > 99.99%).

- *In-situ* Pd deposition: The mixture of TiFe and Pd[acac]$_2$ (Pd loadings 0.5 and 1 wt.%, total mass 0.5 g) was loaded in the reactor of Sievert-type volumetric setup, and heated to 400 ^{o}C under evacuation (vacuum better 10^{-3} mbar) for 3 hrs. After that the sample was cooled to room temperature under vacuum followed by a standard procedure of dynamic H absorption studies.

The materials prepared *ex-situ* was allowed exposure to air (no less than one day) prior to the experimental studies of their hydrogen absorption performances.

3.3.3 Preparation of composites on the basis of metallic hydride – forming materials and nanoscale carbon

5.0 g of TiFe was placed in a quartz sample holder which was placed inside a quartz tube inside a tubular furnace. The tube was evacuated for 15min to remove oxygen from the system. The furnace was then set to 500 ^{0}C under Ar flow. At 500 ^{0}C the Ar flow was terminated and the system was flushed with H_2 gas for 1 hour. This was done to remove any oxides from the surface of the TiFe. The H_2 gas was then stopped and the system was set to 800 ^{0}C under Ar flow. At 800 ^{0}C the Ar flow was terminated and ethylene was introduced into the system for 10 minutes. After ethylene introduction, the system was allowed to cool down to ambient temperature under Ar flow. The CVD setup is shown in figure 3.4 below.
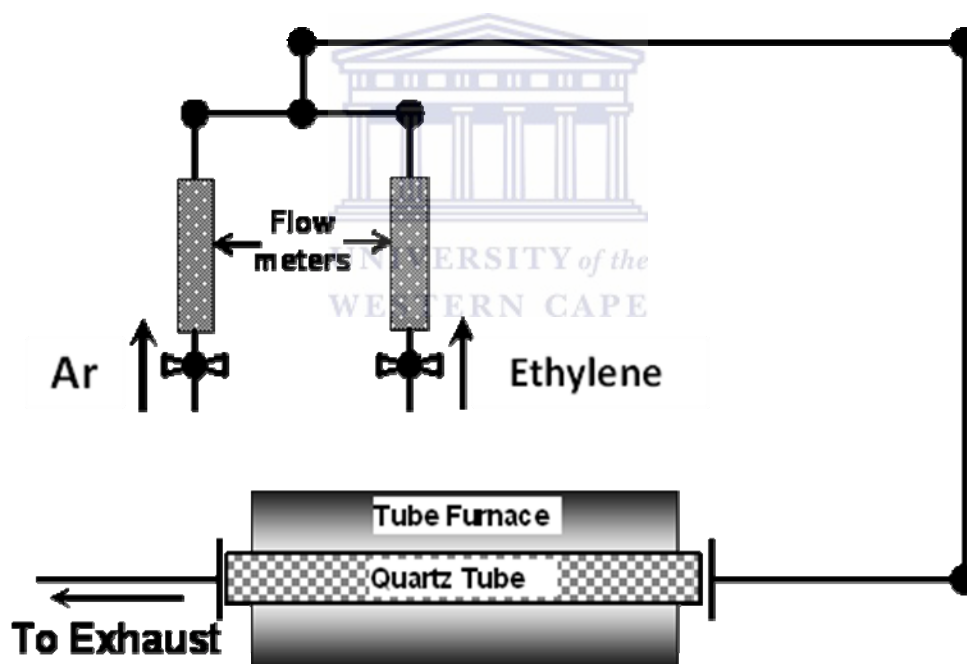
Figure 3.4: *Schematic view of the experimental setup used to deposit carbon nanotubes on the surface of TiFe alloy.*

3.4 Morphological, structural and composition characterisation of Ti – based hydride forming materials

Surface morphology, elemental composition and phase composition / crystal structure plays an important role in the hydrogen sorption performances of Ti–based metal hydride forming–materials. Therefore, alteration of these factors may influence the performance of the alloy during hydrogenation either positively or negatively. Thus, an array of characterisation methods was conducted to determine the effect of the above-mentioned factors on the properties of Ti–based metal hydride–forming materials.

3.4.1 X-Ray Diffractometry (XRD)

X-ray diffraction (XRD) is one of the most important non-destructive tools to analyse crystalline material, ranging from thin films and fluids to powder and crystals. XRD is an indispensable method for material characterisation. XRD is a powerful tool in the study of crystallinity and atomic structure of materials and forms an integral part of a comprehensive characterisation study of Ti–based hydride forming–materials.

In XRD, crystalline solids are exposed to a collimated x-ray beam which causes crystal plane atoms, serving as diffraction gratings, to diffract x-rays in numerous angles. Each set of crystal planes (hkl) with inter-plane spacing (d_{hkl}) can give rise to diffraction at only one angle. The diffraction angle is defined from Bragg's law ($n\lambda = 2d\sin\theta$), where the intensities of the diffracted x-ray are measured and plotted against corresponding Bragg angles (2θ) to produce a diffractogram.

The intensities of the diffraction peaks are proportional to the densities of the abundance of the corresponding crystal facets in the material lattice. Diffractograms are unique for different materials and can therefore qualitatively be used in material identification [130, 131].

In the XRD analysis, the Ti–based metal hydride alloys were placed in a glass sample holder and the surface was flattened to allow maximum x-ray exposure. Experimental parameters for the XRD analysis are given as follows:

X-ray Diffractometer: **Bruker multipurpose powder diffractometer (D8 Advance)**

Tube: Copper

Detector: Sodium Iodide

Monochromator: Graphite

Generator operation (mA):   40

Electron energy (keV):   40

X-ray source: Cu-K_α, λ_1=1.5406 Å, λ_2=1.5444 Å, λ_2/λ_1=0.5

Scan range (2θ, º):   10 – 90

Scan rate (^{0}/min):   0.05

The XRD patterns were processed using Powder Cell software (version 2.4), for the simulation / refinement of powder patterns of starting (unmodified) and surface modified Ti–based metal hydride forming–materials on the basis of crystal structure data of the constituent phases (Rietveld analysis). Precise Rietveld analysis was performed using GSAS software.

3.4.2 Scanning Electron Microscopy (SEM)

Scanning electron microscopy (SEM) is a versatile imaging technique capable of producing three-dimensional images of material surfaces. SEM is one of the most frequently used instruments in material research today because of the combination of high magnification, large depth of focus, greater resolution and ease of sample observation.

In this study, high–resolution scanning electron microscopy (HRSEM) was used in the study of Ti–based AB and AB_2 hydride forming–materials, their particle size and shape. HRSEM was also used to determine the Pd particle dispersion on the surface of the modified alloys as well as the size and shape.

The basic operation in SEM entails electrons generated from a cathode filament to be accelerated towards an anode which contains sample material. The electrons generated by the cathode filament are focused through one or two magnetic, condenser lenses to generate a highly focused electron beam with a very fine focal spot of 0.4 – 5 nm. Using pairs of deflector plates or scanning coils that form part of the microscope's objective lens, this beam is deflected horizontally or vertically across the sample so that it scans a rectangular area of the sample surface in a raster-like manner. The interaction of the highly accelerated electron beam with atoms in the surface of the sample material results in the emission and scattering of electrons which are picked up by a detector. Corresponding electric signals are generated in the detector, modulated and later amplified to produce a 3-dimensional reconstruction of the sample's surface which is captured and stored using an appropriate imaging technique [132].

A prerequisite for effective viewing is that the surface of the samples should be electrically conductive. During operation, electrons are deposited onto the sample. These

electrons must be conducted away to earth thus conductive materials such as metals and carbon can be placed directly into the SEM whereas non-metallic samples have to be coated with a gold or carbon layer to be observed.

The samples of interest were supported on double-sided conductive carbon tape and mounted on an aluminium sample stub. No sputter-coating was required as all the samples were electron-conductive. Two different microscopes were used in the evaluation of the morphology of the Ti–based modified and unmodified metal hydride forming materials. Their description and experimental parameters are given below:

HRSEM - Zeiss Supra 55VP; working distance = 3-11 mm; accelerating voltage = 5-10 kV (Norwegian University of Science and Technology, Trondheim, Norway). The in-lens and secondary electron detectors (SE) of the microscope was used to study the particle size, particle shape, particle size distribution; of the Ti–based modified and unmodified materials.

SEM - Hitachi x-650 microscope; working distance = 15 mm; accelerating voltage = 25 kV; emission current = 75-80 µA at the Department of Physics at the University of the Western Cape. In parallel with the SEM studies, the EDS component analysis of the samples was carried out, by analysing the energy spectra of the secondary X-rays. Both total (averaged along the whole surface) and local (in specified points) analyses were performed.

3.4.3 Elemental analysis of surface-modified TiFe metal hydride materials on the basis of energy-dispersive x-ray spectroscopy (EDS) and atomic absorption spectroscopy (AAS)
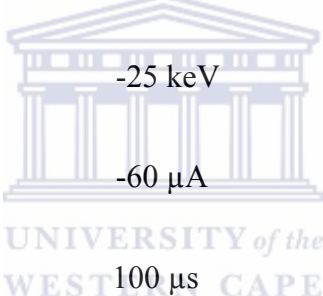
In this study, it was important to determine the density of metal deposited on the surface of the TiFe alloy, as well as the total quantity of the deposited Pd metal. To determine these properties, energy–dispersive x–ray spectroscopy (EDS) and atomic absorption spectroscopy (AAS) were employed.

EDS is a relatively simple yet powerful technique used to identify the elemental composition of as little as a cubic micron of material. The equipment is attached to the SEM to allow for elemental information to be gathered about the specimen under investigation. The technique is non-destructive and has a sensitivity of >0.1% for elements heavier than C. The technique is extremely versatile in that it can be used in the qualitative determination of unknown sample materials, the quantitative analysis of known elemental components, as well as in mapping the elemental distribution on the surface of the sample material.

The basis of the technique is the interaction of the incident electron beam with atoms in the surface of the sample results in the excitation of an electron within the inner shells of atoms in the ground state. If the energy is sufficient, the electrons are ejected from the atom leaving behind electron holes. The filling of these electron holes by electrons in higher-energy outer shells results in the release of excess energy in the form of X-rays. The X-rays produced are characteristic of each element within the sample (since their energy distribution depends on the configuration of the electron shell, which is a unique feature of every element). The X-rays can be detected, modulated and amplified to generate plots with spectral lines characteristic of each element within the sample. The atomic percentage (at %) and weight percentage (wt %) of elements can thus be obtained [133].

Samples were dispersed on double-sided conductive carbon tape, which in turn was adhered to aluminium sample stubs. Analysis of the surface metal loading and elemental composition of the AB and AB_2 type hydride forming materials were done by using an EDAX Genesis coupled with Hitachi X-650 SEM electron microscope. The experimental parameters used are given as follows:

Parameters	**Settings**
Baseline:	1500 counts per second
Time:	100 live seconds
Working distance:	15 mm
Accelerating voltage:	-25 keV
Emission current:	-60 µA
Amperage time:	100 µs

Atomic absorption spectroscopy (AAS) is a spectro-analytical procedure for the qualitative and quantitative determination of chemical elements employing the absorption of optical radiation (light) by free atoms in the gaseous state [134].

The main principle of this technique makes use of absorption spectrometry to measure the concentration of an analyte in a sample. It requires standards with known analyte content to establish the relationship between the measured absorbance and the analyte concentration and relies therefore on Beer-Lambert Law (i.e. $A = \varepsilon \ell C$). The law states a logarithmic dependence of the elemental concentration (C) to the absorbance of the sample (A), the path length that the characteristic light travels through the sample (ℓ), and the absorption

112

coefficient or molar absorptivity (ε) of the sample [135]. In order to analyse a sample for its atomic constituents, it has to be atomised. The atomisers most commonly used today are flames and electrothermal (graphite tube) atomisers. A beam of light from the hollow cathode lamp is passed through the neutral atoms formed by the flame atomiser. The light produced by the hollow-cathode (HCL) lamp is emitted from excited atoms of the same element which is to be determined. Therefore, the radiant energy corresponds directly to the wavelength which is absorbable by the atomised sample. This method provides both sensitivity and selectivity since other elements in the sample will not generally absorb the chosen wavelength and thus, will not interfere with the measurement. Before the analyte is aspirated, a measured signal is generated by the photo multiplier tube (PMT) as light from the HCL lamp passes through the flame. When analyte atoms are present in the flame, while the sample is aspirated, some of that light is absorbed by those atoms leading to a decrease in PMT signal which is proportional to the amount of analyte. By careful construction of the calibration curve using standard solutions, the absorbance of the sample can be related to the concentration of the metal of interest in the sample solution. In this study, AAS was employed for determination of Pd metal deposited on TiFe metal surface. A minimum of 5 standards were prepared in the range depending on the sensitivity of the instrument towards the analyte. A blank solution (i.e. aqua regia and ultrapure water) was measured directly after the calibration standards to rule out contributions from the solvent and in that way ensure the stability of the analytical baseline. 1.0 g of surface-modified materials was dissolved in 50 mL aqua regia solution (1 part HNO_3 per 3 parts HCl) while heating at 50°C for 30 minutes with constant stirring at 300 rpm. The solutions were allowed to cool to room temperature, then filtered and made up to the mark in 100 mL volumetric flask with ultrapure water. The experimental parameters using spectrometer (Philips PU9100) are given as follows:

Parameters	Settings
Wavelength (nm):	247.6
Air-C_2H_2 flow rate (L/min):	0.9-1.2
Lamp current (mA):	15
Band pass (nm):	0.2

3.5 Volumetric characterisation of hydrogen sorption performances

There are basically two means of expressing the amount of hydrogen stored in metal hydride forming materials. It can either be expressed as a volumetric density (volume of hydrogen) or as a gravimetric density (the mass of hydrogen). The gravimetric method measures the variation of mass during the absorption and desorption of hydrogen in the sample. The main drawback of this technique is that it is sensitive to all gases absorbed or desorbed since it is only based on weighting. Floatability is another concern for this method, due to the fact that the apparent weight of the sample in a gas is lower than the real mass of the sample due to forces exerted by the gas on the sample. The mass of the gas displaced pushing against the sample can make the sample "float" in the gas, especially for powdered samples.

In this study, the volumetric method was used to evaluate the hydrogen sorption performances of Ti–based AB and AB_2 hydride forming–materials. The basic operating principle of this method is based on introducing a known amount of gas into a known volume containing an absorbing sample and measuring the pressure. By assuming an equation of

state, usually the ideal gas law with the correction taking into account the gas compressibility, the amount of absorbed gas can be calculated. In order to measure accurately the amount of absorbed gas, it is of prime importance to measure the temperature, volume and pressure of both the reference and the sample chambers with high accuracy. Volumetric measurements using Sievert type apparatus were conducted for the evolution of kinetic behaviour and Pressure–Composite–Temperature (PCT) diagrams of Ti–based AB and AB_2 hydride forming–materials.

3.5.1 Kinetic studies of Ti–based AB and AB_2 hydride forming–materials

The kinetic properties of Ti–based metal hydride materials are affected by both the bulk and surface properties of the material. A study of the sorption kinetics of the modified materials would give valuable information into the surface reactivity, reaction mechanism, poisoning resistance, and catalytic activity towards hydrogen on the surface-modified materials [136].

The construction of kinetic curves was conducted using a Sieverts-type volumetric installation (South African Institute for Advanced Material Chemistry, SAIAMC). The installation conducted accurate volumetric measurements of quantities of hydrogen absorbed or desorbed by hydrogen sorption materials. The procedure consists of determining the quantity of hydrogen absorbed or desorbed by the material at a certain pressure at a fixed temperature, and after thermal activation in vacuum. The installation consists of gas distribution, control, and measurement systems. The pressure within the system was monitored using 2.5, 16, and 160 bar absolute pressure transducers. The accuracy in the determination of the H sorption capacity was estimated as ~ 1.1 cm^3.bar at STP (or ~ 0.04

H/AB formula units). A schematic diagram of the installation at SAIAMC is given below in

Figure 3.5.
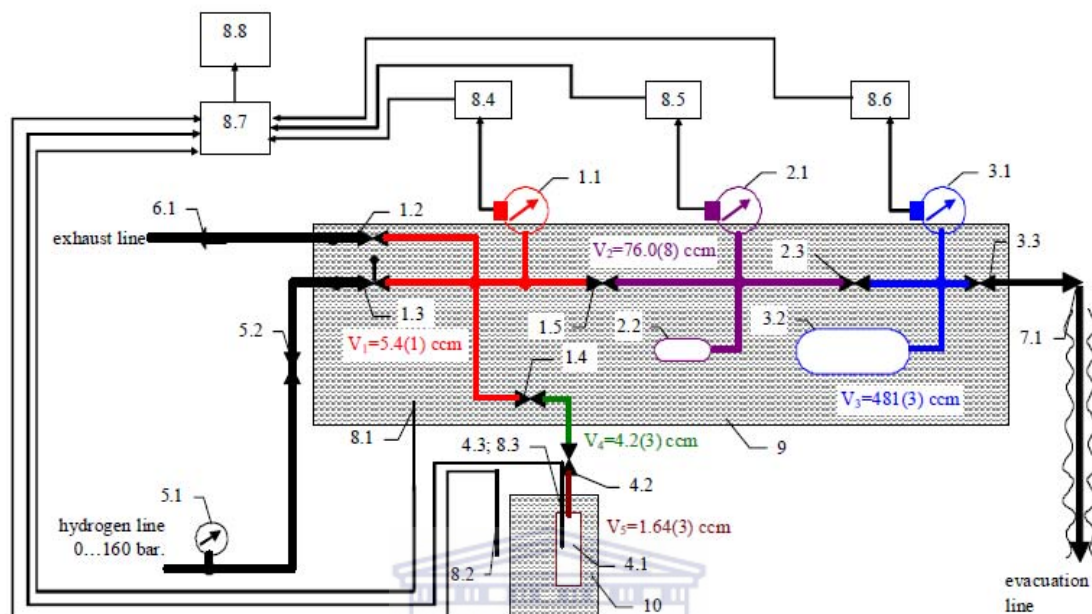
1. High-pressure collector:
    1.1. Pressure sensor 160 bar FS
    1.2. Exhaust valve
    1.3. H_2 input valve
    1.4. Reactor valve
    1.5. Medium-pressure connection valve
2. Medium-pressure collector:
    2.1. Pressure sensor 16 bar FS
    2.2. Buffer cylinder 75 cm^3
    2.3. Low-pressure connection valve
3. Low-pressure collector:
    3.1. Pressure sensor 2.5 bar FS
    3.2. Buffer cylinder 500 cm^3
    3.3. Evacuation valve
4. Reactor assembly
    4.1. Reactor body
    4.2. Gas connection line with locking valve
    4.3. Thermocouple

5. H_2 supply line:
    5.1. Manometer 160 bar FS
    5.2. H_2 supply valve
6. Exhaust line:
    6.1. Check valve
7. Evacuation line
    7.1. Vacuum valve
8. Data acquisition system
    8.1. Thermistor measuring bath temperature
    8.2. Thermistor measuring room temperature
    8.3. Thermocouple measuring sample temperature
    8.4. 160 bar pressure indicator / transmitter
    8.5. 16 bar pressure indicator / transmitter
    8.6. 2.5 bar pressure indicator / transmitter
    8.7. 34970A data acquisition / switch unit
    8.8. PC
9. Bath (filled with ethylene glycol)
10. Thermostat / furnace

Figure 3.5: *Schematic diagram of Sievert apparatus installation at SAIAMC*

The sample (mass 0.5g) was loaded into a 316L stainless steel reactor followed by evacuation to lower than 10^{-3} mbar at room temperature. The starting hydrogen pressure of ~70.0 bar aliquot was then introduced into the appropriate buffer cylinder, and a pressure baseline established, after which the reactor valve was opened and the hydrogen introduced to the sample material. Changes to the reference hydrogen pressure were monitored by the data acquisition system. Scan intervals of 30 seconds were used. The volumetric system and reactor were maintained at 20°C using a thermostated oil bath and the analysis was allowed to commence for ~24 hours.

H_2 absorption capacity was determined by calculating total amount of gaseous H_2 in the internal volumes of the gas-distributing system and reactor, starting from the monitored H_2 pressures, P_i, therein; as well as the temperatures, T_i, of these volumes using the following equation:

$$n = \sum \frac{P_i V_i}{Z(P_i.T_i)RT_i}$$

3.4

Where n is the total number of moles of H_2 in the volumes V_i taken into account (maintained at the corresponding temperatures, T_i), $R=8.3143$ J/ (mole·K) is the gas constant, and Z is the compression factor of hydrogen gas at the specified pressure P_i and temperature T_i. Calculating starting (n_0) and actual (n_1) amounts of hydrogen gas in the system, the hydrogen absorption capacity (x) of the material will be expressed as:

$$x \left[\frac{cm^3}{g} STP \right] = \frac{22400(n_0 - n_1)}{m}$$

3.5

Where m is sample weight; 22400 cm^3/mole is the molar volume of hydrogen at normal conditions (T= 0 °C, P=1 bar).

The starting (n_0) and actual (n_1) number of moles of H$_2$ in the system were calculated as:

$$n_0 = \frac{P_0 V_j}{Z(P_0 \cdot T_0)RT_0} \qquad \textbf{3.6}$$

$$n_1 = P\left(\frac{V_S}{Z(P \cdot T_S)RT_S} + \frac{V_C}{Z(P \cdot T_R)RT_R} + \frac{V_j}{Z(P \cdot T_0)RT_0}\right) \qquad \textbf{3.7}$$

Where P_0 is equal to the pressure in the system before opening reactor valve; P is the actual hydrogen pressure; V_j and V_C are the volumes of thermostated (at T_0) measurement system and connecting pipeline (at room temperature, T_R), respectively; V_S is the internal volume of reactor with the sample kept at temperature T_S. The amount of hydrogen desorbed by the material was calculated in a similar manner as hydrogen absorption capacity.

3.5.2 Construction of pressure-composition isotherms of Ti–based AB and AB$_2$ hydride forming materials

3.5.2.1 Experimental procedure

The performance of Ti–based AB and AB$_2$ hydride forming-materials is best represented by pressure–composition–temperature diagrams (PCT). The PCT diagram provides a clear understanding of the hydrogenation / dehydrogenation properties and phase transformations occurring in the hydrogen sorption material, hydride stability, and equilibrium relationships between the H$_2$ pressure and concentration at a constant

temperature. The isotherms are very sensitive to deviations in composition and homogeneity of MH materials and were therefore an excellent characteristic in assessing the quality of fabricated materials. The PCT relationship describes the dependence of the H_2 equilibrium pressure on the quantity of H_2 absorbed in the metal hydride-forming alloy and temperature [137].

The PCT studies were conducted using automated Sievert apparatus (PCT Pro-2000, Hy-Energy Scientific Instruments) (Figure 3.6).

Approximately, 2 g of sample was loaded into the reactor vessel and activated by heating to 400 °C in a furnace under vacuum for one hour. The activated sample was then subjected to several activation cycles which included charge with hydrogen (P=100 bar at room temperature) followed by vacuum heating at the conditions specified above. The measurements of the PCT characteristics of the starting material were initiated from the third cycle followed by subsequent measurements of absorption and desorption isotherms through the specified temperatures using standard volumetric procedures. The PCT experiments were carried out in temperature range 25 to 80 $^{\mathrm{o}}$C, and at hydrogen pressures from $5 \cdot 10^{-3}$ to 170 bar. The raw PCT data were pre-processed using macros HyDataAnalysis Version 2.2.3, © Hy-Energy 2007 supplied as auxiliary software together with the instrument, in the environment IgorPro Version 6.0.3.1, © WaveMetrics Inc. The pre-processing, in particular, introduced correction into the calculation of amount of absorbed / desorbed hydrogen taking into account displacement volume of the valve V-1 (Figure 3.6).
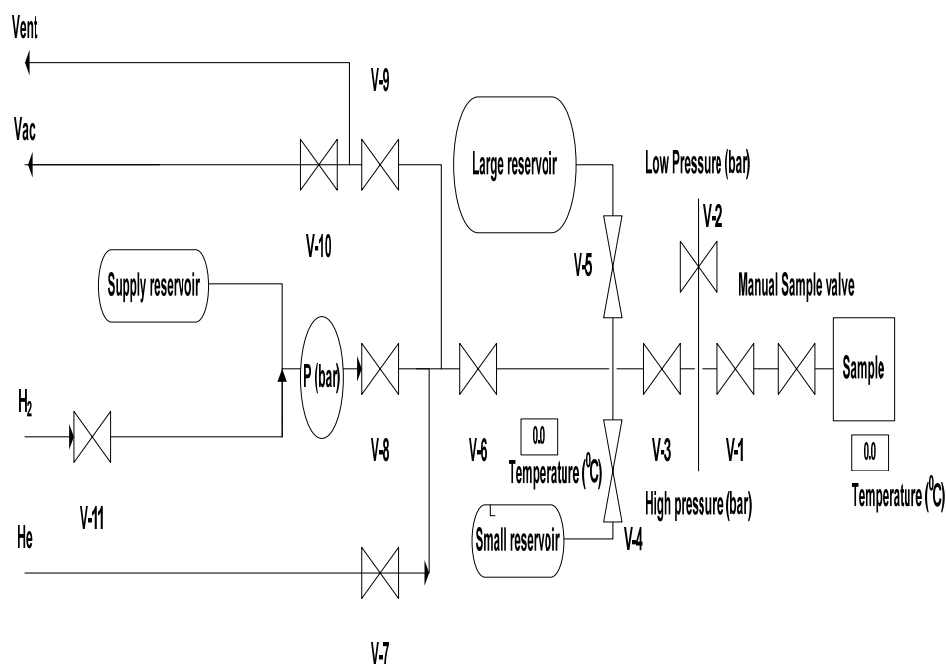
Figure 3.6: *Schematic diagram of experimental PCT Pro - 2000 setup at SAIAMC*

Some PCT studies were carried out using high pressure PCT setup at IFE / Norway (Figure 3.7). The setup provides precise volumetric measurements at the pressure up to 200 bar using a high-pressure differential pressure sensor (a, b) in addition to the absolute low-pressure one (c). Very clean atmosphere is provided by the usage of a turbomolecular pump (T.M.P.) for the evacuation of reactor and system, in addition to the supply of pure high-pressure hydrogen supplied from a metal hydride hydrogen storage and compression unit on the basis of AB_5-type intermetallic alloy.
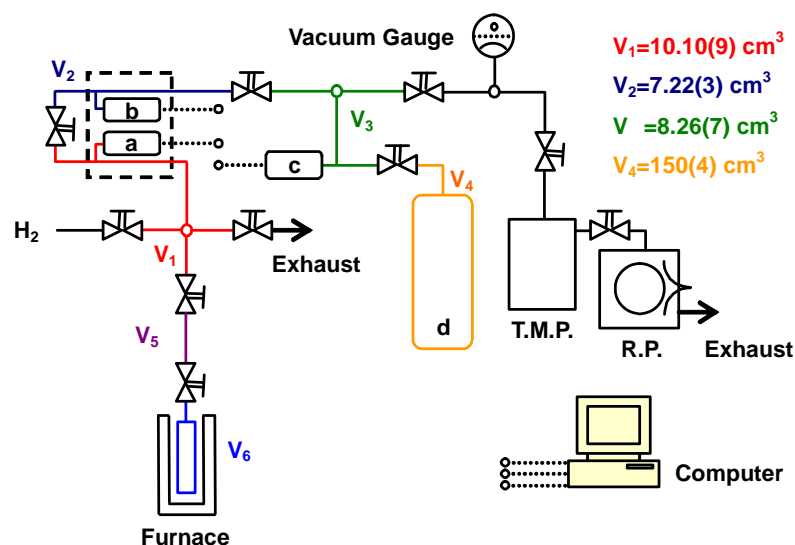
Figure 3.7: *Schematics of high pressure PCT setup at IFE (Norway)*

3.5.2.2 Modelling procedure

The task of modelling of a PCT diagram (or, in particular, a family of pressure–composition isotherms) is in the development of a model describing the relations between pressure of hydrogen gas (P), temperature (T) and hydrogen concentration in metal hydride (C) experimentally observed for the equilibrium of the reaction (2.4). It is important for both the systemic evaluation of the available experimental data and the optimisation of specific applications of metal hydrides.

In the majority of application-oriented studies the formal-empirical approach for the modelling of PCT diagrams, where the experimental PCT data are fitted by arbitrarily selected equations, is used [138]. This approach is rather convenient for engineering solutions, but it is unsatisfactory from the phenomenological point of view, and it can not be applied for the extrapolation of PCT relations outside the limits of the available experimental data.

Another approach is the application of thermodynamic and statistic regularities to hydrogen systems with hydride-forming materials resulting in building up the PCT models based on the description of the equilibrium between molecular hydrogen in a gas phase and hydrogen atoms in interstitials of a metal matrix. These models consider hydrogen in a metal as a lattice gas, and concentration dependence of its partial molar entropy, $\bar{S}(\theta)$, is described by a configuration:

$$\bar{S}(\theta) = \bar{S}_0 - R \ln\left(\frac{\theta}{1-\theta}\right);$$

3.8

where $\theta = C/C_{\max}$ is a fraction of filling of the metal matrix with hydrogen (C and $C_{\max}$ are the actual and maximum hydrogen concentrations, respectively), $\bar{S}_0$ is the entropy of the infinitely diluted solution, R is a gas constant.

In so doing, concentration dependence of the partial molar enthalpy of the lattice gas, $\bar{H}(\theta)$, is determined by the H – H interaction energy [139,140]:

$$\bar{H}(\theta) = \bar{H}_0 + E_{HH}(\theta);$$

3.9

where $\bar{H}_0$ is the enthalpy of the infinitely diluted solution; $E_{HH}(\theta)$ is the energy of H–H interaction corresponding to the excessive chemical potential of hydrogen atoms in a metal matrix, as compared to an ideal lattice gas.

Substituting of (3.8) and (3.9) into equation for the chemical potential of hydrogen atoms in the energetically-equivalent interstitials of the metal matrix, and further equating with the chemical potential of hydrogen in a gas phase yields:

$$x(\theta) \equiv \ln P - \ln P_0 = 2\ln\left(\frac{\theta}{1-\theta}\right) + \frac{E_{HH}(\theta)}{RT},$$

3.10

where P_0 is a plateau pressure calculated by Van't Hoff equation (2.7).

Equation (3.10) above is a general configuration of the PCT diagram whose specific form depends on the kind of the concentration dependence $E_{HH}(\theta)$. In the simplest case (an ideal solid solution), $E_{HH}(\theta) \equiv 0$, and the equation (3.10) looks like adsorption Langmuir's equation. In this case, the shape of pressure–composition isotherm in the $\ln P - \theta$ coordinates does not depend on temperature, and its shift along the $\ln P$ axis, when the temperature is changed, is calculated by eqn. (2.7).

Lacher-type models [141] are the most frequently applied to describe the PCT diagrams. They assume an attractive H–H interaction whose energy is proportional to hydrogen concentration:

$$E_{HH}(\theta) = -h \cdot \theta; \quad h > 0 \; ; \qquad\qquad \textbf{3.11}$$

that finally yields the following equation of hydrogen sorption isotherm:

$$\ln P = \ln P_0 + 2\ln\left(\frac{\theta}{1-\theta}\right) - 8\frac{T_c}{T}\theta \quad . \qquad\qquad \textbf{3.12}$$

Here $T_C = \dfrac{h}{4R}$ is a critical temperature, P is an equilibrium hydrogen pressure, and P_0 is the concentration independent contribution into its value determined from the Van't Hoff equation (2.7).

At temperatures below T_C model isotherms acquire form of a loop-like curve. Such behaviour is interpreted as a phase transition at constant pressure, where θ undergoes discontinuous increase from θ_α to θ_β and plateau appears (Figure 2.4).

Kierstead [142] extended the Lacher model to the consideration of the multi-plateau isotherms. The model isotherm is obtained by a superposition of several, depending on the experimentally observed number of plateaux, single-segment isotherms:

$$C = C_{\max} \sum_{i=1}^{m} g_i \theta_i (P, P_0).$$ **3.13**

Here m is a number of plateaux, g_i is the fraction of the i-th plateau segment. θ_i is calculated for each plateau segment from the equations 3.12 and 2.7.

Lacher-type models describe a simplified, ideal rather than real behaviour of the metal–hydrogen systems. The improvement accounting for the repulsive H–H interaction at $\theta \rightarrow 1$ (Van der Waals lattice gas) was made by Lototsky et. al. [143] who derived the following sorption equation:

$$\ln P = \ln P_0 + 2\ln\left(\frac{\theta}{1-\theta}\right) - \frac{27}{2}\frac{T_c}{T}\theta + 2\frac{\theta}{1-\theta}$$ **3.14**

where $T_c=4h/27R$.

As distinct from the Lacher model (3.12) taking no into account the H–H repulsion, the model of Van der Waals lattice gas (3.14) results in the isotherm shrunk along the θ axis and, by such a way, having asymmetry which is a characteristic feature of the isotherms of real systems "hydrogen–hydride forming material". At $T<T_C$ the Van der Waals lattice gas isotherms, as well as the Lacher ones, have loop-like shape, i.e. exhibit plateau behaviour.
It has to be noted that in the model of the Van der Waals lattice gas, the value of θ_0 corresponding to the plateau midpoint depends on the temperature covering a range from 1/3 ($T = T_C$) to 1/2 (T = 0) whereas in the Lacher model, independently on the temperature, $\theta_0=1/2$. Besides, the relationship between the values of ΔS and ΔH in the eqn. (2.7) and apparent standard entropy and enthalpy, ΔS_a and ΔH_a, calculated from Van't Hoff dependencies of logarithm of plateau pressure (at hydrogen concentration corresponding to θ_0) versus reciprocal temperature are expressed as:

$$\Delta H_a = \Delta H - \frac{27}{2} RT_C \theta_0$$

$$\Delta S_a = \Delta S - 2R \left(\ln \frac{\theta_0}{1-\theta_0} + \frac{\theta_0}{1-\theta_0} \right).$$

3.15

In Lototsky model [143], the isotherms having several plateau segments are also described by the application of the Kierstead approach [142], according to the equation (3.13). Moreover, a similar approach is applied to describe sloping plateaux that is a common feature of sorption isotherms in majority of hydrogen–metal systems. The hydride-forming material is imagined as a mixture of an infinitely big number of the uniform components. Then the equation (3.13) is modified to introduce a convolution of the $\theta(P,P_0)$ function on the argument's partition density. Assuming $X = \ln P - \ln P_0$ as the fluctuating parameter, and Gaussian distribution of ΔS and ΔH in the eqn. (2.7), the isotherm equation is written as:

$$\theta = \frac{C}{C_{max}} = \frac{1}{\sigma\sqrt{2\pi}} \int_{-\infty}^{+\infty} \theta(X) \exp\left[-\frac{(X-u)^2}{2\sigma^2} \right] du ;$$

3.16

where $\theta(X)$ should be calculated from the phase equilibria model (3.14), and σ is a standard deviation of X (or $\ln P_0$) to be calculated as:

$$\sigma^2 = \frac{\sigma_S^2}{R^2} + \frac{\sigma_H^2}{R^2 T^2} - \frac{2\rho_{SH}\sigma_S\sigma_H}{R^2 T} ;$$

3.17

where ρ_{SH} is a Pearson correlation coefficient between ΔS and ΔH.

The experimental PCT data (desorption) taken for arc melted TiFe and sintered $Ti_{1.1}Fe_{0.9}O_x$ as well as absorption and desorption data for AB_2-type alloy (A=Ti, Zr; B= Fe, Cr, Mn, Ni, Cu) were processed by the software HyPCT Version 4.01, © M.Lototsky 2010, for the modelling of phase equilibria in metal–hydrogen systems according to the procedure

described above. The data was fitted using the PCT model (Lototsky *et. al*, 2003 [143]) assuming hydrogen in the solid as a Van der Waals lattice gas together with Gaussian distribution of thermodynamic parameters describing plateau segments. For TiFe and $Ti_{1.1}Fe_{0.9}O_x$, the best fit was achieved when assuming three plateau segments on the PCT diagrams, while for PCT behaviour of the AB_2-type alloy the best fit was obtained assuming two plateau segments of which the first low-pressure one was imaginary, associated with H trapping in the material; similar to first low-pressure segment for TiFe (section 4.1.4).

It is noteworthy that all the PCT models described above assume hydrogen pressure, P, as an independent variable, and hydrogen concentration, C, (or filling fraction, θ) as a dependent one. However, in conventional notation of representing pressure–composition isotherms of hydrogen storage materials, the abscissa (X-axis) represents the concentration, and the ordinate (Y-axis) – hydrogen pressure. So, all the isotherms presented in this work are plotted assuming X-axis as hydrogen concentration and Y-axis as hydrogen pressure.

3.6   Conclusion of Methodology

Ti–based AB and AB_2 hydride forming materials were prepared by various techniques; these include arc-melting, induction melting, sintering and reduction of ilmenite. Methodologies for surface modification of TiFe with Pd via electroless and MO CVD deposition have been comprehensively described. Fundamental characterisation techniques were used in this study to investigate the structure and morphological properties of AB and AB_2 hydride forming materials as well as the modified TiFe alloys. The techniques used in their determination can be summarised as follows:

- Crystal structure and phase composition of unmodified and modified alloys could qualitatively be studied using XRD.

- Surface morphology of prepared AB and AB_2 hydride forming materials and Pd distribution on modified TiFe alloy could qualitatively be studied by SEM.

- Composition of prepared AB and AB_2 hydride forming materials could qualitatively be studied by EDS.

- Total Pd loading on modified TiFe alloy could quantitatively be studied using AAS.

- Hydrogen volumetric capacity and sorption kinetics of AB and AB_2 hydride forming materials could be quantitatively studied using Sievert's type apparatus.

- PCT properties of prepared AB and AB_2 hydride forming materials could be quantitatively studied using Sievert apparatus followed by fitting the data by the usage of PCT modelling procedure.
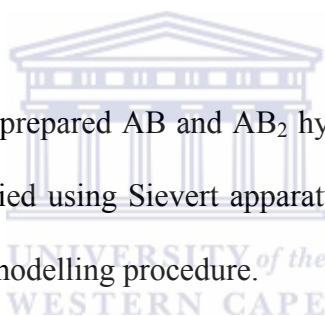
Chapter 4: Results and Discussion

4.1 Comparison of TiFe–based materials synthesised by different methods

4.1.1 Phase and Structural Features of Arc–melt and Sintered TiFe–based materials

The phase analysis of TiFe–based alloy materials was carried out using x–ray diffractometry (XRD). The summary of the obtained data on the phase–structural composition of the samples is presented in table 1 and is given together with relevant reference information on the constituent phases [144-150].

The XRD diffractograms of arc–melted and sintered TiFe–based materials are shown below in figure 4.1 (A) and (B). The XRD patterns illustrate that both arc–melted and sintered TiFe materials contained the bcc–TiFe, space group $Pm\ \bar{3}m$, as a major phase; the lattice period a = 2.9803 Å and a = 2.9780 Å for arc–melted and sintered samples respectively were close to the reference data a = 2.976 Å [151]. In addition, the sintered material contained two extra phases including a suboxide η - $Ti_4Fe_2O_{1-x}$ and a solid solution of iron in β – Ti.

128
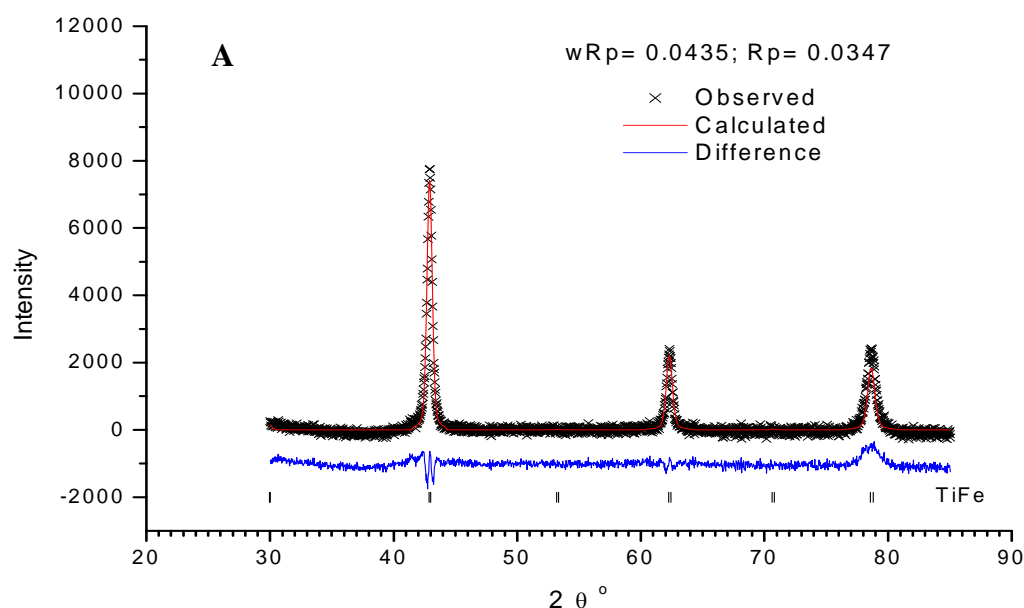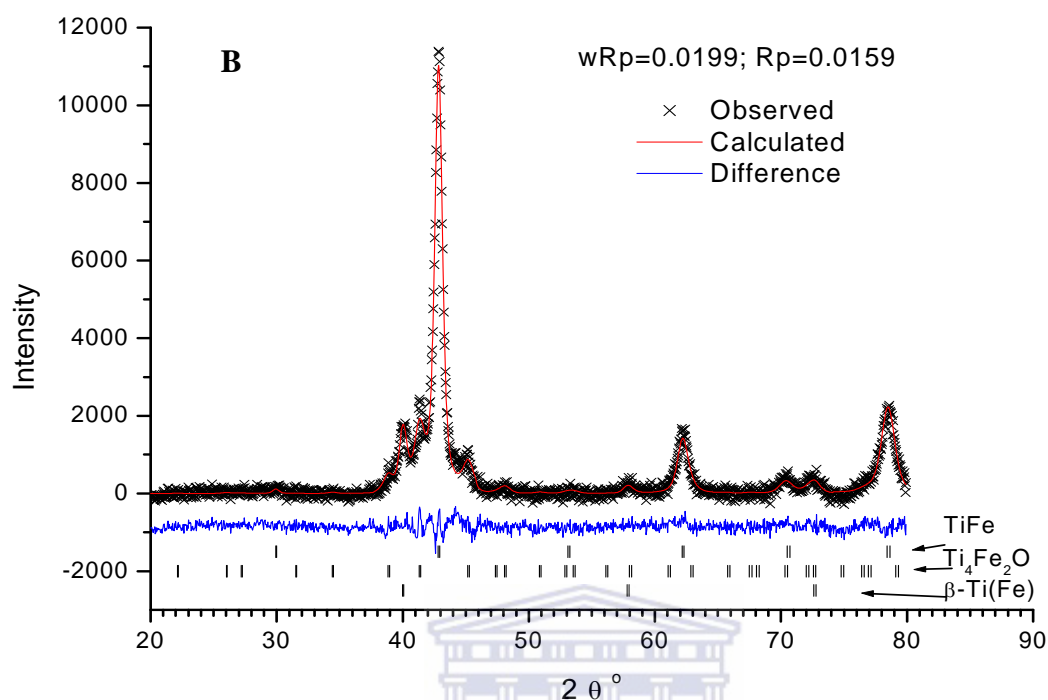
Figure 4.1: *XRD patterns of TiFe substrates: (A) arc – melted TiFe, (B) sintered TiFe*

The XRD diffractograms of the hydrogenated arc–melted and sintered TiFe–based materials are shown in figure 4.2 (A) and (B). The hydrogenated samples contain a mixture of β – TiFeH and γ – TiFeH$_2$ intermetallic hydrides, most probably because of a partial decomposition of unstable at ambient conditions γ – TiFeH$_2$ during the XRD measurements. A significant fraction of non–hydrogenated TiFe was observed during the XRD study of the hydrogenated arc–melted sample. The secondary phases formed in the sintered TiFe–based material formed two hydrides during hydrogenation; η - Ti$_4$Fe$_2$O$_{1-x}$H$_{\sim 7}$ and TiH. The formation of the oxygen containing mixed η - oxide originated from capturing trace amounts of oxygen absorbed on the surface of the starting metal powders during their storage in air.

129
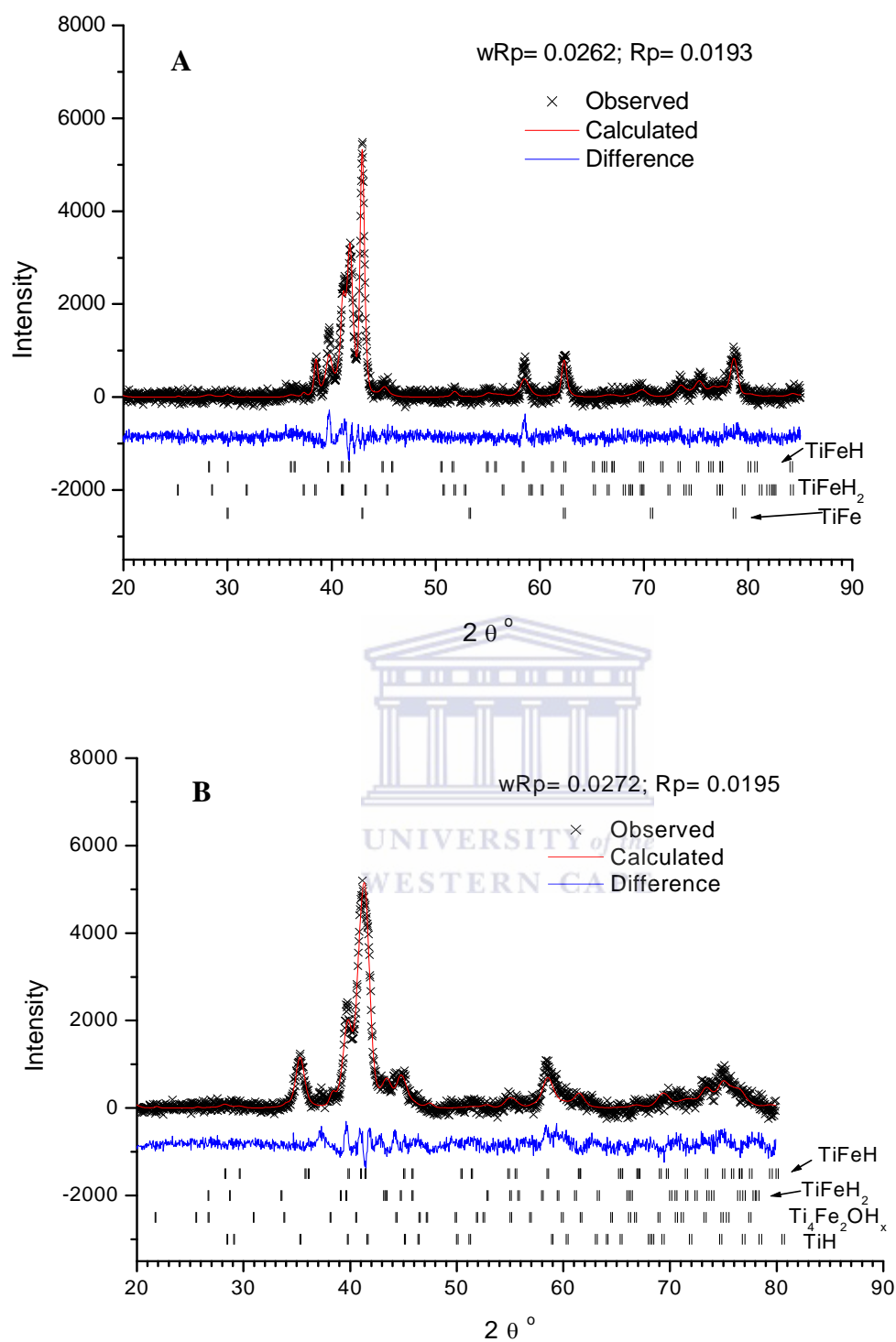
Figure 4.2: *XRD patterns of hydrogenated TiFe: (A) arc–melt hydrogenated TiFe, (B) sintered hydrogenated TiFe*

Table 4.1: *Phase composition of TiFe substrates**

	Arc-melted TiFe	Sintered $Ti_{1.1}Fe_{0.9}O_x$
Non-hydrogenated	TiFe: $a=$ 2.9803(1) Å	TiFe: 64 wt.%; $a=$ 2.9848(1) Å $Ti_4Fe_2O_{1-x}$: 25(3) wt.%; $a=$ 11.350(3) Å β-Ti(Fe): 11(2) wt.%; $a=$ 3.1878(8) Å
Hydrogenated (30 bar H_2, RT)	TiFeH: 59 wt.%; $a=$ 2.9776(9) Å, $b=$ 4.545(1) Å, $c=$ 4.404(2) Å $TiFeH_2$: 15(4) wt.% $a=$ 7.059(6) Å, $b=$ 6.262(4) Å, $c=$ 2.811(1) Å TiFe: 26(2) wt.%; $a=$ 2.9797(1) Å	TiFeH: 62 wt.%; $a=$ 3.0146(9) Å, $b=$ 4.525(2) Å, $c=$ 4.402(1) Å $TiFeH_2$: 15(5) wt.%; $a=$ 6.675(9) Å, $b=$ 6.218(9) Å, $c=$ 2.671(4) Å $Ti_4Fe_2O_{1-x}H_y$: 7(2) wt.%; $a=$ 11.558(6) Å TiH: 16(3) wt.%; $a=$ 4.339(3) Å, $c=$ 4.534(6) Å

* <u>Reference data</u>:

TiFe: Space group $Pm\overline{3}m$ (221); a = 2.976 Å [146]

TiFeH: Space group $P222_1$ (17); $a=$ 2.966 Å, $b=$ 4.522 Å, $c=$ 4.370 Å [147]

$TiFeH_2$:   Space group $Cmmm$ (65); $a=$ 7.029 Å, $b=$ 6.233 Å, $c=$ 2.835 Å [148]

$Ti_4Fe_2O_{1-x}$:   Space group $Fd\overline{3}m$ (227); a = 11.33..11.35 Å (x=0..0.75) [144,145]

$Ti_4Fe_2O_{1-x}H_y$:   Space group $Fd\overline{3}m$ (227); a = 11.4..11.9 Å (x=0.4, y=1.3..5.6) [144]

β-Ti(Fe):   Space group $Im\overline{3}m$ (229); a = 3.14 Å ($Ti_{0.75}Fe_{0.25}$) [149]

TiH: Space group $P4_2/n$ (86); a = 4.21 Å, c = 4.60 Å [150]

4.1.2 Surface morphology and elemental composition of arc–melted and sintered TiFe–based materials

The surface morphologies of the prepared TiFe–based materials were evaluated by SEM analysis. SEM images of arc–melted TiFe–based material are shown in figure 4.3 (A) and (B). The arc–melted TiFe–based material consisted of particles varying in size, which generally exhibited irregular shape and relatively smooth surfaces; the material also exhibited little porosity.
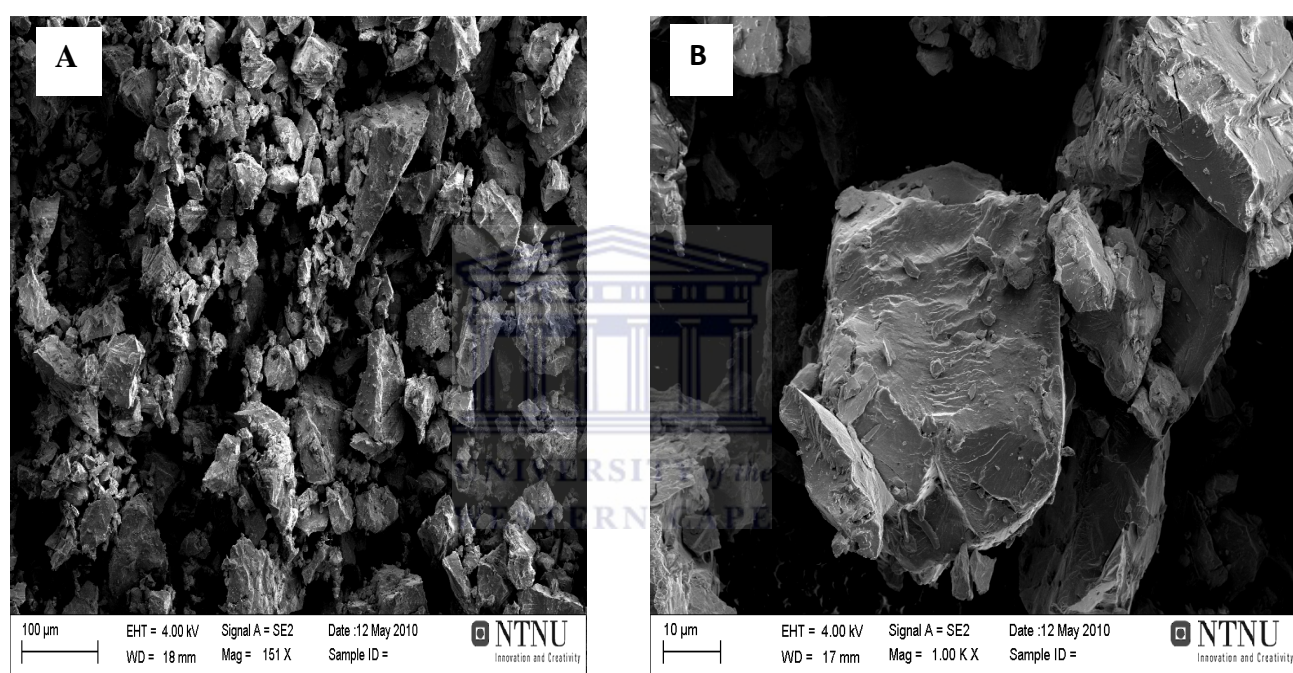
Figure 4.3: *SEM images of arc–melted TiFe, (A) low magnification, (B) high magnification*

The elemental composition of the as prepared TiFe–based materials was evaluated using EDS analysis (table 4.2). It illustrates that the composition of the material corresponds close to that of the target composition of TiFe. The EDS data also shows no oxygen present, which is in agreement with the XRD data. From the EDS and the XRD data, it was clearly demonstrated that the preparation of TiFe–based materials via arc–melt method was free from oxides during synthesis.

Table 4.2: *Quantitative elemental composition data for TiFe-based material prepared by arc–melting*

Elements	EDS Data			
	Line	Net Count	Atom %	Weight %
Ti	TiK	288.80	50.37	49.86
Fe	FeK	187.20	49.63	50.14
Total	-	100	100	100

SEM images of sintered TiFe–based material is shown in figures 4.4 (A) and (B). The sintered TiFe–based material consists of agglomerates of micron–size powders exhibiting a smooth, "fused" surface. The sample also appears to be more porous than that of the arc-melted sample.
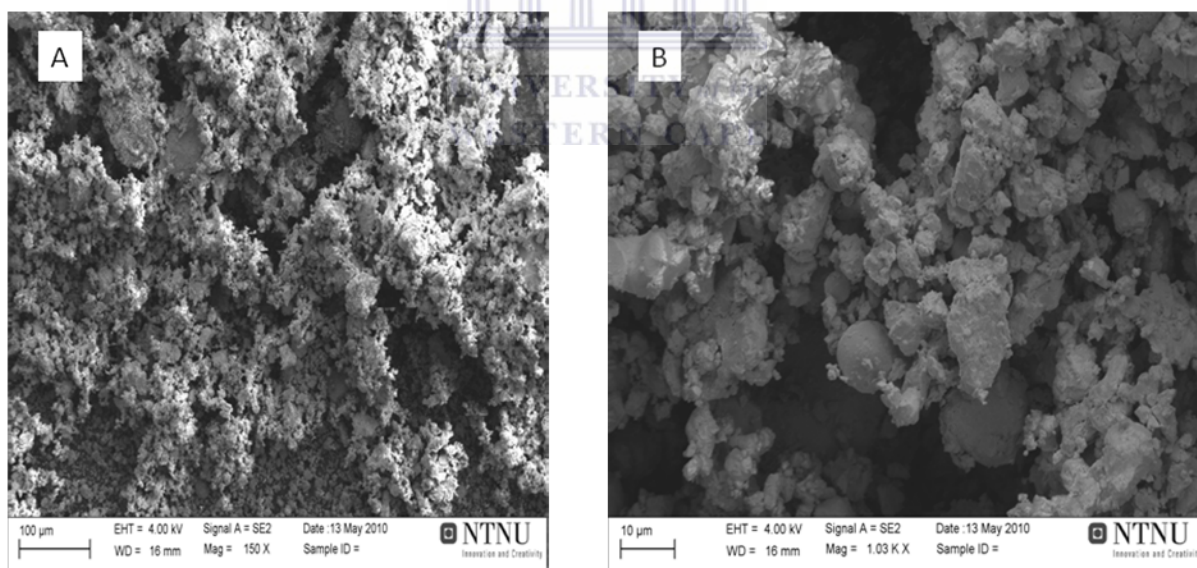
Figure 4.4: *SEM images of sintered TiFe, (A) low magnification, (B) high magnification*

The EDS data evaluation of sintered TiFe–based material are shown below in table 4.3, which illustrates the presence of oxygen within the prepared material. From the EDS analysis the amount of oxygen in the sample was approximately 2.86 wt%. It corresponds to the formation of more than 50 wt. % of Ti_4Fe_2O sub oxide. This value significantly exceeds the corresponding estimations derived from the XRD data (table 4.1). Most probably, the EDS data were overestimated and taken for the oxygen–enriched thin subsurface layer (~ 1μ) where the secondary x – rays were generated, while the XRD data collected the bulk sample.

Table 4.3: *Quantitative elemental composition data for TiFe-based material prepared by sintering*

Elements	EDS Data			
	Line	Net Count	Atom %	Weight %
O	OK	1.61	8.62	2.86
Ti	TiK	352.68	53.77	53.50
Fe	FeK	161.10	37.67	43.64
Total	-	100	100	100

4.1.3 Hydrogen sorption kinetics of arc–melt and sintered TiFe–based materials.

Hydrogenation performances of arc–melt and sintered TiFe–based alloy materials were conducted using Sieverts–type installation. Hydrogenation of the samples was conducted after pre–exposure of the sample materials to air, with and without pre–activation by vacuum heating. Without vacuum activation, the arc–melted (figure 4.5) and sintered (figure 4.6) substrates absorbed hydrogen infinitely slowly (curves 1). This slow rate of absorption is caused by the presence of oxygen–containing layers on the surface, behaving as a diffusion barrier inhibiting the transport of hydrogen atoms through the surface and into the bulk material

The samples were then activated by vacuum heating at 400 ^{0}C for 1 hour. The sintered $Ti_{1.1}Fe_{0.9}O_x$ exhibited better hydrogenation kinetics as compared to the arc–melted TiFe alloy, with an almost eradicated incubation period shown in figures 4.5 and 4.6 curves 2. The first hydrogen absorption after activation by the sintered material yielded a nearly saturated hydride with H/(Ti+Fe) = 0.9 – 0.95, as compared to a decreased hydrogenation activity of the arc–melted sample, which required several vacuum heating hydrogen charging cycles to attain the maximum absorption capacity. These observations are in complete agreement with the data of the XRD analysis shown in figures 4.2 for the sample hydrogenated after first activation. The observed improvement of the hydrogenation activity for the sintered material should be credited to the formation of easy hydrogenated $Ti_4Fe_2O_{1-x}$ and β – Ti acting as hydrogen transfer catalysts. This phenomenon was also observed in [120,144,145].
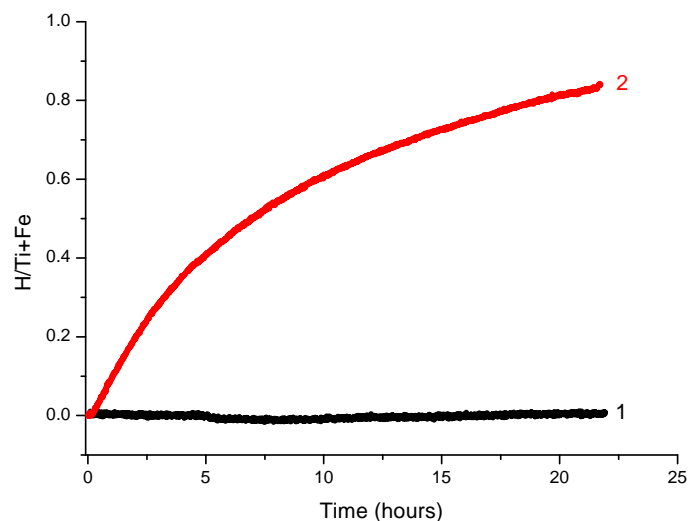
Figure 4.5: *Hydrogen absorption at P_0 = 30 bar and T=20°C for the samples of TiFe prepared by arc-melting: (1) Hydrogenation no vacuum heating, (2) Hydrogenation after vacuum heating to 400 ^{0}C for 1 hour.*
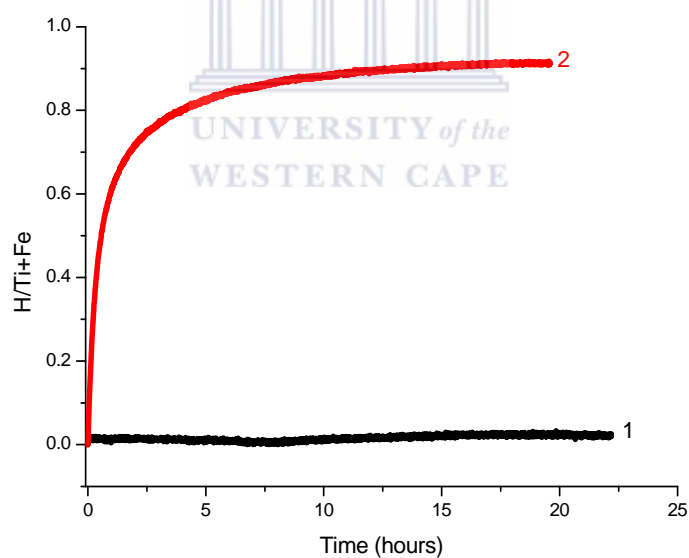
Figure 4.6: *Hydrogen absorption at P_0 = 30 bar and T=20°C for the samples of TiFe prepared by sintered: (1) Hydrogenation no vacuum heating, (2) Hydrogenation after vacuum heating to 400 ^{0}C for 1 hour.*

4.1.4 PCT studies of arc–melted and sintered TiFe

The as-measured hydrogen desorption isotherms for arc-melted TiFe and sintered $Ti_{1.1}Fe_{0.9}O_x$ are presented in Figure 4.7 (A, B). The PCT characteristics calculated from the fitting parameters are presented in Table 4.4. Figure 4.7 (C, D) also presents pressure-composition isotherms calculated for both samples at T = 300 and 400 K.
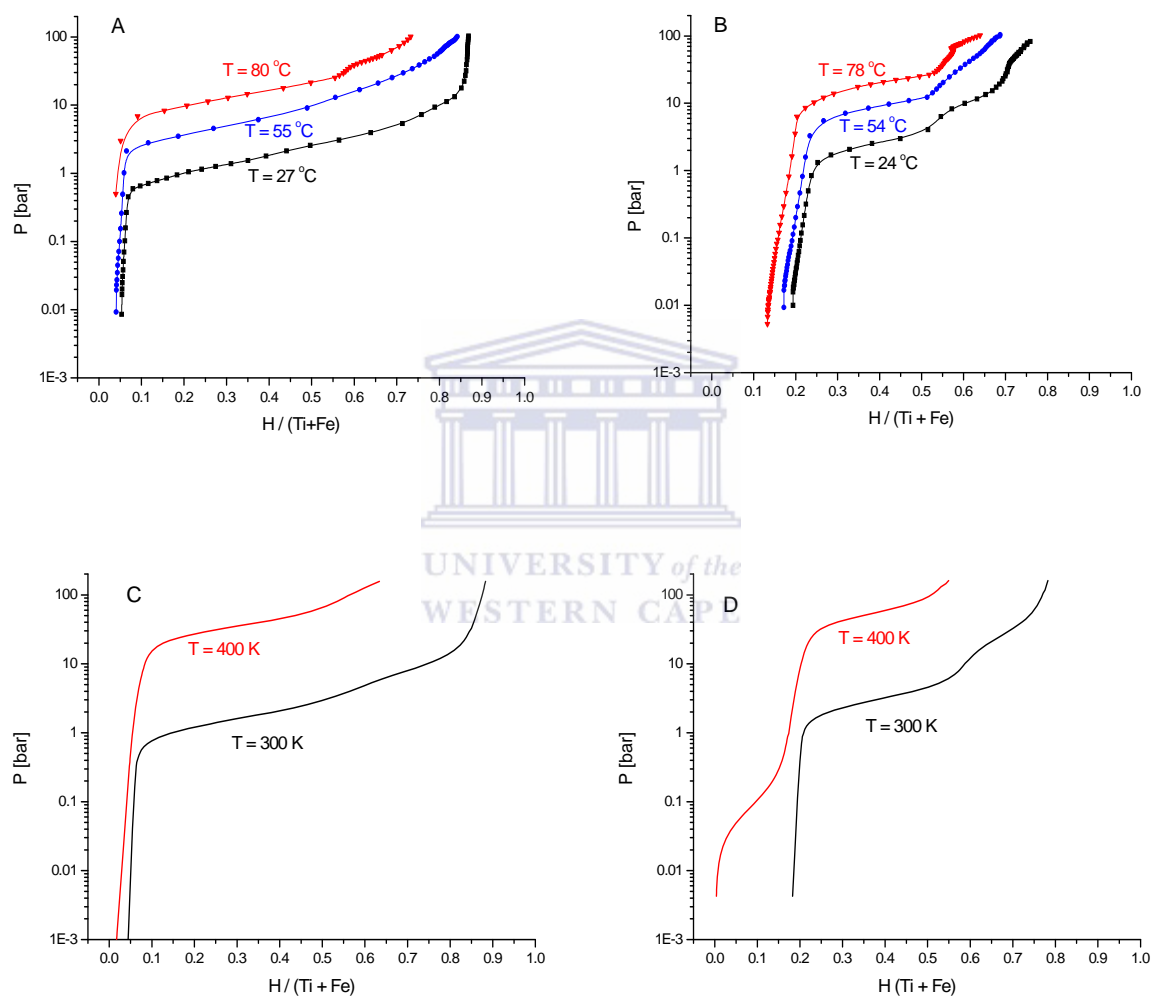
Figure 4.7: *Hydrogen desorption isotherms for arc-melted TiFe (A, C) and sintered $Ti_{1.1}Fe_{0.9}O_x$ (B, D): experimental data (A, B) and calculated curves on the basis of their fitting (C, D).*

Table 4.4: *Calculated PCT parameters for arc-melted TiFe and sintered Ti$_{1.1}$Fe$_{0.9}$O$_x$.*

Parameter[*]	Arc melted TiFe			Sintered Ti$_{1.1}$Fe$_{0.9}$O$_x$		
	Segment 1	Segment 2	Segment 3	Segment 1	Segment 2	Segment 3
Maximum H concentration for the segment [H / (Ti+Fe)]	0.068	0.617	0.383	0.219	0.477	0.264
T_C [K]	~ 0	485	361	460	439	311
ΔS^0 [J/moleH$_2$ K]	–	-101.68	-115.45	-136.33	-101.17	-118.73
ΔH^0 [kJ/moleH$_2$]	–	-29.111	-29.526	-63.072	-27.419	-27.625
P$_D$ [bar]	$3\cdot10^{-5}$	4.03	18.1	$8\cdot10^{-4}$	7.12	54.5
d(ln P)/d(H/(Ti+Fe))	–	2.522	4.802	13.057	3.053	9.107
Asymptotic H concentration, C_{max} [H/(Ti+Fe)]	1.067			0.959		
Calculated fitting error [H/(Ti+Fe)]	0.003			0.001		

As can be seen from Table 4.4 (last row), the fitting for both samples was quite good corresponding to average deviations between experimentally observed and calculated hydrogen concentrations of 0.003 and 0.001 H / (Ti+Fe) for arc-melted and sintered samples, respectively.

The PCT performances of arc-melted TiFe show the existence of two main plateau segments corresponding to β-TiFeH (monohydride) and γ-TiFeH$_2$ (dihydride), in accordance with literature data and XRD results (Figure 4.2 (A)). According to the fitting, the asymptotic hydrogen concentration was found to be about 1 H / (Ti+Fe) that corresponds well to the composition of the higher γ-TiFeH$_2$ hydride. At the same time, both plateau segments were characterised by significant slopes and were difficult to be observed separately, though worse

---

[*] The apparent values of dehydrogenation entropy and enthalpy, as well as plateau pressure and slope were calculated in the midpoints of the corresponding segments at T=50 °C

fit was achieved in the case when only one plateau segment was assumed. The observed discrepancy of the results with literature data [62] reporting about well-pronounced two-plateau behaviour in H–TiFe system (Figure 2.14) can be explained by the fact that the inhomogeneities in the as cast alloy used in this study resulted in higher plateau slopes than in the case of the annealed alloy described in the literature. Nevertheless, the values of thermodynamic parameters calculated from Van't Hoff plots (Figure 4.8) taken from our experimental PCT data at same hydrogen concentrations as in [62] (plateau midpoints for mono- and dihydride) were found to be ΔH^0 = –28.02 and –34.09 kJ/mole H_2; ΔS^0 = –99.24 and –124.08 J/(mole H_2 K), for the mono- and dihydride, respectively, which is quite close to the literature data: ΔH^0 = –28.13 and –33.42 kJ/mole H_2; ΔS^0 = –106.1 and –130.21 J/(mole H_2 K).
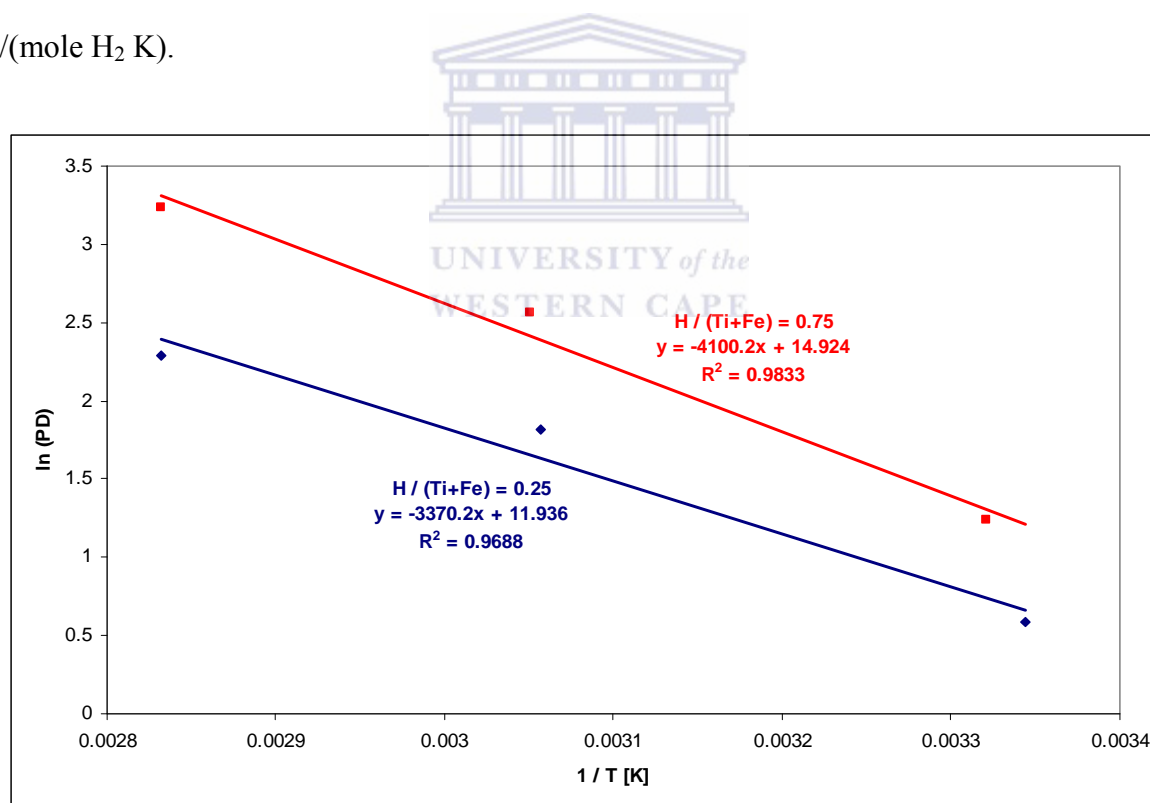
Figure 4.8: *Van't Hoff plots for arc-melted TiFe taken from experimentally observed PCT data (Figure 4.6 (A))*

The calculated parameters for the arc-melted TiFe (Table 4.4) show good correspondence with the literature data only for the monohydride (segment 2), while for the dihydride (segment 3) underestimations of the absolute values of ΔH^0 and ΔS^0 took place. The origin of such deviation is in the different H concentrations (0.306 and 0.675 H / (Ti+Fe) for mono- and dihydride, respectively) at which the thermodynamic parameters were calculated according to the modelling procedure [143]. In combination with the significant plateau slope, it resulted in the different thermodynamic values for the dihydride obtained in this study.

The better PCT fit for the arc-melted TiFe was obtained assuming one more low-pressure plateau segment (segment 1 in Table 4.4) characterised by maximum hydrogen concentration of about 0.07 H / (Ti+Fe) and critical temperature of about zero. This feature is caused by asymptotic behaviour of ln(P) at small H concentrations corresponding to a nonzero H content in the material that is typical for some intermetallic hydrides and has its origin in H trapping by the sample. According to the modelling procedure [143], it was taken into account by the introduction of an imaginary low-pressure plateau segment 1 with a very low critical temperature.

In the sintered $Ti_{1.1}Fe_{0.9}O_x$ the first low-pressure segment, however, was characterised by higher maximum H concentration (about 0.22), and quite high critical temperature. Such behaviour can be clearly observed by comparison of the calculated isotherms for arc-melted and sintered samples (Figure 4.7 (C, D)) and, most probably, is originated from the contribution of stable hydrides $Ti_4Fe_2O_{1-x}H_y$ and TiH also observed in the course of XRD studies (Figure4.2 (B)). The PCT diagram of the sintered sample is also characterised by lower asymptotic maximum hydrogen concentration (about 0.96 H / (Ti+Fe)), lower

stabilities of both mono- and, especially, dihydride, and increased plateau slopes. In our opinion, this effect originates from dissolution of oxygen in TiFe intermetallide in the sintered sample (will be discussed later when presenting results on hydrogen absorption in TiFe surface modified with MO CVD of Pd, Section 4.3.3.3).

In summary, the introduction of oxygen impurity into TiFe observed in the sintered sample significantly influences on its PCT performances, due to the formation of stable hydrides of the impurity phases, as well as the destabilisation of both β-TiFeH and, especially, γ-TiFeH$_2$. This finally results in the decrease of the reversible hydrogen storage capacity of the oxygen-contaminated sample.

4.1.5 Features of oxygen–modified TiFe alloys

The XRD pattern of TiFe modified with different amount of oxygen is presented in Figure 4.9. In addition to TiFe, all the samples contain noticeable amounts of η-suboxide, Ti$_4$Fe$_2$O$_{1-x}$, minor impurity of TiFe$_2$, and trace amounts of tungsten carbide, most probably introduced by ball milling of the ingots before XRD studies. The characteristics of the main phases identified in the samples are presented below in Table 4.5.
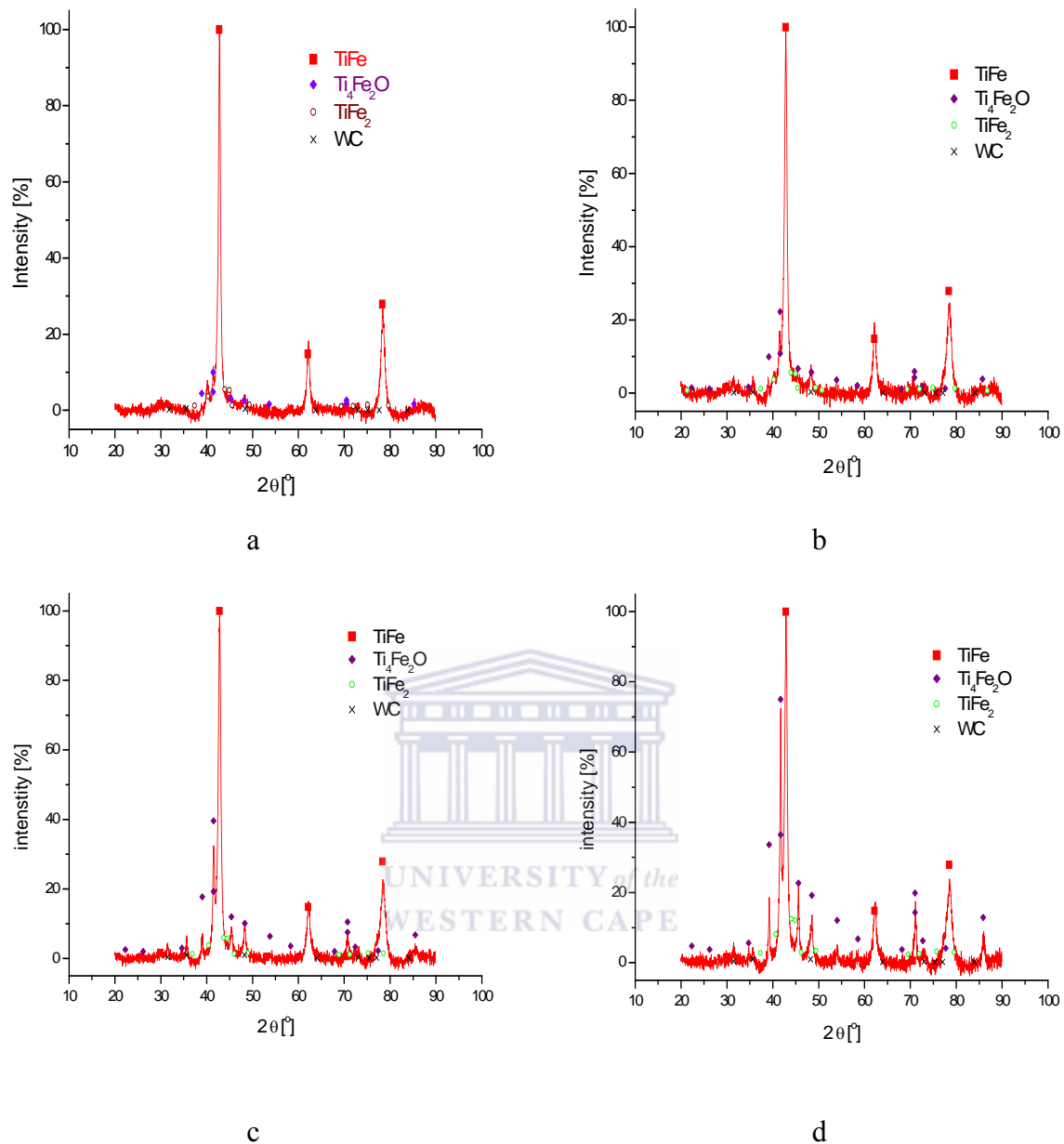
Figure 4.9: *XRD patterns of TiFe containing 0.1 (a), 0.2 (b), 0.5 (c) and 1 (d) wt. % oxygen*

Table 4.5: *Abundances and lattice periods of main constituent phases in oxygen-modified TiFe*

O [wt.%]	TiFe		$Ti_4Fe_2O_{1-x}$		$TiFe_2$		
	wt.%	a [Å]	wt.%	a [Å]	wt.%	a [Å]	c [Å]
0.1	87.53	2.9889	7.68	11.324	4.79	4.8115	7.958
0.2	77.08	2.9866	17.91	11.270	5.01	4.8089	7.985
0.5	67.93	2.9868	27.54	11.300	4.53	4.8663	7.885
1.0	53.13	2.9837	37.29	11.253	9.58	4.8202	7.858

It is notable that the increase of oxygen content in the alloy results in the decrease of the abundance of main TiFe phase, together with the increase in the abundance of $Ti_4Fe_2O_{1-x}$, and, to a lesser extent, $TiFe_2$. The dependence of the phase abundances on oxygen concentration is shown in Figure 4.10. (a). For the comparison, the similar dependence calculated assuming that reaction (2.12) of TiFe with oxygen takes place to yield Ti_4Fe_2O and $TiFe_2$, is presented in Figure 4.10. (b).

The experimental observed tendencies (Figure 4.10. (a)) are adequate to the expected behaviour of TiFe–O system assuming reaction (2.12), Figure 4.10. (b), only qualitatively. At oxygen concentration ≤ 0.2 wt. %, the decrease of TiFe abundance (although obeying linear dependence on wt. % O) is more pronounced than the one calculated from the reaction (2.12).

143

When oxygen content in the sample further increases, the rate of the observed linear decrease of TiFe abundance becomes similar to the calculated one (Figure 4.10. (b)).
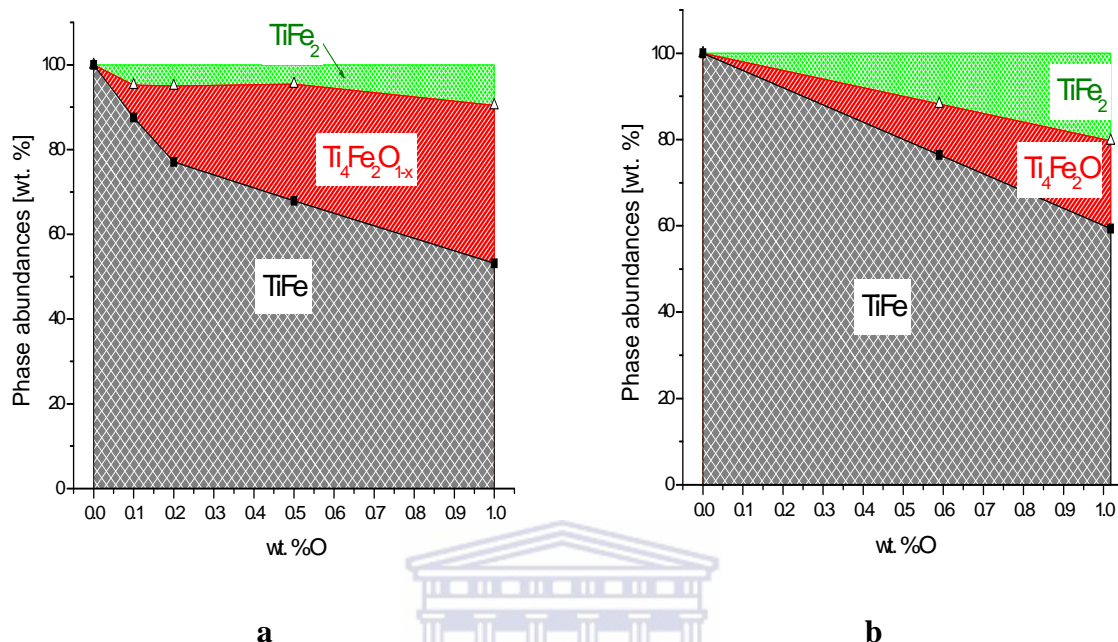
Figure 4.10: *Phase abundances in TiFe containing 0–1 wt.% O calculated from XRD data (a) and (b) from the equation (2.12).*

The observed increase of abundances of $Ti_4Fe_2O_{1-x}$ mixed sub oxide and $TiFe_2$ with the increase of oxygen concentration in the alloy is non-linear, and the amount of $TiFe_2$ is significantly lower than it could be expected from simple theoretical considerations (according equation 2.12, its weight concentration should be equal to the concentration of the sub oxide). From the other hand, the observed abundances of the sub oxide are in 2 times and more higher than the corresponding calculated values.

Figure 4.11 given below presents dependencies of lattice periods of the major phases, TiFe and $Ti_4Fe_2O_{1-x}$, on oxygen concentration in the alloy. For TiFe, there is observed significant increase in the lattice period when passing from oxygen-free arc-melted alloy

144

(Figure 4.1(A), Table 4.1) to the alloy containing 0.1 wt. % O. Most probably, the observed feature originated from the dissolution of interstitial oxygen in TiFe phase. When oxygen concentration further increases, the lattice period shows a tendency to its gradual decrease that can be explained by the substitution of Ti atoms (R_{Ti}=1.76 Å) withdrawn from TiFe lattice due to formation of $Ti_4Fe_2O_{1-x}$ with smaller Fe atoms (R_{Fe}=1.56 Å) which remain in excess. Most probably, it results in the formation of metastable $TiFe_{1+x}$ phase ($x > 0.006$, the highest value according to the Ti–Fe phase diagram), and thus suppresses the formation of $TiFe_2$ according reaction (2.12) whose observed abundance was found to be lower than the calculated one.
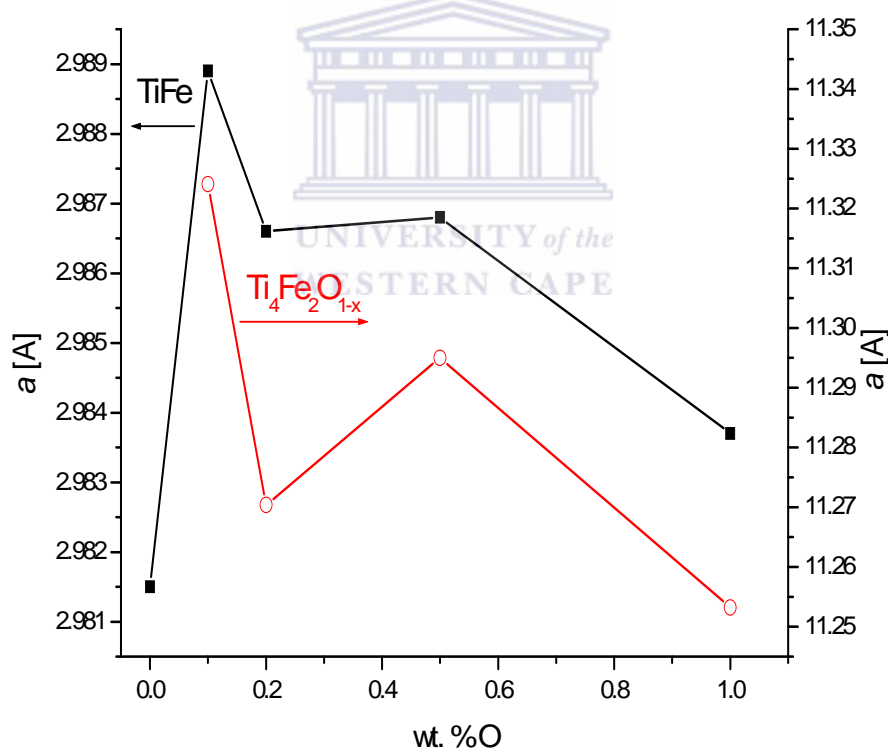
Figure 4.11: *Dependencies of lattice periods of TiFe and $Ti_4Fe_2O_{1-x}$ on oxygen concentration in the alloy*

The observed tendency towards decrease of lattice period in the sub oxide $Ti_4Fe_2O_{1-x}$ has its origin in the increase of oxygen contents in the sub oxide (that is equivalent to the decrease of x) as it was shown in [144, 145].

The lower abundance of TiFe and higher one of $Ti_4Fe_2O_{1-x}$ in the oxygen-modified TiFe (Figure 4.10. (a)) can be thus explained by the fact that the formation of one formula unit of the sub oxide requires less than one oxygen atom, and the amount of the formed sub oxide will be higher than it is expected from reaction (2.12).

In conclusion, the introduction of oxygen into TiFe significantly reduces the amount of TiFe intermetallic phase, almost by two times when oxygen content is of 1 wt.%. It may significantly reduce the reversible hydrogen storage capacity of the material.
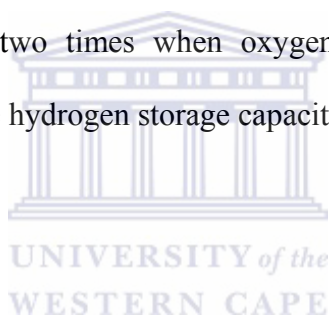
4.1.6 Hydrogen absorption kinetics of oxygen–modified TiFe alloys

Hydrogenation performances of oxygen – modified TiFe – based alloy materials were conducted using Sieverts–type installation. Hydrogenation of the samples was conducted after pre–exposure of the sample materials to air, with and without pre–activation by vacuum heating. Figure 4.12 illustrates the hydrogenation of oxygen–modified TiFe with different wt. % of O_2. It can be seen that the samples did not absorb hydrogen without vacuum heating. After vacuum heating at 400 ^{0}C for 1 hour, both samples absorbed hydrogen. It was observed that the kinetics of the materials are similar but the hydrogen capacities are different. The H / (Ti+Fe) for TiFe doped with 0.1 and 0.2 wt. % O_2 were 0.95 and 0.62, respectively. This is due to the decrease in the amount of TiFe phase and the increase in the $Ti_4Fe_2O_{1-x}$ as shown in table 4.5 for the TiFe synthesised with the addition of 0.1 and 0.2 wt. % O_2.
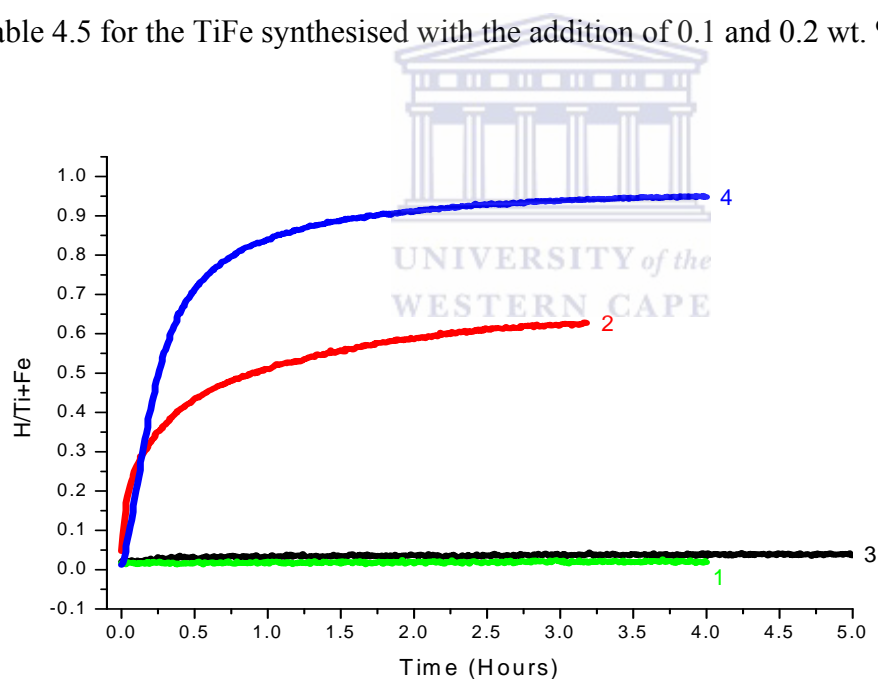
Figure 4.12: *Hydrogen absorption at P_0 = 30 bar and T=20°C for the oxygen modified TiFe–based alloys. 1,2–oxygen modified TiFe with 0.2 wt. % O_2; 3,4–oxygen modified TiFe with 0.1 wt. % O_2; 1,3–hydrogenation #1 (no vacuum heating); 2,4–hydrogenation #2 after vacuum heating at 400 ^{0}C.*

4.1.7 Features of TiFe prepared by induction melting

Figure 4.13 shows the indexed XRD pattern of TiFe prepared by induction melting of the metal powders (same as were used for the preparation of $Ti_{1.1}Fe_{0.9}O_x$ by sintering) using graphite (a) and alumo-silica (b) crucible; the results of refinement are summarised below in Table 4.6.
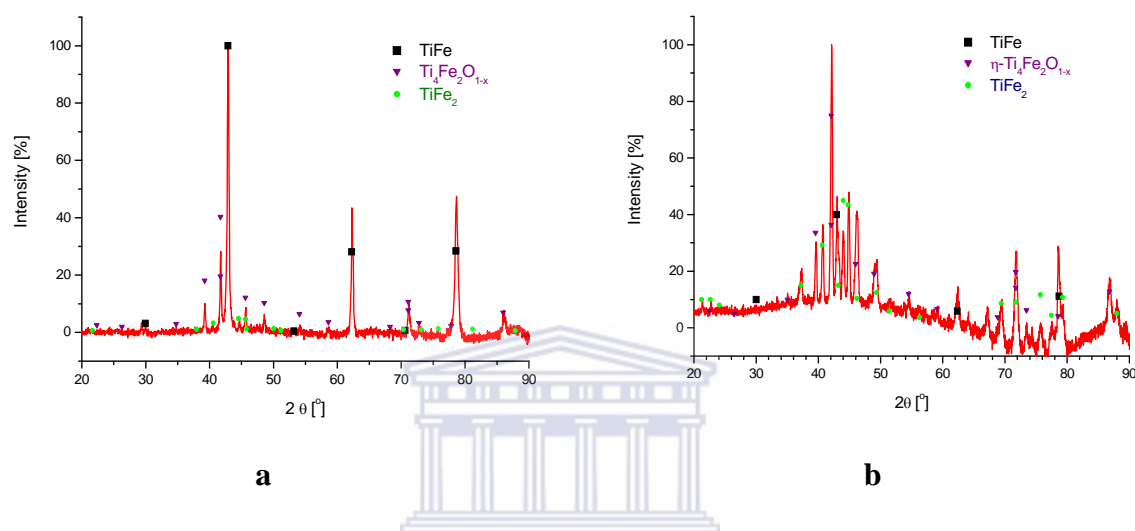
Figure 4.13: *Indexed XRD patterns of TiFe prepared by induction melting in graphite (a) and alumo-silica (b) crucible*

Table 4.6: *Abundances and lattice periods of constituent phases in TiFe prepared by induction melting*

Crucible material	TiFe		$Ti_4Fe_2O_{1-x}$		$TiFe_2$		
	wt.%	a [Å]	wt.%	a [Å]	wt.%	a [Å]	c [Å]
Graphite	70.33	2.9800	26.19	11.240	3.48	4.7359	7.9219
Alumo-silica	10.78	2.9765	53.73	11.146	35.49	4.8278	7.8424

148

The sample prepared in graphite crucible is very similar to arc-melted TiFe which contained 0.2 wt. % of oxygen (Table 4.5). The abundance of η-$Ti_4Fe_2O_{1-x}$ phase (~25 %) is also similar to one in the sintered $Ti_{1.1}Fe_{0.9}O_x$ (Table 4.1) allowing us to suppose that in both cases oxygen contamination took place caused by O_2 and H_2O adsorbed on the surface of starting metal powders. At the same time, in the sintered sample the lattice period of the η-phase was significantly higher (11.35 Å) than in the alloy induction melted in graphite crucible (11.24 Å) and the alloy TiFe + 0.2 wt. % O_2 (11.27 Å). It can be explained by lower oxygen content in η-phase formed in the sintered sample and / or additional contamination of the induction-melted TiFe with carbon additionally occupying oxygen positions in the η-phase and resulting in the total lowering of x in η-$Ti_4Fe_2(O,C)_{1-x}$ associated with the decrease of the lattice period [144, 145].

In contrast, the sample prepared in alumo-silica crucible was characterised by much lower content of TiFe intermetallide and the presence of significant amounts of the η-phase with quite low lattice period (11.15 Å) and $TiFe_2$. It testifies that, in this case, significant contamination of the sample by oxygen additionally introduced from the crucible material took place.

Due to the low content of TiFe intermetallide prepared via induction melt using the alimo-silca crucible the sample was not submitted for hydrogenation experiments. The TiFe intermetallide prepared using the graphite crucible was submitted for hydrogenation experiments. Hydrogenation of the sample was conducted after pre–exposure of the sample materials to air, with and without pre–activation by vacuum heating. The hydrogen absorption kinetics of the TiFe alloy prepared via induction melt using the graphite crucible is shown in figure 4.14.

149

It was observed that the material did not absorb hydrogen without activation by vacuum heating at 400 ^{0}C. After vacuum heating, the sample absorbed hydrogen and had similar hydrogen capacity and hydrogen absorption kinetics to that of the arc-melted TiFe which contained 0.2 wt. % of oxygen (figure 4.12 curves 1, 2). The H/Ti+Fe for the TiFe alloy prepared via induction melt using graphite crucible was 0.63.
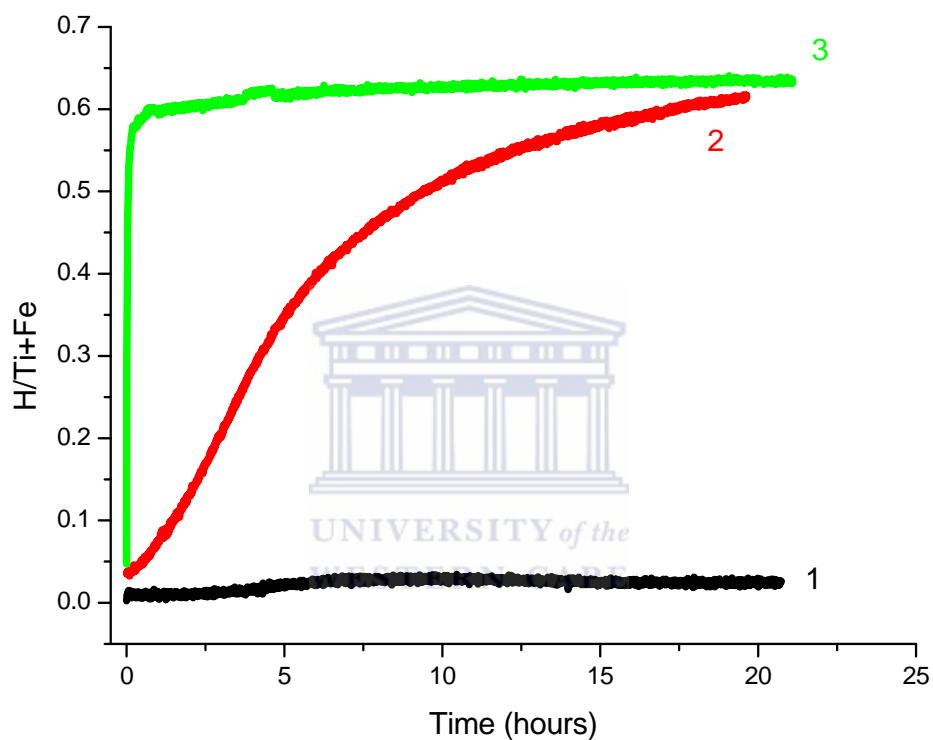
Figure 4.14: *Hydrogen absorption at P_0 = 30 bar and T=20 ^{0}C for the TiFe–based alloy prepared via induction melt using graphite crucible; 1 – hydrogenation #1 (no vacuum heating); 2 – hydrogenation #2 after vacuum heating to 400 ^{0}C; 3 – hydrogenation #3 after vacuum heating to 400 ^{0}C.*

4.1.8 Synthesis of TiFe by reduction of ilmenite

As it was mentioned in the literature review (section 2.3.1.3), separation of iron and titanium when producing Ti from ilmenite requires hard efforts and is the main reason for the sharp increase in the cost of the products in the titanium value chain.

For the preparation of TiFe-based hydride-forming alloys from the ilmenite, the separation of iron and titanium is not necessary, that puts a strong motivation for the development of the corresponding methods related to direct reduction of $FeTiO_3$ to TiFe.

Metal-thermic reduction of TiO_2 with strong reducing agents, like magnesium [152], calcium [153] or calcium hydride [154] was shown to be a simple and efficient way of preparing metallic Ti. However, for the reduction of mixed oxides, like ilmenite, some problems can arise. The main problem is that iron in $FeTiO_3$ can be reduced easier than titanium, so as the first stage of the reduction process follows the mechanism schematically as shown below:

$$FeTiO_3 + R \rightarrow Fe + TiO_2 + RO; \qquad \qquad \textbf{4.1}$$

where R is, for example, Ca or Mg

The formed oxide, RO, where R = Ca or Mg, can easily react with TiO_2 to form very stable perovskite- (M=Ca) or spinel-type (M=Mg) mixed oxides:

$$CaO + TiO_2 \rightarrow CaTiO_3; \qquad \qquad \textbf{4.2}$$

$$2\,MgO + TiO_2 \rightarrow Mg_2TiO_4. \qquad \qquad \textbf{4.3}$$

As a result, the reduction process is hindered and that results either in incomplete yield of the target alloy product, as it was shown above, or, in lower amounts of the reducing agent and / or not high enough process temperature and / or too short process time, even in suppressing its formation at all.

The experimental study described in this section deals with the development of the process of reduction of ilmenite allowing to overcome the above-mentioned problem and to achieve a maximum yield of the target product, TiFe alloy.

4.1.8.1 Procedure of ilmenite reduction; phase composition and morphology of the materials

Natural ilmenite ore was obtained from Saldanha Steel, Western Cape, South Africa; the composition of the ilmenite is given it chapter 3.

SEM image of the natural ilmenite is shown in figure 4.15. The material looks like dense crystals, ~50 to 100 μ in size, of a regular prismatic shape with rounded edges
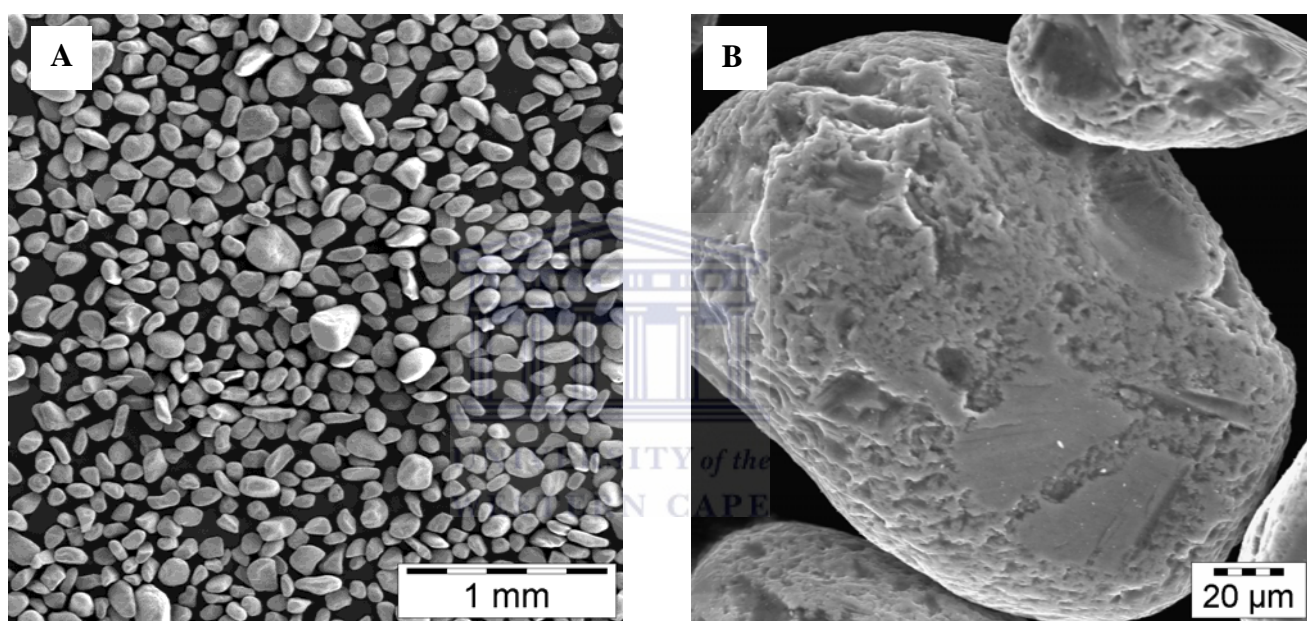
Figure 4.15: *SEM images of natural ilmenite; (A) low magnification, (B) high magnification*

The XRD pattern of the raw ilmenite is shown below in figure 4.16. It shows the presence of single trigonal phase, $FeTiO_3$, space group (#148), with lattice periods a=5.0816 Å, c=14.051 Å corresponding well to literature data [155].
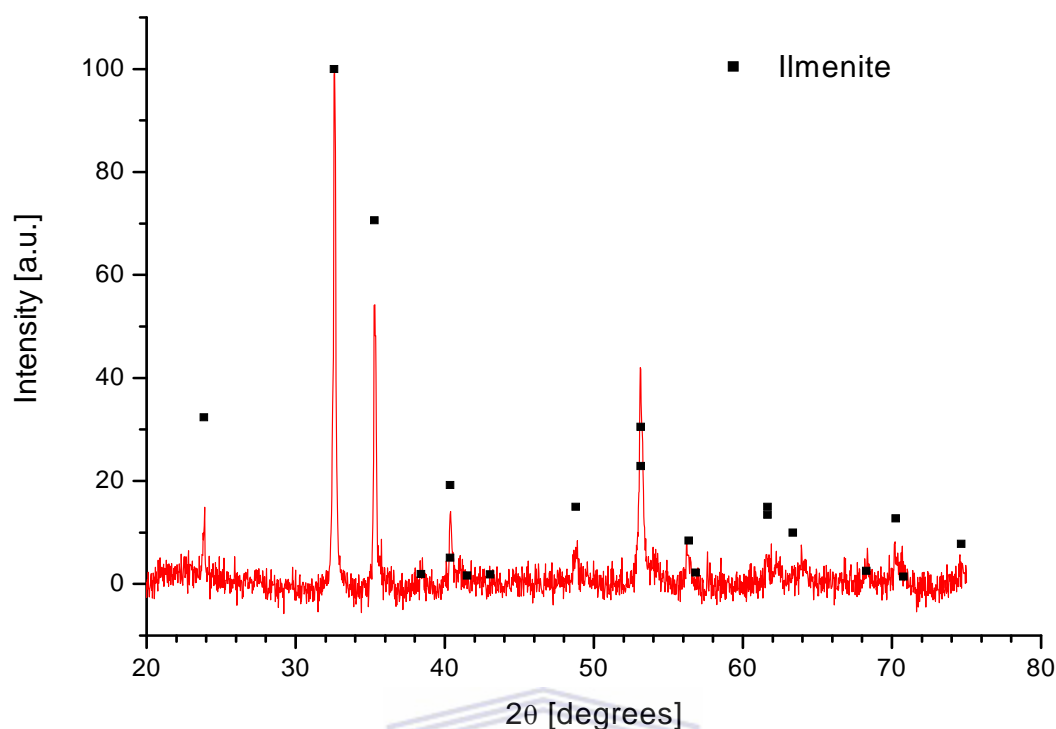
Figure 4.16: *XRD pattern of raw ilmenite (FeTiO3)*

The reduction of ilmenite ($FeTiO_3$) in this study was done using three different experiments, of which the first two demonstrate features of direct metal-thermic reduction of ilmenite.

Experiment 1: The raw ilmenite was mixed with calcium hydride, CaH_2, taken in 20% excess as to stoichiometric amount corresponding to the equation:
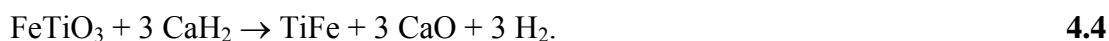
$$FeTiO_3 + 3\ CaH_2 \rightarrow TiFe + 3\ CaO + 3\ H_2. \hspace{3cm} \textbf{4.4}$$

The mixture (amount corresponds to 10 g of ilmenite) was ball milled in argon for 2 hours followed by heating in argon flow at 1000 ^{o}C for 1 hour.

The XRD pattern of the sample after the metal-thermic reaction is shown in figure 4.17. The reduction resulted in complete disappearance of the starting ilmenite. However, the target TiFe alloy presents in the product only in minor amount, and the main products are

metallic iron and perovskite-like $CaTiO_3$ indicating that the side reaction (4.2) is the main process taking place during the reduction. Some amount of $TiFe_2$ was detected as well indicating that the undesired side reaction (2.12) also takes place. The increase of process duration, excess of CaH_2, as well as replacement of CaH_2 with metallic Ca, does not significantly change the final results according to which the yield of TiFe is very low.
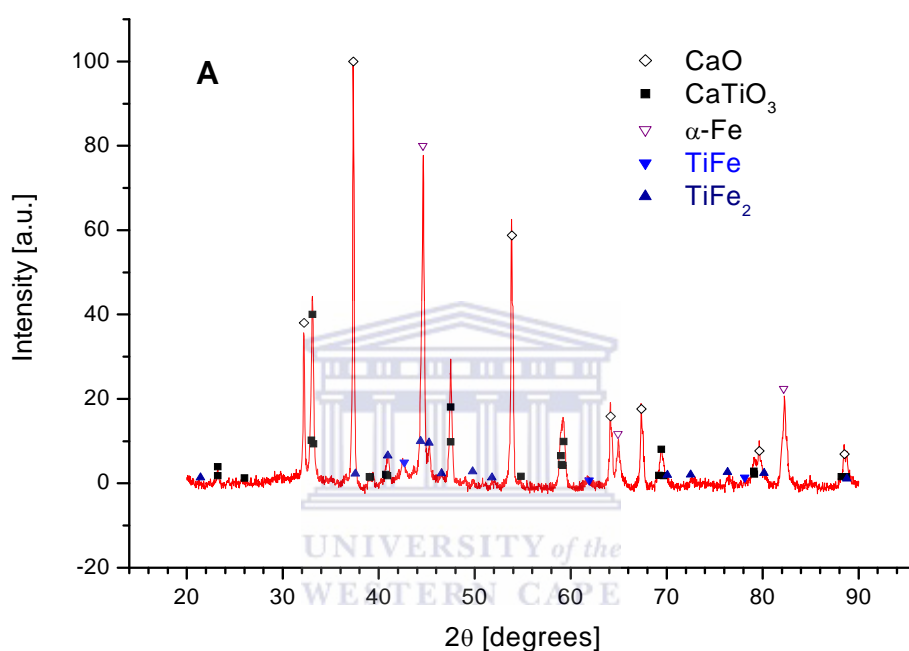
Figure 4.17: *XRD pattern of metal–thermic reduction of ilmenite (FeTiO₃) using CaH₂ as a reducing agent*

Experiment 2: The raw ilmenite was mixed with magnesium hydride, MgH_2, taken in 20% excess as to stoichiometric amount corresponding to the equation:
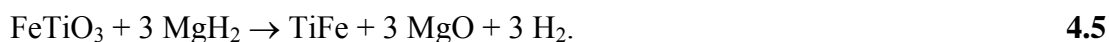
$$FeTiO_3 + 3\,MgH_2 \rightarrow TiFe + 3\,MgO + 3\,H_2. \qquad \textbf{4.5}$$

The mixture (amount corresponds to 10 g of ilmenite) was ball milled in argon for 2 hours followed by heating in argon flow at 1000 ^{o}C for 1 hour. The XRD pattern of the product is shown in figure 4.18. It can be seen that in this case TiFe was not detected in the

product at all, but spinel-like $MgTi_2O_4$ was observed together with Fe and MgO indicating that the side reaction (4.3) is the only process taking place during the heat treatment under applied conditions.
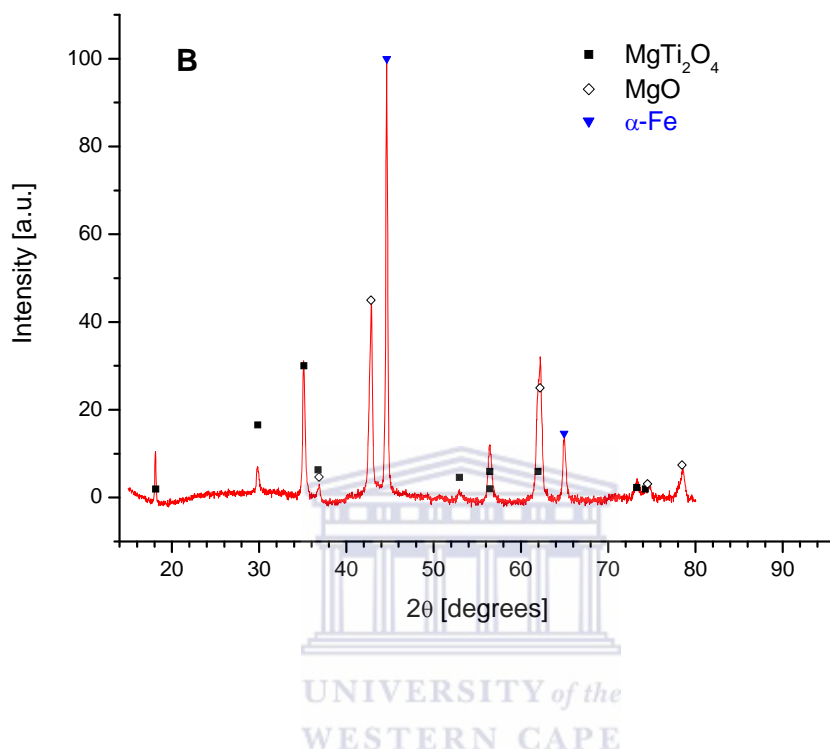
Figure 4.18: *XRD pattern of metal–thermic reduction of ilmenite (FeTiO₃) using MgH₂ as a reducing agent*

The products of the above two experiments were not subjected to hydrogen absorption testing due to the fact the target material, TiFe alloy was not obtained as the major phase in experiment 1, and in experiment 2 the target alloy was not obtained at all.

To increase the yield of target TiFe, a two-stage method of ilmenite reduction was developed [98]. The method includes two stages: (1) gas–phase reduction and (2) metal–thermic reduction, which assisted in overcoming the above-mentioned problems. The method

used for the synthesis of hydride forming alloys from ilmenite ($FeTiO_3$) is shown schematically in figure 4.19.
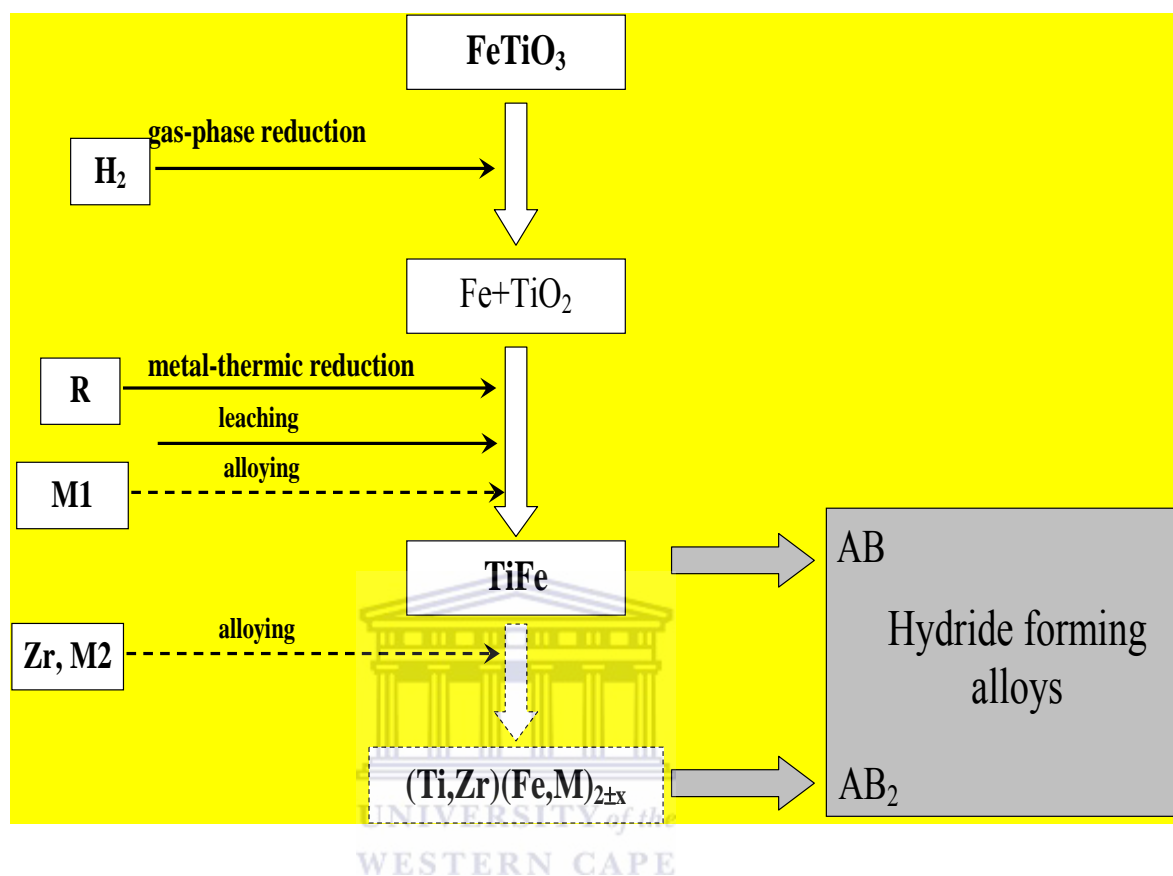
Figure 4.19: *Synthetic route for the reduction of Ilmenite (FeTiO₃)*

According to the method, the primary ilmenite ($FeTiO_3$) is first subjected to the gas-phase reduction to yield a mixture of metallic iron and titanium oxides, $Fe+TiO_2$. The reduction takes place at a high temperature (850–1000 ^{o}C), in the flow of a reducing gas, preferably containing hydrogen, H_2. In so doing, the step of gas-phase reduction can be schematically represented by the following equation:

$$FeTiO_3 \text{ (s)} + H_2 \text{ (g)} \rightarrow Fe \text{ (s)} + TiO_2 \text{ (s)} + H_2O \text{ (g)}, \hspace{2cm} \textbf{4.6}$$

where (s) denotes solid phases, and (g) – gas phase.

For safety reasons, and in order to provide more efficient removal of water vapours, hydrogen in the reducing gas can be mixed with an inert gas (nitrogen or argon), but to provide reasonable process rates, the concentration of hydrogen in the mixture (reducing gas) should be 10% or higher. The flow rate of the reducing gas, recalculated to flow rate of the pure H_2 per 1 kg of the raw ilmenite, should be not less than 0.5 m^3/h to provide high enough conversion of $FeTiO_3$ to $Fe+TiO_2$ for a reasonable process time (1–3 hours). At the same time, there are no reasons to increase the specific flow rate above 5 m^3/h, so as to avoid too high consumption of the reducing gas without noticeable improvement of the process performances.

The next step of the process (Fig. 4.19) is a metal-thermic reduction of the $Fe+TiO_2$ mixture with a reducing agent, R, according to the following scheme:

$$Fe\ (s) + TiO_2\ (s) + R\ (s) \rightarrow TiFe\ (s) + R_xO_y\ (s). \hspace{2cm} \textbf{4.7}$$

The less expensive reducing agent is aluminium (R=Al, R_xO_y=Al_2O_3). However, the option of its usage is not preferable because of possibility of alloying Al into the primary TiFe that significantly reduces reversible hydrogen storage capacity of the material. Usage of magnesium (R=Mg, R_xO_y=MgO) that is also inexpensive is better due to its low solubility in TiFe alloy. However, high vapour pressure of Mg at the process temperature (~1000 ^{o}C) may result in its significant losses.

So, its acceptable from the cost point of view, but it is preferable to use calcium (R=Ca, R_xO_y=CaO) due to its stronger reducing potential, lower vapour pressure, and the easiness of further separation (leaching) of the oxide by-product.

Apart from metals (e.g., Ca and / or Mg), their hydrides (CaH_2 and MgH_2) can be also used as reducing agents since they can be easier dispersed to fine powders that will result in the increase of the efficiency of further metal-thermic reduction. In this case, the process occurs in two stages corresponding to schemes (4.8) and (4.9) below:

$$Fe~(s)+ TiO_2~(s) + RH_2~(s) \rightarrow Fe~(s)+ TiO_{2-x}~(s) + R~(s) + H_2~(g) + H_2O~(g) \qquad \textbf{4.8}$$

$$Fe~(s)+ TiO_{2-x}~(s) + R~(s) \rightarrow TiFe~(s) + RO~(s). \qquad \textbf{4.9}$$
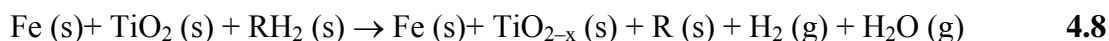
The RH_2 (R=Ca, Mg) hydride thermal decomposition (4.8) preceding the metal-thermic process (4.9) is accompanied by the release of active hydrogen gas which acts as an additional deoxidiser promoting increase of the quality of the final product.

The proposed method was realised in experiment 3 described below

Experiment 3: The details of this experiment were explained in chapter 3. The ilmenite ($FeTiO_3$) was reduced using a two-step process, including gas–phase reduction, followed by metallic–thermic reduction.The SEM image of the product of the gas-phase reduction treatment is shown below in figure 4.20. It illustrates that the material's particles keep their original shape, but significantly change the morphology. Each original particle of the ilmenite was transformed to a porous agglomerate consisting of rather small, few micron-size particles.
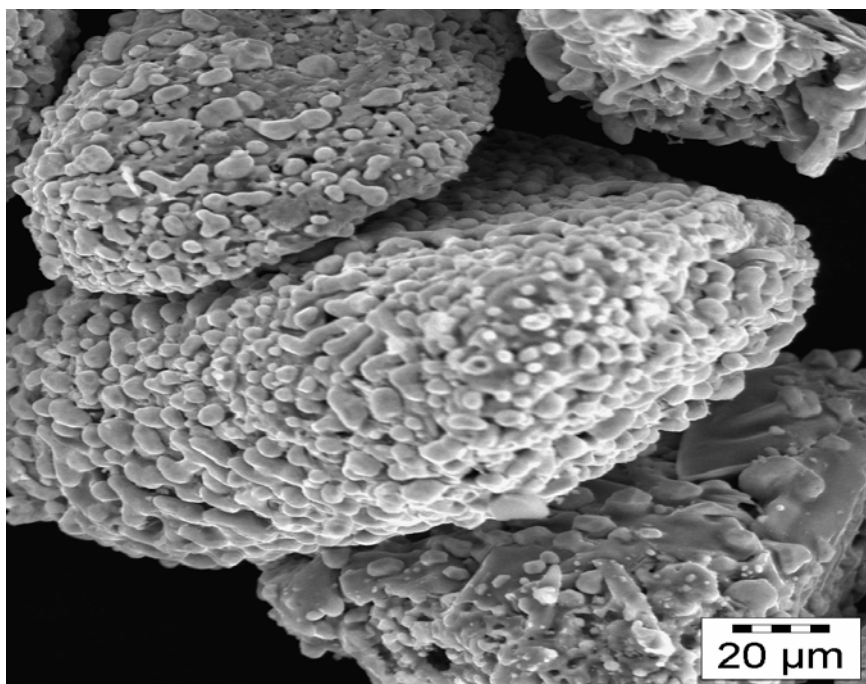
Figure 4.20: *SEM image of gas – phase reduced ilmenite (FeTiO₃)*

The XRD pattern of the gas–reduced ilmenite ($FeTiO_3$) is shown in figure 4.21 that follows. It indicates the absence of initial $FeTiO_3$ which was completely reduced to iron mixed with titanium oxides (mainly rutile and anataze) according to the equation:

$$FeTiO_3 + H_2 \rightarrow Fe + TiO_2 + H_2O. \hspace{3cm} \textbf{4.10}$$
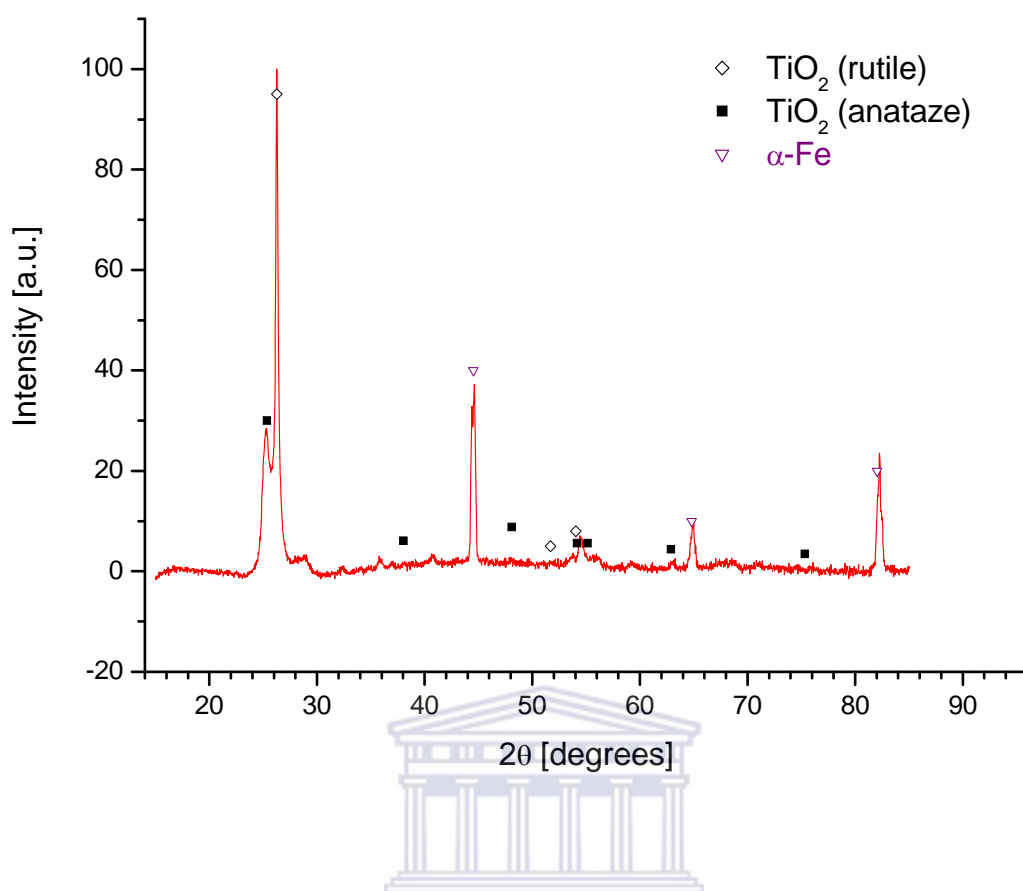
Figure 4.21: *XRD pattern of gas – phase reduced ilmenite (FeTiO₃)*

The product of the gas-phase reduction of ilmenite was further subjected to metal-thermic reduction treatment using CaH_2 as a reducing agent. CaH_2 was taken in 20% excess as to stoichiometric amount corresponding to the equation:

$$Fe + TiO_2 + 2\ CaH_2 \rightarrow TiFe + 2\ CaO + 2\ H_2, \qquad\qquad \textbf{4.11}$$
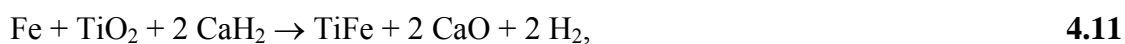
where the amount of TiO_2 was calculated from the starting amount of the raw ilmenite assuming 100% yield of reaction (4.10).

The SEM image of the material after its metal-thermic reduction is shown in figure 4.22. It shows that the product has a flake like structure, and the initial big particles of the raw material (Fig. 4.14, 4.19) are completely disintegrated.
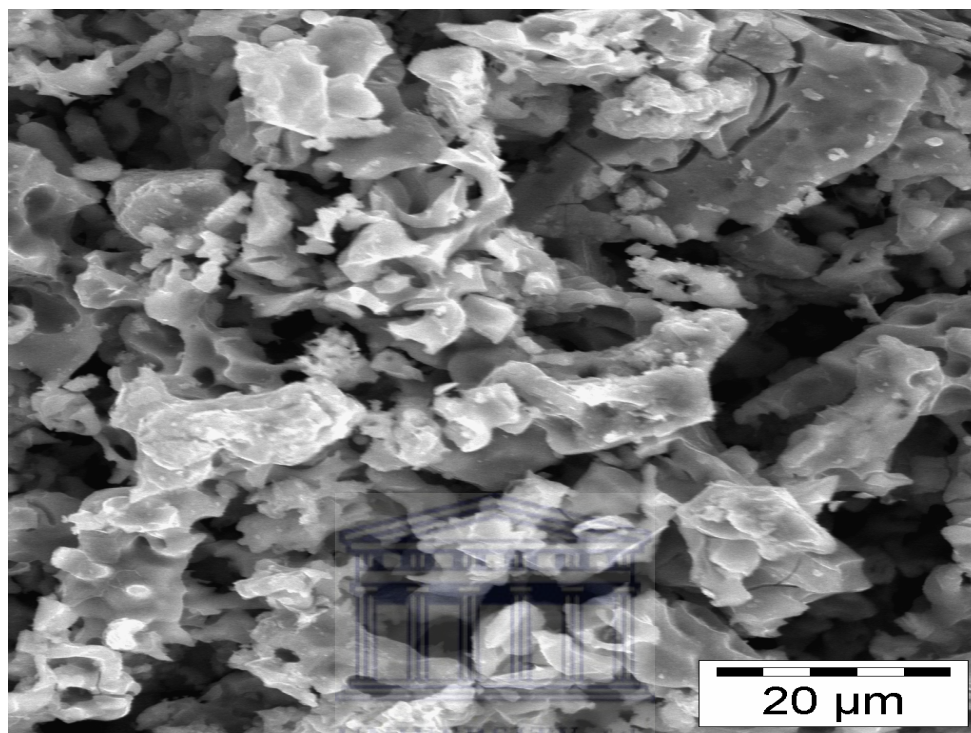
Figure 4.22: *SEM image of metal–thermic reduction after gas phase reduction of ilmenite (FeTiO₃)*

After completion the metal-thermic reduction, the product looking as a sponge body was removed from the sample holder, crushed, washed with distilled water several times, and leached with HCl (20 vol. %), followed by washing with distilled water and drying. All the operations were performed in air.

The XRD pattern of the metal–thermic reduction of ilmenite ($FeTiO_3$) after leaching is shown below in figure 4.23. The leached product indicates that TiFe is the major phase therein. The main impurities present are η-Ti_4Fe_2O and $TiFe_2$.
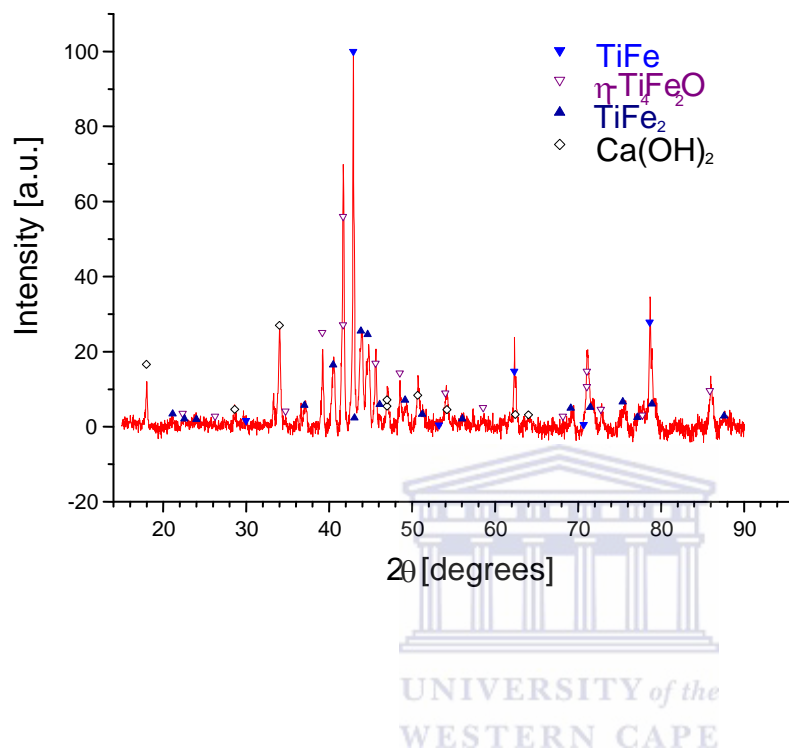
Figure 4.23: *XRD pattern of metal – thermic reduction of ilmenite after leaching in HCl*

4.1.8.2 Hydrogen sorption behaviour of TiFe prepared by FeTiO₃ two-stage reduction

The hydrogen absorption properties of the TiFe alloy prepared by reduction of ilmenite (FeTiO₃) are shown in figure 4.24. The amount of oxygen in the raw TiFe was found to be too high; and the measured reversible hydrogen absorption capacity of different samples prepared as described above was about 0.5 wt.% H, although hydrogen absorption capacity of TiFe reported in the literature should be about 1.8 wt.%. The source of this difference is reaction (2.12) which cannot be completely suppressed at the applied conditions. Thus, for the improvement of hydrogen sorption performances, alloying of the raw TiFe to yield AB₂-type alloy was undertaken in section 4.4.2.
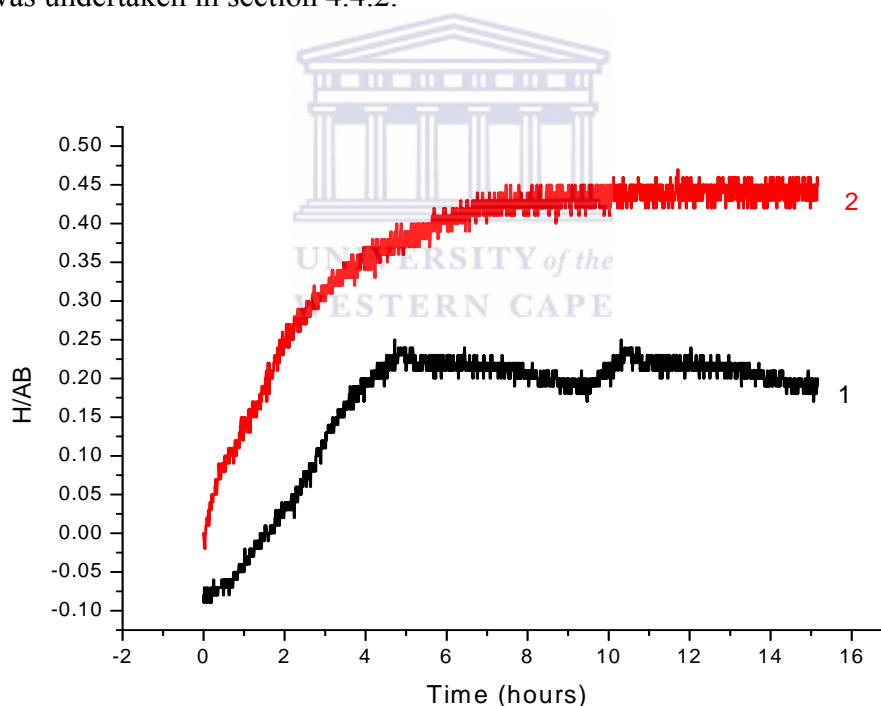
Figure 4.24: *Hydrogen absorption at P₀ = 30 bar and T=20°C for the samples of TiFe prepared by reduction of ilmenite (FeTiO₃) via gas–phase reduction and metal–thermic reduction: (1) Hydrogenation no vacuum heating, (2) Hydrogenation after vacuum heating to 400 ⁰C for 1 hour*

4.2   Surface modification of TiFe-based alloys

The hydrogen sorption kinetics of TiFe–based alloys is greatly improved by the addition of surface catalyst, which enables rapid rates of hydrogen absorption at the surface [156]. The rate of absorption is dependent on the rate of hydrogen dissociation and the rate of hydrogen transport from the surface of the bulk material. Surface poisoning directly affects the rate of hydrogen dissociation, which eventually leads to the rate of hydrogen absorption being affected. Therefore, by increasing the surface catalyst towards hydrogen dissociation on TiFe–based alloys, it is possible to enhance the surface poisoning resistance and increasing the hydrogenation rate.

An efficient solution to this problem is in modification of the material's surface by encapsulation with a metal (including Palladium) overlayer which catalyses the dissociative chemisorption of hydrogen molecules [157]. Reports regarding the introduction of Pd additives onto TiFe substrate by ball milling [120] and physical vapour deposition (PVD) [123] are available. In all cases, the improvement of activation performances and hydrogenation kinetics of the surface modified material was observed. The listed methods, however, have a number of drawbacks including long processing time and high power consumption (ball milling), complexity of the necessary hardware and low productivity (PVD).

Surface modification of TiFe–based alloys was done by depositing palladium on the surface of the metal hydride material via electroless deposition and chemical vapour deposition.

4.2.1 Mechanism for hydrogen absorption through palladium surface–modified TiFe–based alloys

Solution–diffusion mechanism is one of the routes, through which hydrogen is diffused through Pd catalyst. The process starts when H_2 molecules in the gas phase surrounding the Pd surface–modified alloy are transported towards the gas layer flowing over the deposited Pd–based surface layer, driven by a pressure or concentration gradient. Dissociation of the H_2 molecules occurs at the surface of the Pd catalyst layer and then the resultant hydrogen atoms are chemisorbed to the Pd catalyst surface. The H atoms are highly soluble in the Pd catalyst and diffuse through the lattice by occupying the lowest energy face–centred cubic interstitial sites and forming Pd hydrides. The hydrogen atoms then diffuse through the lattice by "interstitial hopping" between octahedral sites via tetrahedral sites. H atoms arrive at the interface between the Pd layer and the surface of the alloy. The H atoms are then integrated into the metal matrix of TiFe–based alloy by chemical bonding to form a hydride.

However, when the Pd layer is not continuous where there is a dispersion of Pd catalyst particles on the surface of the TiFe–based alloy, hydrogen spillover may occur in combination with solution diffusion of hydrogen through the Pd layer. In hydrogen spillover, the hydrogen molecules are dissociated at the surface of the Pd catalyst particles to form hydrogen atoms which then spillover onto the surface of the metal hydride–forming alloy. Some of the dissociated hydrogen atoms remain attached to the Pd catalyst whilst others diffuse to the metal hydride–forming alloy, where they migrate to nearby catalytic sites or into the interstitial sites. This phenomenon is dependent on the catalyst loading, catalyst dispersion, active surface area of the catalyst as well as the interfacial contact area between the catalyst and the surface of the support material [158].

166

4.2.2 Surface–modification of TiFe–based alloy via electroless Pd deposition

Surface modification of TiFe–based alloys, by electroless deposition, was first done by deposition of Pd nuclei by sensitisation and activation in a Pd − Sn colloidal solution. The activated TiFe–based alloy was then accelerated to remove the Sn component using 10% Na_2EDTA, the material was then immersed in a Pd bath containing H_2PO_4 as a reducing agent. Pd then grows on the surface of the TiFe–based alloy, which forms a film covering the alloy. Figure 4.25 shows how Pd was deposited on TiFe–based alloys via electroless deposition.
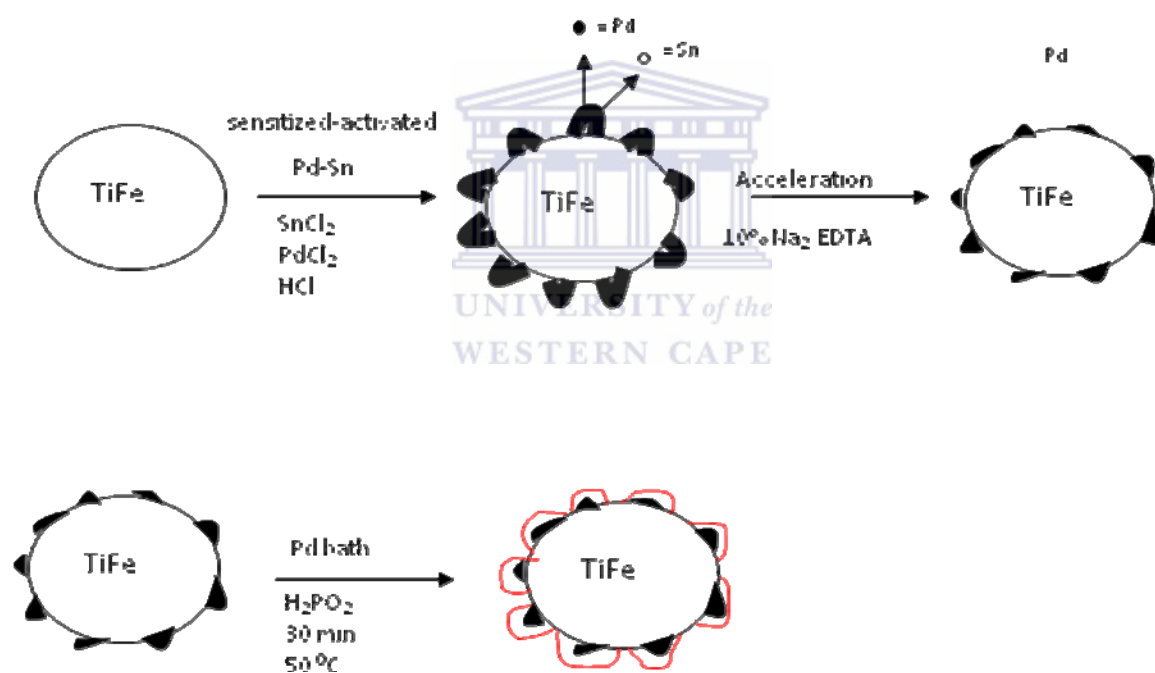
Figure 4.25: *Schematic diagram of electroless deposition method of Pd on TiFe–based material.*

4.2.2.1 Morphology and elemental composition of surface–modified TiFe–based metal hydride alloy

The morphological studies were carried out using HR–SEM due to smaller particle size of Pd, usually in the nano–range scale. Figure 4.26 and 4.27 illustrates SEM images of Pd surface–modified arc–melted and sintered TiFe–based alloys. It can be seen that the deposited Pd particles were somewhat spherical in appearance. The Pd coating on the surface of the TiFe–based alloys were found to be discontinuous. A denser dispersion of the Pd particles on the surface of the arc-melted TiFe alloy was observed upon deposition. The average Pd particle size was ~ 70 nm.
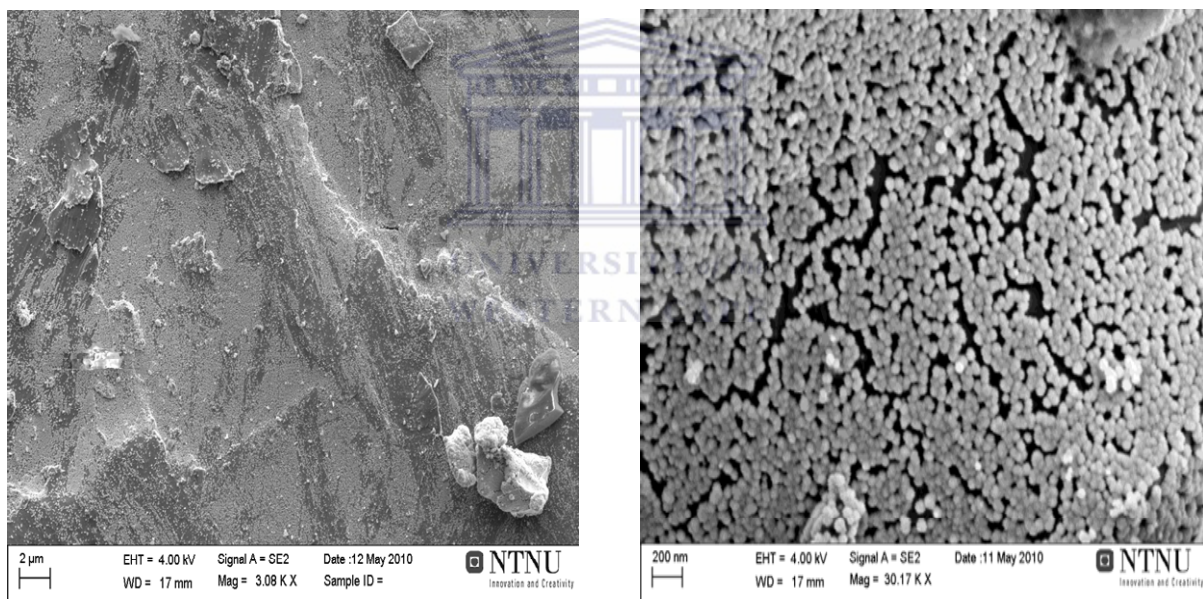
Figure 4.26: *SEM image of Pd surface – modified arc – melted TiFe*
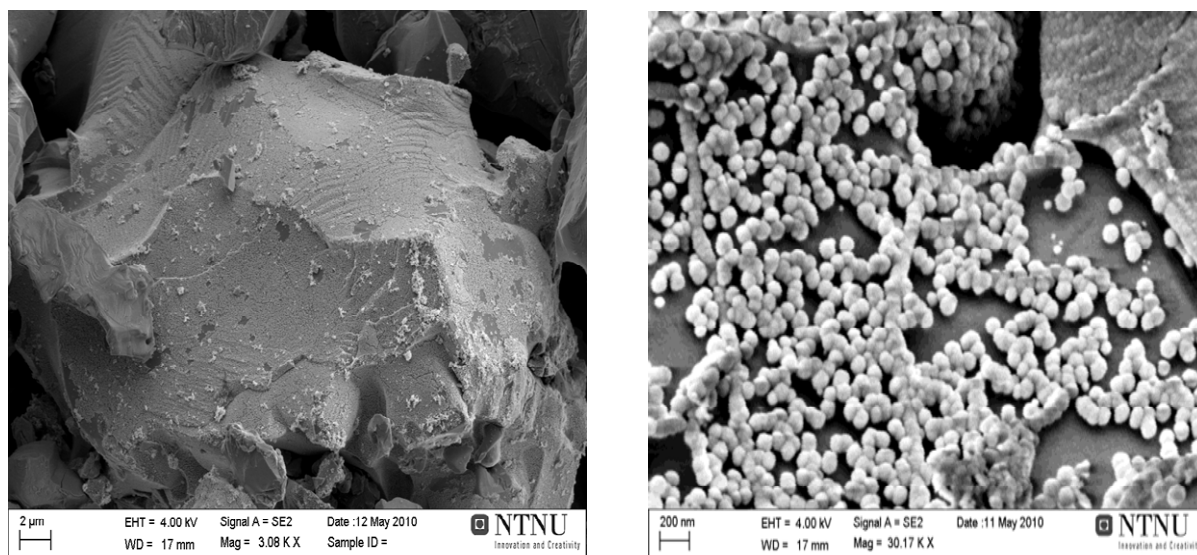
Figure 4.27: SEM image of Pd surface – modified sintered TiFe

The Pd loading on the surface – modified TiFe–based alloys was conducted by EDS. It was observed that the arc–melted sample had a higher Pd surface loading than that of the sintered sample, which was 15.47 wt. % and 12.23 wt. %, respectively.

Table 4.7: *EDS data for arc–melted and sintered TiFe alloys*

Elemental line	TiFe–Pd (arc–melt)		TiFe–Pd (sintered)	
	Wt%	At%	Wt%	At%
O K	-	-	2.52	9.05
Pd K	15.47	9.20	12.23	7.45
Ti K	42.77	50.18	44.29	52.36
Fe K	41.76	40.62	40.96	31.14
Total	100	100	100	100

Atomic absorption spectroscopy (AAS) was used to determine the total Pd loading and revealed Pd concentration of 0.61 wt% and 0.65 wt% for the sintered and arc – melted TiFe–based alloys. It was also observed from figure 4.26 that the Pd layer on the surface of the arc–melted sample formed a denser packing than the Pd layer on the sintered sample (figure 4.27). This observation indicates that significantly lower oxygen content at the surface of the arc–melted sample facilitates improved electroless deposition, which is in agreement with EDS and AAS results.

4.2.2.2 Hydrogen absorption kinetics of surface–modified TiFe–based alloys

Studies of the hydrogenation performances of Pd surface modified samples were conducted after pre–exposure of the sample materials to air, with and without pre–activation by vacuum heating. The hydrogenation kinetics of the surface–modified materials, carried out without activation by vacuum heating was significantly faster as compared to that of the unmodified material. The hydrogen absorption kinetics of the Pd surface–modified TiFe–based alloys are shown below in figure 4.28.

It is observed that both sintered and arc–melted materials absorbed hydrogen without activation, but there was the presence of an incubation period. The incubation period for the sintered sample was ~ 1hour and the incubation period for the arc–melted sample was ~ 6 hours. The reason why the sintered sample had a shorter incubation period is the synergetic effect between the surface Pd, suboxide η - $Ti_4Fe_2O_{1-x}$ and β – Ti, present in the sintered sample, which facilitates the diffusion of hydrogen to the bulk material. .After activation by heating to 400 ^{0}C under vacuum for 1 hour, both samples were fully activated. The improvement in the hydrogen absorption kinetics of the Pd surface–modified TiFe–based

alloys can be credited to the enhanced activity of the modified surface towards the H_2 dissociation, due to the presence of Pd nanoparticles catalyzing H_2 molecules splitting. Similarly, to the surface modified AB_5 type materials [159], it facilitates subsequent diffusion of H atoms into the bulk material and quick attainment of the maximum absorption capacity (curves 2 and 4).
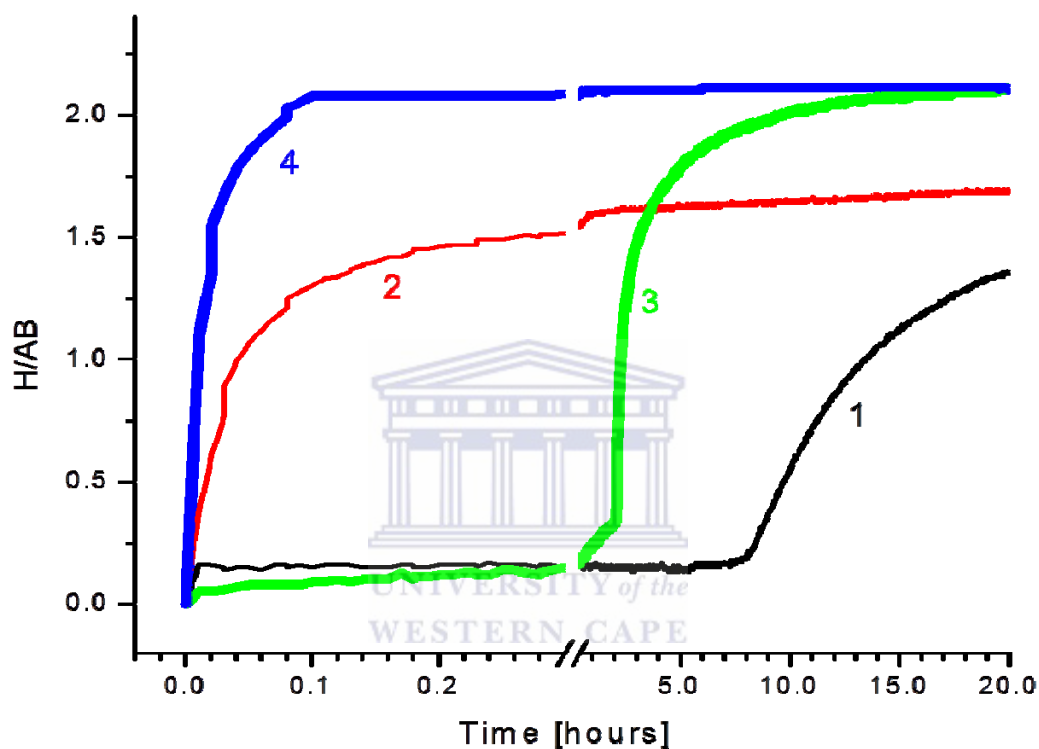
Figure 4.28: *Hydrogen absorption at P_0 = 30 bar and T=20°C for the surface modified arc – melted and sintered TiFe–based alloys. 1,2 – surface-modified arc-melted TiFe; 3,4 – surface-modified sintered TiFe; 1,3 – hydrogenation #1 (no vacuum heating); 2,4 – hydrogenation #2 after vacuum heating to 400 ^{0}C.*

4.2.3 Surface–modification of TiFe–based metal hydride alloys via chemical vapour deposition of Pd

The chemical vapour deposition of metal organic substances (MO CVD) was identified as a suitable alternative method for the deposition of catalytic layers on the surface of TiFe–based alloy. This technique is attractive due to simplicity, flexibility, ability to be scaled up to industrial-scale production with relative ease, and the wide range of precursors available. The technique involves the transportation of volatile precursor molecules (group-III metal-organics and group-V hydrides or alkyls) by a carrier gas (Ar, N_2) onto a heated substrate, where surface chemical reactions will occur to form thin layers of the metal. The MO CVD technique is also known to facilitate the deposition of small amounts of finely dispersed catalytic particles on the surface of substrate materials [160]. CVD of noble metals is achieved almost exclusively from metal-organic complexes (i.e. typically metal atoms with a number of alkyl ligands attached).

This section describes the improvement of activation performances and poisoning tolerance of TiFe hydrogen storage alloy, via surface modification by CVD technique using palladium (II) acetylacetonate (Pd[acac]$_2$ where acac=$C_5H_7O_2$), as the metal organic precursor. Pd[acac]$_2$ is a commercially available compound used as a catalyst in organic synthesis. It is known to demonstrate good volatility, suitable vapour pressure at moderate temperatures, adequate thermal stability, and a decomposition mechanism which is not known to produce species (chlorine and sulphurous fragments, etc.) which may give rise to catalytic surface poison of substrate materials [161]. Among a number of Palladium β-Diketonates, Pd[acac]$_2$ is characterised by the lowest thermal stability towards thermal decomposition which takes place in vacuum above 305–330 °C following radical mechanism [162].

4.2.3.1 Features of the chemical vapour deposition (CVD) process

The methodologies used for the deposition of Pd on the surface of TiFe – based alloys via CVD method are described in chapter 3. The deposition of Pd by means of CVD was done via two methods, viz. *ex-situ* and *in-situ* deposition. During *ex-situ* MO CVD, the output carrier gas was analysed using a QMS200 mass spectrometer.

The behaviour of the *ex-situ* MO CVD process was estimated from the data collected from the mass spectrometry analysis of the carrier gas exhausted from the reactor (Figure 4.29). Figure 4.29 and Table 4.8 present typical mass spectra taken before heating (1) and after ~2 hours of heating (2). The most intensive peaks (m/z=20, 40) correspond to argon to be the major component of the gas phase; the lighter isotopes (m/z=36, 38) present in the natural argon also produced peaks with noticeable intensities.
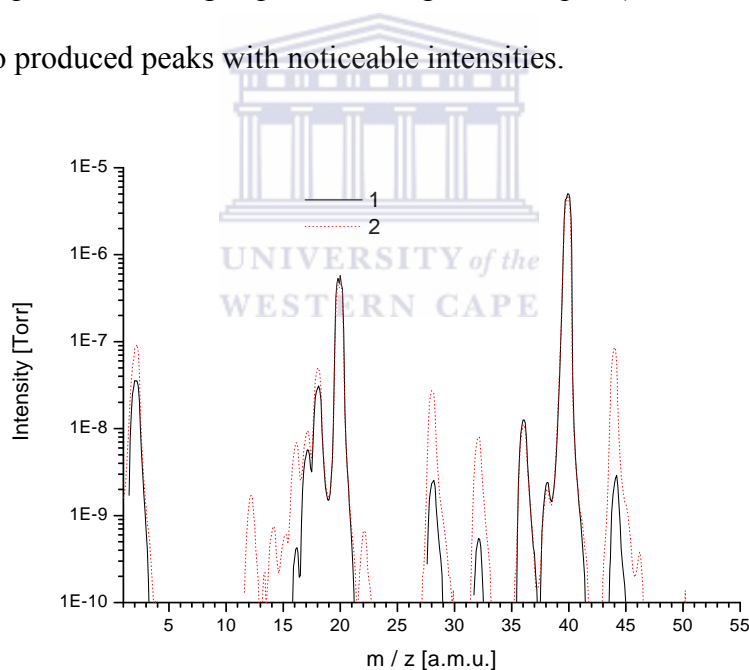
Figure 4.29: Mass spectrometry analysis of gas from running – flow reactor during MO CVD of Pd (5 wt.%) onto TiFe alloy by thermal decomposition of Pd[acac]$_2$. Flow rate of the carrier gas 0.5 L/min. Mass spectra of the gas before heating (1) and after (2). 3 hours of heating (2; T = 402 ^{0}C).

Table 4.8: *Mass spectra of the gas from running-flow reactor during the MO CVD process (Figure 4.29)*

m/z	Before heating (curve 1)		During heating (curve 2)	
	Intensity [Torr]	Assumed components	Intensity [Torr]	Assumed components
2	$3.55 \cdot 10^{-8}$	$(H_2)^+$	$9.25 \cdot 10^{-8}$	$(H_2)^+$
12	-	-	$1.7 \cdot 10^{-9}$	$(C)^+$
13	-	-	$2.1 \cdot 10^{-10}$	$(CH)^+$
14	-	-	$7.49 \cdot 10^{-10}$	$(CH_2)^+$
15	-	-	$6.02 \cdot 10^{-10}$	$(CH_3)^+$
16	$4.28 \cdot 10^{-10}$	$(CH_4)^+, (O)^+$	$6.9 \cdot 10^{-9}$	$(CH_4)^+, (O)^+$
17	$5.7 \cdot 10^{-9}$	$(OH)^+$	$9.48 \cdot 10^{-9}$	$(OH)^+$
18	$3.1 \cdot 10^{-8}$	$(H_2O)^+$	$5 \cdot 10^{-8}$	$(H_2O)^+$
20	$5.75 \cdot 10^{-7}$	$(Ar)^{2+}$	$5.05 \cdot 10^{-7}$	$(Ar)^{2+}$
28	$2.54 \cdot 10^{-9}$	$(N_2)^+$	$2.75 \cdot 10^{-8}$	$(CO)^+, (N_2)^+$
29	-	-	$8.98 \cdot 10^{-10}$	(C_2H_5)
32	$5.47 \cdot 10^{-10}$	$(O_2)^+$	$8.05 \cdot 10^{-9}$	$(O_2)^+$
36	$1.26 \cdot 10^{-8}$	$(^{36}Ar)^+$	$1.11 \cdot 10^{-8}$	$(^{36}Ar)^+$
38	$2.41 \cdot 10^{-9}$	$(^{38}Ar)^+$	$2.01 \cdot 10^{-9}$	$(^{38}Ar)^+$
40	$5.01 \cdot 10^{-6}$	$(Ar)^+$	$4.81 \cdot 10^{-6}$	$(Ar)^+$
44	$2.89 \cdot 10^{-9}$	$(CO_2)^+$	$8.61 \cdot 10^{-8}$	$(CO_2)^+$
45	-	-	$1.39 \cdot 10^{-9}$	$(HCO_2)^+$
46	-	-	$3.38 \cdot 10^{-10}$	$(^{14}CO_2)^+$

The main impurities found in the carrier gas before starting the MO CVD process include water vapours (m/z=17,18), as well as minor amounts of carbon dioxide (m/z=44), nitrogen (m/z=28), oxygen (m/z=32) and hydrogen (m/z=2). The sensitivity of the mass spectrometer on hydrogen was determined to be 40–60 times higher than on other gaseous components. The close values of intensities of peaks m/z=16, 32 allow us to assume the presence of trace amounts of methane contributing to the former peak. During the MO CVD process the mass spectrum changes significantly exhibiting appearance of CO_2 (m/z=44; estimated concentration in the mixture up to 3%), CO (m/z=28; up to 0.4%), O_2 (m/z=32; up to 0.2%) and a number of light ions (see Table 4.8) to be fragments of the organic species formed during decomposition of Pd[acac]$_2$. In the absence of a nitrogen source, the increase of intensity of peak m/z=28 during MO CVD was ascribed to CO. Slight increase of intensities of peaks corresponding to hydrogen and water vapours was observed as well. No peaks with intensities above background ($\sim 10^{-10}$ Torr) were observed in the range of m/z=50–200.

Figure 4.30 below presents time dependencies of the intensities of main impurity peaks during the MO CVD; the process temperature (T) is plotted as well. It can be seen that the intensities of the peaks (m/z=44,28,16,32,12) initially follow the temperature increase with the delay of about 0.5 hours, gradually decrease after reaching maxima for ~1 hour, and quickly fall to the background values in 2.5–3 hours after initiation of the process. Interestingly, the increase of intensity of the hydrogen peak (m/z=2) was observed during the last step.

The presence of significant amounts of CO_2, CO and O_2 impurities, together with carbonaceous species, in the gas phase contacting with the TiFe substrate heated up to ~400 °C may affect the surface of the intermetallide and thus influence on its hydrogen sorption performances.
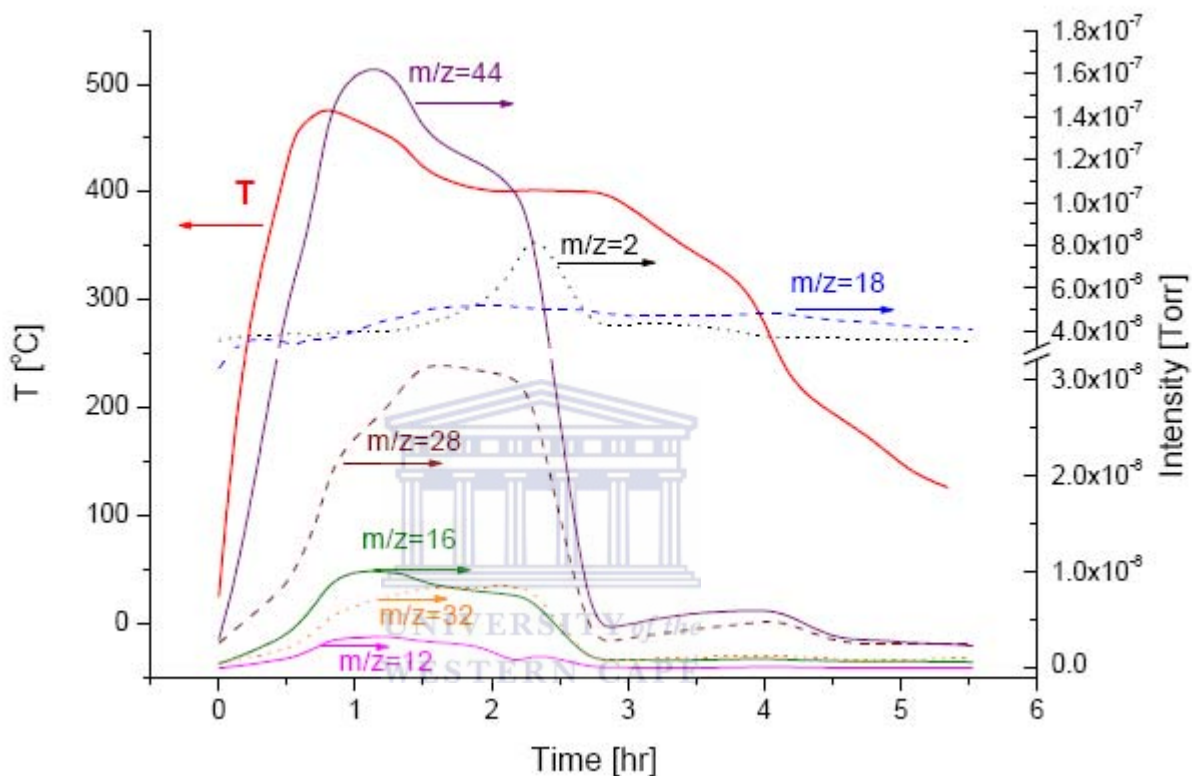
Figure 4.30: *Mass spectrometry analysis of gas from running–flow reactor during MO CVD of Pd (5 wt. %) on o TiFe alloy by thermal decomposition of Pd[acac]$_2$. Flow rate of the carrier gas 0.5 L/min. Change of reactor temperature (T) and intensities of main impurity peaks during the MO CVD process.*

4.2.3.2 Morphological and phase–structural features of TiFe–based alloys after chemical vapour deposition (CVD)

Figure 4.31 presents SEM images of the TiFe samples after surface modification by MO CVD (*ex-situ* procedure). It can be seen that Pd loading significantly influences the coating morphology. For the sample loaded with 0.5% Pd, the uniform but discontinuous deposition of near-spherical Pd particles, approximately 20 to 50 nm in diameter, was observed on the surface of the substrate. The sample with 1% Pd loading exhibits denser coating formed by agglomerated Pd particles of a smaller size. Finally, the sample with 5% Pd loading had significantly different morphology: in addition to Pd coating of the substrate particles, a porous structure formed by separate Pd agglomerates (Figure 4.31, bottom left). The Pd covering of the substrate is very dense and multilayered; some "pinholes", most probably, formed by the release of gaseous $Pd[acac]_2$ decomposition products through already formed continuous Pd coating, can be observed as well (Figure 4.31, bottom right).

177

0.5 wt.% Pd

1 wt.% Pd

5 wt.% Pd
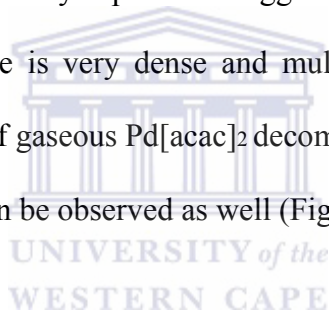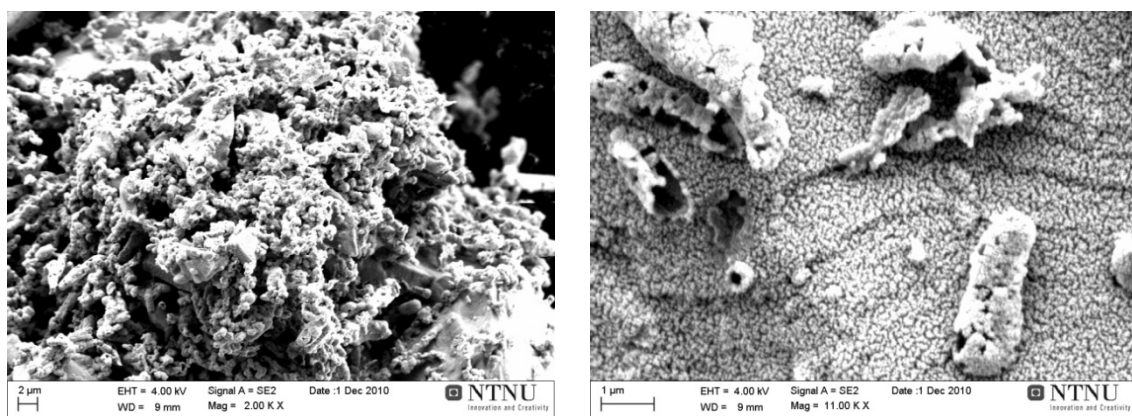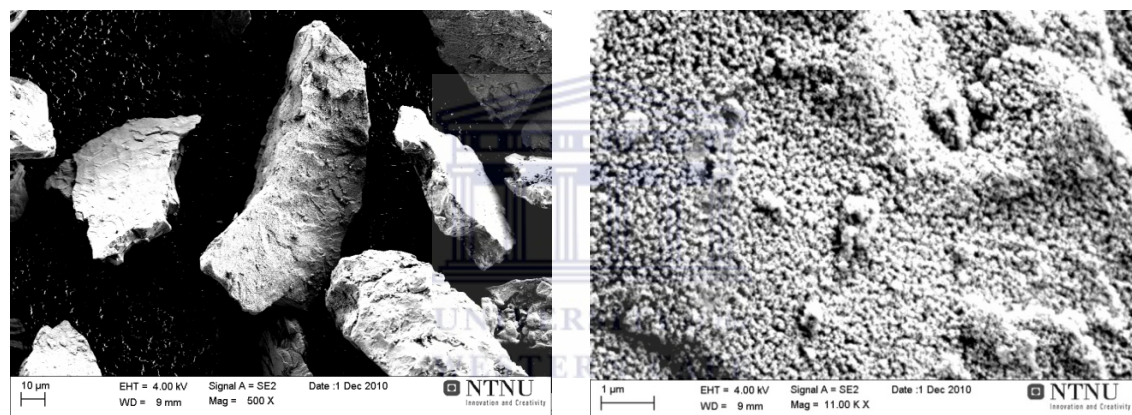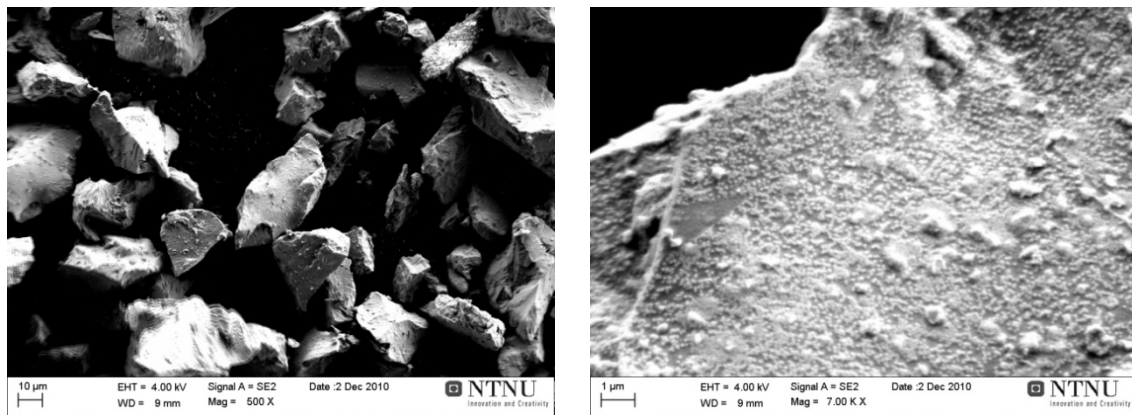
Figure 4.31: *Low- (left) and high-(right) magnification SEM images of TiFe-modified by the CVD deposition of Pd*

The XRD pattern of the unmodified TiFe and the alloy surface modified by ex-situ MO CVD are shown in Figure 4.32, and results of the refinement are presented in Table 4.8. The parent alloy (Figure 4.32 a) contains single TiFe phase whose lattice period corresponds well to literature data [146]. The alloy modified by 0.5 wt. % Pd (Figure 4.32 b) exhibits a value close to the lattice period of the unmodified TiFe; no Pd phase was detected in this. A weak peak at $2\theta = 40.5^0$ corresponding to reflection from (111) plane of Pd appears for the alloy modified by 1 wt.% Pd (Figure 4.32 c); in this sample TiFe phase has the lattice period about 0.4% higher than one for the unmodified alloy, and the pattern exhibits significant overestimation (~3x) of the calculated intensity of the (200) peak. In the sample with 5 wt. % Pd (Figure 4.32 d), the broad peaks of the Pd phase are clearly observed; the Pd crystalline size estimated from the lines broading was about 9.6 nm. The non-indexed peak at 33.9^0 for this sample (circled) may belong to the residual Pd[acac]2 [163]. The lattice period of the major TiFe phase is similar to that for the unmodified alloy.
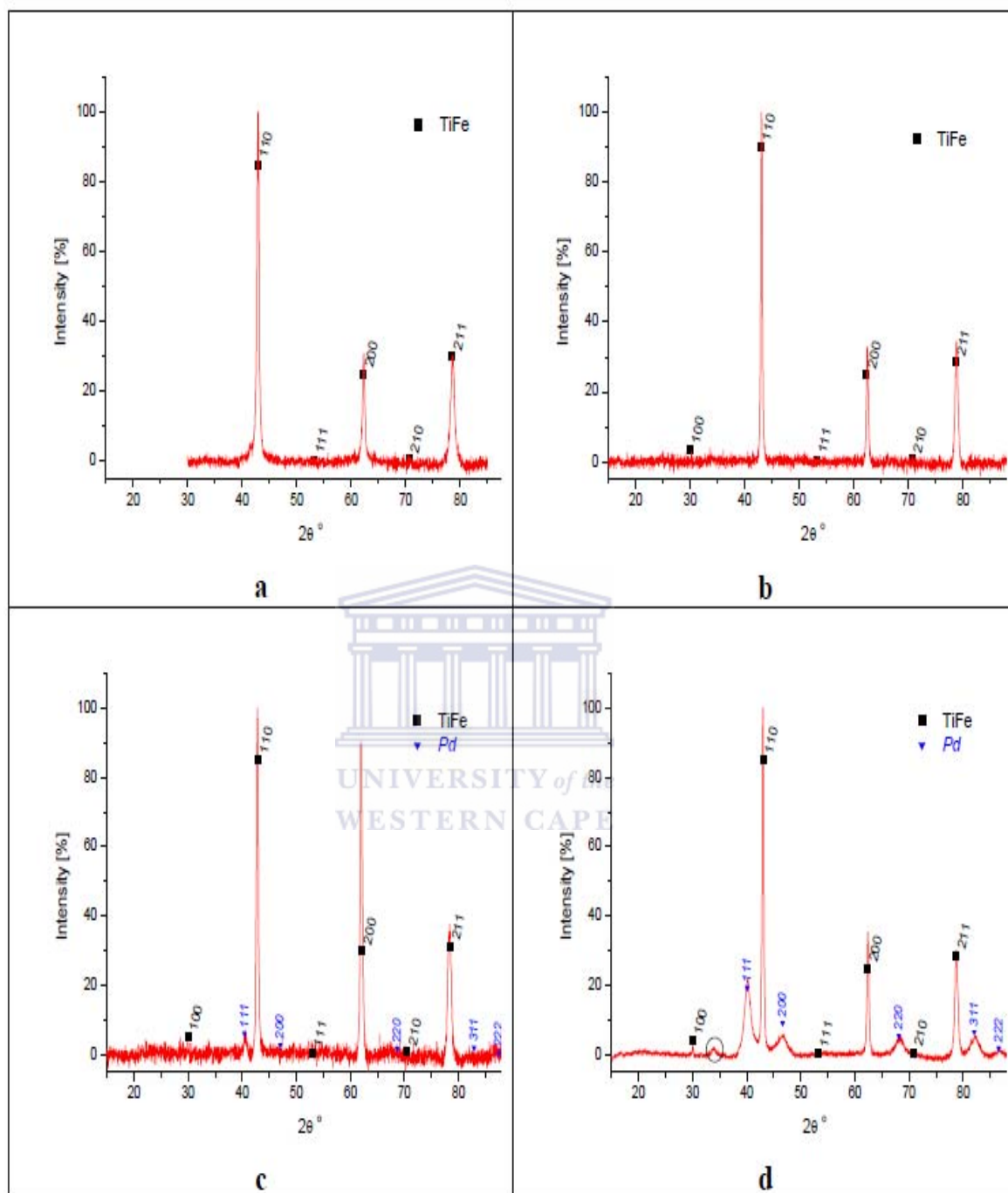
Figure 4.32: *The XRD pattern of unmodified TiFe (a) and TiFe modified by ex-situ CVD deposition of 0.5 wt.% (b), 1 wt.% (c), and 5 wt.% (d) of Pd.*

Table 4.9: *Results of refinement of the XRD data* (Figure 4.32)*

Sample	TiFe: a [Å]	Pd: a [Å]
Unmodified alloy	2.9760(5)	–
0.5 wt.% Pd	2.9709(9)	–
1 wt.% Pd	2.988(2)	3.851
5 wt.% Pd	2.9737(4)	3.881(2)

* Reference data:

TiFe: Space group $Pm\bar{3}m$ (221); $a = 2.976$ Å [158]

Pd: Space group $Fm\bar{3}m$ (225); $a = 3.9031$ Å [160]
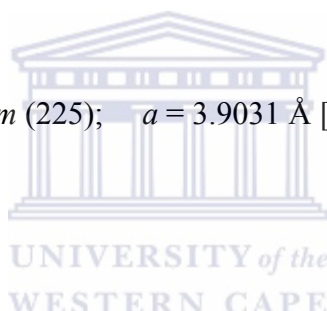
4.2.3.3 Hydrogen absorption kinetics of Pd MO CVD modified TiFe–based alloy

Figure 4.33 shows dynamics of hydrogen absorption by the unmodified TiFe alloy (A) and the material after *ex-situ* MO CVD (B–D). Without activation by vacuum heating, the unmodified TiFe (Figure 4.33A, curve 1) does not absorb noticeable amounts of hydrogen in 24 hours, and two cycles of activation by vacuum heating to 400 ^{0}C followed by H$_2$ absorption at room temperature (curves 2, 3) are necessary to achieve fast and reproducible hydrogenation. 10 minute exposure to air results in almost complete suppression of hydrogen absorption in the unmodified alloy (curve 4).

In contrast, all the surface modified materials (Figure 4.33 B–D, curve 1) do absorb hydrogen without vacuum heating, although with the observation of an incubation period varying from 2 to 5 hours. The incubation period is shorter for the samples possessing lower Pd loadings. After vacuum heating, the surface modified samples (Figure 4.33 B–D, curve 2) exhibit fast and reproducible (as compared to next vacuum heating–hydrogenation cycles) hydrogen absorption performances. However, the hydrogenation rates are slower than for fully activated unmodified TiFe. The maximum hydrogen absorption capacities for the surface modified alloys were found to be lower than that for the unmodified TiFe (H/TiFe=1.9), corresponding to the values H/TiFe=1.84, 1.3 and 1.34 for Pd loading of 0.5, 1 and 5 wt. %, respectively. After exposure to air, the surface modified samples did not lose their ability to absorb hydrogen, exhibiting somewhat slower absorption rates than those for the activated materials and lower hydrogen absorption capacities attained in 24 hours (H/TiFe=1.4, 1.21 and 1.34 for Pd loading of 0.5, 1 and 5 wt.%, respectively). The tendency of improving the hydrogenation dynamics with the increase of Pd loading was observed as well.

Figure 4.34 given below illustrates the hydrogenation behaviour of the materials (0.5 and 1 wt. % Pd) after *in-situ* MO CVD. The first hydrogenation of the samples (curves 1, 3) is slower than one for the activated samples prepared using *ex-situ* procedure (Figure 4.33 B,C; curve 2). After exposure to air (curves 2, 4), the samples exhibit hydrogenation behaviour similar to that for the *ex-situ* prepared samples (Figure 4.33 B,C; curve 3) with slightly longer incubation periods, but significantly higher maximum hydrogen absorption capacities, H/TiFe=2.0 for 0.5 wt.% Pd and H/TiFe=1.8 for 1 wt.% Pd.
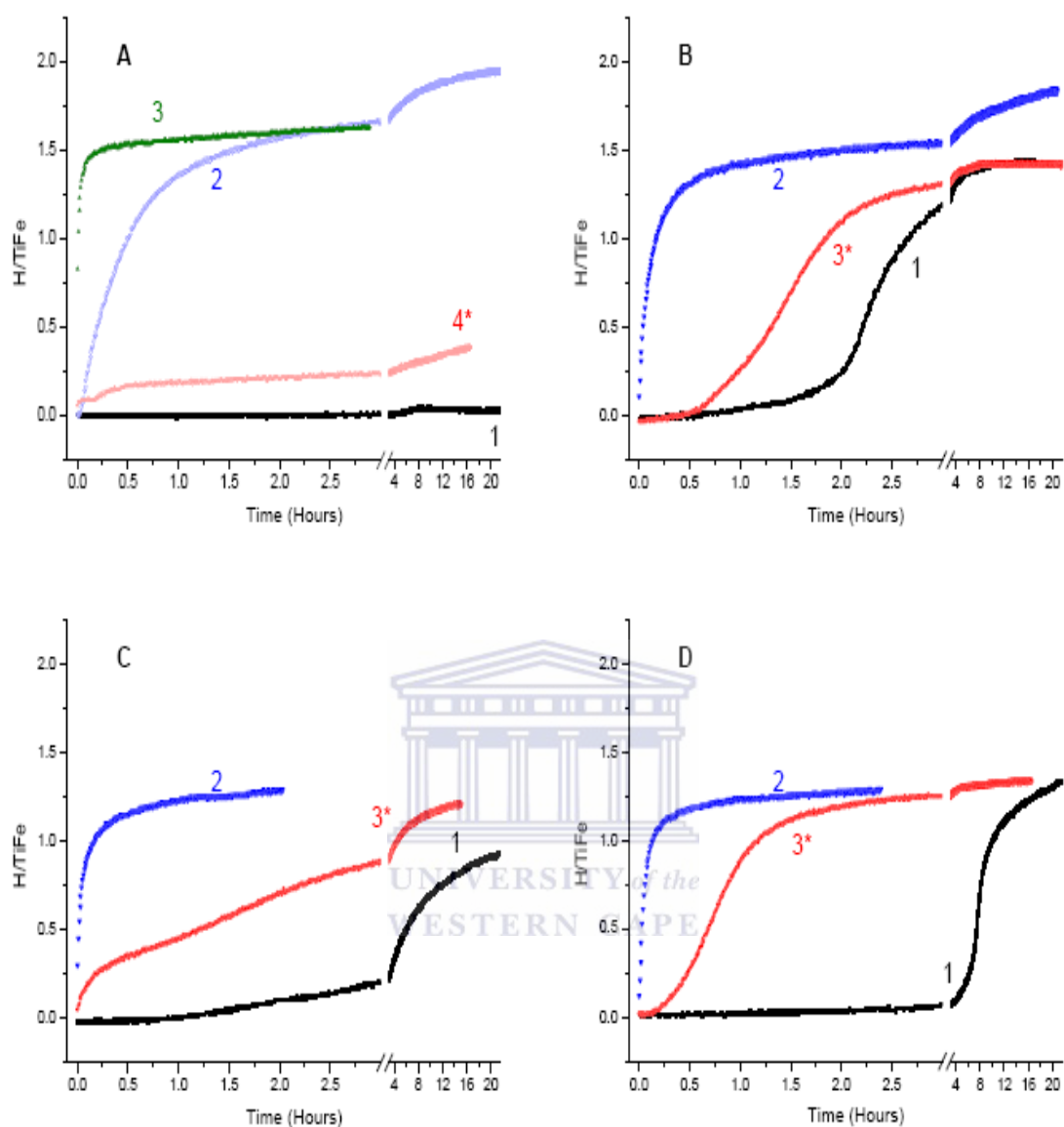
Figure 4.33: *Dynamics of hydrogen absorption (T=20 ⁰C, P_{H2}=30 bar) by the unmodified TiFe alloy (A) and the alloy surface-modified by ex-situ MO CVD of Pd: 0.5 wt.% (B), 1 wt.% (C) and 5 wt.% (D). Curve labelling corresponds to number of H_2 absorption cycle after 1 hour evacuation of the sample heated to T=400 ⁰C (cycle # 1 was carried out without heating). Curve labels marked by asterisk (*) correspond to hydrogen absorption after 10 minutes long exposure of the sample to air at T=20 ⁰C.*
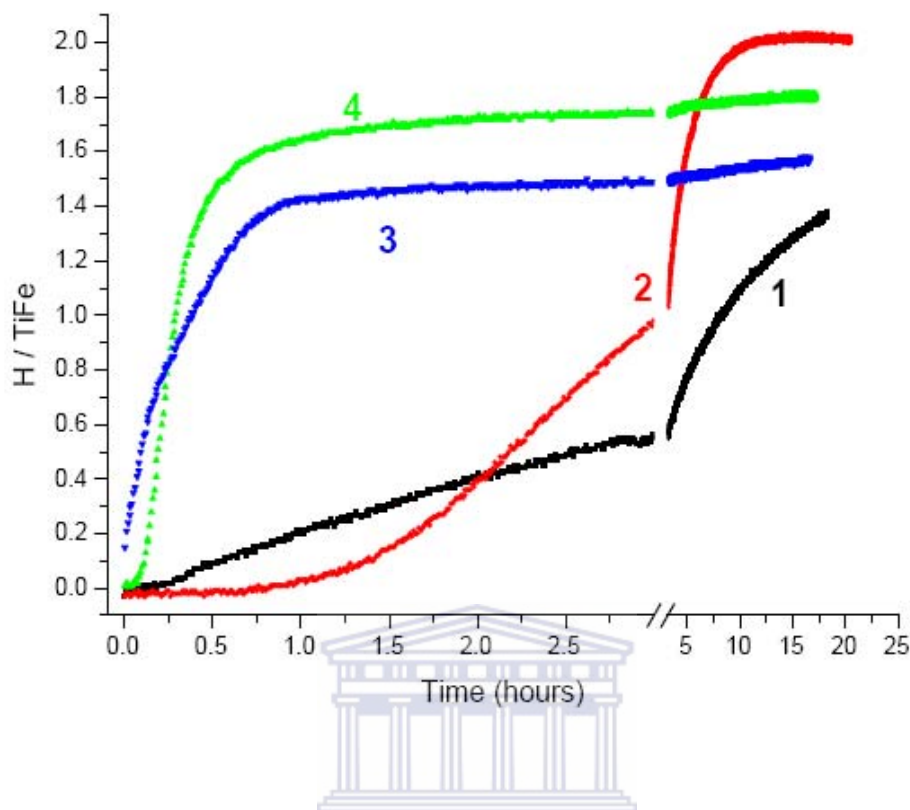
Figure 4.34: *The dynamics of hydrogen absorption (T=20 ºC, P$_{H2}$=30 bar) by TiFe alloy surface modified by in-situ MO CVD of Pd: 0.5 wt. % (1,2) and 1 wt.% (3,4). 1, 3 – first H$_2$ absorption after 3 hour evacuation of the sample heated to T=400 ºC; 2,4 – second H$_2$ absorption after 1 hour evacuation of the sample at T=400 ºC followed by exposure to air at T=20 ºC.*

MO CVD of rather small quantities (0.5–1 wt.%) of Pd onto TiFe substrate can be considered as an efficient method in improving activation performances and poisoning tolerance of TiFe. Some issues, however, should be taken into account in the course of the implementation of this route.

As can be seen from the results of mass spectrometry analysis (Figure 4.29 and 4.30, Table 4.8), the decomposition of Pd[acac]$_2$ at T~400 ºC is accompanied by a significant release of carbon– and oxygen– containing species into gas phase. These species may be

184

chemisorbed on the surface of TiFe followed by the diffusion of oxygen and carbon atoms into the bulk material. A similar mechanism is recognised to be responsible for the activation of TiFe, by the dissolution of the surface oxides in the bulk alloy at T~400 °C [151].

As it was shown by Lee and Perng [165], the dissolution of small amounts (0.1 at.%) of boron and carbon in TiFe results in the suppression of the formation of the $TiFeH_2$ phase. It was associated with the appearance of significant local deformations randomly distributed in the metal matrix, due to the formation of interstitial solid solution of boron (atomic radius, R_B=0.795 Å) and carbon (R_C=0.77 Å). In turn, this results in the increase of pressure and slope of the plateaux corresponding to the formation of the hydride phases, as well as in their shortening.

Most probably, similar effects take place in our case. The dissolution of carbon and oxygen (R_O=0.73 Å) in TiFe may be an origin of the reduction of hydrogen absorption capacity of the material, especially at higher Pd loadings (≥1 wt.%), corresponding to higher amounts of the metal-organic precursor. It also can indirectly contribute in the distortion of intensities in the XRD pattern (Figure 4.32).

The effect of the interaction of the volatile products formed during $Pd[acac]_2$ decomposition with TiFe will be less pronounced in a vacuum when these species have longer free path, and the probability of their reaction with the substrate surface will be lower. As a result, the *in-situ* prepared samples have higher hydrogen absorption capacities than *ex-situ* ones approaching, in the case of the sample with 0.5 wt. % Pd, to the capacity of the substrate material.

The improvement of activation performances and poisoning tolerance of TiFe after MO CVD of Pd was associated with improved catalytic activity of the modified surface, covered with Pd nanoparticles, towards the H_2 dissociation.

4.2.4 Chemical vapour deposition of carbon nanotubes (CNTs) deposited on TiFe–base alloys followed by electroless Pd plating

In literature there are several different techniques (laser ablation, arc–discharge and chemical vapour deposition) that can be used for surface modification of metal catalysts [166], but due to the availability of materials for experimental set–up, ease of set–up, production of high quality and purity of carbon nanotubes on substrates compared to other techniques, we adopted the chemical vapour deposition (CVD) for the synthesis of carbon nanotubes. The synthesis of CNTs by CVD method involves the catalytic decomposition of a carbon precursor (e.g. hydrocarbons) on transition metal catalyst like Ti, Co, Ni or Fe.

Carbon nanotubes have been found to possess a wide diversity of extremely remarkable properties most notably high electrical and thermal conductivity, mechanical strength and catalytic surface area. The primary objective is to use carbon nanotubes as scaffolds for the alloy, adding specific surface moieties to enhance hydrogen storage properties of the material. Carbon nanotubes are well recognised absorbents of gases due to their comparatively high surface area.

In this study, carbon nanotubes were deposited directly on the surface of the TiFe-based alloy using chemical vapour deposition method. This was then followed by the deposition of Pd on the CNTs by electroless deposition.

4.2.4.1 Morphological and Phase–structural features

The SEM images of the modified TiFe–based alloys with carbon nanotubes and Pd are shown in figures 4.35 and 4.36, respectively. The SEM images illustrate that the carbon nanotubes were deposited on the TiFe–based alloys and is covering the surface of the alloy. This will assist in the TiFe–based alloys not to oxidise easily due to the carbon layer on the

186

surface of the alloy. The diameter of the carbon nanotubes is ~ 33.13 nm. Figure 4.35 given below shows CNTs deposited on the surface of the TiFe–based alloy and figure 4.36 (B) shows that after electroless deposition, Pd was deposited on the CNTs and on the alloy surface.
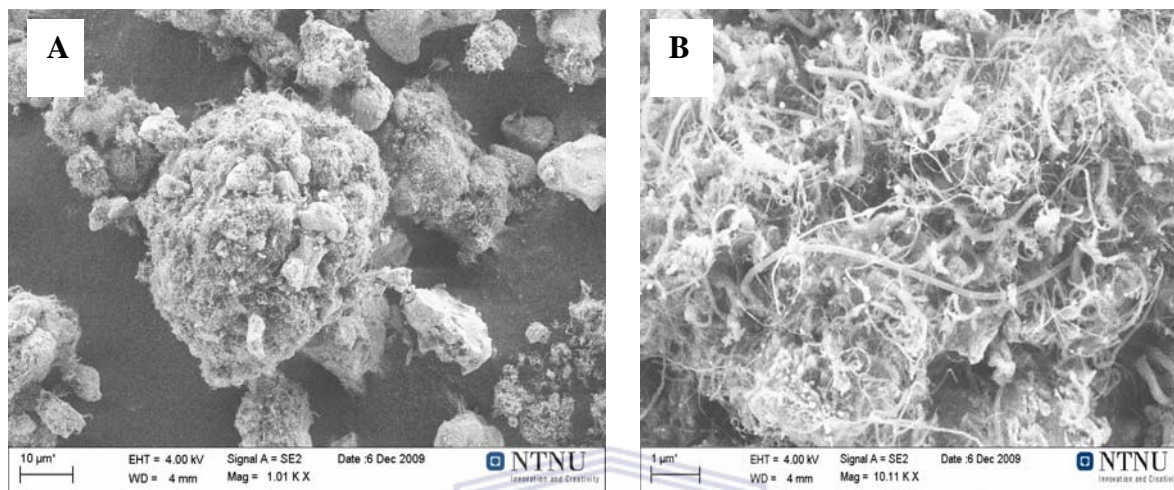
Figure 4.35: *Carbon nanotubes deposited on TiFe–based alloy via CVD method; (A) low magnification, (B) high magnification*
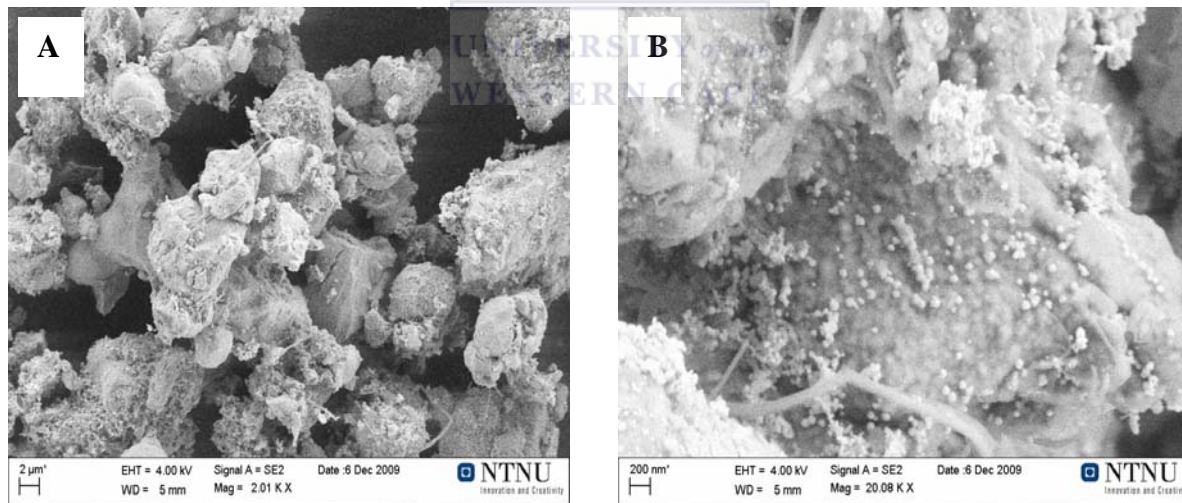
Figure 4.36: *Carbon nanotubes deposited on TiFe–based alloy via CVD method and Pd deposition by electroless deposition; (A) low magnification, (B) high magnification*

The XRD pattern of TiFe after deposition of CNT is shown in figure 4.37.
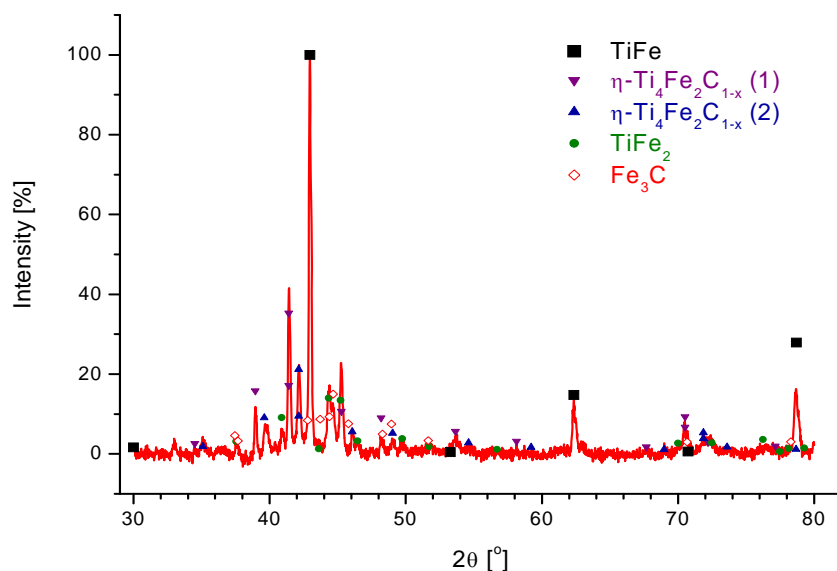
Figure 4.37: *The indexed XRD pattern of TiFe after deposition of CNT*

The TiFe intermetallic phase was found to be significantly contaminated: the best refinement was obtained when assuming presence of two main impurities, η-phases (similar to $Ti_4Fe_2O_{1-x}$ suboxide) whose abundances are related as 1.5:1 and lattice periods are equal to 11.332 and 11.146 Å, respectively. In addition, the sample contains minor amount of $TiFe_2$ and traces of iron carbide, Fe_3C, space group *Pnma* (#62); lattice periods a = 5.108 Å, b = 6.777 Å, c = 4.540 Å [167]. Most probably, the CNT deposition was accompanied by a noticeable diffusion of carbon atoms into TiFe lattice to form the observed phases.

4.2.4.2 Hydrogen absorption performances

The hydrogen absorption performances of TiFe–based alloy modified by CVD deposition of CNTs and electroless deposition of Pd are shown in figure 4.38. It illustrates that after the

deposition of CNTs on the surface of TiFe, the hydrogen capacity was drastically reduced. The hydrogen capacity for the TiFe modified with CNTs is 0.33 wt. % and the TiFe modified with CNTs and Pd is 0.36 wt. %. The decrease in the hydrogen storage capacity of the CNTs surface modified TiFe–based alloy was, most probably, caused by its contamination with carbon resulting in the appearance of mixed Ti–Fe carbides (see XRD results above) and corresponding decrease of the abundance of TiFe intermetallic phase (down to 30–50% according our estimations based on the XRD data). An additional reason for the decrease of the hydrogen storage capacity may be in the suppression of the formation of TiFeH$_2$ due to carbon contamination, similar to our results on study of TiFe surface-modified by CVD via thermal decomposition of Pd[acac]$_2$ (see section 4.3.3.)
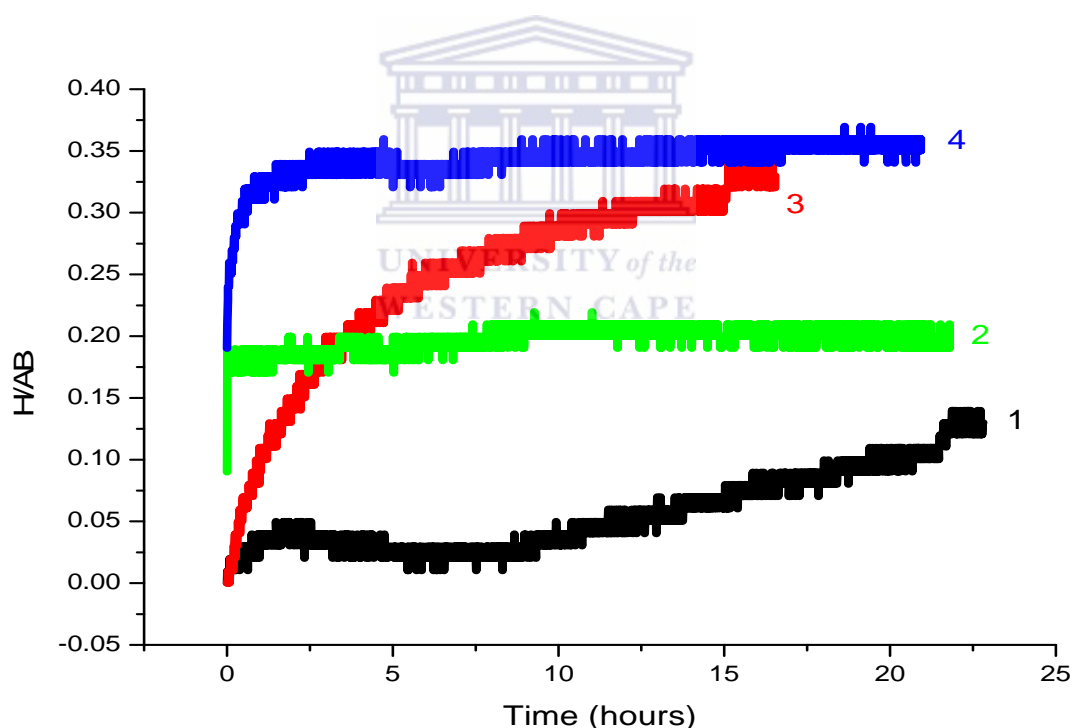
Figure 4.38: Dynamics of hydrogen absorption (T=20 $^{\circ}$C, P$_{H2}$=30 bar) by TiFe alloy surface modified by CVD of CNTs: (1,3) and TiFe alloy surface modified by CVD of CNTs and electroless deposition of Pd:.(2,4). Curves 1, 2 – first H$_2$ absorption without vacuum heating; Curves 3,4 – second H$_2$ absorption after 1 hour evacuation of the sample at T=400 $^{\circ}$C.

4.3   Summary of TiFe–based metal hydride alloys

- Sintering of Ti and Fe powder mixtures (1.1:0.9) yielded a formation of $Ti_4Fe_2O_{1-x}$, further to TiFe. The sintered $Ti_{1.1}Fe_{0.9}O_x$ was characterised by a better activation and kinetic performances as compared to the arc–melted TiFe. The effect was associated with the influence of the formed hydrogen transfer catalyst, viz. oxygen containing $Ti_4Fe_2O_{1-x}$ and β-Ti.

- The addition of oxygen (0.1, 0.2, 0.5, 1wt. %) to TiFe has shown that the hydrogen capacities decrease with increasing oxygen content. This was due to the increase of oxygen content in the alloy that results in the decrease of the abundance of main TiFe phase, together with the increase in the abundance of $Ti_4Fe_2O_{1-x}$, and, to a lesser extent, $TiFe_2$.

- The synthesis of TiFe–based materials via induction melting using alumo-silica and graphite crucibles has shown that in both cases, the target material is contaminated, but much more pronounced for the alumo–silica crucible. It appears that, in this case, significant contamination of the sample by oxygen additionally introduced from the crucible material took place.

- The synthesis of TiFe via the reduction of ilmenite ($FeTiO_3$) was achieved by a two–step process, which was gas–phase reduction to yield a mixture of TiO_2 and Fe metal, which was then followed by metal–thermic reduction using CaH_2 as a reducing agent to TiFe. The hydrogen absorption capacity of the as prepared TiFe from reduction of ilmenite ($FeTiO_3$), was about 0.5 wt. % H. This low hydrogen capacity is due to the impurities η-Ti_4Fe_2O and $TiFe_2$ within the reduced sample.

- The surface modification of the TiFe-based materials by electroless deposition of Pd results in the formation of discontinuous surface deposits of Pd nanoparticles, causing significant improvement of the activation performances and hydrogen absorption kinetics, despite a long-term exposure of the initial samples to air. The effect was associated with improved catalytic activity of the modified surface towards the H_2 dissociation.

- Surface modification of TiFe alloy by MO CVD of Pd using Pd[acac]$_2$ as a precursor results in the formation of coatings constituted by Pd nanoparticles which facilitate the hydrogenation ability of the material even after its exposure to air. The effect was associated with improved catalytic activity of the modified surface towards the H_2 dissociation.

- The hydrogenation performances of the surface modified TiFe were found to be quite sensitive to MO CVD conditions that, most probably, originate from the side process of the interaction of gaseous products of Pd[acac]$_2$ decomposition with TiFe.

- The deposition of carbon nanotubes on the surface of TiFe via chemical vapour deposition was successful. The carbon nanotubes covered the surface of the alloy. However, the hydrogen absorption capacity was considerably reduced due to contamination of TiFe with carbon.
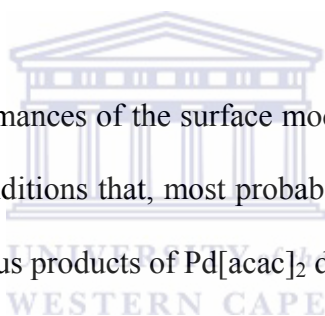
4.4 AB$_2$ –type hydride forming materials on the basis of Ti

The reduction of ilmenite via gas–phase and metal–thermic reduction to synthesize TiFe–based alloy (Section 4.1.8) was shown to be a very useful method for the preparation of Ti–based metal hydride materials. However, the target TiFe alloy had low reversible hydrogen storage capacity, and this was due to the formation of Ti_4Fe_2O + $TiFe_2$ mixture present within the target material. To address this problem, it is preferable to carry out alloying of the primary TiFe with additional metal components, to yield an AB$_2$–type hydrogen storage alloy.

The target AB$_2$-type alloy can be prepared by alloying of the primary TiFe with zirconium; and a transition metal, e.g. chromium, manganese, nickel, etc. In doing so, the kinds and amounts of the alloying components will greatly influence on the thermal stability of the corresponding AB$_2$-type hydride. To match the thermodynamic properties of the material with application requirements, we developed a simple empirical model allowing us to identify composition of the target AB$_2$-type alloy.

4.4.1 Analysis of hydrogen sorption performances of multi-component (Ti,Zr)(Fe,Mn,Cr,Ni)$_{2\pm x}$ intermetallides

Numerous data on hydrogen sorption performances of AB$_2$-type hydrogen storage materials (where A = Ti, Zr; B = Cr, Mn, Fe, Ni, Cu, V) were published since late 1970s. To reveal the interrelationship between composition of the material and thermodynamic performances of the corresponding hydride, we made a regression analysis of the relevant literature data about AB$_{2\pm x}$ intermetallic alloys of 87 different compositions (139 records in total).

The reference data presented in Appendix (Table A1) were fitted using the simplest linear regression according to the formula:

$$Y = Y_0 + \sum_{i=1}^{n} A_i X_i \qquad \textbf{4.12}$$

Seven independent fitting variables $X_1 \ldots X_7$ are listed in Table 4.10. Among them, one variable (X_1) represents atomic fractions of the A-components (Ti and Zr), and five others ($X_2 \ldots X_6$) − atomic fractions of the B-components (Fe, Cr, Mn, Ni, Cu, V). The variable X_7 represents deviation of the intermetallide composition from AB_2 stoichiometry.

Table 4.10: *Fitting variables for the regression analysis of composition dependence of thermodynamic properties of AB_2-type intermetallides*

i	Notation	Description	Variation range
1	$X_1 = X_{Zr}$	Atomic fraction of Zr in A-component	0…1
2	$X_2 = X_{Cr}$	Atomic fraction of Cr in B-component	0…1
3	$X_3 = X_{Mn}$	Atomic fraction of Mn in B-component	0…1
4	$X_4 = X_{Ni}$	Atomic fraction of Ni in B-component	0…0.4
5	$X_5 = X_{Cu}$	Atomic fraction of Cu in B-component	0…0.3
6	$X_4 = X_{V}$	Atomic fraction of V in B-component	0…1
7	$X_7 = (B/A - 2)$	Deviation from AB_2 stoichiometry	−0.5…+1.8

In doing so, the variable set $X_1=X_2=\ldots=X_6=X_7=0$ corresponds to the composition TiFe$_2$, non-zero value of X_1 describes substitution of Ti with Zr ($X_{Ti}=1-X_1$), and non-zero values of $X_2\ldots X_6$ correspond to Fe substitution with Cr, Mn, Ni, Cu and V, respectively $\left(X_{Fe} = 1 - \sum_{i=2}^{6} X_i \right)$ The meaning of the regression coefficients, A_i, is the change of a response function, Y, with the increment of the ith composition parameter from 0 to 1. The regression coefficient Y_0 in eqn 4.12 presents the calculated response function for TiFe$_2$ intermetallide.

The fitted values of regression coefficients in eqn 4.12, A_i, assuming response function, Y, as hydrogenation enthalpy, entropy, or logarithms of equilibrium hydrogen pressures calculated from the reference data (see Table A1 in Appendix) according to Van't Hoff equation at various temperatures (25, 100 and 150 ^{o}C), are presented in Table 4.11.

Table 4.11: *Fitted regression coefficients in eqn. 4.12 assuming different response functions*

Coefficients (eqn 4.12)	Response function, Y				
	$-\Delta H$ [kJ/mol H$_2$]	$-\Delta S$ [J/(mol H$_2$ K)]	ln(P_{EQ} [atm]) at T [^{o}C]		
			25 ^{o}C	100 ^{o}C	150 ^{o}C
Y_0	3.4443	118.7807	12.9035	13.1830	13.3142
A_1	20.6555	-10.1020	-9.5524	-7.8768	-7.0897
A_2	25.3876	-8.2488	-11.2394	-9.1799	-8.2124
A_3	16.0261	-18.1750	-8.6555	-7.3554	-6.7447

A_4	-0.1844	-9.2996	-1.0447	-1.0596	-1.0666
A_5	0.7516	-67.9505	-8.4803	-8.4193	-8.3907
A_6	54.1771	-23.2591	-24.6655	-20.2705	-18.2060
A_7	-8.0679	-2.5677	2.9473	2.2928	1.9854

A certain correlation of the observed and calculated values of the hydrogenation enthalpy was noted (Figure 4.39 A). The influence of the fitting variables related to the alloy's composition can be estimated from the values of the regression coefficients $A_1 \ldots A_7$ (Table 4.11, second column). It is evident that the substitution of both Ti and Fe in $TiFe_2$ mainly results in a significant increase of the thermal stability of the corresponding intermetallic hydride ($A_i > 0$), and the influence of the substitution decreases in series V (A_6) $\gg$ Cr (A_2) > Zr (A_1) > Mn (A_3) $\gg$ Cu (A_5). The introduction of Ni (A_4) results in a slight decrease of thermal stability of the hydride on the basis of the substituted intermetallide. Finally, increase of B/A ratio results in a significant decrease of a hydride thermal stability, although this influence is less pronounced than components substitution (except for Cu and Ni).

There was no evidence for a correlation between calculated and observed values of the entropy of hydrogenation (Fig. 4.39 B) that allows us to conclude that the entropy change upon hydrogenation of AB_2 does not directly depend on the composition of the alloy.
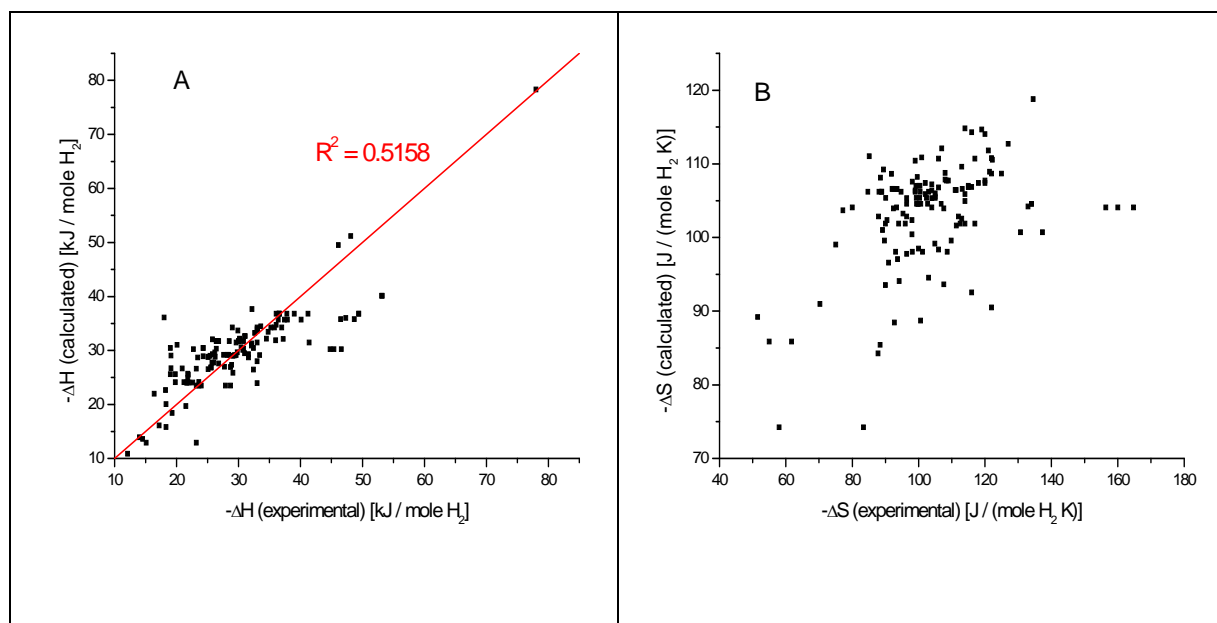
Figure 4.39: *Relations between experimental (reference data) and calculated (eqn. 4.12) values of hydrogenation enthalpy (A) and entropy (B) of AB$_2$-type intermetallides*

At the same time, the values of equilibrium hydrogen pressures for AB$_2$-type intermetallic hydrides at various temperatures calculated from the reference thermodynamic data show very good correlation with the corresponding values calculated from the alloy's compositions using eqn. 4.12 (Figure 4.40). The influence of the alloy's composition on the stability of the hydride (Table 4.11, last three columns) shows similar tendency as it was found assuming hydrogenation enthalpy as a response function.

196
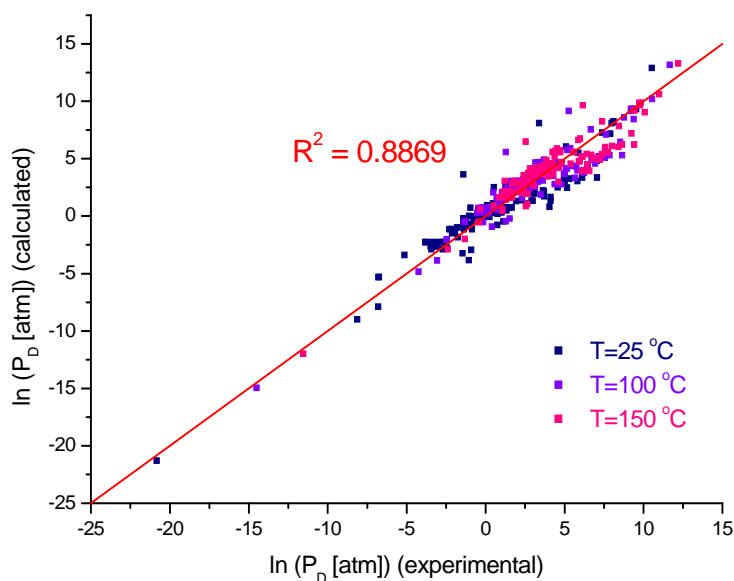
Figure 4.40: *Relations between experimental (calculated using Van't Hoff equation from the reference ΔH and ΔS data) and calculated (eqn. 4.12) values of equilibrium hydrogen pressures for AB₂-type intermetallic hydrides at various temperatures*

It can be concluded that assuming simple linear regression (eqn. 4.12) between composition of $AB_{2\pm x}$ alloys (A=Ti, Zr; B= Fe, Cr, Mn, Ni, Cu, V) and hydrogen equilibrium pressures of the corresponding hydrides, a realistic estimation of the hydride thermal stabilities can be done on the basis of their compositions.

4.4.2 Experimental studies of selected AB₂–type alloys

4.4.2.1 (Ti,Zr)(Fe,Cr,Mn,Ni,Cu)₂₋ₓ hydrogen compression alloy

To verify the approach undertaken in the previous section, we carried out an in-depth experimental study of hydrogen sorption performances of a multi-component AB₂-type alloy. The material of the composition $Ti_{0.77}Zr_{0.3}Cr_{0.85}Fe_{0.7}Mn_{0.25}Ni_{0.2}Cu_{0.03}$ was manufactured in

197

the quantity about 100 kg by Guangzhou Research Institute of Non Ferrous Metals (China), by SAIAMC custom order, and was used at SAIAMC for the development of second stage of 10–200 bar MH hydrogen compressor. Results of preliminary studies of this material (XRD, SEM / EDS, hydrogen sorption performances at $P_{H_2} \leq 50$ bar) were reported earlier [168]. The alloy's composition is close to AB_2-type hydrogen compression alloy produced by Japan Steel Works, Ltd. (trade mark FRN-118 [169]); the difference is that in our case the alloy was hypo-stoichiometric, with B/A ratio about 1.9.

Hydrogen absorption and desorption experiments were carried out using high-pressure Sieverts setup at IFE / Norway. It is noteworthy that this instrument provides a very clean atmosphere, by using a turbomolecular pumping station for evacuation and high pressure hydrogen desorbed from AB_5-type metal hydride for sample hydrogenation. At the specified conditions, the material showed rather good activation performances absorbing hydrogen at P~100 bar after short time evacuation at room temperature, without heating (Figure 4.41). However, long-time ($\geq$ 6 months) exposure of the as delivered alloy on air and application of a rotary pump for the evacuation in combination with the usage of H_2 gas from a cylinder, resulted in a worsening of the activation performances: reproducible hydrogen absorption / desorption kinetics could be reached only after 5 activation cycles including 2 hours long evacuation of sample at T $\geq$ 100 ^{o}C followed by hydrogen absorption at P $\geq$ 75 bar and T = 15–20 ^{o}C.
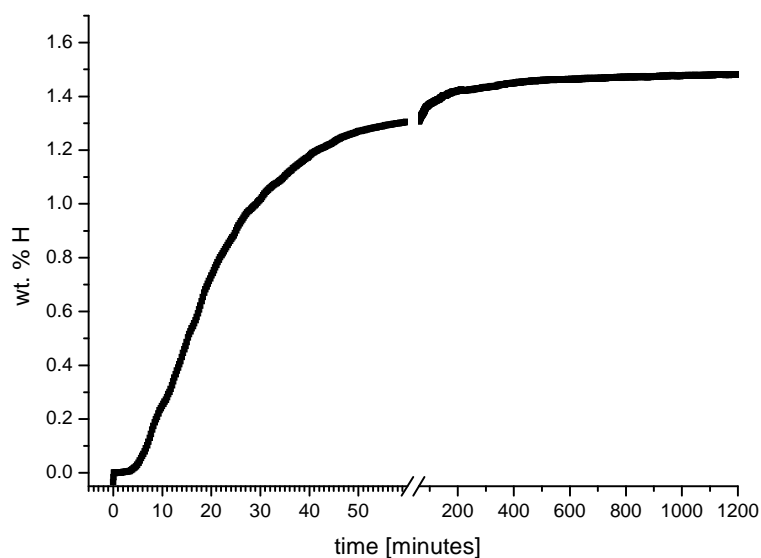
Figure 4.41: *First hydrogenation of the as-delivered AB$_2$-type alloy at P=100 bar (H$_2$ desorbed from AB$_5$-type hydride) and T=25 ^{o}C, after evacuation with turbomolecular pump to 10^{-5} mbar at room temperature.*

Figure 4.42 shows isotherms of hydrogen absorption and desorption for the activated material in the temperature range –25 to +75 ^{o}C and hydrogen pressures up to 200 bar. The experimental points were processed using the model [143] of phase equilibria in metal hydrogen systems; fitting results are shown as lines in the figure, and the thermodynamic values derived from the fitting parameters are presented in Table 4.12.
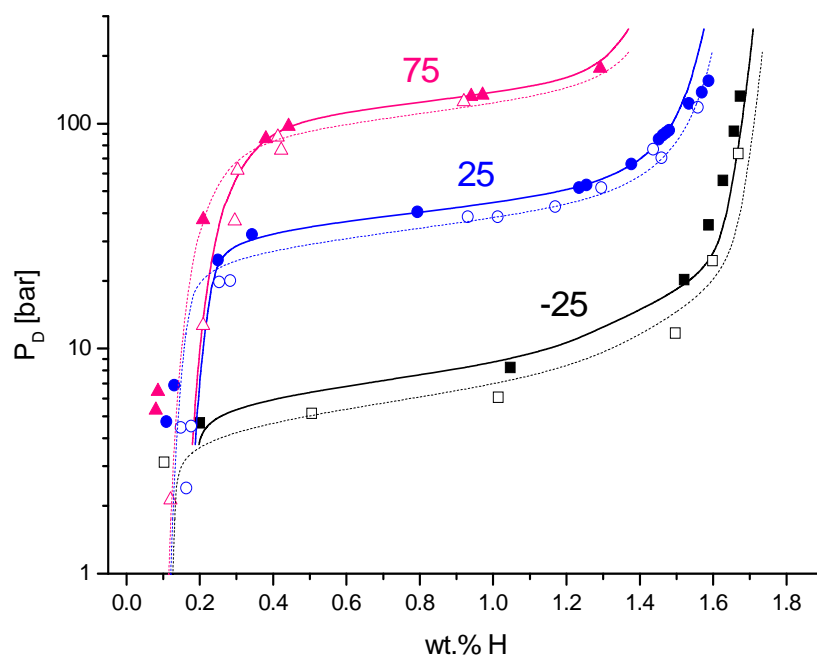
Figure 4.42: *Hydrogen absorption (filled symbols, solid lines) and desorption (empty symbols, dashed lines) isotherms for (Ti,Zr)(Fe, Cr, Mn, Ni, Cu)$_{2-x}$ hydrogen compression alloy. Points represent experimental data and lines – results of their fitting by model [138]. Curve labels correspond to the temperatures [^oC].*

Table 4.12: *Apparent PCT properties of the AB$_2$-type alloy calculated from the fitting parameters*

Parameter		Absorption	Desorption
ΔS^0, J/moleH$_2$/K (*T=50 ^oC*)		-91.83	-92.77
ΔH^0, kJ/moleH$_2$ (*T=50 ^oC*)		-18.208	-18.891
d(Ln *P*)/d(H/ M) (*T=50 ^oC*)		0.472	0.507
P$_D$ (C=0.9 wt% H) at T= [^oC]	25	42.3	36.1
	100	205	186
	150	439	408

Comparison of the observed plateau pressures (Table 4.12) with the values calculated from the alloy's composition (eqn. 4.12; 51, 319 and 757 bar at 25, 100 and 150 $^{\circ}$C, respectively) shows that the simple linear regression model presented in section 4.5.1 overestimates the plateau pressures by 40 (20 $^{\circ}$C) to 85% (150 $^{\circ}$C) in our particular case. Nevertheless, due to its simplicity, it can be rather useful for making starting estimations of the target compositions of multicomponent Ti-based AB_2-type alloys with thermodynamic properties required by hydrogen storage and compression applications.

4.4.2.2 $(Ti,Zr)(Fe,Cr,Mn,Ni,Cu)_{2-x}$ alloy prepared from raw TiFe obtained by the reduction of ilmenite

To improve reversible hydrogen storage capacity of raw TiFe obtained by the reduction of ilmenite (section 4.1.8), we suggested its additional alloying to yield AB_2-type material [98]. The primary TiFe and the alloying metals are taken in amounts corresponding to the formula $(TiFe)_x Zr_{1-x} Mn_y Cr_z Ni_t$ where x=0.5–0.8 and (y+z+t)=1–1.7. The minimum amount of zirconium is 20 at. % as related to the mixture TiFe + Zr (x=0.8). This amount is necessary to provide reasonably high thermal stability of the final AB_2-type alloy which otherwise will have too high hydrogen equilibrium pressures and, correspondingly, low reversible hydrogen storage capacity in reasonable pressure–temperature ranges. The relationship between amounts of manganese, chromium and nickel is selected in such a way that the stability of final AB_2-type material would match into the requirements of this or that application (pressure / temperature ranges for hydrogen storage system, hydrogen compression module, etc.). The relationship between component composition of the target alloy and thermal stability of the corresponding hydride can be estimated using approach described in section 4.5.1. To remain within AB_2 homogeneity region that prevents formation

of other intermetallic phases reducing reversible hydrogen storage capacity, the sum (y+z+t) must be in the range from 1 to 1.7 that corresponds to the composition $AB_{2\pm\delta}$ where δ varies from 0 to 0.5.The mixture of primary TiFe and the alloying components (Zr, Mn, Cr, Ni) may additionally comprise 1 to 1.5 wt. % copper that significantly improves activation performances and poisoning tolerance of the target material without reduction of hydrogen storage capacity (may occur at higher copper concentrations).

The raw TiFe obtained by the metal-thermic reduction followed by leaching-off the by-products was placed, together with the other metallic components, into alumina-silica crucible of a laboratory induction melter. The composition of the charge corresponded to the formula $(TiFe)_{0.7}Zr_{0.3}Cr_{0.4}Mn_{0.57}Ni_{0.19}Cu_{0.04}$, or as shown in the Table 4.13 below.

Table 4.13: *Composition of the as prepared AB2 – type hydride forming alloy*

Component	at%	wt%	M [g]
Raw TiFe	31.82	43.80	20.9
Zr	13.64	16.51	7.9
Cr	18.27	12.61	6.0
Mn	25.90	18.89	9.0
Ni	8.64	6.73	3.2
Cu	1.73	1.46	0.7
TOTAL	*100*	*100*	*47.7*

The plateau pressure of the material of the composition specified above estimated using eqn. 4.12 was identified to be 65 to 80 bar at T=25 $^{\circ}$C. Note that the higher value was obtained through the fitting of all the reference data on AB$_2$-type materials presented in Appendix; the lower value was obtained after excluding the V-containing compounds from the starting dataset.

The melting was carried out in the flow of purified argon, at the temperature of ~1500 $^{\circ}$C, during 2 minutes. XRD pattern of the as-cast AB$_2$ alloy is shown below in figure 4.43. The XRD pattern shows the presence of major hexagonal Laves phase (C14; a=4.9107 Å, c=8.0151 Å) with minor impurities of η-Ti$_4$Fe$_2$O and ZrO$_2$ (less than 5% in total).
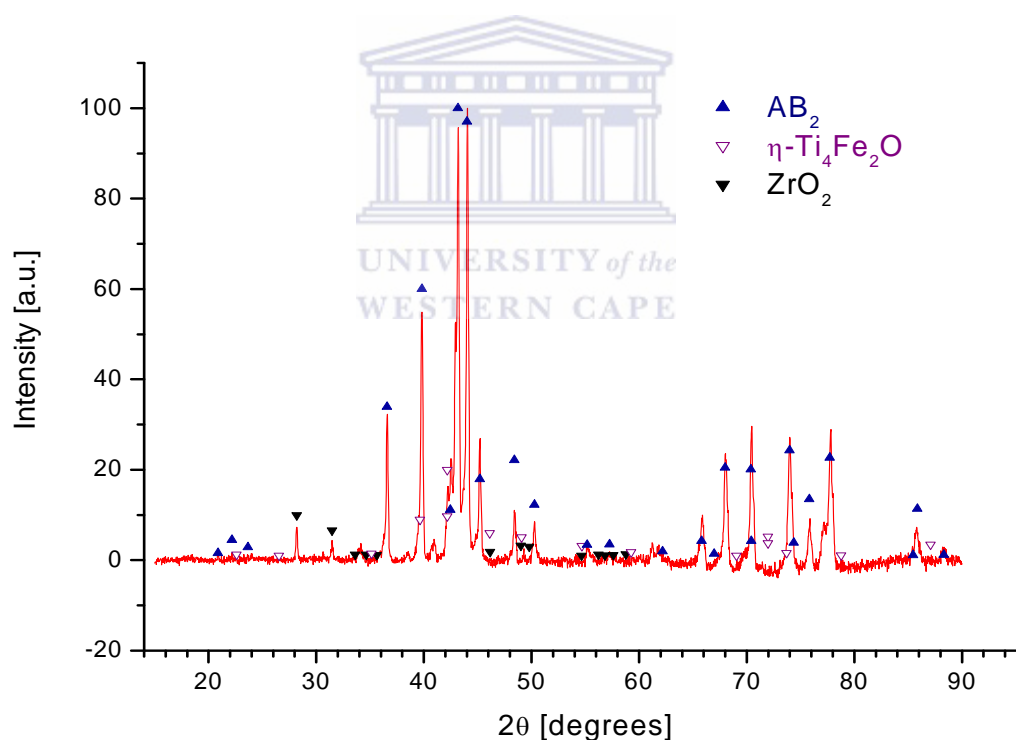
Figure 4.43: *The XRD pattern of the AB$_2$-type hydride-forming alloy prepared by alloying of the product of reduction of ilmenite.*

The hydrogenation performances of the AB_2–type alloy were conducted with and without pre–activation by vacuum heating. The hydrogen absorption kinetics of the AB_2-type alloy are shown below in figure 4.44. The alloy exhibits excellent dynamics of hydrogenation, which starts even without vacuum heating, after evacuation of the sample at room temperature (curve A), and proceeds very fast after vacuum heating of the hydrogenated sample to 300 ^{o}C during 1 hour (curve B). The reversible hydrogen sorption capacity of the material (P=40 bar) was about 1.3 wt. % H. Finally, the material was superior as compared to known AB_2-type alloys, as regards to its poisoning tolerance: 10-minutes long exposure of the dehydrogenated alloy to air results in a slight decrease of the hydrogen absorption capacity, but almost does not reduce the rate of the hydrogenation (curve C).
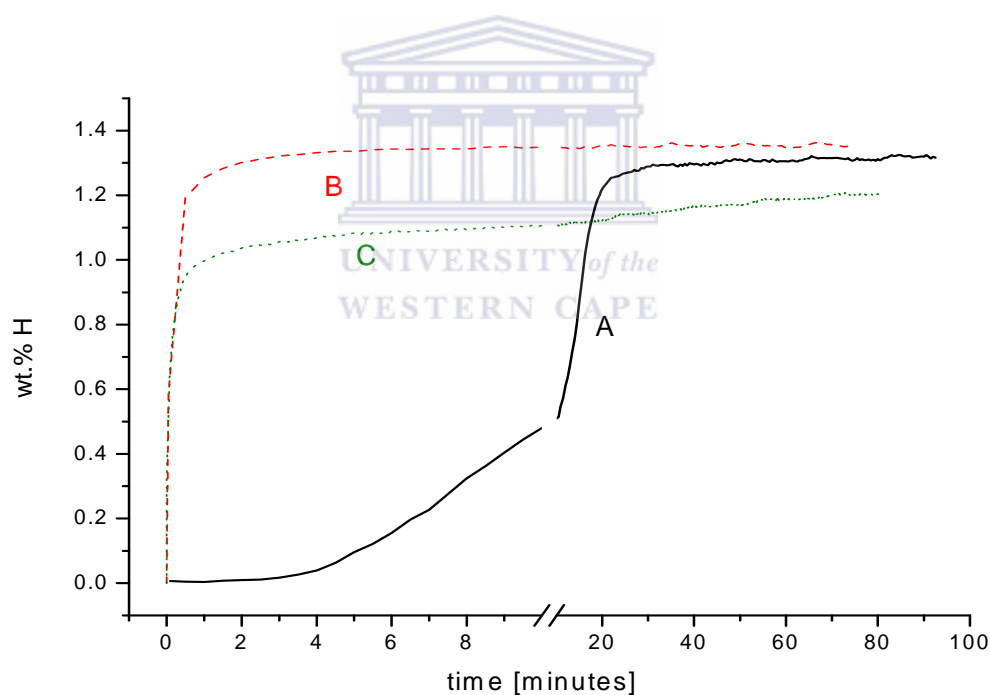
Figure 4.44: *Hydrogenation performances of the AB_2-type hydride-forming alloy prepared from ilmenite (P=40 bar, T=20°C): A – first hydrogenation without vacuum heating, B – second and consequent hydrogenations of the material dehydrohenated by heating to 300 ^{o}C in vacuum during 1 hour, C – hydrogenation of the de-hydrogenated material after 10 minutes-long exposure to air.*

Note that the hydrogenation of the alloy was observed at hydrogen pressure of about 40 bar, which is quite lower than the values calculated for the alloy's composition using eqn. 4.12.

High-pressure hydrogenation / dehydrogenation studies of the material carried out using PCTPro-2000 instrument showed that hydrogen absorption capacity achieved at P=150 bar at room temperature was higher than 1.8 wt.% H. The hydrogen desorption isotherm (Figure 4.45) exhibits the presence of two plateaux where the upper one (65…80 bar) corresponds well to our thermodynamic estimations. At the same time, the two-plateau behaviour, most probably originated from alloy's inhomoheneity (the as cast alloy was used for hydrogen sorption studies), and further annealing is necessary to improve the PCT behaviour of the material.
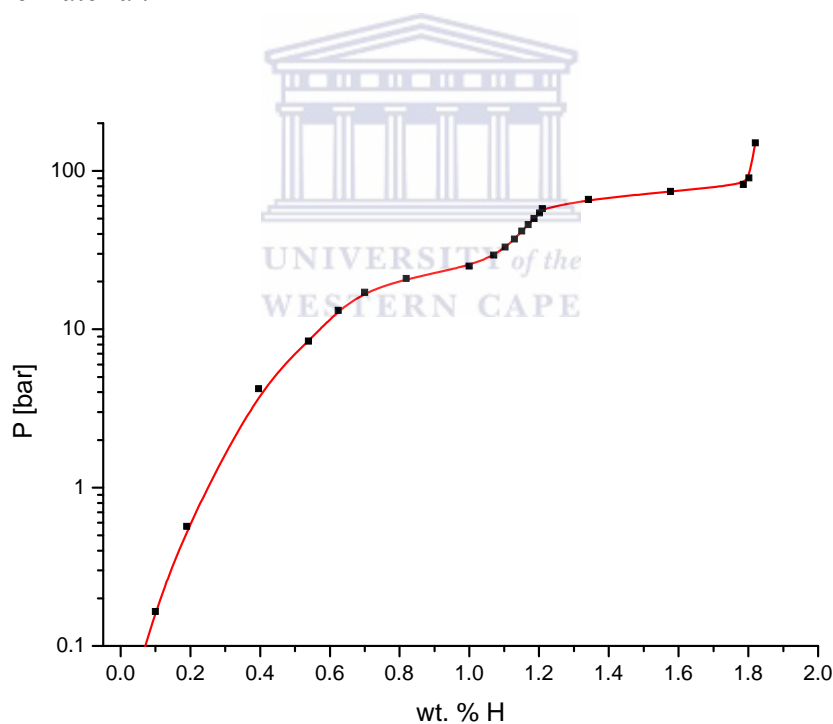
Figure 4.45: *Isotherm of hydrogen desorption from the hydrogenated AB₂-type hydride-forming alloy prepared from ilmenite (T=22ᵒC). The line is plotted just to guide an eye.*

Chapter 5: Conclusions and Recommendations

The ultimate scientific goal of this project was to study titanium–based intermetallic compounds belonging to AB (TiFe) and AB_2 (A=Ti, Zr; B=Fe, Mn, Cr). One of the main shortcomings of Ti–intermetallic compounds is that they have poor activation performances and poisoning tolerance resulting in significant impeding of the hydrogen sorption kinetics. Consequently, the synthesis routes for the preparation of Ti–based metal hydride forming materials are extremely important and special precautions must be taken during the synthesis because of the ability of the Ti–based metal hydride material to easily pick up oxygen. In this study, TiFe alloy was synthesised via arc–melting, sintering, induction melting and via reduction of ilmenite ($FeTiO_3$). The AB_2 alloy was prepared via induction melting using the product of the reduced ilmenite.

To improve the activation performances and poisoning tolerance of TiFe alloy we adopted an approach of nano–engineering of Pd catalytic mantles on the surface of the TiFe alloy. Palladium was considered as the catalytic mantle as a result of its high affinity towards hydrogen and its high hydrogen selectivity. The deposition of Pd on the surface of the TiFe alloy was done by electroless plating and chemical vapour deposition, both these techniques allow for the ability to control the surface chemistry of the modified system.

In this research study, standard characterisation tools were used in the investigation of Ti–based AB and AB_2 type metal hydride forming materials, in terms of phase structural characteristics, surface morphology and elemental composition, hydrogen sorption kinetics and PCT characteristics using XRD, SEM/EDS and volumetric (Sievert) techniques.

Results of the synthesis, surface modification and characterisation of the Ti–based AB and AB$_2$ type metal hydride forming materials are summarised as follows:

1. The synthesis of TiFe alloy via arc-melting and sintering was shown to be successful, due to the fact that the XRD patterns illustrated that both arc-melted and sintered TiFe alloy contained the bcc − TiFe as the major phase. In addition, the sintered material contained two extra phases including η - Ti$_4$Fe$_2$O$_{1-x}$ and β − Ti. Experimental studies of hydrogenation of both samples revealed that the sintered TiFe alloy exhibited better hydrogenation kinetics as compared to the arc–melted TiFe alloy. This observed improvement of the hydrogenation activity for the sintered material was credited to the formation of easy hydrogenated Ti$_4$Fe$_2$O$_{1-x}$ and β − Ti acting as hydrogen transfer catalysts. It was observed that the PCT performances of the arc–melted TiFe alloy show the existence of two main plateau segements corresponding to β − TiFeH (monohydride) and γ − TiFeH$_2$ (dihydride). According to the fitting, the asymptotic hydrogen concentration was found to be about 1 H / (Ti + Fe). The PCT performance of the sintered TiFe alloy shows that the first low–pressure segment was characterised by higher maximum H concentration. This was probably due to the contribution of the stable hydrides Ti$_4$Fe$_2$O$_{1-x}$ and TiH. The PCT diagram of the sintered TiFe alloy shows that the asymptotic hydrogen concentration was about 0.96 H / (Ti + Fe). In summary, the introduction of oxygen impurity into TiFe observed in the sintered sample significantly influences on its PCT performances, due to formation of stable hydrides of the impurity phases, as well as destabilisation of both β-TiFeH and,

especially, γ-TiFeH$_2$. This finally results in the decrease of the reversible hydrogen storage capacity of the oxygen-contaminated sample.

2. The effect of oxygen addition into TiFe alloy was also investigated. Different weight percentages (0.1, 0.2, 0.5 and 1) of oxygen were introduced into the bulk parent alloy. It was observed that the increase of oxygen content in the alloy results in the decrease of the abundance of the main TiFe phase, together with the increase in the abundance of Ti$_4$Fe$_2$O$_{1-x}$ and, to a lesser extent, TiFe$_2$. The hydrogen absorption kinetics of the oxygen modified TiFe alloys illustrated that the hydrogen absorption rates are the same, but the hydrogen capacities decrease with the increase of oxygen concentration. The ratios H / (Ti+Fe) for the 0.1 and 0.2 wt% O substitution in TiFe were 0.95 and 0.62, respectively.

3. TiFe alloy was also prepared via induction melting using two different crucibles, which were graphite and alumo–silica. The samples prepared using the graphite crucible contain TiFe as the major phase ($\sim$ 70%) as well as η - Ti$_4$Fe$_2$O$_{1-x}$ phase ($\sim$ 25%) and TiFe$_2$ ($\sim$5%). However, the sample prepared in the alumo–silica crucible was characterised by much lower content of TiFe phase ($\sim$10%) and the presence of significant amounts of η - Ti$_4$Fe$_2$O$_{1-x}$ phase ($\sim$55%) and TiFe$_2$ phase ($\sim$35%). This result clearly indicates that significant contamination of the sample by oxygen is introduced from the crucible material.

4. An attempt of direct synthesis of TiFe from ilmenite (FeTiO$_3$) as the cheapest raw material for the manufacturing of Ti-based hydride-forming alloys was undertaken. It was shown that the direct metal thermic reduction of the ilmenite with CaH$_2$, Ca or MgH$_2$ results in a very low (CaH$_2$, Ca) or zero (MgH$_2$) yield of the target TiFe

because of side reactions which result in the formation of stable perovskite- ($CaTiO_3$) and spinel-like ($MgTi_2O_4$) compounds.
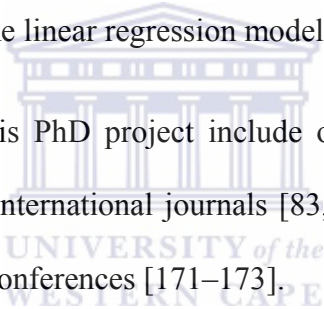
5. We have developed a new technique for the synthesis of TiFe alloy via reduction of ilmenite ($FeTiO_3$) using a two–step process: (1) gas–phase reduction and (2) metal–thermic reduction. The XRD pattern of the sample after gas–phase reduction showed that the $FeTiO_3$ was completely reduced to iron mixed with titanium oxides. The product of the gas–phase reduction was further subjected to metal–thermic reduction using CaH_2 as a reducing agent. The XRD pattern of the metal–thermic reduced $FeTiO_3$ after leaching in HCL indicated that TiFe is the major phase and the main impurities present in the sample were η - Ti_4Fe_2O and $TiFe_2$. The reversible hydrogen absorption capacity of the synthesised TiFe alloy via reduction of $FeTiO_3$ was ~0.5 wt.% H. The main reason for this low hydrogen capacity is due to reaction of TiFe with oxygen impurity to yield η-Ti_4Fe_2O and $TiFe_2$, which cannot be completely suppressed at the applied conditions.

6. To improve the hydrogen sorption kinetics of the arc–melted and sintered TiFe, the materials were subjected to Pd deposition onto their surface. After electroless Pd deposition, discontinuous surface layers of fine Pd particles were observed with an average particle size of about ~70 nm. Atomic absorption spectroscopy was used to determine the total Pd loading and revealed Pd concentration of ~0.6 wt. %. The hydrogenation kinetics of the surface modified materials was significantly faster as compared to that of the unmodified material, even though with the presence of an incubation period. The enhanced hydrogenation kinetics can be credited to the partial removal of the surface oxide layers during the chemical treatment, as well as the

enhanced activity of the modified surface towards H_2 dissociation, due to the presence of the Pd nanoparticles catalysing H_2 molecule splitting, which facilitates subsequent diffusion of H atoms into the bulk material and quick attainment of the maximum absorption capacity.

7. In addition, we successfully improved the activation performances and poisoning tolerance of TiFe alloy, via surface modification by CVD technique using Pd[acac]$_2$ as a metal precursor. During CVD process different Pd loadings were used, viz. 0.5, 1.0 and 5 wt. %. The SEM images illustrated that the Pd loading significantly influences on the coating morphology. The sample loading with 0.5 wt.% Pd, had a uniform but discontinuous deposition, the 1 wt.% Pd loading exhibited a denser coating formed by agglomerated Pd particles, while the 5 wt.% Pd loading illustrates a very dense and multilayered Pd covering. All the surface modified materials absorbed hydrogen without vacuum heating. The incubation period was shorter for the samples possessing lower Pd loadings. However, the maximum hydrogen absorption capacities for the surface modified alloys were found to be lower than that of the unmodified TiFe. The surface–modified materials were exposed to air and they did not lose their ability to absorb hydrogen, exhibiting only a slower absorption rate and a lower hydrogen capacity. The reason for the lower hydrogen absorption capacity observed for the surface–modified material is that when Pd[acac]$_2$ is decomposed at T~400 ^{0}C it releases carbon and oxygen containing species into the gas phase. These species may be chemisorbed onto the surface of the TiFe alloy followed by the diffusion of carbon and oxygen atoms into the metal matrix. It could lead to the reduction of hydrogen absorption capacity, especially for higher Pd loadings, corresponding to higher amounts of the metal–organic precursor.

8. An attempt was made to improve the hydrogen sorption kinetics of TiFe alloy by depositing carbon nanotubes (CNTs) directly on the surface of the alloy. From the results, it was observed that CNTs were successfully deposited on the surface of the alloy. However, the XRD data revealed that the TiFe intermetallic phase was found to be significantly contaminated with η-phases (similar to $Ti_4Fe_2O_{1-x}$ sub oxide), resulting in the significant reduction of the hydrogen capacity, down to ~0.33 wt. % H.

9. On the basis of linear regression analysis of abundant reference data on thermodynamic performances of $AB_{2\pm x}$ alloys; where A=Ti, Zr; B=Fe, Cr, Mn, Ni, Cu, V; a correlation between the alloy's composition and stability of the corresponding intermetallic hydride was revealed. It was shown that the substitution of both Ti and Fe in $TiFe_2$ mainly results in a significant increase of the thermal stability of the corresponding intermetallic hydride, and the influence of the substitution decreases in series V >> Cr > Zr > Mn >> Cu. The introduction of Ni results in a slight decrease of thermal stability of the hydride on the basis of the substituted intermetallide. Finally, increase of B/A ratio results in a significant decrease of a hydride thermal stability. However, this influence is less pronounced in components substitution (except for Cu and Ni).

10. To improve the reversible hydrogen storage capacity of the raw TiFe obtained by the reduction of ilmenite, it was further alloyed with additional metals (Zr, Mn, Cr, Ni and Cu) to yield an AB_2–type material. The composition of the as prepared alloy corresponded to the formula $(TiFe)_{0.7}Zr_{0.3}Cr_{0.4}Mn_{0.57}Ni_{0.19}Cu_{0.04}$. The XRD pattern of the as-cast AB_2 alloy revealed the presence of a major hexagonal AB_2 Laves phase

with minor impurities of η - Ti_4Fe_2O and ZrO_2. The hydrogenation performances of the AB_2–type alloy exhibited excellent absorption dynamics of hydrogenation which starts even without vacuum heating. The reversible hydrogen sorption capacity at P=40 bar was about 1.3 wt. % H. The as-cast AB_2 alloy revealed good sorption kinetics even after exposure in air. It only had a slight decrease in hydrogen absorption capacity, but did not reduce the rate of hydrogenation. High–pressure hydrogenation / dehydrogenation studies showed that the hydrogen absorption capacity achieved at P=150 bar and ambient temperature was higher than 1.8 wt. % H. The plateau pressure of the corresponding AB_2-type intermetallic hydride at room temperature corresponded well to the value calculated from the composition of the intermetallic alloy using the linear regression model.

11. Research outputs from this PhD project include one patent application [98], three articles in peer-reviewed international journals [83,108,170], and three presentations at international and local conferences [171–173].

The knowledge emanating from this research project is expected to pave the way for the industrialisation in the preparation of AB and AB_2–type metal hydride forming materials mainly using South African raw materials. These metal hydride materials can be used in various stationary and special mobile applications and thus reduce the dependence of energy supply from fossil fuels.

Based on the analyses and conclusions of this study, a number of recommendation regarding future R&D activities were made:

- Further development of technological routes for the manufacturing of high-quality hydride forming materials from South African feedstock should be focused on the preparation of the AB$_2$-type alloys where A=Ti, Zr; B= Fe, Cr, Mn, Ni, Cu, V. Special attention should be paid to the materials with Ti:Fe = 1:1 since they can be produced using cheap ilmenite as a main raw material.

- Efforts should be made to up-scale the method of synthesising Ti–based alloys via reduction of ilmenite (FeTiO$_3$) and to increase the yield of the target alloy. This can be achieved by using a method of Self propagating High temperature Synthesis (SHS) on the stage of metal-thermic reduction.

- To study the effect of bulk- and surface modification of Ti–based metal hydrides by different metals (PGM, V, Cu, Ni) on the hydrogenation performances.

- The poisoning resistance of the modified materials should be evaluated in details using gaseous mixtures containing hydrogen contaminated with O$_2$, CO, CO$_2$ and H$_2$O.

Chapter 6: References

[1]   Zuttel. A., Schlapbach. L.; *Nature*, 414, (2001) 772-782.

[2]   Zhou. L.; *Renewable and   Sustainable Energy Review*, 9, (2005) 395-408.

[3]   Zuttel. A.; *Naturwissenschaften*, 94 (2004) 157-172.

[4]   Fakioglu. A., Yurum. Y., Veziroglu. T.N.; *Int. J. Hydrogen Energy*, 29, (2004) 1371-1376.

[5]   Lamari Darkrim. F., Malbrunot. P, Tartaglia. G.P.; *Int. J. Hydrogen Energy*, 27, (2002) 193-202.

[6]   Hamburg. Y.Du., Dubovkin. N.F. (Editors); *Hydrogen. Properties, Production, Storage, Transportation, Applications: Reference Book, "Khimia",* Moscow, (1989).

[7]   Mariolakes. I., Kranioti. A., Markatsels. E., Papageorgiou. M.; *Water Mythology and Environmental Education*, (2007), 213-218.

[8]   Arrhenius. S, *Philos. Mag.*, 41, (1896), 237.

[9]   *US Energy Information Administration, Report No.: DOE/EIA-0484* (May 27th, 2009).

[10]   Tarasov. B.P., Lototskyy. M.V., Yartys. V.A.; *Russian Journal of General Chemistry*, 77, (2007) 694-711.

[11]   Hydrogen Composite Tank Program; Proc. (2002) U.S. *DOE Hydrogen Program review*, NREL/CP – 610 -32405.

[12]   Weitkamp. J.; *Zeolites as Media for Hydrogen Storage* (1996) [ONLINE] Available: http://www.uni-stuttgart.de/sfb270/B7_E.htm.

[13]   Yu. M, Li. S, Falconer. J.L, Noble. R.D. (2008) *Microporous and Mesoporous Materials*, 110: 579–582.

[14]   Schur. D.V., Tarasov. B.P., Zaginaichenko. S.Yu.; *Int. J. Hydrogen Energy*, 2002, vol. 27, no. 10, p. 1063.

[15]   Tarasov. B.P., Maehlen. J.P., Lototsky. M.V., Muradyan. V.E., and Yartys. V.A.; *J. Alloys and Compounds*, 2003, vols. 356-357, p. 510.

[16]   Yartys. V.A, Lototsky. M.V.; in: *Hydrogen Materials Science and Chemistry of Carbon Nanomaterials*, *Kluwer Academic Publishers*, *Dordrecht / Boston / London*, (2004), 75-104.

[17]   Hynek. S, Fuller. W, Bentley. J.; *Int. J. Hydrogen Energy*, 22(6) :(1997), 601-610.

[18]   Zhou. L, Zhou. Y, Sun. Y.; *Int. J. Hydrogen Energy*, 29 (2004), 319- 322.

[19]   Sandrock. G. A.; *J. Alloys and Compounds*, 293-295, (1999) 877-888.

[20]   Dantzer. P.; *Materials Science and Engineering*, A329–331, (2002) 313–320.

[21]   Eigen. N., Kunowsky. M., Klassen. T., Bormann. R.; *J. Alloys and Compounds*. 430 (2007) 350-355.

[22]   Wang. J., Ebner. A.D., Ritter. J. A.; *J. Phys. Chem*. C.111 (2007) 14917-14924.

[23]   Kim. J.W., Shim. J.H., Kim. S.C., Remhof. A., Borgschulte. A., Friedrichs. O., Gremaud. R., Pendolino. F., Zuttel. A., Cho. Y.W., Oh. K.H.; *J. Power Sources, 192* (2009), 582-587.

[24]   Zhou. L.; *Renewable & Sustainable Energy Reviews*. 9 (2005), 395-408.

[25]   Züttel. A, Wenger. P, Rentsch. S.; *J. Power Sources*, 118 (2003),: 1-7.

[26]   Bogdanovic. B., Scwickardi. M.; *J. Alloys and Compounds*. 253-254 (1997) 1–9.

[27]   Bogdanovic. B., Brand. R.A., Marjanovic. A., Schwickardi. M., Tölle. J.; *J. Alloys and Compounds*. 302 (2000) 36–58.

[28]   Loutfy. R.O, Wexler. E.M.; (2001) *Investigation of Hydrogen Storage in Fullerene Hydrides*, IEA Task 12: Metal Hydrides and Carbon for Hydrogen Storage.

[29]   Crabtree. G.W, Dresselhaus. M.S, Buchanan. M.V.; *Physics Today*,(2004), 57:39.

[30]   Murphy. K. (2005) *Not Hydrogen - Ammonia!* [ONLINE] Available: http://www.interocitor.com/archives/000659.html.

[31]   *Hydrogen, Fuel Cells & Infrastructure Technologies Program. Multi-Year Research, Development and Demonstration Plan*. Planned program activities for 2003-2010.– U.S. Department of Energy, Energy Efficiency and Renewable Energy, Draft (June 3, 2003).

[32]   Tarasov. B.P., Burnasheva. V.V., Lototsky. M.V., Yartys. V.A.; *Int. Scientific Journal for Alternative Energy and Ecology (ISJAEE)*, 11 (31) (2005) 14–37.

[33]   Tarasov. B.P., Shilkin. S.P.; *Russ. J. Applied Chemistry*, 86 (1) (1995) 21–26.

[34]   Sandrock. G.D., Goodell. P.D.; *J. Less-Common Metals*, 104 (1984) 159–173.

[35]   Dantzer. P.; Hydrogen in Metals III. Properties and Applications. – Ed. by H.Wipf, *Springer-Verlag*, 1997, p.279–340.

[36]   Das. D., Ram Gopal. M.; *Int. J. of Hydrogen Energy* 29 (2004) 103– 112.

[37]   Yartys. V.A., Lototsky. M.V.; Metal Hydride High Pressure Hydrogen Compression: Present Status. – Review, *Institute for Energy Technology*, Department of Energy Systems, 2002.

[38]   Podgorny. A.N., Shmal'ko. Yu.F., Solovey. V.V., Lototsky. M.V.; Hydrogen Energy Progress VII. *Proc. 7-th World Hydrogen Energy Conf.*, Moscow, USSR, 25–29 Sept., 1988. Vol.2. / Ed. by T.N. Veziroglu, A.N. Protsenko. Pergamon Press, 1988. P.1401–1417.

[39]   Busch. G., Fischer. P., Andersen. A.F.; *Int. J. of Hydrogen Energy*, 4, (1978) 29-39.

[40]   Jianxin. M, Hongge. P., Xinhua. W, Changpin. C.; *Int. J. Hydrogen Energy*, 25, (2000) 779-782.

[41]   Ederle. U., Arnold. G., Von Helmot. R.; *J. Power Sources*, 231, (2005) 551-557.

[42]   Sandrock. G.; *Proceeding of the NATO Advance Study Institute of Hydrogen Energy Systems*, Utilization of Hydrogen and Future Aspects, Akçay Turkey, August 21 – September 3, (1994).

[43]   Schlapbach. L.; Hydrogen in Intermetallic Compounds II; Topics in Applied Physics, *Springer-Verlag*.67 (1992).

[44]   Bloch. J.; *J. Alloys and Compounds*. 312 (2002) 135-153.

[45]   Wang. C. S., Wang. X.H., Lei. Q., Chen. P., Wang. Q. D.; *Int. J. Hydrogen Energy*, 21 (1996) 471- 478.

[46]   Martin. M., Gommel. G., Borkhardt. C., Fromm. E.; *J. Alloys and Compounds*, 238 (1996) 193-201.

[47]   David E.; *J. of Material Processing Technology*, 162-163, (2005), 169-177.

[48]   Guo. Z.X., Shang. C., Aguey-Zinsou. K.F.; *J. European Ceramic Society*, 28, (2008), 1467-1473.

[49]   Mao. J., Guo. Z., Yu. X., Liu. H., Wu. Z., Ni. J.; *Int. J. Hydrogen Energy*, 35, (2010), 4569-4575.

[50]   Avrami. M.; *J. Chemical Physics*, 7, (1939), 1103-1112.

[51]   Jackson. K.A.; *Wiley-VCH*, Weinheim, (2004).

[52]   Gerasimov. K. B., Goldberg. E. L., Ivanov. E.Y.; *J. Less-Common Metals*, 131 (1987), 99-107.

[53]   Léon. A., Knystautas. E. J., Huot. J., Schulz. R.; *J. Alloys and Compounds*, 345 (2002), 158-166.

[54]   Léon. A., Knystautas. E.J., Huot. J., Schulz. R.; *Thin Solid Films*, (2005).

[55]   Chuang. K., Cui. N., Luo. J.; *J. Electroanalytical Chem.*, Vol. 503, pp. 92-98, (2001).

[56]   Sieverts. A., Krumbhaar. N., Jurich. Z., *Phys. Chem*, 77, (1911) 591-603.

[57]   Schlapbach. L.; Introduction. In: Hydrogen in Intermetallic Compounds I, Ed. Schlapbach, *Springer-Verlag*, Germany (1988).

[58]   Hagström. M.; *Improved Metal Hydrides for Energy Applications Based on Gas-Solid Reactions*, doctor's dissertation, Helsinki University of Technology Publications in Engineering Physics, TKK-F-A793, Finland (1999).

[59]   Fujii. H., Orimo. S-I.; *Physica B*, 328, (2003) 77-80.

[60]   Satyapal. S.; *Overview of Hydrogen storage activities*, U.S Department of Energy, June 20, (2005).

[61]   Kolachev. B.A., Shahn. R.E.; A A Il'in Alloys for Hydrogen Storage Reference Book, "Metallurgy", Moscow. (1995) 87-138.

[62]   Reilly. J.J., Wiswall. R.H.; *Inorg. Chem*. 13(1) (1974) 218-222.

[63]   Kivalo. L.I., Antonova. M.M., Skorokhod. V.V.; *Hydrogen Storage in Titanium – Iron Intermetallide*, Institute for Problems of Materials Science of Academy of Science of Ukraine, Preprint IPM #6.83, 1983.

[64]   Muhlbauer. A.; *Modelling for Materials Processing*, (2006), 8-9.

[65]   Pericleous. K., Bojarevics. V., Jambazov. G.D., Harding. R.A., Wickins. M.; *Applied Mathematical Modelling* 30, (2006),1262-1280.

[66]   Frenzel. J., Zheng. Z., Neuking. K., Eggeler. G.; *J. Alloys and Compounds*, 385, (2004), 214-223.

[67]   Syvajarvi. M., Yakimova. R., Ciechonski R.R., Janzen. E.; *Diamond and Related Materials*, 12, (2003), 1936-1939.

[68]   Chiang. C.H., Chin. Z.H., Perng. T.P.; *J. Alloys and Compounds*, 307, (2000), 259-265.

[69]   Hotta. H., Abe. M., Kuji. T., Uchida. H.; *J. Alloys and Compounds*, 439, (2007), 221-226.

[70]   Zaluski. L., Zaluska. A., Tessier. P., Storm-Olsen. J.O., Schulz. R.; *J. Alloys and Compounds*, 227, (1995), 53-57.

[71]   Abe. M., Kuji. T.; *J. Alloys and Compound*, 446-447, (2007), 200-203.

[72]   U.S. Geological Survey, 2008, Titanium statistics, in Kelly, T.D., and Matos, G.R., comps., Historical statistics for mineral and material commodities in the United States: U.S. Geological Survey Data Series 140, available online at http://pubs.usgs.gov/ds/2005/140/.

[73]   D.S. Van Vuuren. Keynote address: Titanium–an opportunity and challenge for South Africa; in *The 7th International Heavy Minerals Conference*, The Southern African Institute of Mining and Metallurgy, 2009, pp.1–7.

[74]   U.S. Department of the Interior, U.S. Geological Survey, Mineral Commodity Summaries,(2004).
(http://minerals.usgs.gov/minerals/pubs/commodity/titanium/timinmcs04.pdf).

[75]   Hideyuki Yoshikoshi, Keisuke Nakahara. *Production of synthetic rutile*; Japanese Patent JP62056323, 1987.

[76]   Joseph. A.A., Whellock. J.G.; *Low cost high speed titanium and its alloy production*; US Patent Application US 2004/0103751 Al, 2004.

[77]   Wu. Y., Yin. C., Zou. Z., Wei. H., Li. X.; *Rare Metals*, 25 (6), Suppl. 1 (2006) 280-283.

[78]   Ma. M., Wang. D., Hu. X., Jin. X., Chen. G.Z.; *Chem. Eur. J.*, 12 (2006) 5075-5081.

[79]   Ye. X.S., Lu. X.G., Li. C.H., Ding. W.Z., Zou. X.L., Gao. Y.H., Zhong. Q.D.; *Int. J. Hydrogen Energy*, 36, (2011), 4573-4579.

[80]   Amano. M., Sasaki. Y., Watanabe. R., Shibata. M.; *J. Less-Common Met.* 89 (1983) 513-518.

[81]   Lanyin. S., Fangjie. L., Deyou. B.; *Int. J. Hydrogen Energy* 15 (4) (1990) 259-262.

[82]   Ma. J., Pan. H., Wang. X., Chen. C., Wang. Q.; *Int. J. Hydrogen Energy* 25 (2000) 779-782.

[83]   Williams. M., Lototsky. M.V., Davids. M.W., Linkov. V., Yartys. V.A., Solberg. J.K.; *J. Alloys and Compounds*, 509S (2011) S770– S774.

[84]   Yamanaka. K., Saito. H., Someno. M.; *J. Chemistry Society. Japan*, 8, (1975), 1267.

[85]   Nambu. T., Ezaki. H., Yukawa. H., Morinanga. M.; *J. Alloys and Compounds*, 293-295, (1999), 213-216.

[86]   Wenzl. H.; *J. Less-Common Metals*, 74 (1980) 351 – 361.

[87]   Kivalo. L.I., Antonova. M.M., Skorokhod. V.V.; Hydrogen Storage in Titanium – Iron Intermetallide, *Institute for Problems of Materials Science of Academy of Science of Ukraine*, Preprint IPM #6.83, 1983.

[88]   Murray. J.L.; *Binary Alloy Phase Diagrams*, Second Edition, Ed. T.B. Massalski, ASM International, Materials Park, Ohio (1990) 3, 2615-2617.

[89]   Piper. J.; *J. Applied Physics*, 37(2): (1966), 715-721.

[90]   Uchida. H.; *Int. J. Hydrogen Energy*, 24, (1999) 861 – 869.

[91]   Dufour. J, Huot. J.; *J. Alloys and Compounds*, 439: L5-L7. (2007).

[92]   Block. F.R., Bahs. H.J.; *J. Less-Common Metals*, 89, (1983), 77-84.

[93]   Schlapbach. L., Seiler. A., Stucki. F., Siegmann. H.C.; *J. Less-Common Metals*, 73, (1980), 145 – 160.

[94]   Bratanich. T.I., Bulanov. V.N., Skorokhod. V.V., Klimenko. V.P.; *Powder Metallurgy and Metal Ceramics*, 39 (11-12): (2000), 575-583.

[95]   Sandrock. G.D., Goodell. P.D.; *J. Less-Common Metals*, 73 (1990) 161–168.

[96]   Rupp. B.; *J. Less-Common Materials*. 104 (1984) 51-63.

[97]   Lavrentyev. A.A., Gabrelian. B.V., Shkumat. P.N., Nikiforov. I.Ya., Zavaliy. I.Yu., Sinelnichenko. A.K., Izvekov. A.V., Khyzhun, O.Yu.; *J. Alloys Compds,* 492, (2010), 39-43.

[98]   Lototskyy. M.V., Davids. M.W.; *Method for preparing hydride-forming alloys*, Patent application ZA 2011/03817, 2011.

[99]   Sawa. H., Wakao. S.; *Mater. Trans. JIM*, 31, (1991), 487-492.

[100]   Yoshida. M., Akiba. E.; *J.Alloys and Compounds*, 224, (1995), 121-126.

[101]   Hout. J., Akiba. E., Ogura. T., Ishido. Y.; *J. Alloys and Compounds*, 218, (1995).

[102]   Bobet. J.L., Darriet. B.; *International Journal of hydrogen Energy*, 25, (2000), 767-772.

[103]   Guanping. Li., Nobuyuki. N., Hirobisa. S., Naoki. K.; *J. Alloys and Compounds*, 393, (2005), 231-238.

[104]   Davidson. D.J., Srivastava. O.N.; *Int. J. Hydrogen Energy*, 26, (2001), 219-223.

[105]   Sudipta. R., Singh. B.K., Lototsky, M.V., Srivastava. O.N.; *J. Alloys and Compounds*, 397, (2005), 140-148.

[106]   Yali. J., Xiaopeng. L., Jing. M., Xiumei. G., Zhinian. L., Lijun. J., Shumao, W.; *Rare Metals*, Vol. 29, No. 6, Dec 2010, p. 589.

[107]   Williams. M., Nechaev. A.N., Lototsky. M.V., Yartys. V.A., Solberg. J.K., Denys R.V.; *Material Chemistry and Physics*., 115, (2009), 136-141.

[108]   Ren. J., Williams. M., Lototskyy. M.V., Davids. W., Ulleberg. Ø.; *Int. J. Hydrogen Energy*, 35(16), (2010), 8626-8630.

[109]   Roa. F., Way. J.D., McCormick. R.L, Paglieri. S.N.; *Chemical Engineering Journal*, 93, (2003), 11-22.

[110]   Lewis. F.A.; (1967) The Palladium / Hydrogen System, *London, Academic Press*, 1-12, 48-49.

[111]   Bratanich. T.I., Bulanov. V.N., Skorokhod. V.V., Klimenko. V.P.; *Powder Metallurgy and Metal Ceramics*, 39 (11-12): (2000), 575-583.

[112]   Geng. M.; *J. Alloys and Compounds*, 215:(1994), 151-153.

[113]   Nakamura. K., Uchida. H., Fromm. E.; *J. Less-Common Metals*, 80, (1981), 19-30.

[114]   Harris. I.R., Willey. D.B., Pederzollic. D., Pratt. A.S., Swift. J.,   Walton. A.; *J. Alloys and Compounds*, 330-332, (2002), 806–809.

[115]   Yun. S., Ted Oyama. S.; *J. Membrane Science,* 375, (2011), 28-45.

[116]   Züchner. H., Barlag. H., Majer. G.; *Journal of Alloys and Compounds*, 330–332, (2002), 448–453.

[117]   Wu. H., Anan. A. A.; U.S. Patent. 5,451,474(1995).

[118]   Harris. I.R., Willey. D.B., Pederzollic. D., Pratt. A.S., Swift. J., Walton. A.; *J. Alloys and Compounds*, 330-332, (2002), 806-809.

[119]   Ambrosio. R.C., Ticianelli. E.A.; *Surface and Coatings Technology*, 197, (2005), 215-222.

[120]   Zaluski. L., Zaluska. A., Tessier. P., Strom-Olsen. J.O., Schulz. R.; *J. Alloys and Compounds*, 217, (1995), 295-300.

[121]   Shan. X., Payer. J.H., Wainright. J.S*.; J. Alloys and Compounds*, 430, (2007) 262-268.

[122]   McCool. B.A., Lin. Y.S.; *J. Materials Science*, 36, (2001), 3221 – 3227.

[123]   Heller. E.M.B., Vredenberg. A.M., Boerma. D.O.; *Appl Surf Sci* 2006; 253: 771-777.

[124]   Jowes. A.L., Hitchmen. M.L.; Chemical Vapour Deposition Precursors, *Processes and   Application*, (2009), 570.

[125]   Xomeritaks. G., Lin. Y.; *ALCHE Journal*, 44, (1998), 174-183.

[126]   Ye. J., Dan. G., Yuan. Q.; *Key Eng. Material*, 61, (2001), 437-442.

[127] Xomeritaks. G., Lin. Y.S.; *J. Membrane Science*, 120, (1996), 261-272.

[128]   Jun. C.S., Lee. K.H.; *J. Membrane Science*, 176, (2000), 121-130.

[129] Fazle. A.K.M, Sakamoto. Y.; *Materials Science and Engineering*, B53, (1998), 256–261.

[130]   Hawkins. J.A., Rittenhouse. J.L.; *J. Chemical Education* .**85 (1)**   (January2008).

[131] Lattice geometry, lattice vectors and reciprocal vectors. Available [ONLINE] http://ocw.mit.edu/courses/earth-atmospheric-and-planetary-sciences/12-108-structure-of-earth-materials-fall-2004/lecture-notes/lec7.pdf.

[132] Scanning   Electron   Microscopy,   Available   [ONLINE] http://en.wikipedia.org/wiki/Scanning electron microscope.

[133] Energy   Dispersive   X-Ray   Spectroscopy,   Available   [ONLINE] http://en.wikipedia.org/wiki/Energy-dispersive X-ray spectroscopy.

[134] Welz. B., Sperling. M.; (1999) *Atomic Absorption spectroscopy, 3rd   Completely Revised Edition*, Weinheim, Wiley-VCH Verlag GmbH, **1**: 1-3, **8**: 335, **9**: 537-540, 500-502, 553.

[135] Lajunen. L.H.J.; (1992) *Spectrochemical Analysis by Atomic Absorption and Emission*, Bath, Royal Society of Chemistry, **2**: 45-48.

[136] Sastri. M.V.C., Viswanathan. B, Murthy. S.S.; (1998) *Metal Hydrides: Fundamentals and Applications*, New Delhi, Narosa Publishing House, 11-13.

[137] Bliznakov. S., Lefterova. E., Bozukov. L., Popov. A., Andreev. P.; *Techniques for Characterization of Hydrogen Absorption/Desorption in Metal Hydride Alloy*, Proceedings of the International Workshop" Advanced Techniques for Energy Sources Investigation and Testing" Sofia, Bulgaria.4-9 September 2004.

[138] Pons. M., Dantzer. P.; Hydrogen Energy Progress. IX. Proc. 9-th World Hy-drogen Energy Conf., Paris, France, 22-25 June (1992).– Ed. by T.N.Veziroğlu, C.Derive and J.Pottier., MCI, Paris, vol.2, p.961-970.

[139] Fukai. Y.; Springer-Verlag, Berlin e.a., (1993).– 355 pp.

[140] Flanagan. T.B., Oates. W.A.; Hydrogen in Intermetallic Compounds. I.– Ed. by L.Schlapbach, Springer-Verlag, 1988, p.49–85.

[141] Lacher JR.; Proc. Roy. Soc. (London) A161 (1937) 525-545.

[142] Kierstead HA.; *J. Less-Common Metals,* 71 (1980) 303 - 309.

[143] Lototskyy. M.V., Yartys. V.A., Marinin. V.S., Lototskyy. N.M.; *J. Alloys and Compounds* .356–357 (2003) 27–31.

[144] Rupp. B.; *J. Less-Common Met.* 104 (1984) 51-63.

[145] Lavrentyev. A.A., Gabrelian. B.V., Shkumat. P.N., Nikiforov. I.Ya., Zavaliy. I.Yu., Sinelnichenko. A.K., Izvekov. A.V., Khyzhun. O.Yu.; *J. Alloys and Compounds* 492 (2010) 39-43.

[146] Stuwe. H.P., Shimomura. Y.; *Metallkd,* 51 (1960) 180-181.

[147] Busch. G., Schlapbach. L., Stucki. F., Fischer. P., Andresen. A.F.; *Int. J. Hydrogen Energy* 4 (1979) 29-39.

[148] Fischer. P., Schefer. J., Yvon. K., Schlapbach. L., Riesterer. T.; *J. Jess-Common Metals* 129 (1987) 39-45.

[149] Sumiyama. K., Ezawa. H., Nakamura. Y.; *Physica Status Solidi A* 93 (1986) 81-86.

[150] Numakura. H., Koiwa. M.; *Acta Metallurgica* 32 (1984) 1799-1807.

[151] Saita. I., Sato. M., Uesugi. H., Akiyama. T.; *J. Alloys Compds* 446-447 (2007).

[152] Nersisyan. H.H., Lee. J.H., Won. C.W.; *Materials Research Bulletin* 38 (2003) 1135–1146.

[153] Zheng. H., Ito. H., Okabe. T.H.; *Materials transactions*, (48) (8) (2007) 2244-2251.

[154] Meerson. G.A., Kolchin. O.P.; Atomic Energy, 2 (3) 305-312, DOI: 10.1007/BF01514612.

[155] Barth. F.W., Posnjak. E.; The Crystal Structure of Ilmenite, Z. Kristailographie. 88 (1934) 265-270.

[156] Voløen. L.O.; *Metal Hydrides for Rechargeable Batteries*, Published PhD Thesis, Norway: Norwegian University of Science and Technology, (2000).

[157] Fromm. E., Uchida. H.; *J Less-Common Met* 1987; 131: 1-12.

[158] Holmberg. M., Lundström. I.; *Applied Surface Science*, 93: 67-76, (1996).

[159] Lototsky. M.V., Williams. M., Yartys. V.A., Klochko, Ye.V., Linkov, V.M.; *J. Alloys and Compounds*. (2010).

[160] Wunder. V.K., Schmid. S., Popovska. N., Emig. G.; *Surf Coatings Tech* (2002); 151-152: 96-99.

[161] Hierso. J.C., Feurer. R., Kalck. P.; *Coord Chem Rev* (1998); 178-180:1811-1834.

[162] Semyannikov. P.P., Grankin. V.M., Igumenov. I.K., Bykov. A.F.; *J de Physique IV (*1995); C5: 205-211.

[163] Knyazeva. A.N., Shugam. E.A., Shkol'nikova. L.M.; Crystal chemical data regarding intracomplex compounds of beta diketones. VI. Crystal and molecular structure of palladium acetylacetonate. Zhurnal Strukturnoi Khimii 1970; 11(5): 938-939.

[164] Anderson. E.; *J. Less-Common Met* 1964; 6: 81-84.

[165] Lee. S.M., Perng. T.P.; *Int J Hydrogen Energy* 2000; 25: 831-836.

[166] Popov. V.N., *Material Science and Engineering*, R, 43, (2004) 61-102.

[167] D. Fruchart., P.Chaudouet., R.Fruchart., A.Rouault., J.P.Senateur.; *J. Solid State Chem*. 51 (1984) 246 – 252.

225

[168] Ntsendwana. B.; *Advanced Low Temperature Metal Hydride Materials for Low Temperature Proton Exchange Membrane Fuel Cell Application*, MSc Thesis, University of the Western Cape, 2010.

[169] Halldors. H., Sigfusson. T.I., Ingason. H.Th., Yartys. V.A., Lototsky. M.V.; Geothermally Driven Metal Hydride Hydrogen Compression; 2006 *NORSTORE conference/workshop*, Jyllinge, Denmark, May 29–31, 2006.

[170] Davids. M.W., Lototskyy. M.V., Nechaev. A., Naidoo. Q., Williams. M., Klochko. Ye.; Surface modification of TiFe hydrogen storage alloy by metal-organic chemical vapour deposition of palladium; *Int. J. Hydrogen Energy*, 36 (2011) 9743-9750.

[171] Davids. W., Lototsky. M., Williams. M.; Bulk- and surface-modified hydrogen storage materials on the basis of TiFe; HYDROGEN MATERIALS SCIENCE AND CHEMISTRY OF CARBON NANOMATERIALS / ICHMS'2009, *XI International Conference, Yalta − Crimea − UKRAINE*, August 25−31, 2009; Ed. by D.V. Schur, S.Yu. Zaginaichenko, T.N., Veziroglu, V.V. Skorokhod. AHEU, Kiev-2009, pp.14-15.

[172] Williams. M., Lotolsky. M.V., Davids. M.W., Linkov. V., Yartys. V.A., Solberg. J.K.; Chemical Surface Modification for the Improvement of the Hydrogenation Kinetics and Poisoning Resistance of TiFe and MmNi5; *International Symposium "Metal-Hydrogen Systems. Fundamentals and Applications" (MH-2010)*, Moscow, Russia July 19-23, 2010, Book of Abstracts, p.213.

[173] Davids. W.; Advanced Ti-based AB and AB2 Hydride-forming Materials; oral presentation at UWC, *Faculty of Natural Science Postgraduate Research Open day*, 25-26 October 2011, University of the Western Cape, Bellville.

APPENDIX

Reference data on compositions and thermodynamic properties of Ti- and Zr-based AB$_2$-type hydride forming intermetallides

Table A1 presents reference data on compositions and thermodynamic properties of Ti- and Zr-based AB$_2$-type hydride forming intermetallides. Most of the data were taken from reference book [1] published in 1995 and review [2] published in 1988, as well as the original works mainly published in 1980th. These data were supplemented by the results of the recent study [3] of Fe-containing Ti- and Zr-based intermetallides characterised by high equilibrium pressures of the corresponding hydrides.

The table contains 139 records presenting the data about 87 AB$_{2\pm x}$ intermetallic alloys where A=Ti,Zr; B=Cr,Mn,Fe,Ni,Cu,V. The compositions specified in the formula column are formalised to yield the matrix containing the data on B:A stoichiometric ratio, as well as fractions (0…1) of the components on the A- and B-sides. Of these data, the fractions of Zr, Cr, Mn, Ni, Cu and V, as well as deviation, $x = B/A–2$, of the alloy's composition from the AB$_2$ stoichiometry were selected as independent variables for further fitting / regression analysis. The corresponding

columns in the table are shadowed in grey. The absolute values of hydrogenation enthalpy and entropy (all presented per 1 mole of H_2) characterising thermodynamic behaviours of the intermetallides in systems with gaseous hydrogen are presented in the next columns shadowed in light turquoise.

#	Formula	B:A	Ti	Fe	Zr	Cr	Mn	Ni	Cu	V	(B:A-2)	-ΔH [kJ/mol H_2]	-ΔS [J/(mol H_2 K)]	Notes	Ref
					Fitting variables										
1	Ti0.05Zr0.95Cr0.8Fe1.2	2.000	0.050	0.600	0.950	0.400	0.000	0.000	0.000	0.000	0.000	32.600	102.00	H/f.u.=1	1, 7
2	Ti0.1Zr0.9Cr0.6Fe1.4	2.000	0.100	0.700	0.900	0.300	0.000	0.000	0.000	0.000	0.000	29.800	104.00	H/f.u.=1	1 ,7
3	Ti0.1Zr0.9Cr0.7Fe1.3	2.000	0.100	0.650	0.900	0.350	0.000	0.000	0.000	0.000	0.000	32.100	106.00	H/f.u.=1	1 ,7
4	Ti0.1Zr0.9Cr0.8Fe1.2	2.000	0.100	0.600	0.900	0.400	0.000	0.000	0.000	0.000	0.000	34.500	104.00	H/f.u.=1	1, 7
5	Ti0.1Zr0.9Cr0.8Fe1.2	2.000	0.100	0.600	0.900	0.400	0.000	0.000	0.000	0.000	0.000	30.200	99.00	H/f.u.=1	1, 7
6	Ti0.1Zr0.9Cr0.9Fe1.1	2.000	0.100	0.550	0.900	0.450	0.000	0.000	0.000	0.000	0.000	34.800	105.00	H/f.u.=1	1, 7
7	Ti0.1Zr0.9CrFe	2.000	0.100	0.500	0.900	0.500	0.000	0.000	0.000	0.000	0.000	36.100	105.00	H/f.u.=1	1, 7
8	Ti0.2Zr0.8Cr0.15Mn0.85Fe	2.000	0.200	0.500	0.800	0.075	0.425	0.000	0.000	0.000	0.000	23.400	90.50		1, 8
9	Ti0.2Zr0.8Cr0.15Mn0.85Fe	2.000	0.200	0.500	0.800	0.075	0.425	0.000	0.000	0.000	0.000	31.600	98.00		1, 8
10	Ti0.2Zr0.8Cr0.25Mn0.75Fe	2.000	0.200	0.500	0.800	0.125	0.375	0.000	0.000	0.000	0.000	29.600	96.40		1, 8
11	Ti0.2Zr0.8Cr0.25Mn0.75Fe	2.000	0.200	0.500	0.800	0.125	0.375	0.000	0.000	0.000	0.000	33.400	112.00		1, 8
12	Ti0.2Zr0.8Cr0.5Mn0.5Fe	2.000	0.200	0.500	0.800	0.250	0.250	0.000	0.000	0.000	0.000	26.400	93.40		1, 8
13	Ti0.2Zr0.8Cr0.5Mn0.5Fe	2.000	0.200	0.500	0.800	0.250	0.250	0.000	0.000	0.000	0.000	30.800	104.00		1, 8
14	Ti0.2Zr0.8Cr0.6Fe1.4	2.000	0.200	0.700	0.800	0.300	0.000	0.000	0.000	0.000	0.000	26.800	99.60	H/f.u.=0.5-2.0	1, 9

#	Formula													Notes	Ref
15	Ti0.2Zr0.8Cr0.6Fe1.4	2.000	0.200	0.700	0.800	0.300	0.000	0.000	0.000	0.000	0.000	26.800	99.60		2, 9
16	Ti0.2Zr0.8Cr0.75Mn0.25Fe	2.000	0.200	0.500	0.800	0.375	0.125	0.000	0.000	0.000	0.000	29.600	96.40		1, 8
17	Ti0.2Zr0.8Cr0.75Mn0.25Fe	2.000	0.200	0.500	0.800	0.375	0.125	0.000	0.000	0.000	0.000	33.000	104.00		1, 8
18	Ti0.2Zr0.8Cr0.8Fe1.2	2.000	0.200	0.600	0.800	0.400	0.000	0.000	0.000	0.000	0.000	30.700	102.00	H/f.u.=1	1, 7
19	Ti0.2Zr0.8CrFe	2.000	0.200	0.500	0.800	0.500	0.000	0.000	0.000	0.000	0.000	31.100	93.50	H/f.u.=1	1, 7
20	Ti0.2Zr0.8CrFe	2.000	0.200	0.500	0.800	0.500	0.000	0.000	0.000	0.000	0.000	31.000	93.40		1, 8
21	Ti0.2Zr0.8Mn2	2.000	0.200	0.000	0.800	0.000	1.000	0.000	0.000	0.000	0.000	47.300	116.00		1, 10
22	Ti0.2Zr0.8MnFe	2.000	0.200	0.500	0.800	0.000	0.500	0.000	0.000	0.000	0.000	33.000	111.40		2, 11
23	Ti0.2ZrFe2	2.000	0.200	1.000	1.000	0.000	0.000	0.000	0.000	0.000	0.000	19.800	125.00		3
24	Ti0.3Zr0.7Cr0.6Fe1.4	2.000	0.300	0.700	0.700	0.300	0.000	0.000	0.000	0.000	0.000	21.900	89.40	H/f.u.=0.5-2.0	1, 9
25	Ti0.3Zr0.7Cr0.6Fe1.4	2.000	0.300	0.700	0.700	0.300	0.000	0.000	0.000	0.000	0.000	21.900	89.40		2, 9
26	Ti0.3Zr0.7CrFe	2.000	0.300	0.500	0.700	0.500	0.000	0.000	0.000	0.000	0.000	30.400	98.10	H/f.u.=0.75-2.0	1, 12
27	Ti0.3Zr0.7CrFe	2.000	0.300	0.500	0.700	0.500	0.000	0.000	0.000	0.000	0.000	30.400	98.10		2, 13
28	Ti0.3Zr0.7Mn2	2.000	0.300	0.000	0.700	0.000	1.000	0.000	0.000	0.000	0.000	33.000	90.00		2, 14
29	Ti0.4Zr0.6Fe2	2.000	0.400	1.000	0.600	0.000	0.000	0.000	0.000	0.000	0.000	18.300	127.00		3
30	Ti0.4Zr0.6Mn2	2.000	0.400	0.000	0.600	0.000	1.000	0.000	0.000	0.000	0.000	36.000	103.00		1, 10
31	Ti0.5Zr0.5Cr0.8Fe1.2	2.000	0.500	0.600	0.500	0.400	0.000	0.000	0.000	0.000	0.000	33.000	99.00	H/f.u.=1	1, 7
32	Ti0.5Zr0.5CrFe	2.000	0.500	0.500	0.500	0.500	0.000	0.000	0.000	0.000	0.000	32.400	113.00	H/f.u.=1	1, 7
33	Ti0.6Zr0.4Mn1.9Cu0.1	2.000	0.600	0.000	0.400	0.000	0.950	0.000	0.050	0.000	0.000	27.745	94.14	DH & DS calcurated from PD vs T	1, 10
34	Ti0.6Zr0.4Mn2	2.000	0.600	0.000	0.400	0.000	1.000	0.000	0.000	0.000	0.000	25.700	91.00		1, 10
35	Ti0.7Zr0.3Cr0.85Mn0.25Fe0.7Ni0.2Cu0.03	2.030	0.700	0.345	0.300	0.419	0.123	0.099	0.014	0.000	0.030	16.394	88.54	JSW (FRN118)	4
36	Ti0.7Zr0.3Fe1.4V0.6	2.000	0.700	0.700	0.300	0.000	0.000	0.000	0.000	0.300	0.000	29.100	108.00		3
37	Ti0.8Zr0.2Cr0.8Mn1.2	2.000	0.800	0.000	0.200	0.400	0.600	0.000	0.000	0.000	0.000	28.900	113.00		1, 10
38	Ti0.8Zr0.2Fe1.6V0.4	2.000	0.800	0.800	0.200	0.000	0.000	0.000	0.000	0.200	0.000	19.300	107.00		3

39	Ti0.8Zr0.2FeNi0.8V0.2	2.000	0.800	0.500	0.200	0.000	0.000	0.400	0.000	0.100	0.000	23.200	106.00		3
40	Ti0.8Zr0.2FeNi0.8V0.2	2.000	0.800	0.500	0.200	0.000	0.000	0.400	0.000	0.100	0.000	15.100	117.00		3
41	Ti0.9Zr0.1Fe1.5Ni0.3V0.2	2.000	0.900	0.750	0.100	0.000	0.000	0.150	0.000	0.100	0.000	12.100	120.00		3
42	Ti0.9Zr0.1Fe1.7V0.3	2.000	0.900	0.850	0.100	0.000	0.000	0.000	0.000	0.150	0.000	14.500	116.00		3
43	Ti1.05Cr2	1.900	1.000	0.000	0.000	1.000	0.000	0.000	0.000	0.000	-0.100	26.193	122.00	TiCr1.9	15
44	Ti1.11Cr2	1.800	1.000	0.000	0.000	1.000	0.000	0.000	0.000	0.000	-0.200	19.001	85.15	TiCr1.8 (C15), low H/f.u.; DH & DS calcurated from PD vs T	1
45	Ti1.1Cr1.2Mn0.8	1.820	1.000	0.000	0.000	0.600	0.400	0.000	0.000	0.000	-0.180	25.100	115.00		1, 16
46	Ti1.2Cr1.2Mn0.8	1.670	1.000	0.000	0.000	0.600	0.400	0.000	0.000	0.000	-0.330	26.000	118.00		1, 16
47	Ti1.2Cr1.9Mn0.1	1.670	1.000	0.000	0.000	0.950	0.050	0.000	0.000	0.000	-0.330	20.100	101.00		1, 16
48	Ti1.2CrMn	1.667	1.000	0.000	0.000	0.500	0.500	0.000	0.000	0.000	-0.333	25.600	111.00		1, 16
49	Ti1.2CrMn	1.667	1.000	0.000	0.000	0.500	0.500	0.000	0.000	0.000	-0.333	25.500	111.30		2, 17
50	Ti1.33Mn2	1.500	1.000	0.000	0.000	0.000	1.000	0.000	0.000	0.000	-0.500	23.200	90.00	TiMn1.5, H/f.u.=0.75	1, 18
51	Ti1.33Mn2	1.500	1.000	0.000	0.000	0.000	1.000	0.000	0.000	0.000	-0.500	23.600	94.00	TiMn1.5, H/f.u.=1	1, 18
52	Ti1.33Mn2	1.500	1.000	0.000	0.000	0.000	1.000	0.000	0.000	0.000	-0.500	24.000	96.00	TiMn1.5, H/f.u.=2	1, 18
53	Ti1.33Mn2	1.500	1.000	0.000	0.000	0.000	1.000	0.000	0.000	0.000	-0.500	27.900	112.50	TiMn1.5	1, 18
54	Ti1.33Mn2	1.500	1.000	0.000	0.000	0.000	1.000	0.000	0.000	0.000	-0.500	28.700	114.00	TiMn1.5, H.f.u.=1.8	1, 18
55	Ti1.3Cr1.2Mn0.8	1.540	1.000	0.000	0.000	0.600	0.400	0.000	0.000	0.000	-0.460	25.100	109.00		1, 16
56	Ti1.3Cr1.2Mn0.8	1.538	1.000	0.000	0.000	0.600	0.400	0.000	0.000	0.000	-0.462	25.100	108.40		2, 17
57	TiCr0.4Fe1.4V0.2	2.000	1.000	0.700	0.000	0.200	0.000	0.000	0.000	0.100	0.000	14.000	114.00		3

58	TiCr2	2.000	1.000	0.000	0.000	1.000	0.000	0.000	0.000	0.000	0.000	26.220	122.20	(C14), alfa-beta	1
59	TiCrFe	2.000	1.000	0.500	0.000	0.500	0.000	0.000	0.000	0.000	0.000	17.200	119.00		3
60	TiFe1.4V0.6	2.000	1.000	0.700	0.000	0.000	0.000	0.000	0.000	0.300	0.000	21.500	121.00		3
61	TiFe2	2.000	1.000	1.000	0.000	0.000	0.000	0.000	0.000	0.000	0.000	14.000	134.50	(calc)	3
62	Zr1.05Fe2	1.900	0.000	1.000	1.000	0.000	0.000	0.000	0.000	0.000	-0.100	21.800	121.40	ZrFe1.9	3
63	ZrCr0.25MnFe	2.250	0.000	0.444	1.000	0.111	0.444	0.000	0.000	0.000	0.250	25.800	75.00		2, 19
64	ZrCr0.2Fe1.8	2.000	0.000	0.900	1.000	0.100	0.000	0.000	0.000	0.000	0.000	23.200	108.00		3
65	ZrCr0.4Fe1.6	2.000	0.000	0.800	1.000	0.200	0.000	0.000	0.000	0.000	0.000	28.200	100.20	H/f.u.=0.6-2.1 (DH recalculated from ../mol H)	1, 6
66	ZrCr0.4Fe1.6	2.000	0.000	0.800	1.000	0.200	0.000	0.000	0.000	0.000	0.000	28.400	99.20	H/f.u.=0.6 (DH recalculated from ../mol H)	1, 6
67	ZrCr0.4Fe1.6	2.000	0.000	0.800	1.000	0.200	0.000	0.000	0.000	0.000	0.000	27.600	100.40	H/f.u.=2.1 (DH recalculated from ../mol H)	1, 6
68	ZrCr0.5Fe1.5	2.000	0.000	0.750	1.000	0.250	0.000	0.000	0.000	0.000	0.000	24.300	92.60	H/fu=1	1, 7
69	ZrCr0.5Fe1.5	2.000	0.000	0.750	1.000	0.250	0.000	0.000	0.000	0.000	0.000	32.400	113.10	H/fu=1	1, 7
70	ZrCr0.5Fe1.5	2.000	0.000	0.750	1.000	0.250	0.000	0.000	0.000	0.000	0.000	24.300	92.00		1, 7
71	ZrCr0.5Fe1.5	2.000	0.000	0.750	1.000	0.250	0.000	0.000	0.000	0.000	0.000	24.300	92.10		20, 21
72	ZrCr0.6Fe1.4	2.000	0.000	0.700	1.000	0.300	0.000	0.000	0.000	0.000	0.000	26.800	88.90	H/fu=0.5-2.25	1, 9
73	ZrCr0.6Fe1.4	2.000	0.000	0.700	1.000	0.300	0.000	0.000	0.000	0.000	0.000	26.400	84.70	H/fu=0.5	1, 9
74	ZrCr0.6Fe1.4	2.000	0.000	0.700	1.000	0.300	0.000	0.000	0.000	0.000	0.000	26.670	88.10	H/fu=2.25	1, 9

75	ZrCr0.6Fe1.4	2.000	0.000	0.700	1.000	0.300	0.000	0.000	0.000	0.000	0.000	30.000	100.50	H/f.u.=0.6-2.1 (DH recalculated from ../mol H)	1, 6
76	ZrCr0.6Fe1.4	2.000	0.000	0.700	1.000	0.300	0.000	0.000	0.000	0.000	0.000	30.000	99.00	H/f.u.=0.6 (DH recalculated from ../mol H)	1, 6
77	ZrCr0.6Fe1.4	2.000	0.000	0.700	1.000	0.300	0.000	0.000	0.000	0.000	0.000	30.800	103.00	H/f.u.=2.1 (DH recalculated from ../mol H)	1, 6
78	ZrCr0.6Fe1.4	2.000	0.000	0.700	1.000	0.300	0.000	0.000	0.000	0.000	0.000	28.500	94.70		20, 21
79	ZrCr0.6Fe1.4	2.000	0.000	0.700	1.000	0.300	0.000	0.000	0.000	0.000	0.000	26.400	88.90		2, 9
80	ZrCr0.8Fe1.2	2.000	0.000	0.600	1.000	0.400	0.000	0.000	0.000	0.000	0.000	33.000	99.30	H/fu=1	1, 7
81	ZrCr0.8Fe1.2	2.000	0.000	0.600	1.000	0.400	0.000	0.000	0.000	0.000	0.000	29.000	90.10	H/fu=1	1, 7
82	ZrCr0.8Fe1.2	2.000	0.000	0.600	1.000	0.400	0.000	0.000	0.000	0.000	0.000	35.800	102.40	H/f.u.=0.6-2.1 (DH recalculated from ../mol H)	1, 6
83	ZrCr0.8Fe1.2	2.000	0.000	0.600	1.000	0.400	0.000	0.000	0.000	0.000	0.000	35.200	100.30	H/f.u.=0.6 (DH recalculated from ../mol H)	1, 6
84	ZrCr0.8Fe1.2	2.000	0.000	0.600	1.000	0.400	0.000	0.000	0.000	0.000	0.000	37.000	105.00	H/f.u.=2.1 (DH recalculated from ../mol H)	1, 6
85	ZrCr2	2.000	0.000	0.000	1.000	1.000	0.000	0.000	0.000	0.000	0.000	46.100	98.00	(C15)	1, 22

86	ZrCr2Fe0.8	2.800	0.000	0.286	1.000	0.714	0.000	0.000	0.000	0.000	0.800	46.500	130.70	H/f.u.=1	1, 5
87	ZrCr2Fe0.8	2.800	0.000	0.286	1.000	0.714	0.000	0.000	0.000	0.000	0.800	48.700	137.30	H/f.u.=1.5	1, 5
88	ZrCr2Ni0.8	2.800	0.000	0.000	1.000	0.714	0.000	0.286	0.000	0.000	0.800	36.400	93.10	H/f.u.=1	1, 5
89	ZrCr2Ni0.8	2.800	0.000	0.000	1.000	0.714	0.000	0.286	0.000	0.000	0.800	37.400	98.10	H/f.u.=1.25	1, 5
90	ZrCr2Ni0.8	2.800	0.000	0.000	1.000	0.714	0.000	0.286	0.000	0.000	0.800	37.900	101.20	H/f.u.=1.5	1, 5
91	ZrCr2Ni0.8	2.800	0.000	0.000	1.000	0.714	0.000	0.286	0.000	0.000	0.800	40.100	108.60	H/f.u.=1.75	1, 5
92	ZrCrFe	2.000	0.000	0.500	1.000	0.500	0.000	0.000	0.000	0.000	0.000	49.400	134.00		1, 22
93	ZrCrFe	2.000	0.000	0.500	1.000	0.500	0.000	0.000	0.000	0.000	0.000	36.600	99.80	H/fu=0.5-1.75	1, 12
94	ZrCrFe	2.000	0.000	0.500	1.000	0.500	0.000	0.000	0.000	0.000	0.000	36.100	96.40	H/fu=0.5	1, 12
95	ZrCrFe	2.000	0.000	0.500	1.000	0.500	0.000	0.000	0.000	0.000	0.000	36.500	100.70	H/fu=1.75	1, 12
96	ZrCrFe	2.000	0.000	0.500	1.000	0.500	0.000	0.000	0.000	0.000	0.000	39.000	102.70	H/f.u.=0.6-2.1 (DH recalculated from ../mol H)	1, 6
97	ZrCrFe	2.000	0.000	0.500	1.000	0.500	0.000	0.000	0.000	0.000	0.000	37.800	99.40	H/fu=0.6 (DH recalculated from ../mol H)	1, 6
98	ZrCrFe	2.000	0.000	0.500	1.000	0.500	0.000	0.000	0.000	0.000	0.000	41.200	106.80	H/fu=2.1 (DH recalculated from ../mol H)	1, 6
99	ZrCrFe	2.000	0.000	0.500	1.000	0.500	0.000	0.000	0.000	0.000	0.000	49.400	134.00		20, 21
100	ZrCrFe	2.000	0.000	0.500	1.000	0.500	0.000	0.000	0.000	0.000	0.000	36.600	99.80		2, 13
101	ZrCrFe1.4	2.400	0.000	0.583	1.000	0.417	0.000	0.000	0.000	0.000	0.400	41.400	133.00	H/fu=1-2 (DH and DS recalculated from ../mol H)	1, 21
102	ZrCrFe1.5	2.500	0.000	0.600	1.000	0.400	0.000	0.000	0.000	0.000	0.500	45.400	160.00	H/fu=1-2; (DH and DS recalculated from ../mol H)	1, 23

103	ZrCrFe1.5	2.500	0.000	0.600	1.000	0.400	0.000	0.000	0.000	0.000	0.500	44.800	156.40	H/fu=1; (DH and DS recalculated from ../mol H)	1, 23
104	ZrCrFe1.5	2.500	0.000	0.600	1.000	0.400	0.000	0.000	0.000	0.000	0.500	46.600	164.80	H/fu=2; (DH and DS recalculated from ../mol H)	1, 23
105	ZrCrFe1.5	2.500	0.000	0.600	1.000	0.400	0.000	0.000	0.000	0.000	0.500	22.700	80.00		2, 19
106	ZrCrFe1.6	2.600	0.000	0.615	1.000	0.385	0.000	0.000	0.000	0.000	0.600	29.100	107.60		2, 11
107	ZrCrFe1.6	2.600	0.000	0.615	1.000	0.385	0.000	0.000	0.000	0.000	0.600	25.400	92.40		24
108	ZrCrFe1.8	2.800	0.000	0.643	1.000	0.357	0.000	0.000	0.000	0.000	0.800	19.100	77.20		24
109	ZrCrFeCu0.8	2.800	0.000	0.357	1.000	0.357	0.000	0.000	0.286	0.000	0.800	28.700	87.80		2, 24
110	ZrCrFeNi0.8	2.800	0.000	0.357	1.000	0.357	0.000	0.286	0.000	0.000	0.800	20.900	89.10		2, 24
111	ZrCrMn0.8Fe	2.800	0.000	0.357	1.000	0.357	0.286	0.000	0.000	0.000	0.800	32.100	99.99		2, 24
112	ZrFe1.2Ni0.8	2.000	0.000	0.600	1.000	0.000	0.000	0.400	0.000	0.000	0.000	21.700	114.00		3
113	ZrFe1.4Ni0.6	2.000	0.000	0.700	1.000	0.000	0.000	0.300	0.000	0.000	0.000	21.600	114.00		3
114	ZrFe1.5V0.5	2.000	0.000	0.750	1.000	0.000	0.000	0.000	0.000	0.250	0.000	32.200	87.90		22
115	ZrFe1.6Ni0.4	2.000	0.000	0.800	1.000	0.000	0.000	0.200	0.000	0.000	0.000	22.000	115.00		3
116	ZrFe1.8Cu0.2	2.000	0.000	0.900	1.000	0.000	0.000	0.000	0.100	0.000	0.000	23.600	117.00		3
117	ZrFe1.8Ni0.2	2.000	0.000	0.900	1.000	0.000	0.000	0.100	0.000	0.000	0.000	22.600	120.00		3
118	ZrFe2	2.000	0.000	1.000	1.000	0.000	0.000	0.000	0.000	0.000	0.000	21.200	122.00		3
119	ZrFe2.5	2.500	0.000	1.000	1.000	0.000	0.000	0.000	0.000	0.000	0.500	18.300	120.00		3
120	ZrFeV	2.000	0.000	0.500	1.000	0.000	0.000	0.000	0.000	0.500	0.000	48.100	93.70		22
121	ZrMn0.2Fe1.8	2.000	0.000	0.900	1.000	0.000	0.100	0.000	0.000	0.000	0.000	21.800	116.00		3
122	ZrMn0.6Fe1.4	2.000	0.000	0.700	1.000	0.000	0.300	0.000	0.000	0.000	0.000	24.300	95.30		2, 25
123	ZrMn1.11Fe1.22	2.330	0.000	0.524	1.000	0.000	0.476	0.000	0.000	0.000	0.330	29.400	104.90		2, 11
124	ZrMn1.22Fe1.14	2.360	0.000	0.483	1.000	0.000	0.517	0.000	0.000	0.000	0.360	31.000	106.00		2, 11
125	ZrMn1.2Fe0.8	2.000	0.000	0.400	1.000	0.000	0.600	0.000	0.000	0.000	0.000	33.100	96.40		1, 22

126	ZrMn2	2.000	0.000	0.000	1.000	0.000	1.000	0.000	0.000	0.000	0.000	53.200	122.00		1, 22
127	ZrMn2	2.000	0.000	0.000	1.000	0.000	1.000	0.000	0.000	0.000	0.000	53.100	122.00		20, 26, 27, 28
128	ZrMn2.5	2.500	0.000	0.000	1.000	0.000	1.000	0.000	0.000	0.000	0.500	18.000	51.50		20, 27, 29
129	ZrMn2.7	2.700	0.000	0.000	1.000	0.000	1.000	0.000	0.000	0.000	0.700	33.600	100.60		2, 11
130	ZrMn2.8	2.800	0.000	0.000	1.000	0.000	1.000	0.000	0.000	0.000	0.800	29.900	92.70		2, 21
131	ZrMn2Cu0.8	2.800	0.000	0.000	1.000	0.000	0.714	0.000	0.286	0.000	0.800	31.600	83.40		2, 30
132	ZrMn2Cu0.8	2.800	0.000	0.000	1.000	0.000	0.714	0.000	0.286	0.000	0.800	25.800	58.00		2, 31
133	ZrMn2Fe0.8	2.800	0.000	0.286	1.000	0.000	0.714	0.000	0.000	0.000	0.800	29.300	107.60		2, 11
134	ZrMn2Ni0.8	2.800	0.000	0.000	1.000	0.000	0.714	0.286	0.000	0.000	0.800	19.100	70.30		2, 31
135	ZrMn3.8	3.800	0.000	0.000	1.000	0.000	1.000	0.000	0.000	0.000	1.800	19.000	55.00		20, 26
136	ZrMn3.8	3.800	0.000	0.000	1.000	0.000	1.000	0.000	0.000	0.000	1.800	19.800	61.70		27, 29
137	ZrMnFe	2.000	0.000	0.500	1.000	0.000	0.500	0.000	0.000	0.000	0.000	30.200	89.70		1, 22
138	ZrMnFe	2.000	0.000	0.500	1.000	0.000	0.500	0.000	0.000	0.000	0.000	37.200	109.80		2, 25
139	ZrV2	2.000	0.000	0.000	1.000	0.000	0.000	0.000	0.000	1.000	0.000	78.000	88.40		27

UNIVERSITY *of the*
WESTERN CAPE

References to the appendix

[1]   B.A.Kolachev, R.E.Shanin, A.A.Il'in. Hydrogen Storage Alloys / Reference Book, Moscow, "Metallurgy" Publ., 1995.

[2]   P.Dantzer, F.Meuner. What materials to use in hydride chemical heat pumps. - Materials Science Forum, vol.31 (1988), pp.1-18.

[3]   R.B.Sivov. Intermetallic hydrides of Ti and Zr with structures of Laves Phases with high dissociation pressures; PhD thesis abstract, Moscow State Univ. 2011.

[4]   H.Halldors, T.I.Sigfusson, H.Th.Ingason, V.A.Yartys, M.V.Lototsky. GeothermallyDriven Metal Hydride Hydrogen Compression; 2006 NORSTORE conference/workshop, Jyllinge, Denmark, May 29–31, 2006.

[5]   Drasner A., Blazina Z. //J. Less-Common Metals. 1991. V. 168. P. 289-294.

[6]   Quian S., Northwood D.O. //J. Less-Common Metals. 1989. V. 147. P. 149-150.

[7]   Jong-Man Park, Jai-Jong Lee//J. Less-Common Metals. 1990. V. 160. P. 259-261.

[8]   Park John-Man, Lee Jai-Young. //J. Less-Common Metals. 1991. V. 167. P. 245-253.

[9]   Pourarian F., Wallace W.E. //J. Less-Common Metals. 1985. V. 107. P. 69-78.

[10]   Oesterreicher H., Bittner H. //Mat. Res. Bull. 1978. V. 13, # 1. P. 83-89.

[11]   M.Uchida, H.Bjurstrom, S.Suda, Y.Matsubara. - J.Less-Common Met., 1986, 119, 69.

[12]   J. Less-Common Metals. 1985. V. 106, p. 79.

[13]   G.Y.Yu, F.Pourarian, W.E.Wallace. - J. Less-Common Met., 1985, 106, 79.

[14]   H.Fujii, V.K.Sinha, W.E.Wallace. - J. Phys. Chem., 1981, 85, 3112.

[15]   J.R.Johnson. Reaction of Hydrogen with the high temperature (C14) Form of TiCr2.- J.Less-Common Met., 1980, v.73, 345-354.

[16]   Proceedings of International Symposium on the Properties and Application of Metal Hydrides. Toba. 1982. Part III. IV. Int. J. Less-Common metals. 1983. V. 89, # 1, 2. p. 257.

[17]   Y.Osumi, H.Suzuki, A.Kato, K.Oguro, T.Sugioka, T.Fujita.- J.Less-Common Met., 1983, 89, 257).

[18]   J. Less-Common Metals. 1985. V. 106, p. 199.

[19]   V.K.Sinha, W.E.Wallace. - J.Phys.Chem., 1985, 88, 105.

[20]   Padurets L.N., Chertkov A.A., Mikheeva V.I. Synthesis and properties of hydrogen ternary compounds in systems Zr-M-H (M=V,Cr,Mn,Fe,Co,Ni). // Proc. Acad.Sci. USSR, inorganic materials.- 1978.- V.14.- P.1624-1628.

[21]   Pedziwiatr A.T., Craig R.S., Wallace W.E., Pourarian F. Calorimetric entalpies of formation and decomposition of ZrMn2, ZrCr2 and related systems. // J.Solid State Chem.- 1983.- Vol.46.- P.336-341.

[22]   Shaltiel D., Jacob I., Davidov D. Hydrogen absorption and desorption properties of AB2 Laves-phase pseudobinary compounds. // J.Less-Common Met.- 1977.- Vol.53.- P.117-131.

[23]   J. Less-Common Metals. 1985. V. 106, p. 67.

[24]   F.Pourarian, W.E.Wallace. - J. Solid St. Chem, 1981, 55, 181.

[25]   A.Suzuki, N.Nishimiya, S.Ono. - J.Less-Common Met., 1983, 89, 263.

[26]   Padurets L.N., Chertkov A.A., Mikheeva V.I. Synthesis and properties of hydrogen ternary compounds in systems Zr-M-H (M=V,Cr,Mn,Fe,Co,Ni). // Proc. Acad.Sci. USSR, inorganic materials.- 1978.- V.14.- P.1624-1628.

[27]   Shilov A.L., Padurets L.N., Kost M.E. Thermodynamics of hydrides of intermetallic compounds of transition metals. // Russ. J. Phys. Chem.- 1985-V.59, No 8.- P.1857-1875.

[28]   Van-Essen R.M., Buschow K.H.J. Composition and hydrogen absorption of C14 type Zr-Mn compounds. // Mater. Res. Bull. - 1980. - Vol.15. - P.1149-1155.

[29]   Buschow K.H.J., Bouten P.C.P., Miedema A.R. Hydrides formed from intermetallic compounds of two transition metals: a special class of ternary alloys. // Rep.Prog.Phys. - 1982. - Vol.45, No 9. - P.937-939.

[30] Ivey D.G., Northwood D.O. Hydriding properties of Zr(FexCr1-x)2 intermetallic compounds. // Int. J. Hydrogen Energy. - 1986- Vol.11, No 9. - P.583-591.

[31] F.Pourarian, V.K.Sinha, W.E.Wallace. - J.Less-Common Met., 1984, 96, 237.

UNIVERSITY *of the*
WESTERN CAPE